Metal Substitution Studies of an Extradiol Dioxygenase
and
X-Ray Absorption Studies of High-Valent Nonheme Iron Complexes

A DISSERTATION
SUBMITTED TO THE FACULTY OF THE GRADUATE SCHOOL
OF THE UNIVERSITY OF MINNESOTA
BY

Erik Rejman Farquhar

IN PARTIAL FULFILLMENT OF THE REQUIREMENTS
FOR THE DEGREE OF
DOCTOR OF PHILOSOPHY

Professor Lawrence Que, Jr.

July 2010

Acknowledgements

First and foremost, I would like to thank my advisor, Prof. Larry Que, for the wonderful opportunity to work in his lab for the past six years. One of the best things about working in Larry's group is the sheer number of projects there are on offer, as well as Larry's flexibility in both the breadth and depth of what his students can work on. I have been greatly privileged to be able to sink my claws into a wide range of synthetic and biochemical projects involving many different members of the Que lab through my involvement in the group's XAS efforts. The other facet of Larry's approach to science that I find invaluable is his emphasis on collaboration, not only within the group itself in the form of the XAS team, but also with scientists scattered across the US and the rest of the world. Sometimes I dreaded those e-mails from collaborators ("could you send us more protein next week?"), but on the whole, I found it to be a priceless education in terms of learning to play nice in the sandbox with others professionally, which is something that I know will serve me well in the future.

I also want to thank Prof. John Lipscomb for the opportunity to be involved in several projects involving members of his group, and especially for his insights into reaction mechanisms through enzyme kinetics. Larry and John, together with Prof. Bill Tolman, have made a real effort to foster a collegial, collaborative atmosphere in the bioinorganic community at Minnesota. As a result I have had the chance to talk with many graduate students and postdocs from other groups, sharing a lot of science and juicy gossip in the process.

The Que lab, as one former student of Larry's once stated, is an "ever-evolving" place, and all of the many, many people who have been in the group in my time here have contributed in their own way to my experiences. However, there are a number of people to whom I am especially grateful. My coworkers in the "bio lab" have made daily life over the past several years a real joy. When I joined the group, I had no clue about expression vectors, purifying proteins, or any of that stuff, but Dr. Joe Emerson took me under his wing and turned me into a reasonably functional biochemist, imparting a great

deal of his "Southern"-influenced wisdom in the process. I am grateful for a lot of his practical advice in the early stages of my graduate career about both science and non-scientific matters. More recently, I have shared the bio office with Van Vu and Andy Fielding, with whom I always enjoyed talking about science, making jokes, and doing ridiculous things in the lab. It has been a real pleasure for me to watch Van and Andy become independent, well-rounded, and responsible scientists over the past few years.

I have also thankful to all of the members of the Que lab "EXAFS team" with whom I have had the pleasure of going on synchrotron trips and talking about XAS data (in chronological order): Dr. Jan-Uwe Rohde, Dr. Kevin Koehntop, Dr. Xiaopeng Shan, Dr. Tim Jackson, Dr. Adam Fiedler, Van Vu, Dr. Kallol Ray, Dr. Matt Cranswick, Feifei Li, Dr. "Ken" Xue, and Dr. Kathy Van Heuvelen. All of you made those long nights at the beamline worthwhile and fun, even when we were photoreducing everything in sight. I enjoyed all the excellent lunches and dinners in Palo Alto and on Long Island, the periodic trips to the beach, and the time spent just hanging out at the beamline during data collection. I know that some of you look forward to seeing me working with you as your beamline scientist at the NSLS.

Outside of the bio lab and EXAFS team, I want to thank Dr. David Klein ("The Klein") for his sense of humor, derring-do, and forthright honesty when it was desperately necessary. Dr. Eric Klinker and Dr. Paul Oldenburg both exhibited an inspiring ability to take a leadership role among the graduate students in managing the lab, equipment, and group responsibilities during the first half of my time in the group. Morever, both were excellent drinking companions after softball or on Friday afternoons. Dr. Jason England was a font of knowledge about both chemistry and quality-of-life issues, and I always enjoyed my conversations with him, especially during our more cynical moments. Jason contributed significantly to the work presented in this thesis, and I am grateful for his tireless sample preparation efforts (I am always amazed at the sheer scope of his work in Larry's lab over the past four years) and the many discussions we had about the results of my EXAFS analyses. In that vein, I also want to thank Dong Wang and Dr. Aidan McDonald for their contributions to the work presented here and their continued interest in the results I obtained on their samples. Dong in particular

spent a ridiculous amount of time making XAS samples which we then cheerfully photoreduced at the synchrotron, undoubtedly to his dismay. Finally, I want to thank Feifei Li for her friendship and the many insightful conversations about science and non-scientific topics. I have enjoyed watching Feifei grow intellectually by leaps and bounds during her time in the group through her unstinting hard work and curiosity to become a better scientist. I greatly appreciated all of the coffee and ice cream breaks with her that went a long way towards keeping me sane over the past year, and especially the little pearls of wisdom she shared with me when I was feeling hopelessly overwhelmed by everything.

Much of the work published in this thesis would not have been possible without access to X-ray absorption beamlines at the Stanford Synchrotron Radiation Lightsource at SLAC and the National Synchrotron Light Source at Brookhaven National Lab, as well as the expert technical assistance provided by scientific and technical staff at both facilities (at SSRL: Dr. Matthew Latimer, Dr. Allyson Aranda, and Dr. Erik Nelson; at NSLS: Dr. Sandeep Rekhi, Dr. Jen Bohon, and Mike Sullivan).

The National Institutes of Health are acknowledged for financial support of this work, and for the provision of my Chemistry-Biology Interface Training Grant fellowship during a portion of my studies in Larry's group. I want to thank LeeAnn Higgins (Center for Mass Spectrometry and Proteomics, University of Minnesota) for technical assistance with the mass spectrometry studies. I am also grateful to Prof. Michael Jensen and his student Huaibo Ma (Department of Chemistry, Ohio University) for providing several of the compounds studied in Chapter 3 and for sharing structural data in advance of publication.

Finally, I would like to thank my parents for their support throughout my graduate career here at Minnesota, and for their continued interest in all of the strange experiments I was doing in the name of scientific research. I wouldn't have gotten nearly as far without all of the important lessons that both of you taught me about hard work and dedication when I was growing up.

Abstract

An understanding of the mechanisms by which Nature employs mononuclear nonheme iron centers and dioxygen to carry out biological oxidative transformations of substantial biological and environmental relevance is of great fundamental and practical interest. Direct biochemical studies of nonheme iron oxygenases themselves can be complemented by spectroscopic studies of small model complexes to afford significant mechanistic insight, and this work employs a combination of these approaches.

Substitution of Fe(II) into the active center of a Mn(II)-dependent extradiol dioxygenase under aerobic expression conditions leads to *in vivo* formation of a self-hydroxylated form of the enzyme that is not observed for the native Mn(II) form, and we suggest that this reflects a significantly lowered redox potential for the Fe(II) form. We have also found that Co(II) substitution into an Fe(II)-dependent extradiol dioxygenase affords active enzyme, with X-ray absorption spectroscopy (XAS) providing metrical parameters for the resting state of this enzyme and its complexes with substrates.

XAS studies were carried out for an assortment of high-valent nonheme iron complexes of relevance to the oxoiron(IV) intermediates proposed in the catalytic cycles of mononuclear nonheme iron oxygenases. Studies of a series of pseudo-octahedral low-spin oxoiron(IV) complexes employing pentadentate ligands with a pendant axial ligand *trans* to the oxo moiety demonstrated that the properties of the oxoiron unit were not significantly affected by the identity of the *trans* ligand, in agreement with earlier observations on chemically similar systems. We also characterized the products of oxo

transfer to a thiolate-ligated nonheme iron(II) complex, providing structural evidence for conversion of the thiolate to an O-bound sulfinate. We structurally characterized the first example of a high-spin oxoiron(IV) complex in a trigonal bipyramidal (TBP) geometry, and also examined the XAS properties of a series of TBP iron complexes with different axial ligands as part of efforts to provide a basis for interpretation of the spectroscopic properties of TBP iron centers. Finally, in studies of a diiron(IV) complex of relevance to intermediate Q in methane monooxygenase, we demonstrated that the μ-oxo bridge of its diiron(III) precursor is retained upon oxidation.

Table of Contents

List of Tables

List of Figures

List of Schemes

Chapter 1

Oxygen Activation by Non-Heme Iron Enzymes Viewed through the Lens of Post-Translational Self-Hydroxylation: A Mechanistic Perspective.

Portions of this work have been previously published as:
Erik R. Farquhar, Kevin D. Koehntop, Joseph P. Emerson, and Lawrence Que, Jr. "Post-Translational Self-Hydroxylation: A Probe for Oxygen Activation Mechanisms in Non-Heme Iron Enzymes" *Biochem. Biophys. Res. Commun.*, **2005**, *338*, 230-239.

Portions reprinted from *Biochem. Biophys. Res. Commun.*, **2005**, *338*, 230-239 with kind permission of Elsevier, Inc.

1.1 Introduction

Non-heme iron centers are utilized throughout living systems to activate dioxygen to catalyze a remarkably diverse array of transformations.[1-4] The potential oxidizing power of this class of enzymes is strikingly illustrated by the diiron cluster of the hydroxylase component of methane monooxygenase (MMOH), which is capable of breaking the high energy C–H bond (104 kcal/mol) in methane to yield methanol.[5,6] This potent reactivity stems from the generation of high-valent iron-oxo intermediates through pathways that involve either a dinuclear or mononuclear iron center (Scheme 1.1).

For mononuclear non-heme iron enzymes, two distinct pathways are proposed for the generation of the high-valent intermediate (*c.f.* Scheme 1.1). In the first, associated with the Rieske dioxygenases, binding of O_2 and injection of an electron from a nearby iron-sulfur cluster leads to an iron(III)-peroxo species, and subsequent cleavage of the O–O bond presumably generates an iron(V)-oxo species.[2,7] This scheme is mechanistically analogous to the generally accepted process in the heme-containing cytochrome P450 enzymes.[8-10] In the second pathway, the iron center utilizes an external cofactor, such as α-ketoglutarate (αKG) or pterin, to supply two electrons for O_2 reduction. This processes is expected to afford an iron(IV)-oxo species, and direct spectroscopic evidence for this intermediate and its involvement in substrate oxidation has recently been obtained for five different mononuclear nonheme oxygenases, including the αKG-dependent enzymes taurine/αKG dioxygenase (TauD) [11-17] and prolyl 4-hydroxylase,[18], the αKG-dependent halogenases CytC3[19,20] and SyrB2[21,22], and the pterin-dependent oxygenase tyrosine hydroxylase.[23]

Diiron non-heme enzymes also share a common oxygen activation process (*c.f.* Scheme 1.1), which begins with O_2 binding to the diiron(II) center, forming a μ-1,2-peroxo diiron(III) complex, termed intermediate **P** (or H_{peroxo}) in the MMOH catalytic cycle. The O–O bond then is cleaved to yield an oxo-bridged diiron(IV) moiety termed **Q**.[1,6,24] Oxidative transformation of the substrate may be effected by either of these species.[25,26] Moreover, the situation can be further complicated by one-electron steps, which are required for the assembly of the diiron-tyrosyl radical center of the R2 protein of ribonucleotide reductase from *E. coli*.[27]

O_2 activation in the non-heme iron enzyme family is a well regulated process, as the substrate is typically required to prime the active-site iron for the binding and reduction of oxygen to generate high-valent iron-oxo intermediates.[1,28] Nevertheless, this process occasionally appears to break down, with unexpected results. Under certain circumstances, O_2 or its reduced counterparts can be activated in the absence of substrate in the active site, in which case the high-valent intermediate produced must find an alternative reductive outlet, typically at the expense of further catalytic activity, in a process termed oxidative inactivation. One reductive pathway, which has attracted much recent attention, involves the oxidation of an aromatic amino acid located near the active site to yield a hydroxylated amino acid residue. In some instances these hydroxylated amino acids remain coordinated to the iron center, generating brightly colored complexes that are amenable to analysis by a variety of techniques, as shown in Table 1.1. Herein we describe the oxidative self-hydroxylation of several non-heme iron enzymes, as well as the spectroscopic evidence used to characterize these modified enzymes.

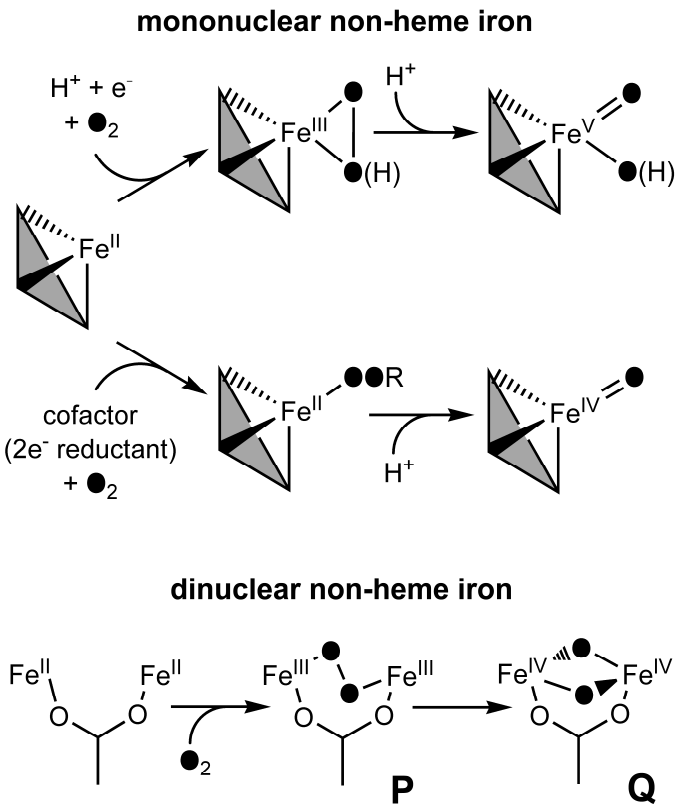

Scheme 1.1. General pathways for the activation of dioxygen to yield high-valent iron-oxo intermediates in both mononuclear and dinuclear non-heme iron enzymes.

Table 1.1. UV/Vis absorption maxima and spectroscopic methods used to characterize non-heme iron enzymes that self-hydroxylate an aromatic amino acid residue.[a]

residue	oxidative modification	enzyme	λ_{max} (nm)	ε_{max} ($M^{-1}cm^{-1}$)	spectroscopic methods
Phe	*m*-OH-Phe	Y122F/E238A R2	515	not reported	XRD
		W48F/D84E R2	550	1000-2100	XRD, rR
		TyrH-7,8-dihydrobiopterin [b]	–	–	XRD
	phenoxy radical	Y122H R2	–	–	ENDOR
	tyrosinate	HPPD	595	2600	rR
		Y325F PheH	–	–	ESI-MS
Tyr	DOPA	F208Y R2	720	2500	XRD, rR
		Y122F/F208Y R2	*ca.* 700	not reported	–
		W48F/F208Y R2	675	not reported	Mössbauer
		TauD-αKG	550	700	rR
		TauD-succinate	720	380	rR, ESI-MS
		PMI	680	2100	rR
		HppE	680	450	rR
Trp	hydroxyindole	TfdA-αKG	580	1000	rR
		AlkB-αKG	590	960	ESI-MS
		Y325F PheH	–	–	ESI-MS
		FIH-1	583	3000	ESI-MS

[a] Abbreviations: αKG: α-ketoglutarate, AlkB: alkylated DNA repair protein, DOPA: dihydroxyphenylalanine, ENDOR: electron nuclear double resonance, ESI-MS: electrospray ionization mass spectrometry, FIH-1: factor inhibiting hypoxia inducible factor, HPPD: 4-hydroxyphenylpyruvate dioxygenase, HppE: (*S*)-2-hydroxypropylphosphonic acid epoxidase, PheH: phenylalanine hydroxylase, PMI: phosphomannose isomerase, R2: the R2 subunit of ribonucleotide reductase, rR: resonance Raman, TauD: taurine/αKG dioxygenase, TfdA: 2,4-dichlorophenoxyacetate/αKG dioxygenase, TyrH: tyrosine hydroxylase, XRD: X-ray diffraction.

[b] The observed self-hydroxylation[29] is an artifact of the crystallography conditions and is not catalytically relevant.[30]

1.2 Ribonucleotide Reductase

Chronologically, a mutant form of ribonucleotide reductase R2 (RNR R2, from *E. coli*) was the first example of a self-hydroxylation process recognized in non-heme iron enzymes and was subjected to a detailed structural and spectroscopic analysis. The oxygen activation mechanism for R2 deviates from that of MMOH by the injection of an electron following the formation of **P**, producing an iron(III)-iron(IV) intermediate termed **X**;[31-34] **X** is then responsible for the generation of a one-electron oxidized tyrosyl radical (Y122•) adjacent to the dinuclear metal center[35,36] that initiates the reduction of ribonucleotides by forming a substrate radical in the active site of the R1 subunit[37,38] via a long-range electron transfer pathway.[39-41] Extensive site-directed mutagenesis studies on RNR R2 have revealed a diverse range of post-translationally generated self-hydroxylation products (*c.f.* Table 1.1) and shed light on the factors contributing to its favored one-electron oxidation pathway, rather than the two-electron process observed in other evolutionarily related enzymes such as MMOH and soluble fatty acid desaturases.[1,5,6,42]

Mutation of F208, one of the residues comprising a hydrophobic pocket that houses the reaction site for O_2 [43] and stabilizes the Y122 radical, [44] to tyrosine results in the generation of a blue chromophore (λ_{max} = 720 nm, ε = 2500 $M^{-1}cm^{-1}$) both *in vivo* and *in vitro* (upon the addition of iron(II) and O_2 to apoR2). Resonance Raman vibrations associated with this chromophore are characteristic of an iron(III)-catecholate complex.[45] X-ray crystallography confirmed a catecholate moiety (derived from F208Y) chelated to Fe_a at the diiron(III) core, as shown in Figure 1.1A.[46] These seminal studies demonstrate

that the active site of R2 can support a two-electron oxidation outcome in addition to the wild-type one-electron oxidation of Y122.

Subsequent crystallographic studies on apo and diferrous F208Y R2 suggested that Y208 is bound to the iron site throughout the catechol formation cycle.[43] Moreover, oxidation of Y208 in F208Y R2 in the presence of isotopically labeled O_2 and H_2O demonstrated that the inserted oxygen atom derives from solvent.[47] Intriguingly, a small amount of a short-lived tyrosyl radical was also generated during *in vitro* reconstitution of F208Y R2, while radical formation was abolished in the double mutant Y122F/F208Y.[46] The identification of this radical as Y122• on the basis of electron paramagnetic resonance (EPR) studies [44,48] led to the suggestion that the reaction pathway for F208Y R2 may partition between hydroxylating Y208 (major pathway) and generating the wild-type product Y122• (minor pathway),[45] and a later study gave insight into the origin and control of this partitioning process.[49] A key step in the wild-type reaction is the rapid injection of a single electron from an exogenous reductant, which is believed to commit the reaction to a one-electron oxidation outcome (Y122•).[50] Since Y208 is hydroxylated in F208Y R2 in preference to the normal reaction, Y208 presumably competes with the electron injection step by acting as an exogenous reductant. However, Y122• predominates in the F208Y mutant in the presence of a high concentration of ascorbate, which favors one-electron injection but is dependent upon a hydrogen-bond network involving the near-surface residue W48 acting as an electron-transfer pathway into the diiron active site.[39,51-53] Significantly, the W48F/F208Y mutant inhibits the electron-transfer pathway, irrespective of the ascorbate concentration, thus strongly favoring Y208 hydroxylation. Therefore, the electron injection step (mediated

by the electron-transfer pathway) may ensure that an intermediate containing two oxidizing equivalents is not generated during the normal reaction in R2, thereby precluding self-hydroxylation reactions that could compete with the one-electron oxidation of Y122.

Based on the premise that the introduction of non-native mutations such as F208Y in the active site may engender reactivity that is not relevant to the wild-type protein, another double mutant, W48F/D84E R2, was engineered to enforce a two-electron oxidation outcome while retaining a ligand set characteristic of the diiron-carboxylate family.[54] Exposure of W48F/D84E R2 to O_2 gives rise to a transient μ-1,2-peroxodiiron(III) species,[55] which appears to be structurally similar to intermediate **P** in MMOH.[56,57] X-ray crystallographic analysis of the vividly purple-colored product (λ_{max} = 550 nm, ε = 1000-2100 $M^{-1}cm^{-1}$) generated by decay of this **P**-like species revealed hydroxylation at the *meta* position of F208.[54] Interestingly, resonance Raman spectroscopic studies of the purple chromophore demonstrated that the oxygen atom incorporated into F208 derives from O_2, rather than H_2O,[54] in contrast to the solvent derived oxygen in F208Y R2.[47] The contrasting labeling results observed for the F208Y and W48F/E238A self-hydroxylation reactions raise the possibility that subtly different oxidizing species are responsible for the transformation.[54]

Two further instances of hydroxylation of F208 in mutant R2 enzymes have been reported. First, a crystal structure of the double mutant Y122F/E238A R2, in which one of the ligands of Fe_b (E238) was removed by mutation, also revealed hydroxylation of F208 at the *meta* position, with a relatively long 2.8 Å coordination to Fe_b, as indicated in Figure 1.1B (λ_{max} *ca.* 475 and 515 nm).[43] When combined with the crystallographic data

for F208Y R2, this result suggests that the ligands of the diiron site contribute towards control of the reaction direction in R2. In particular, the hydroxylating species of F208Y R2 resembles the wild-type situation in which the high-valent species is exposed on Fe_a near Y122, resulting in the observed partitioning between Y208 hydroxylation and Y122• formation. Conversely, Y122F/E238A R2 presents a defective activation since the oxidizing species is exposed on the wrong iron atom as a result of the lower coordination number of Fe_b caused by the introduction of an alanine residue at position 238. Therefore, the iron ligand E238 appears to play a role in directing the reactivity of the activated oxygen species, thereby protecting R2 from harmful self-oxidation reactions.[43]

In the second example, electron nuclear double resonance (ENDOR) studies on the R2 mutant Y122H, which was engineered in an attempt to generate a histidine radical at position 122, revealed that the enzyme contains a small amount (*ca.* 5%) of a stable paramagnetic species, termed center **H**, that was proposed to be a diferric center with a strongly coupled radical.[58] Recently, a more detailed spectroscopic characterization of this mutant utilizing EPR and ENDOR spectroscopies with specific isotope labels on the ligands of the diferric cluster, as well as MALDI-TOF mass spectrometry of trypsin-digested Y122H and wild-type R2, suggested that center **H** is a diferric center strongly coupled to a phenoxy radical, with hydroxylation likely taking place at the *para* position of the ring, rather than the *meta* position.[58] Since F208 is the only Phe residue proximate to the iron site, this residue was proposed to be the likely target for hydroxylation, with subsequent one-electron oxidation yielding a phenoxy radical. The absence of evidence for a histidine radical suggests that either intermediate **X** is not powerful enough to generate a histidine radical, or else the oxidation of F208 to form a coordinating phenoxy

radical is energetically more favorable.[58] Taken together, these three examples of self-hydroxylation at F208 in R2 are an especially impressive illustration of the oxidative power of the iron-oxo intermediate, which not only attacks the aromatic ring of tyrosine but also that of the more inert phenylalanine.

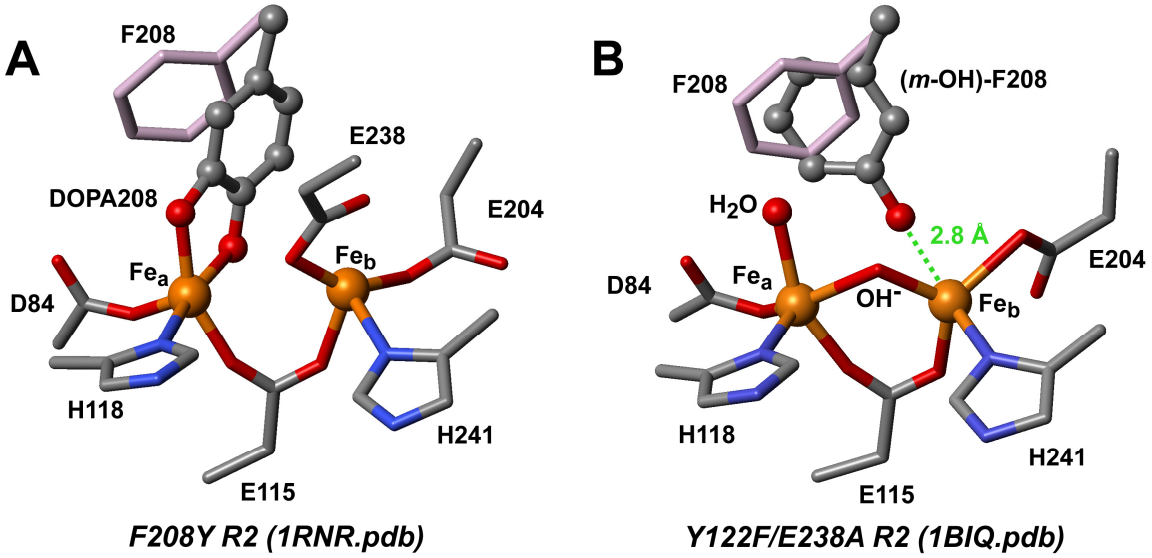

Figure 1.1. Active site structures of crystallized non-heme diiron enzymes showing either the self-hydroxylated residue or proximity of that residue to the metal center. (A) The Fe(III)-catecholate complex generated in F208Y R2 (1RNR.pdb). Shown in light pink is the position of F208 in the crystal structure of differic wild type R2 (1RIB.pdb). The image was generated by alignment of the two active sites using both Fe atoms, E115, H241, H118, and Y122 (not shown) as anchors. The oxo bridge in diferric wild-type R2 is not present in the oxidized F208Y crystal structure and is not shown for clarity. (B) The 2.8 Å interaction between Fe and *meta*-hydroxylated F208 in oxidized Y122F/E238A R2 (1BIQ.pdb). Hydroxylation was observed in only one subunit of the dimeric protein,[43] and the position of non-hydroxylated F208 in the second subunit is shown in light pink. The image was generated by alignment of the active sites of the two subunits using the same anchor points as in A.

1.3 Mononuclear Non-Heme Iron Enzymes

Self-hydroxylation reactions have also been demonstrated for a number of members of a superfamily of mononuclear non-heme iron enzymes possessing a common active-site structure termed the 2-His-1-carboxylate facial triad,[28] a recurring motif which acts as a versatile platform for the activation of dioxygen. Included within this superfamily are the α-ketoglutarate (αKG) dependent dioxygenases, which catalyze a diverse range of metabolic transformations.[3] It has long been known that αKG dependent dioxygenases undergo uncoupled reactions and self-inactivate in the absence of prime substrate.[1] The earliest such examples involved the prolyl and lysyl hydroxylases, in which uncoupled turnover was shown to result in metal oxidation that was reversible by the addition of ascorbic acid.[59] More recently, the self-hydroxylation of a phenylalanine, tyrosine, or tryptophan residue has been reported (or suggested) for a number of different αKG-dependent enzymes in the absence of substrate.

The αKG dependent enzyme taurine/αKG-dioxygenase (TauD) utilizes Fe(II), αKG, and O_2 to hydroxylate taurine.[60] Recent work has shown a complex surface of pathways leading to the generation of a green chromophore in the uncoupled reaction of TauD with O_2 as well as insight into the identity of the hydroxylating intermediate. Exposure of the lilac-colored Fe(II)TauD-αKG complex (λ_{max} = 530 nm; ε_{530} = 140 $M^{-1}cm^{-1}$)[61] to O_2 in the absence of taurine generates a transient yellow species (λ_{max} = 408 nm; $\varepsilon_{408} \geq 1600$ $M^{-1}cm^{-1}$) en route to the formation of a greenish-brown chromophore (λ_{max} = 550 nm; ε_{550} = 700 $M^{-1}cm^{-1}$).[62] The latter displays resonance Raman vibrations consistent with the formation of an Fe(III)-catecholate moiety arising from the self-

hydroxylation of an active site tyrosine residue.[62] This residue has been identified by site-directed mutagenesis as Y73, which is *ca.* 6.5 Å away from the Fe center (Figure 1.2A).

The hydroxylation of Y73 in TauD demonstrates that the Fe(II)TauD-αKG complex can activate O_2 even in the absence of substrate, albeit more slowly as subsequently demonstrated by transient kinetic studies.[11,16] The active oxidant oxidizes Y73 first to a tyrosyl radical, corresponding to the yellow intermediate (as shown by EPR analysis),[62] which is subsequently converted to a catecholate. Interestingly, isotope-labeling resonance Raman studies show that the incorporated oxygen derives from solvent.[62] These spectroscopic results implicate an oxidant that can exchange with solvent, most likely the oxoiron(IV) species identified in transient kinetic studies of the reaction of the ternary Fe(II)TauD-αKG-taurine complex with O_2.[11-14,16]

A second bright green chromophore (λ_{max} = 720 nm, ε_{720} *ca.* 300 - 400 $M^{-1}cm^{-1}$) arises from the O_2 or H_2O_2 dependent self-hydroxylation of Fe(II)TauD in the presence of succinate, the decarboxylated product of αKG.[63,64] Resonance Raman spectroscopy reveals that the succinate-derived 720 nm chromophore also arises from an iron(III)-catecholate complex.[63,64] The species responsible for this bright green chromophore is related to that of the αKG-derived brownish green chromophore by a bicarbonate binding equilibrium. For example, upon the addition of excess bicarbonate the 720-nm species slowly converts to the 550-nm chromophore.[63] Conversely, the 550 nm chromophore converts to the 720-nm species upon standing for several days (or incubation with taurine for two hours). The color changes reflect a modulation of the Lewis acidity of the metal center by the interchange between anionic bicarbonate and a neutral solvent ligand.

Intriguingly, when the TauD self-hydroxylation reaction is carried out using succinate and H_2O_2, chromophore formation is at least two orders of magnitude more rapid than when O_2 is employed with either αKG or succinate.[64]

While the self-hydroxylation reaction of TauD has been investigated in considerable detail, there are other examples of similar reactions amongst the αKG dependent dioxygenases. In the case of the herbicide degrading 2,4-dichlorophenoxyacetate/αKG dioxygenase (TfdA), exposure of the Fe(II)TfdA-αKG complex to O_2 results in the formation of a bluish-purple chromophore (λ_{max} *ca.* 580 nm, ε *ca.* 1000 $M^{-1}cm^{-1}$).[65] Resonance Raman experiments reveal ligand vibrations distinct from those of a phenolate or a catecholate but similar to those of 5-hydroxyindole, implying the hydroxylation of a tryptophan residue.[65] This residue has been identified as W112 on the basis of electrospray mass spectral analysis. Furthermore, labeling experiments show that the incorporated oxygen atom derives from solvent,[65] as with TauD, suggesting that a common self-hydroxylation mechanism is operative in the αKG dependent dioxygenases. A blue chromophore (λ_{max} = 590 nm, ε = 960 $M^{-1}cm^{-1}$) is also generated under similar conditions in the case of AlkB, an αKG-dependent enzyme that repairs methylated bases in DNA and RNA.[66] The hydroxylated residue has been identified by ESI-MS to be W178. Notably, this self-hydroxylation was also observed in a control sample, implying that W178 may be hydroxylated *in vivo*.[66] Finally, very recent studies of FIH-1 (factor inhibiting hypoxia inducible factor), an enzyme involved in regulating the eukaryotic hypoxic response,[67] revealed generation of a purple chromophore (λ_{max} = 583 nm, ε = 3000 $M^{-1}cm^{-1}$) upon air exposure of solutions of *apo*

FIH-1 that had been anaerobically reconstituted with Fe(II) and αKG.[68,69] LC/ESI-MS/MS studies revealed hydroxylation of W269, a residue that lies *ca.* 4.3 Å away from the iron center in the crystal structure. Interestingly, the hydroxylation of W269 appears to occur preferentially over hydroxylation of the more distant Y93 and Y102 residues, which are located 12.2 Å and 9.0 Å from the iron center.[68,69]

Self-hydroxylation of a phenylalanine residue may occur in the case of 4-hydroxyphenylpyruvate dioxygenase (HPPD), an α-ketoacid-dependent enzyme involved in tyrosine catabolism. The isolated, oxidized enzyme exhibits a blue color (λ_{max} *ca.* 595 nm, ε = 2600 $M^{-1}cm^{-1}$)[70] that arises from a tyrosinate-to-iron(III) LMCT transition, as demonstrated by resonance Raman spectroscopy.[71] However, the subsequent crystal structure of the reduced enzyme[72] shows the iron(II) center coordinated to a characteristic 2-His-1-carboxylate facial triad motif with no coordinated tyrosine ligand. This result suggests that the chromophore may result from the uncoupled self-hydroxylation of a nearby phenylalanine residue.

Self-hydroxylation reactions also occur in several pterin-dependent hydroxylases. Crystallographic studies of tyrosine hydroxylase (TyrH) show the active site residue F300 to be hydroxylated in two structures, one of the catalytic domain crystallized in the presence of the substrate analog 7,8-dihydrobiopterin and the other of the catalytic and tetramerization domains.[29] Subsequently, MALDI-TOF mass spectrometry and amino acid sequencing demonstrated that F300 is only hydroxylated in the isolated catalytic domain upon incubation with an excess of 7,8-dihydrobiopterin, the reductant DTT, and Fe(II) in the absence of substrate,[30] indicating that the observed hydroxylation was likely an artifact of the crystallography conditions. More recently, studies have shown that the

Y325F mutant of human phenylalanine hydroxylase (PheH) has an activity identical to that of the wild-type enzyme.[73,74] ESI-MS analyses of trypsin digests of the Y325F variant and wild-type PheH revealed the *in vivo* hydroxylation of F325 in Y325F PheH to tyrosine, as well as possible hydroxylation of an outer-sphere tryptophan residue.[74] Y325 is thought to be involved in hydrogen bonding interactions that stabilize binding of the pterin cofactor; thus, this example may represent an instance of enzyme self-repair.

Self-hydroxylation processes have also been described for two other mononuclear non-heme enzymes with a 2-His-1-carboxylate metal binding site. In the first instance, the substitution of iron for the native zinc ion in recombinant phosphomannose isomerase (PMI) leads to the development of a green chromophore (λ_{max} = 680 nm, ε = 2100 $M^{-1}cm^{-1}$/Fe) attributable to hydroxylation of Y257 (as demonstrated by resonance Raman spectroscopy),[75] which is *ca.* 5.4 Å distant from the metal center in the Zn(II) crystal structure (Figure 1.2B).[76] Likewise, (*S*)-hydroxypropylphosphonic acid epoxidase (HppE), which catalyzes the formation of the antibiotic fosfomycin, also develops a green color (λ_{max} = 680 nm, ε = 450 $M^{-1}cm^{-1}$) as a result of tyrosine self-hydroxylation upon reconstitution of the apo enzyme with Fe(II) under aerobic conditions.[77] Isotope-labeling resonance Raman experiments demonstrated that oxygen is not incorporated into the catechol from either O_2 or H_2O, indicating that the post-translational modification event occurs *in vivo*.[77] Reconstitution of the enzyme under O_2 in the presence of excess ascorbate generated a greater yield of the green chromophore, with the incorporated oxygen deriving from O_2, as demonstrated by isotope-labeling studies.[77] This observation implies that ascorbate provides the electrons necessary to activate dioxygen, a role similar to that of pterin and αKG in pterin- and αKG-dependent oxygenases,

respectively.[77] Site directed mutagenesis studies suggested that Y105, which is *ca.* 8.7 Å away from the metal center,[78] is the principal target of self-hydroxylation. Interestingly, studies of Y105F HppE and the double mutant Y105F/Y103F HppE showed that the more distant residue Y103 (~10.8 Å) is also hydroxylated, although the green chromophore formed in Y105F HppE is less intense relative to wild-type HppE, suggesting that self-hydroxylation of Y103 is less favorable.[77,78]

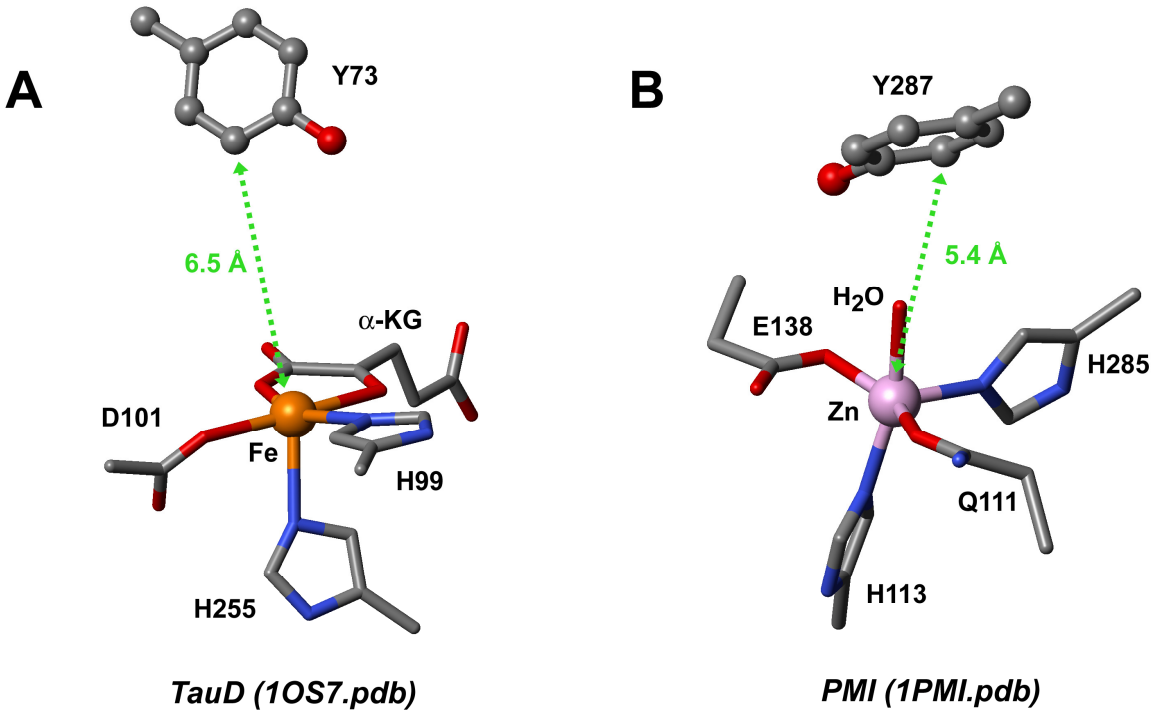

Figure 1.2. Active site structures of crystallized non-heme monoiron enzymes showing either the self-hydroxylated residue or proximity of that residue to the metal center. (A) The crystal structure of the active site of Fe(II)TauD with αKG bound (taurine is not shown) shows the proximity of Y73 to the metal center prior to self-hydroxylation (1OS7.pdb). (B) The crystal structure of the Zn(II)PMI active site shows the position of Y257 relative to the metal center prior to self-hydroxylation (1PMI.pdb). Self-hydroxylation is not seen in the native Zn(II) protein but is observed upon Fe(II) substitution.[75]

1.4 Mechanistic Implications

The self-hydroxylation reactions described above serve as probes for the mechanisms of oxygen activation at non-heme iron sites, as these transformations give rise to visible chromophores readily probed by resonance Raman spectroscopy to reveal the source of the oxygen atom (either from O_2 or water) that is incorporated into the residue. Although high-valent iron-oxo species are generally believed to be involved in biological oxidations catalyzed by iron centers, there has been recent discussion regarding the possibility that metal-peroxo or metal-superoxo species may also be involved under some circumstances.[9,25,79,80] For self-hydroxylation reactions, the fact that solvent-derived oxygen can be incorporated in several examples excludes the possibility of a direct oxygen-atom transfer from a metal-peroxo species and requires O–O bond cleavage to occur prior to C–O bond formation in order to allow the active oxygen species to exchange with solvent water.

An oxoiron(IV) intermediate has been directly demonstrated to act as the kinetically competent oxidant in the wild-type reactions of TauD[12,14] and several other mononuclear nonheme iron oxygenases.[18,20,21,23,81]. This species is proposed to form via a mechanism first proposed in 1982 by Hanauske-Abel (Scheme 1.2) for the αKG-dependent dioxygenases,[82] in which the initial binding of O_2 to the binary Fe(II)enzyme-αKG complex generates a putative iron(III)-superoxo species.[80] Nucleophilic attack by the terminal superoxo oxygen onto the α-keto carbon of αKG affords a yet unobserved peroxo species that undergoes subsequent C–C bond cleavage to generate the oxoiron(IV) intermediate with CO_2 and succinate as by-products. The fact that self-hydroxylation occurs in TauD shows that oxygen activation can occur even in the

absence of substrate, albeit more slowly. Instead of oxidizing taurine, the Fe(IV)=O species hydroxylates the nearby Y73 residue.

The resonance Raman experiments on self-hydroxylated TauD establish that the incorporated oxygen atom derives from water. Thus, solvent exchange with the oxidizing species in TauD must occur prior to the formation of the C–O bond. Although the nature of the taurine hydroxylation product does not allow the source of its oxygen atom to be established by product analysis, it is clear from the resonance Raman data on the Fe(IV)=O intermediate derived from the enzyme-cofactor-substrate complex that solvent exchange does not occur within the lifetime of that intermediate,[15] nor does it appear to occur for resonance-Raman detected species that form from the decay of the Fe(IV)=O intermediate in the presence of taurine.[17] To rationalize the labeling result for the self-hydroxylated TauD, it is necessary to postulate that either the presence of substrate serves to restrict access of solvent water into the active site, thereby hindering oxygen atom exchange with the Fe(IV)=O species observed in taurine hydroxylatrion, or that the exchange specifically occurs at a subsequent stage of the *self-hydroxylation reaction* but prior to C–O bond formation. A tyrosyl radical intermediate has been identified as the precursor to the catecholate chromophore in TauD.[62] This observation indicates that the first step of Y73 oxidation involves the abstraction of its O–H hydrogen atom by the Fe(IV)=O intermediate to form the tyrosyl radical and an Fe(III)–OH center (Scheme 1.2). Solvent exchange with the latter prior to oxygen rebound with the aromatic radical introduces label from $H_2{}^{18}O$ into the catecholate ring. Similar solvent label incorporation into the hydroxylated tryptophan residue of TfdA suggests a comparable mechanism is likely to be operative in this reaction as well.[65]

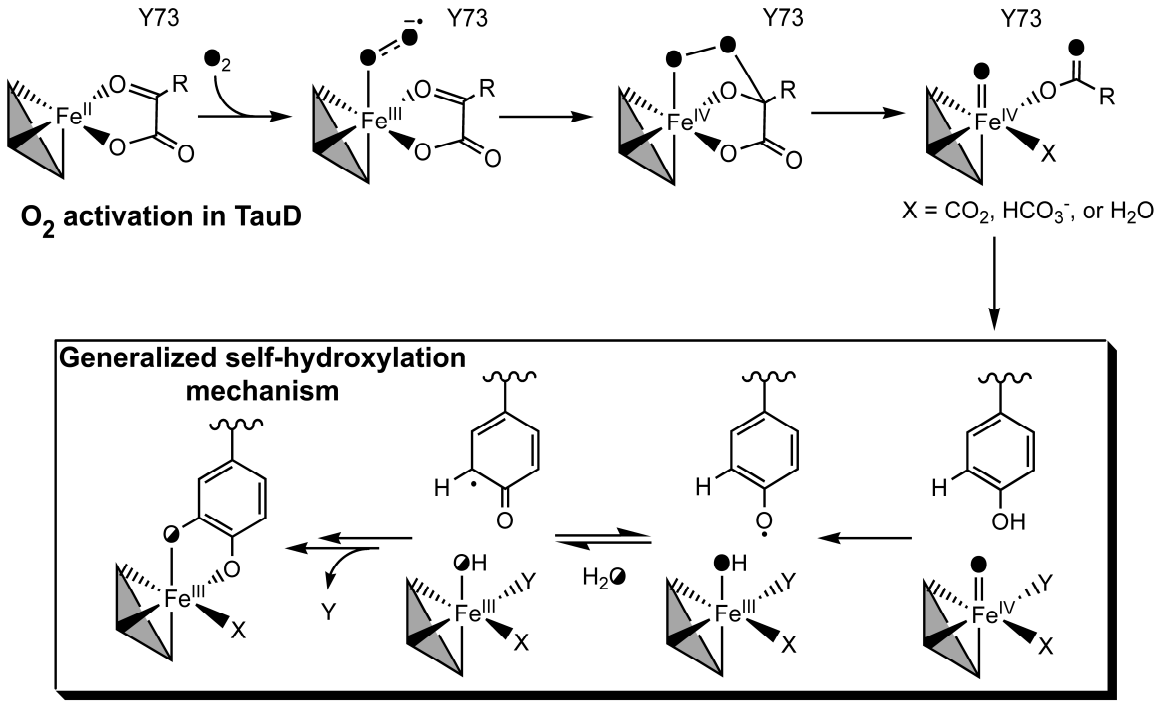

Scheme 1.2. Proposed mechanism for the self-hydroxylation of a nearby tyrosine residue in mononuclear non-heme iron enzymes utilizing an oxoiron(IV) intermediate as the oxidant. The three protein-derived ligands which form the 2-His-1-carboxylate facial triad are shown as a shaded triangle. Shown first is the specific pathway for O_2 activation in the α-KG dependent dioxygenases. It should be noted that following the decarboxylation of α-KG, there are several possibilities for the identity of the ligand at position X, including CO_2, HCO_3^-, H_2O, or an equilibrium mixture thereof. The boxed portion depicts a more general process for hydroxylation of a tyrosine residue through a tyrosyl radical, where ligands X and Y are variable. O_2-derived oxygen atoms are depicted as filled circles, with half-filled circles reflecting the possibility of exchange with H_2O.

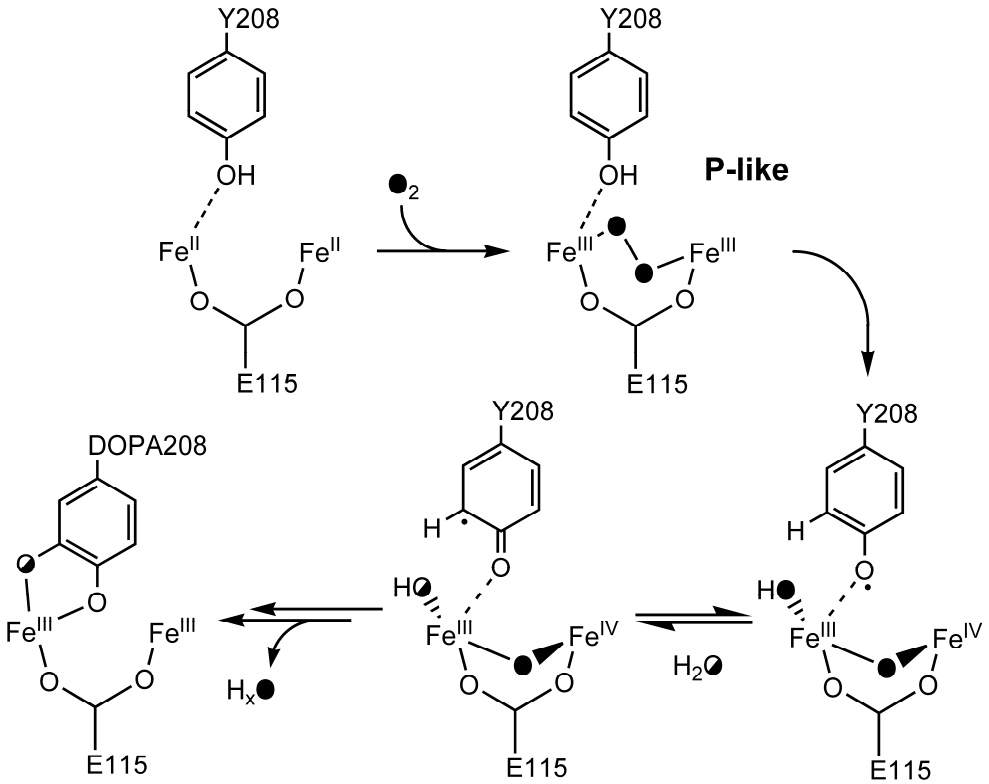

Scheme 1.3. Proposed mechanism for the self-hydroxylation of Y208 in F208Y R2 to afford an Fe(III)-catecholate product, consistent with the crystallographic observation of a weak interaction between Fe and Y208 in the initial diferrous state. The μ-1,2-peroxodiiron(III) species analogous to intermediate **P** of MMOH is labeled as such. For clarity, ligands other than the bridging residue E115 are not shown. O_2-derived oxygen atoms are shown as filled circles, with the half-filled circles reflecting the possibility of exchange with H_2O. The second bridging oxygen derived from O_2 is thought to depart as either hydroxide or water.[47,54]

The newly introduced oxygen atom in DOPA208 R2 similarly derives from water, suggesting that the diiron center of R2 can perform chemistry analogous to the monoiron centers of TauD and TfdA. Again, O–O bond cleavage must precede C–O bond formation to account for water-derived oxygen incorporation into the DOPA residue. Oxygen activation by the diiron site of R2 is proposed to follow a mechanism analogous to that proposed for MMOH involving initial formation of a peroxodiiron(III) intermediate (**P** in Scheme 1.1), as demonstrated for the D84E and W48F/D84E R2 mutants.[54-57] In wild-type R2, injection of an electron from an exogenous reductant converts this **P**-like species into the iron(III)-iron(IV) intermediate **X**,[31-34] which is the oxidant of Y122. For F208Y R2 however, the nearby Y208 residue[43] can instead provide an electron that effects cleavage of the O–O bond. This electron transfer step presumably leads to a putative Y208•/iron(III)-iron(IV) species that must have a sufficient lifetime to permit solvent exchange before subsequently collapsing to the diiron(III)-catecholate chromophore (Scheme 1.3).

In contrast, the oxygen atom incorporated into F208 in the self-hydroxylation of W48F/D84E R2 derives from O_2.[54] Unlike F208Y R2, intermediate **X** does not accumulate in the reaction sequence for W48F/D84E R2, suggesting that this intermediate either does not participate in the hydroxylation mechanism in this mutant or has too short a lifetime to allow solvent exchange.[54] The analogous one-electron transfer from F208 to the **P**-like intermediate would be expected to have a higher activation barrier, since a phenylalanine residue is not a very good one-electron reductant. Alternatively, direct oxygen-atom transfer from the **P**-like intermediate to F208 would account for the observed oxygen-atom incorporation from O_2. Such an oxygen-atom

transfer has also been recently observed in MMOH, in which intermediate **P** is shown to effect the epoxidation of olefins,[26] a result that may well reflect the mechanistic diversity of non-heme iron enzymes.

The *in vitro* self-hydroxylation of HppE also results in oxygen incorporation from O_2, in contrast to TauD and other αKG dependent dioxygenases, with ascorbate required as an exogenous reductant.[77] Assuming that ascorbate acts as a one electron reductant, the incorporation of oxygen from O_2 suggests that oxygen activation proceeds via an Fe(III)–OOH intermediate (Scheme 1.1), as implicated for the Rieske dioxygenases.[2,7,83] This intermediate may hydroxylate the nearby tyrosine residue directly or convert to an HO–Fe(V)=O oxidant that does not undergo solvent exchange prior to attacking tyrosine. Additional mechanistic and spectroscopic analyses should give further insight into this intriguing transformation.

In closing, Nature employs a variety of redox centers to carry out oxygenation reactions, often utilizing iron centers to generate powerful oxidizing species that carry out energetically difficult transformations. Occasionally, uncoupling can result in self-hydroxylation of nearby aromatic amino acids by these high-valent iron-oxo species, as observed for a number of non-heme iron enzymes. In some cases, this process may serve to protect enzyme active sites from the inimical effects of adventitious oxygen activation in the absence of substrate[84] or may even provide a mechanism for enzyme repair;[74] in others, they may simply be aberrations that serve no physiological function. Nevertheless, the several well-studied examples of self-hydroxylation processes have shed light into the mechanisms of oxygen activation at non-heme iron centers, nicely complementing the more direct studies of enzyme mechanism described by Krebs and

Bollinger and coworkers,[81] and have contributed towards our understanding of the delicate dance between iron and O_2 in achieving a remarkable range of oxidative transformations.

1.5 Scope and Aims of Thesis

The principal goal of our work is the elucidation of the spectroscopic and reactivity properties of both mononuclear and dinuclear nonheme iron oxygenases through a combination of studies of the enzymes themselves and suitable model complexes.

In the first part of this thesis, we describe metal substitution experiments for a pair of extradiol dioxygenases that employ either manganese or iron cofactors.[85] Chapter 2 discusses the characterization of an iron-substituted form of the manganese-dependent homoprotocatechuate 2,3-dioxygenase MndD from *Arthrobacter globiformis*, revealing that self-hydroxylation of an aromatic residue in close proximity to the activity site occurs *in vivo* under aerobic conditions.[86] Chapter 3 describes X-ray absorption spectroscopy studies of a Co(II)-substituted homoprotocatechuate 2,3-dioxygenase from *Brevibacterium fuscum*, providing insight into the metrical structure of the resting state of the enzyme and its substrate complexes.

In the second part of this work, we turn our attention to the characterization of high-valent nonheme iron model complexes by X-ray absorption spectroscopy.[87-90] The objective of these studies was primarily to develop an understanding of the structural and electronic properties of these complexes in conjunction with data from other techniques such as Mössbauer and EPR spectroscopies, and not to devise novel methods of analyzing X-ray absorption data. As such, the work was highly collaborative and

involved interactions with several members of the Que lab as well as individuals at other institutions. In Chapter 4, we describe the XAS characterization of a series of pseudo-octahedral low-spin oxoiron(IV) complexes employing pentadentate ligands with a pendant axial ligand *tran*s to the oxo moiety, and compare their spectroscopic properties to those of other series of low-spin oxoiron(IV) complexes. Chapter 5 discusses the XAS characterization of the metal- and ligand-centered oxidation products generated via treatment of a nonheme iron(II) complex containing a bound thiolate with oxidant.[91] Chapter 6 addresses the characterization of a series of trigonal bipyramidal iron complexes with varying axial ligands using a ligand that was initially employed to generate the first example of a high-spin oxoiron(IV) model complex analogous to those found in enzymatic active sites.[92,93] Finally, Chapter 7 describes the characterization via XAS of a strongly oxidizing nonheme μ-oxo bridged diiron(IV) complex of relevance to intermediate **Q** in MMO.[94]

Collectively, the work presented in this thesis provides additional insights into the factors that modulate O_2 reactivity at nonheme iron enzyme active sites, and provides a basis for the interpretation of structural and spectroscopic data obtained for intermediates trapped during the catalytic cycles of nonheme iron oxygenases.

Chapter 2

In Vivo Self-Hydroxylation of an Fe-Substituted Manganese Dependent Extradiol Dioxygenase

This work has been submitted in its entirety for publication to *J. Biol. Inorg. Chem.* as: "*In Viv*o Self-Hydroxylation of an Fe-Substituted Manganese Dependent Extradiol Dioxygenase." Erik R. Farquhar, Joseph P. Emerson, Kevin D. Koehntop, Mark F. Reynolds, Milena Trmčić, Lawrence Que, Jr.

2.1 Introduction

The activation of dioxygen by transition metal centers such as iron or copper in enzymatic systems has attracted considerable attention over the past half-century. Of these, enzymes utilizing a mononuclear nonheme iron center have been of especial interest in recent years, primarily as a consequence of the large range of metabolically and environmentally important transformations that they effect.[1-4] This superfamily of enzymes almost universally shares a common iron(II) binding triad consisting of two His residues and one Glu or Asp residue, a motif that has been termed the 2-His-1-carboxylate facial triad.[28] The three protein-derived ligands occupy one face of the (pseudo)octahedral iron coordination sphere, allowing the three remaining sites to bind substrate, cofactor, and O_2 in close proximity in order to tune and direct the desired oxidative outcome. An array of mechanistic studies[1,2,7,28] have suggested a common framework for O_2 activation in this enzyme superfamily that involves an initial metal-superoxo species following O_2 binding to the iron(II) center, although the identity of the ultimate oxidant may vary. For example, the extradiol dioxygenases, which carry out oxidative cleavage of aromatic C–C bonds,[95] do not employ a high-valent oxidant to effect their chemistry.[4,7,96] Following bidentate binding of the catechol substrate to the iron(II) center, addition of O_2 affords a putative iron(III)-superoxo-catecholate intermediate. The electron-rich aromatic substrate then readily donates an electron to give an iron(II)-superoxo-semiquionine that undergoes radical recombination to give an iron(II)-alkylperoxo adduct. Heterolytic O–O bond cleavage and a Criegee rearrangement complete the oxidative transformation leading to the ring-cleavage product. Kovaleva and Lipscomb recently employed X-ray crystallography techniques

using the iron(II)-dependent homoprotocatechuate 2,3-dioxygenase (HPCD) from *Brevibacterium fuscum* (2,3-HPCD) and an electron-deficient 4-nitrocatechol (4NC) substrate to provide direct evidence for both the iron(II)-superoxo-semiquionine and iron(II)-alkylperoxo intermediates.[97] For the former intermediate the non-planarity of the 4NC ring and the bond lengths associated with the Fe–O_2 moiety in the X-ray crystal structure led to an iron(II)-superoxo formulation, thus representing the first structurally characterized example of this moiety at a nonheme iron site[98] and providing experimental corroboration of the proposed mechanism. Conversely, other nonheme oxygenases with a 2-His-1-carboxylate metal binding site employ high-valent iron-oxo intermediates to carry out substrate transformations. In the α-ketoglutarate (αKG) and pterin-dependent oxygenases, binding of O_2 to the ternary enzyme-cofactor-substrate complex elicits formation of a putative Fe–O_2 adduct. The cofactor then supplies two additional electrons necessary to promote heterolytic O–O bond cleavage, yielding a potent oxoiron(IV) oxidant capable of reacting with strong C–H bonds.[2,28] Krebs, Bollinger, and coworkers have obtained direct kinetic and spectroscopic evidence for the oxoiron(IV) intermediate for several members of this family, lending credence to the proposed mechanism.[11,21,23,81]

A common thread in the proposed mechanisms of O_2 activating enzymes in the 2-His-1-carboxylate superfamily is the requirement for substrate to be present in the active site prior to O_2 binding and activation. Structural and spectroscopic studies on many members of this family have shown that substrate binding, either directly to the iron center or nearby in the second coordination sphere, promotes loss of solvent-derived ligands to afford a coordinatively unsaturated iron(II) center with an open site for O_2 binding. This is also generally thought to lower the reduction potential of the iron site to

facilitate its oxidation following O_2 binding.[1,2,28] One might imagine that the requirement for substrate binding prior to any O_2 activation chemistry represents a mechanism to protect both the intracellular milieu and the protein itself from the effects of aberrant oxygen activation leading to formation of reactive oxygen species. Indeed, studies of αKG-dependent enzymes in particular have shown that O_2 activation nevertheless occurs in the absence of substrate, albeit significantly more slowly.[11,16] This slow O_2 activation process leads to chromophoric protein preparations that have been shown to contain protein-derived hydroxylated amino acids such as phenylalanine (Phe), tyrosine (Tyr), and tryptophan (Trp) that bind directly to the iron center following hydroxylation.[99] To date, the majority of reported examples of this process have involved nonheme iron enzymes such as the αKG-dependent dioxygenases and the R2 subunit of ribonucleotide reductase (RNR R2) that are known to employ high-valent iron-based oxidants in effecting substrate transformations. Similar high-valent oxidants have thus been proposed for enzyme self-hydroxylation, reflecting the inertness of the target Phe, Tyr, and Trp sidechains.[99] Conversely, there have been no reported examples of this transformation in enzymes that employ alternative iron-based oxidants, such as the extradiol dioxygenases.

We have had a long-standing interest in the homoprotocatechuate 2,3-dioxygenase from *Arthrobacter globiformis* (MndD), an extradiol dioxygenase that exhibits an unusual preference for divalent manganese, rather than the more common iron(II) cofactor.[100-102] MndD employs this Mn(II) center and O_2 to carry out oxidative C–C bond cleavage of homoprotocatechuate (HPCA) to 5-carboxymethyl-2-hydroxymuconic semialdehyde (5-CHMSA), a key transformation in the bacterial tyrosine catabolism pathway (Scheme 2.1). Surprisingly, MndD exhibits 83% sequence

identity with the iron(II)-dependent *B. fuscum* 2,3-HPCD, which carries out the same biochemical transformation.[103,104] Crystallographic studies of both Mn(II)-MndD and Fe(II)-HPCD and their respective complexes with HPCA substrate established that both the as-isolated forms and HPCA complexes of MndD and HPCD are isostructural, as the active sites of both MnMndD and FeHPCD being nearly superimposable with a root-mean-square-deviation of 0.19 Å for all atoms in the first and second coordination sphere.[105] We later found that substitution of the nonnative metal into both MndD and HPCD, giving Fe(II)-MndD and Mn(II)-HPCD, resulted in enzyme preparations having steady-state activities towards HPCA cleavage identical to those of the native forms. Notably, both Fe(II)-HPCD and Fe(II)-MndD were readily oxidized and made inactive by simple oxidants such as H_2O_2 and ferricyanide, while both Mn(II) enzymes were unaffected. X-ray crystallography and electron paramagnetic resonance (EPR) studies indicated that the structural and electronic environment of the MndD and HPCD active sites was unaffected by this metal substitution. These striking observations led to a proposed mechanism in which the Mn(II) and Fe(II) centers of MndD and HPCD, respectively, act as conduits for electron flow between O_2 and the HPCA substrate, and thus formation of a discrete Mn(III)- or Fe(III)-superoxo adduct is not required.[85] Subsequent rapid-freeze-quench EPR studies of the reaction of wild type MnHPCD-HPCA with O_2 showed the formation of small quantities of an intermediate at very short timescales (*ca.* 10 ms) having EPR properties consistent with a Mn(III)–radical combination, which was tentatively assigned to a Mn(III)-superoxo intermediate.[106] This species then converts to a Mn(II) species that exhibited kinetics consistent with assignment to a Mn(II)-alkylperoxo adduct analogous to the Fe(II)-alkylperoxo species

observed *in crystallo*.[97] While this observation might appear to contradict our proposal that the metal center acts as a wire for electron flow, we note that both intermediates observed by EPR occur prior to the irreversible and rate-limiting O–O bond cleavage step, and these steps would, in fact, be expected to be sensitive to metal redox potentials, which are thought to be different for the Fe(II)-substituted enzymes compared to the Mn(II) forms based on the greater susceptibility of the former to chemical oxidants.[85] Specifically, the transient M(III)-superoxo intermediate would be expected to form more slowly when Mn(II) is present in the HPCD active site, while electron donation from the substrate to return to the M(II) oxidation state of the second intermediate would be rapid for Mn(III) and slow for Fe(III). Thus, the rates for these steps will self-compensate for one another, giving rise to identical overall steady-state kinetic parameters for the Mn- and Fe-substituted forms of HPCD.[106] The accumulated experimental data reported to date for HPCD and MndD collectively suggests that this pair of homologous enzymes represents an attractive platform for obtaining further molecular-level insights into the factors that modulate O_2 activation chemistry at transition metal centers.

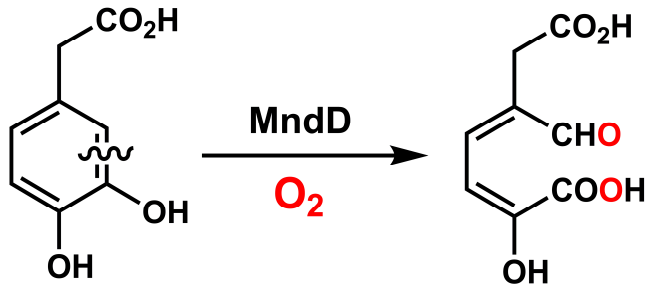

Scheme 2.1. Extradiol catechol cleavage reaction catalyzed by MndD.

In this work, we describe the generation of a unique blue-green form of Fe-substituted MndD (BG-FeMndD) generated *in vivo* under aerobic expression conditions in *E. coli*. Characterization of this species using several spectroscopic techniques and mass spectrometry suggests that the chromophore arises from a post-translationally generated self-hydroxylated form of FeMndD, indicating that the active center of FeMndD can support oxygen activation chemistry that is clearly different from that of the typical extradiol dioxygenase chemistry. This unexpected reactivity provides further evidence for an altered, lowered reduction potential for the metal center in Fe-substituted MndD compared to both MnMndD and FeHPCD.

2.2 Materials and Methods

2.2.1 Reagents and General Procedures. Reagents and buffers were of the highest grade commercially available and were used as received. All solutions and media were prepared using water purified by a Millipore Ultrapurification system. *E. coli* DH5α cells harboring the pYB2 plasmid[101] for the *A. globiformis* MndD were cultured in media containing 100 mg/L ampicillin.

2.2.2 Preparation of Fe-MndD. Fe-MndD was over-expressed and purified as described previously,[85] with some modifications. 4 – 5 mL of LB media containing 100 mg/L ampicillin were inoculated with a single colony from a fresh LB/agar plate of E. coli DH5α harboring the pYB2 plasmid for *A. globiformis* MndD and allowed to grow at 37 °C with shaking for *ca.* 5 hours. This culture was then transferred to 4 × 75 mL of M9 minimal media (100 mg/L ampicillin), which were allowed to grow overnight at 37 °C with shaking for periods of 12 to 16 hours. The blue-green form of FeMndD was

generated by transferring the overnight cultures to 4 × 1 L of M9 minimal media (100 mg/L ampicillin) and allowing the cultures to grow aerobically with shaking at 37 °C until OD_{600} reached 0.5 – 0.7. At this point, 50 mg/L of isopropyl β-D-1-thiogalactopyranoside (IPTG) and 30 mg/L of $Fe(NH_4)_2(SO_4)_2$ was added, and the culture was allowed to grow for periods of up to 24 hours prior to harvesting by centrifugation. The colorless form of FeMndD was obtained using a similar approach, except that the large scale growths were carried out anaerobically. Specifically, the overnight culture was transferred to 4 L of M9 minimal media (100 mg/L ampicillin) in a 5 L fermenter (Bioflow 2000 Fermentor, New Brunswick Scientific) which had been thoroughly sparged with N_2 and the entire growth was carried out under a low flow of N_2 gas (less than 0.5 L/min) to exclude O_2. Anaerobic cell cultures were allowed to grow for 24 hours past induction to ensure a good yield of the colorless enzyme before being harvested via centrifugation. Isolation and purification of both the blue-green and colorless forms of FeMndD was carried out aerobically using previously described methods.[104]

2.2.3 Metal and Protein Analysis. The metal content of all proteins was determined by Inductively Coupled Plasma Emission Spectroscopy (ICP analysis) performed at the Soils Research Analytical Laboratory (University of Minnesota, St. Paul). Protein concentrations were determined using the Bio-Rad protein assay (Bio-Rad Laboratories, California), using bovine serum albumin (BSA) as a standard. Samples were prepared as described previously.[102] The molar absorptivity at 280 nm of FeMndD preparations containing the blue green chromophore was found to be 40000 $M^{-1}cm^{-1}$, and this value was routinely used to quantify FeMndD concentrations in subsequent studies.

2.2.4 Enzyme Assays and Activation/Inactivation Studies. Activity studies were conducted using spectroscopic changes associated with the rate of formation of 5-CHMSA, the HPCA ring cleavage product, which has a molar extinction coefficient of $\varepsilon_{380} \sim 36000\ M^{-1}cm^{-1}$ in MOPS buffer (pH 7.5). All measurements were carried out at room temperature (23 °C) on a Beckman DU 640 spectrophotometer. All assays employed 100 – 300 nM enzyme in air saturated 50 mM MOPS buffer (pH 7.5) unless stated otherwise. The steady-state kinetic parameters were determined by using non-linear regression techniques to fit a Michaelis-Menten curve to the experimentally derived initial velocities of 5-CHMSA formation plotted versus the concentration of HPCA in the assay mixture.

2.2.5 EPR and Resonance Raman Spectroscopy. EPR samples were prepared by adding 300 μL of the as isolated enzyme (200 – 300 μM) solution in quartz tubes with an inner diameter of 3 mm, which were subsequently frozen by slow immersion in liquid nitrogen. X-band EPR spectra (9.64 GHz) were measured at liquid helium temperature (4 K) in perpendicular applied magnetic fields on a Bruker E-500 spectrometer equipped with an Oxford ESR-10 cryostat.

Resonance Raman spectra were collected on an Acton AM-506 spectrometer (1200 groove grating) using Kaiser Optical Systems holographic supernotch filters and a Princeton Instruments liquid N_2-cooled CCD detector (LN-1100 PB) with 4 cm^{-1} spectral resolution. Laser excitation lines at 100 mW power were obtained with a Spectra Physics 2060-KR-V krypton ion laser or a Spectra Physics 2030-15 argon ion laser and a 375B continuous wave dye (Rhodamine 6G). Raman spectra were collected at room temperature by 90^o scattering from a spinning flat-bottomed NMR tube, and the Raman

frequencies were referenced to indene with an accuracy of ± 1 cm^{-1}. For each sample the entire spectral range was obtained by collecting spectra at two different frequency windows, each containing the nonresonance enhanced 1005 cm^{-1} band corresponding to a phenylalanine ring mode.[107] Laser exposure totaled 60 to 90 minutes for each window. In each spectral window, the fluorescent background was subtracted prior to normalizing the intensity of the 1005 cm^{-1} bands and splicing the spectra together. Baseline corrections (polynomial fits) and curve fits (Gaussian functions) to ascertain peak positions were performed using Grams/32 Spectral Notebook (ThermoGalactic). Excitation profiles were generated by comparing peak intensities to that of the nonresonance enhanced vibration at 1005 cm^{-1}.

2.2.6 Trypsin Digests and MS-MS Experiments. MndD was digested in solution using trypsin (Sigma), using standard techniques.[108] Trypsin digested peptides were diluted with a water:acetonitrile (98:2) solution containing 0.1 % formic acid. The samples were desalted with a C18 trap (1mm). The digested peptide fragments were then separated using a 10 cm long C18 column (packed in-house), where the fragments were eluted with a linear gradient increasing at 1.6 % mobile phase B (95:5 acetonitrile:water solution containing 0.1 % formic acid) per minute for 65 minutes starting with 100 % mobile phase A (95:5 water:acetonitrile solution containing 0.1 % formic acid). The liquid chromatography system was coupled to a QSTAR pulsar quadrupole-time-of-flight mass spectrometer (Applied Biosystems, CA, USA) equipped with a nano-electrospray source (Pro-exon, Denmark). A spray voltage of 2.25 kV was applied distal to the analytical column. The TOF region acceleration voltage was 4 kV, and the injection pulse repetition rate was 6.991 kHz. The MS-MS data were collected using the information-dependant

acquisition mode using Analyst QS software (Applied Biosystems), with rolling collision energy. The search engines ProID (Applied Biosystems) and Mascot were used to confirm the presence of MndD. The peptide sequences corresponding to the product ion spectra of the control and modified peptides were confirmed using the BioAnalyst software package (Applied Biosystems).

2.3 Results

2.3.1. Properties of Aerobically Grown FeMndD

We previously obtained Fe-MndD by growing *E. coli* DH5α[pYB2] cells in iron-enriched minimal media under *anaerobic* conditions. Isolation and purification afforded colorless Fe-MndD enzyme preparations ($FeMndD_{colorless}$) which were readily inactivated by air exposure, but could be fully reactivated by treatment with appropriate reductants such as ascorbate.[85] Conversely, growth of *E. coli* DH5α[pYB2] cells in iron-enriched minimal media under aerobic conditions leads to isolation of a bluish-green colored protein (BG-FeMndD). BG-FeMndD exhibits a broad visible absorption centered at 675 nm with a molar extinction coefficient of *ca.* 750 $M^{-1}cm^{-1}$ on a per monomer basis (Figure 2.1). Interestingly, while the blue green enzyme can be obtained from cells harvested four hours after induction with IPTG, the yield of this form is maximized for cells grown up to 24 hours following induction, implying that the biochemical process generating the green protein occurs fairly slowly *in vivo*. We have been unable to identify conditions under which BG-FeMndD can be generated *in vitro*; extended exposure of reduced $FeMndD_{colorless}$ to air simply results in oxidation of the iron center to iron(III), but without any apparent color change.

ICP metal analyses indicate that our preparations of BG-FeMndD typically contain *ca.* 0.6 equiv of iron and trace amounts of manganese. BG-FeMndD exhibits weak steady-state reactivity towards HPCA, with a turnover number (k_{cat}) of ca. 10 min^{-1} on a per metal per monomer basis, considerably lower than the value of 420 min^{-1} previously reported for fully reduced Fe(II)-MndD, but comparable to the value of 29 min^{-1} obtained for as-isolated $FeMndD_{colorless}$.[85] Unlike $FeMndD_{colorless}$, treatment with 20-fold excesses of ascorbate or the strong reductant dithinonite results in only modest increases in HPCA cleavage activity, affording k_{cat} values of *ca.* 20 – 30 min^{-1}. Pre-treatment of stock solutions of BG-FeMndD with 20 equiv. of H_2O_2 resulted in further diminution of as-isolated enzyme activity by *ca.* 30%. These observations strongly suggest that the majority of enzyme-bound iron is in the form of iron(III), which is incapable of supporting oxidative extradiol ring cleavage. We may further conclude that the modest amount of activity observed for BG-FeMndD arises primarily from small amounts of contaminating MnMndD and enzyme-bound iron(II), much as was the case for $FeMndD_{colorless}$. However, our inability to reduce the iron center of BG-FeMndD points either to an active site that is no longer accessible to small molecule reductants, or else to an iron(III) site possessing a significantly depressed reduction potential relative to the colorless form, perhaps as a consequence of changes in iron-binding ligands. Treatment of the as-isolated enzyme with exogenous anions such as cyanide, azide, or fluoride did not perturb either the position or intensity of the green chromophore centered at 675 nm, consistent with the notion of a coordinatively saturated or inaccessible iron center.

The green color and depressed reactivity of BG-FeMndD are reminiscent of other mononuclear nonheme iron enzymes that have been shown to oxidatively inactivate themselves via hydroxylation of a protein derived aromatic amino acid in close proximity to the active site.[99] We therefore employed EPR and resonance Raman spectroscopies to further characterize the putative Fe(III) center in BG-FeMndD.

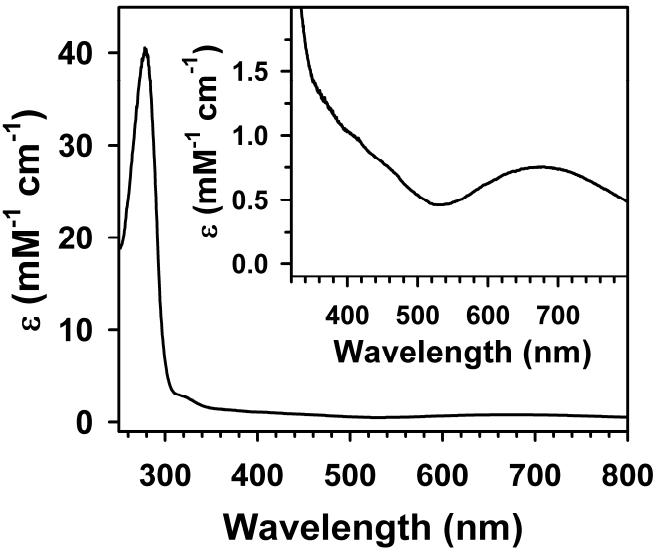

Figure 2.1. UV-Vis absorption spectrum of BG-FeMndD. The inset shows an expansion of the visible region of the spectrum.

2.3.2 Spectroscopic Studies of BG-FeMndD

EPR represents an obvious technique to test for the presence of iron(III) in our preparations of BG-FeMndD. The X-band EPR spectrum of BG-FeMndD at 4K in perpendicular applied fields exhibits prominent absorption features at g = 8.3, 7.8, and 5.6, a derivative-shaped feature at g = 4.3, and an extremely broad depression centered at g = 2.8 (Figure 2.2). These EPR features arise from moderately axial high spin Fe(III) (S = 5/2) centers present in the sample with transitions involving both the ground and first

excited Kramers doublet. Both the g = 8.3 feature and g = 7.8 feature correspond to ground state transitions involving two different S = 5/2 centers having E/D values of 0.12 and 0.085, respectively, while the asymmetric g = 5.6 feature is associated with transitions in the first excited Kramers doublet for both of the E/D = 0.12 and 0.085 species. We note that the intensity of the g = 4.3 signal is weak, indicating that BG-FeMndD does not contain a significant quantities of a highly rhombic (E/D ~ 0.33) Fe(III) center. $FeMndD_{colorless}$ exhibits a surprisingly similar EPR spectrum with features at g = 8.4, 8.3, 6.5, 5.5, 4.3, and 2.0 consistent with the presence of multiple S = 5/2 Fe(III) centers in the enzyme, though $FeMndD_{colorless}$ exhibits a much more intense g = 4.3 feature than BG-FeMndD, pointing towards a greater fraction of rhombic (E/D = 0.33) Fe(III).[85] The similar EPR spectra of BG-FeMndD and $FeMndD_{colorless}$ suggest that the species giving rise to the observed chromophore accounts for only a small fraction of the EPR-observable iron present in the sample. The EPR properties of BG-FeMndD are reminiscent of those reported for iron-substituted phosphomannose isomerase (blue PMI),[75] which contained a dihydroxyphenylalanine (DOPA) residue chelated to the oxidized Fe(III) center, as well as those of tyrosine hydroxylase (TyrH)[109] and phenylalanine hydroxylase (PheH)[110] in the presence of catecholamines such as dopamine. For example, EPR studies of blue PMI revealed the presence of at least three distinct high-spin Fe(III) centers with E/D values of 0.064, 0.135, and 0.33, similar to our BG-FeMndD observations.

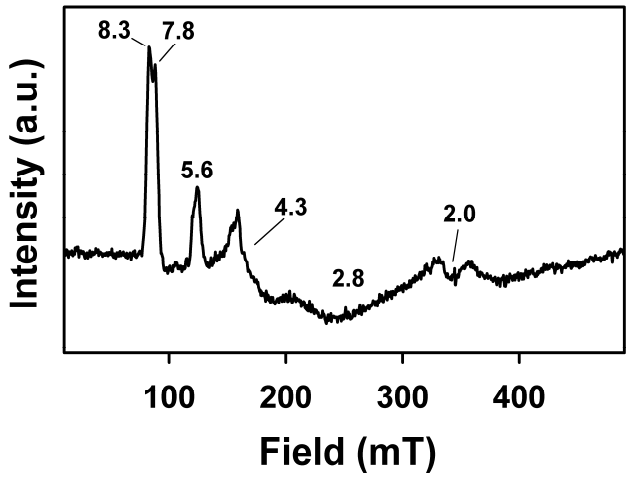

Figure 2.2. Perpendicular-mode X-band EPR spectrum of as-isolated BG-FeMndD. Conditions: microwave frequency, 9.64 GHz; microwave power, 0.2 mW, modulation amplitude, 0.8 mT.

Resonance Raman studies of BG-FeMndD provided compelling evidence for self-hydroxylation of an aromatic amino acid in the FeMndD active site. Laser excitation into the 675 nm chromophore afforded a set of resonance enhanced vibrations at *ca.* 530, 569, 586, 646, 666, 1161, 1271, 1318, and 1423 cm^{-1} (Figure 2.3a) that gain intensity as the excitation wavelength approaches the absorption maximum (Figure 2.3b and Figure A2.1) The pattern of vibrations is evocative of those observed previously for the F208Y variant of RNR R2,[47] TyrH in complex with dopamine and other catecholamines,[111,112] blue PMI,[75] (*S*)-2-hydroxypropylphosphonic acid epoxidase (HppE),[77] and taurine/α-ketoglutarate dioxygenase (TauD),[62-64] all of which were shown to contain DOPA moieties chelated to Fe(III) centers (Table 2.1). The vibrations in the 500 – 670 cm^{-1} region can be assigned to metal-ligand vibrations associated with the iron(III)-catecholate chelate, while features between 1100 and 1500 cm^{-1} reflect catecholate ring deformation modes. The pattern of vibrations is distinct from those observed for uteroferrin[113,114] or

the W48F/D84E mutant of RNR R2,[54] both of which contain iron(III)-phenolate moieties (derived from self-hydroxylation of a Phe residue in the case of W48F/D84E RNR R2), as well as that of the 2,4-dichlorophenoxyacetate/αKG dioxygenase (TfdA), which contains a self-hydroxylated Trp residue (Table 2.1).[65] This distinction can be made from the presence of multiple vibrations in the 500 – 670 cm^{-1} region, whereas iron(III) adducts with phenolates and hydroxylated Trp residues will give only a single ν(Fe–O) mode. Similarly, the feature at 1318 cm^{-1} has been shown to be uniquely associated with a catechol ring vibration,[112] and is not observed in resonance Raman studies of chromophores containing phenolates or hydroxylated Trp. The excitation profiles obtained for BG-FeMndD also closely resemble those reported earlier for other examples of iron(III)-catecholate moieties in enzymes, including the TyrH-dopamine complex[112] and self-hydroxylated HppE.[77] Unfortunately, our inability to identify conditions for the preparation of BG-FeMndD *in vitro* precluded the use of oxygen isotope ($H_2{}^{18}O$, $^{18}O_2$) labeling methods to gain further insight into the vibrational properties of the bound DOPA moiety. Nonetheless, our resonance Raman data provide strong evidence for self-hydroxylation of a tyrosine residue in MndD to yield an Fe(III)-DOPA adduct, and we therefore turned to mass spectrometry methods to identify the site of this modification.

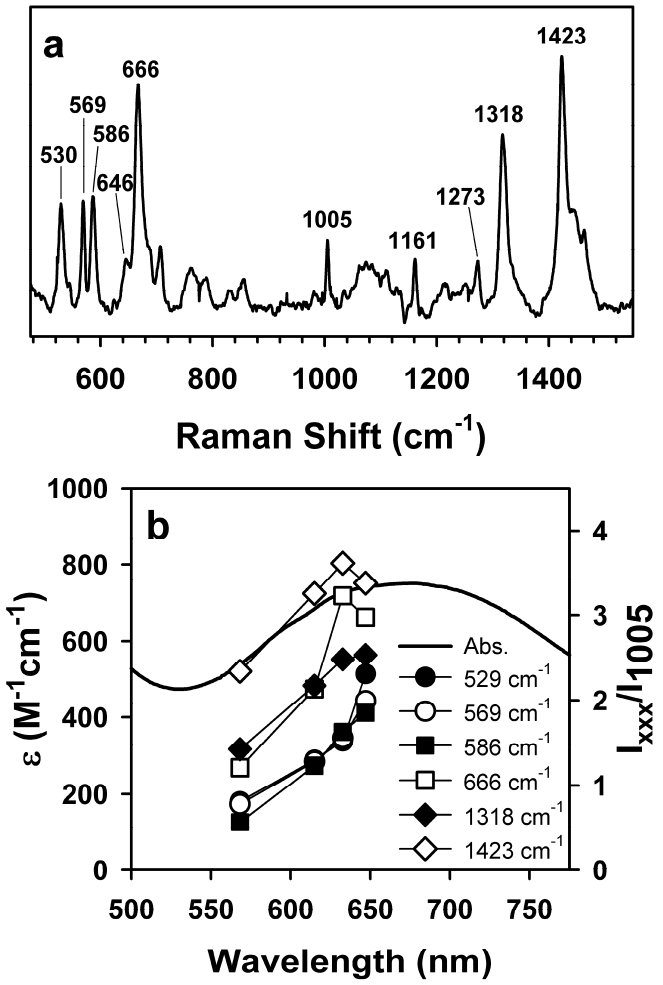

Figure 2.3. (a) Resonance Raman spectrum of BG-FeMndD obtained with 632.8 nm laser excitation. (b) Excitation profiles for selected bands as a function of excitation wavelength. The intensities are relative to the normalized intensity of the non-resonance enhanced 1005 cm^{-1} band corresponding to a phenylalanine ring mode.[107]

Table 2.1. Resonance Raman vibrations of nonheme iron proteins with Fe(III)-catecholate and related chromophores.[a]

Enzyme Complex	Resonance Raman Vibration (cm^{-1})									Reference
Fe(III)-catecholate										
Fe(III)MndD-DOPA	530	569 586	646	666	1273	1318	1423	1464		this work
Fe(II)TauD-αKG + O_2	544	580	623	644	1261	1314	1425	1475		62
Fe(II)TauD-succinate + O_2	534	582	623	646	1263	1314	1421	1474		64
Fe(II)HppE + O_2	531	591	636		1264	1315	1425	1478		77
Fe(II)[F208Y]RNR R2 + O_2	512	592	619		1263	1319	1420	1475		47
Fe(III)TyrH-dopamine	528	592	631		1275	1320	1425	1475		112
blue PMI[b]		591	631		1266	1330	1428	1482		75
Fe(III)-phenolate and hydroxylated Trp										
uteroferrin (O-Tyr)		575		805 872	1168 1285			1503	1603	114
W48F/D84E RNR R2 (*m*-O-Phe)			615		1281			1484	1580	54
Fe(II)TfdA-αKG + O_2 (O-Trp)		564	750	898 970	1240 1274	1344			1622	65

[a] MndD, Mn(II)-dependent homoprotocatechuase 2,3-dioxygenase; DOPA, dihydroxyphenylalanine; αKG, α-ketoglutarate; TauD, taurine/αKG dioxygenase; HppE, (*S*)-2-hydroxypropylphosphonic acid epoxidase; RNR R2, R2 subunit of ribonucleotide reductase; TyrH, tyrosine hydroxylase; PMI, phosphomannose isomerase; TfdA, 2,4-dichlorophenoxyacetate/αKG dioxygenase.

[b] PMI is a zinc(II)-dependent metalloprotein, but up to 0.5 equiv Fe / PMI monomer are present in the as-isolated enzyme.

2.3.3 Mass Spectrometry of BG-FeMndD.

Consideration of the X-ray crystal structures of nonheme iron oxygenases in which self-hydroxylation has been shown to occur shows that the modified residue is typically within 10 Å of the iron center, presumably reflecting the importance of proximity to the incipient iron-based oxidant.[22,99] The crystal structure of as-isolated MnMndD (1F1U.pdb) reveals three tyrosine residues, Tyr255 (8.3 Å distant), Tyr257 (5.2 Å), and Tyr269 (7.2 Å) within 10 Å of the Mn(II) center.[105] We carried out nanoscale capillary LC/MS/MS studies of trypsin digests of BG-FeMndD, and obtained evidence for hydroxylation of one of these residues. Specifically, the mass of the triply charged parent ion (*m/z* = 697.3) for the peptide His248–Arg265 is 16 Da higher than the predicted value of 2073 Da, consistent with incorporation of a single oxygen atom. MS/MS fragmention of this peptide indicated that fragment ions containing Tyr255 (b8, b8, b9, b9, and b10 in Figure 2.4b) have masses some 16 Da higher than would be expected, consistent with incorporation of one oxygen atom into Tyr255. There is no evidence for hydroxylation of Tyr257, based on the lack of an additional +16 Da mass increase for fragment ions containing this residue (b10 and y9 in Figure 2.4b). A parent ion corresponding to the peptide containing Tyr269 was not observed in our mass spectrometry studies, presumably due to the large mass of the peptide containing Tyr269 that would be obtained by trypsin digestion. Studies with alternate proteases are presently ongoing. Nonetheless, our mass spectrometry results support the hydroxylation of Tyr255 while excluding modification of Tyr257, but cannot exclude hydroxylation of Tyr269. Finally, we also found that only a portion of the protein was modified, as a significant amount of a quadruply charged parent ion (*m/z* = 519.2) corresponding to the predicted mass (2073

Da) of the His248–Arg265 peptide was observed. Tandem MS/MS studies of this parent ion gave the expected fragmentation pattern (Figure 2.4a) for this peptide, with no evidence for +16 Da mass increases associated with any residue. The presence of significant amounts of unmodified peptide is not unexpected given the extinction coefficient of $\varepsilon_{675} \sim 750\ M^{-1}cm^{-1}$ observed for our BG-FeMndD preparations, which is considerably lower than the typical values of 2000 – 2500 $M^{-1}cm^{-1}$ associated with Fe(III)-catecholate model complexes.[115] Analogous LC/MS/MS studies of MnMndD (not shown) indicated that no enzyme self-hydroxylation occurred in the native Mn(II)-substituted form.

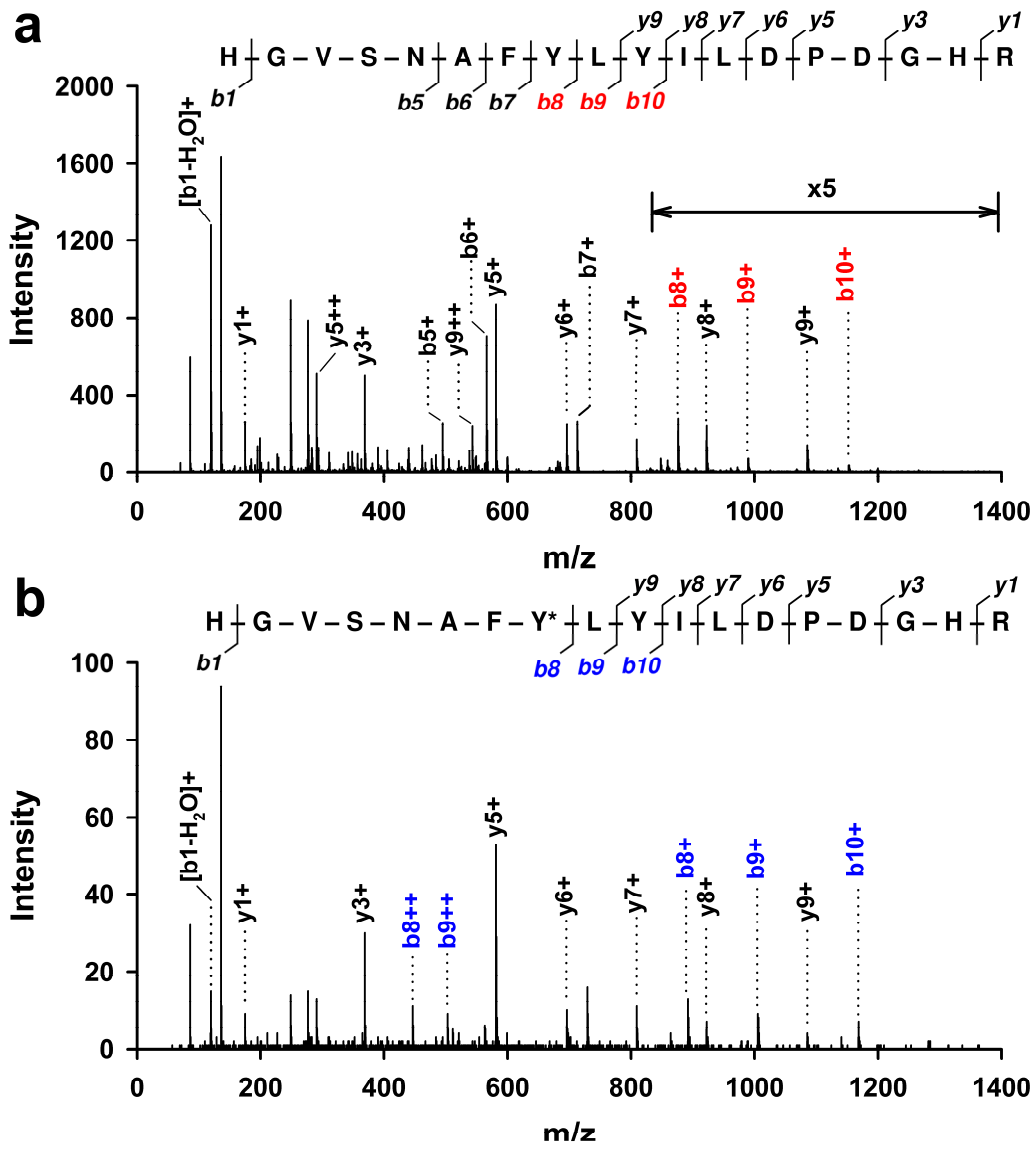

Figure 2.4. MS/MS spectra of (a) the quadruply charged parent ion of the His248-Arg265 peptide containing unmodified Tyr255 (519.2 *m/z*) and (b) the triply charged parent ion of the His248-Arg265 peptide containing hydroxylated Tyr255 (Y*) (697.3 *m/z*) obtained from the same sample of BG-FeMndD. Ions containing unmodified Tyr255 are shown in red and those containing modified Tyr255 are shown in blue, while remaining ions are shown in black. The labeled y and b fragmentation ions are given in the fragmentation map located just above each spectrum. Singly and doubly charged ions are represented by + and ++, respectively. The y-axis intensity of a portion the spectrum shown in (a) has been multiplied by a factor of 5 for clarity.

2.4 Discussion

In this work, we have shown that growth of the normally manganese(II)-dependent extradiol dioxygenase MndD under aerobic conditions in the presence of excess iron(II) in *E. coli* leads to isolation of an inactive greenish blue protein, BG-FeMndD. Based on our UV/Vis, resonance Raman, and mass spectrometry results, this chromophore can be attributed to self-hydroxylation of one of the tyrosine residues near the active site, affording an Fe(III)-DOPA adduct. Fe-substituted MndD thus represents a new addition to a growing collection of nonheme iron enzymes that can self-hydroxylate an endogenous aromatic amino acid close to the active site in the absence of their prime substrate.[99]

Our results suggest that only a portion of the protein contains hydroxylated Tyr residues. The strongest evidence for this comes from the extinction coefficient associated with Fe(III)-bound DOPA, which we found to be approximately 750 $M^{-1}cm^{-1}$ at the 675 nm absorption maximum on a *per monomer basis*. Given that this feature is a LMCT transition specifically associated with the Fe(III) center, correcting for our typical metal occupancy of 0.6 equiv iron per monomer would afford an ε_{675} value of 1250 $M^{-1}cm^{-1}$ on a *per iron, per monomer basis*, assuming that all iron is present as iron(III) with bound DOPA. This value is approximately half of the values of 2000 – 2500 $M^{-1}cm^{-1}$ that have been reported for iron(III) model complexes containing a single catecholate ligand.[115] The incomplete modification suggested by our UV/Vis absorption data is consistent with the presence of multiple $S = 5/2$ Fe(III) centers as shown by EPR spectroscopy as well as the large amount of unmodified His248-Arg265 peptide observed in our mass spectrometry studies of trypsin digested BG-FeMndD. Indeed, the majority of self-

hydroxylated nonheme iron enzymes reported to date show only partial modification, based primarily on the lower extinction coefficients associated with their LMCT transitions and mass spectrometry results.[69,99] For example, *in vitro* self-hydroxylation of Tyr73 of TauD affords chromophores with extinction coefficients ranging from 300 – 700 $M^{-1}cm^{-1}$ depending upon the reaction conditions employed,[62-64] and a significant fraction of enzyme activity can be restored simply by treating self-hydroxylated TauD with dithionite.[63] The only examples where the iron(III)-catecholate absorptivity approaches the expected values are those where the transformation occurs *in vivo*, including F208Y RNR R2 (ε_{720} = 2500 $M^{-1}cm^{-1}$) and iron-substituted PMI (ε_{680} = 2100 $M^{-1}cm^{-1}$). It is, however, simplistic to attribute this to a distinction between *in vivo* and *in vitro* conditions, as illustrated by the observation that the *in vivo* generated chromophore of HppE exhibited a molar absorptivity at 680 nm of ε_{680} = 450 $M^{-1}cm^{-1}$.[77]

An alternate, and perhaps more plausible, explanation is that the extent of modification will be related to both proximity of the target residue to the iron center and the dynamic flexibility of the protein. This is nicely illustrated by a structural analysis of unmodified forms of F208Y RNR R2 and HppE. The crystal structure of diiron(II) R208Y RNR R2 shows direct ligation of the mutant Tyr208 residue to Fe_1 of the active site,[43] assuring that the target residue is in close proximity to the diiron cluster during the entire chemical cycle leading to formation of DOPA208.[46,47] Studies of HppE showed that both Tyr103 and Tyr105 could be modified,[77] and crystallographic analysis of the unmodified HppE indicated that Tyr105 is 8.7 Å away from the iron(II) center, while Tyr103 is even more distant at 10.8 Å,[78] thus suggesting that HppE must rearrange itself more extensively than F208Y RNR R2 to self-hydroxylate the target amino acids.

Although a crystal structure of Fe-substituted MndD has not been reported to date, the near identity of the reported FeHPCD, MnHPCD, and MnMndD structures to one another[85,105] suggests that the FeMndD structure should be quite similar to that of MnMndD. Our mass spectrometry studies of BG-FeMndD showed evidence for hydroxylation of Tyr255, which is 8.3 Å away from the metal center in MnMndD while excluding hydroxylation of the significantly closer residue Tyr257 that is 5.2 Å away from the metal center. While it is perhaps surprising that Tyr257 residue is not modified based on mass spectrometry, it is possible that dynamic flexing of the protein in solution favors motions that bring Tyr255 into a more optimal position for formation of DOPA255. Furthermore, as we were unable to identify peptide fragments containing Tyr269 (7.2 Å away from the metal center) via mass spectrometry, it is possible that some fraction of the chromophore arises from iron(III)-bound DOPA269. Indeed, this is an attractive rationale to account for the multiplicity of $S = 5/2$ Fe(III) centers observed by EPR, as well as the fact that the intensity of the green chromophore in BG-FeMndD is greater than those observed for other self-hydroxylated enzymes other than F208Y RNR R2 and PMI. Also, the resonance Raman spectrum of BG-FeMndD is considerably more complex in the 500 – 700 cm^{-1} region than expected (Figure 2.3), as there are at least five distinct resonance-enhanced vibrations as opposed to the three vibrations expected for a typical Fe(III)-DOPA adduct (Table 2.1).[112] This is reminiscent of earlier observations for self-hydroxylated TauD generated by reaction of Fe(II)TauD-succinate with H_2O_2, in which the addition of bicarbonate anion was shown to result in the appearance of a new feature in the low-frequency region of the resonance Raman spectrum. This was attributed to a downshift of the Fe–O_4 vibration of the bound DOPA residue caused by

bicarbonate modulation of the Lewis acidity of the Fe(III) center in modified TauD.[63,64] A similar effect may also be operant in BG-FeMndD, such that there are two Fe(III)-DOPA adducts in slightly different environments giving rise to different Raman vibrations.

With the notable exception of iron-substituted PMI, ordinarily a zinc(II)-dependent isomerase, all reported instances of aromatic self-hydroxylation have involved nonheme iron enzymes known to employ a high-valent iron oxidant in their catalytic cycles. Although no such intermediate has been directly detected during enzyme self-hydroxylation, the oxygen-isotope incorporation patterns observed by resonance Raman spectroscopy [47,54,62-65,77] and the EPR characterization of a tyrosyl radical + Fe(III) combination in TauD[63] that presumably arises via H-atom abstraction from Tyr73 by an oxoiron(IV) oxidant strongly implicate the involvement of high-valent iron centers in carrying out self-hydroxylation of Phe, Tyr, and Trp moieties as well.[99] How then might this chemistry occur in Fe-substituted MndD, which employs a very different O_2 activation pathway for extradiol catechol ring cleavage?[85,95,96] We have found that self-hydroxylation does not occur in the native Mn(II) form of MndD, nor has it been observed in FeHPCD, which exhibits a very similar sequence and active site structure.[104,105] The metal-substitution studies of HPCD and MndD showed that the as-isolated forms of FeHPCD and FeMndD were susceptible to inactivation by oxidants such as H_2O_2 and ferricyanide, while their Mn-substituted congeners were not oxidized. Furthermore, FeMndD oxidized to the inactive colorless Fe(III) form upon air exposure much more readily than FeHPCD.[85] These observations logically imply that the reduction potentials (E^o for the $M^{III/II}$ couple) of Fe-substituted HPCD and MndD are

lower than those of the Mn-substituted enzymes. This is not unexpected given that the structural congruence of FeHPCD and MnHPCD suggests that the protein environment alters the intrinsic aqueous $Fe^{III/II}$ (E^o = +0.77 V) and $Mn^{III/II}$ (E^o = +1.56 V) reduction potentials[116] to a comparable degree for both metal centers, and presumably this applies to MnMndD and FeMndD as well. FeMndD also appears to exhibit a lower $Fe^{III/II}$ reduction potential relative to FeHPCD, based on its increased susceptibility to air oxidation and the generation *in vivo* of the self-hydroxylated BG-FeMndD described herein. The fact that BG-FeMndD is only generated during aerobic growths implies that an O_2-derived oxidant is likely to be involved in effecting self-hydroxylation of FeMndD. Similarly, as anaerobically-grown $FeMndD_{colorless}$ does not convert to the blue-green form during aerobic purification or incubation, a simple combination of iron and O_2 is insufficient to catalyze self-hydroxylation. We therefore propose that intracellular biological reductants play a role in the *in vivo* O_2 activation process that leads to BG-FeMndD. Iron-substituted PMI,[75] HppE,[77] and the DNA repair enzyme AlkB[66] provide precedent for this proposal, as all three have been found to self-hydroxylate *in vivo*, and only AlkB utilizes a well-defined biologically available cofactor (αKG). We favor the involvement of a high-valent iron-oxo intermediate in the self-hydroxylation of FeMndD, by analogy to past examples of this transformation that suggest a potent oxidant is required to carry out this modification (Scheme 2.2). The lack of self-hydroxylation in MnMndD implies that the 2-His-1-carboxylate facial triad may not be able to support analogous O_2 activation chemistry at a Mn(II) center that would lead to a putative high-valent manganese-oxo oxidant. This is consistent with observations on several αKG-dependent dioxygenases, in which Mn(II) was found to be unable to support substrate

turnover.[117,118] Indeed, Mn(II) substitution has frequently used as a means to obtain crystal structures of several mononuclear nonheme oxygenase enzyme-substrate complexes, such as isopenicillin N-synthase and AlkB, under aerobic conditions, further highlighting the lack of O_2 reactivity of Mn(II)-substituted nonheme oxygenases.[118-120]

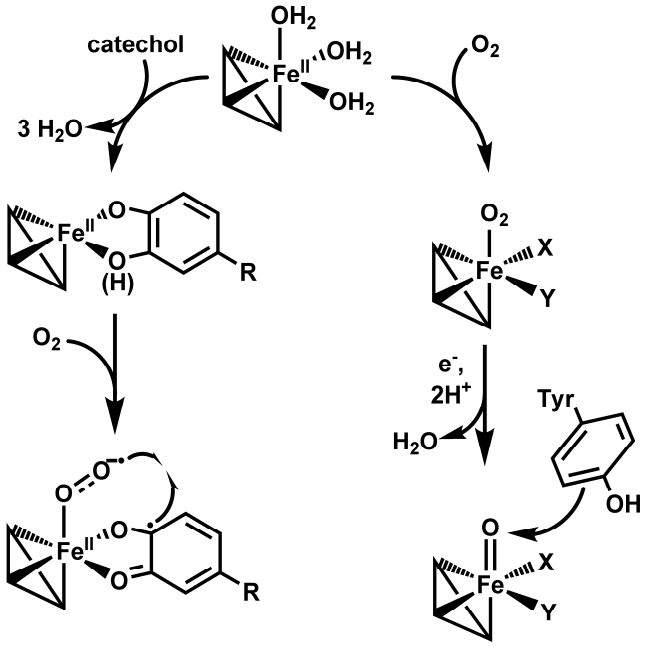

Scheme 2.2. Two distinct O_2 activation pathways in FeMndD. The iron coordination sites X and Y in the structures on the left may be vacant or consist of ligands derived from solvent or some other unidentified source.

In closing, we have shown that substitution of iron into the manganese(II)-dependent extradiol dioxygenase MndD results in self-hydroxylation of one or more endogenous Tyr residues under *in vivo* conditions. This reactivity indicates that FeMndD possesses an altered $Fe^{III/II}$ reduction potential relative to MnMndD, as well as the closely related enzyme FeHPCD, that allows O_2 activation in the absence of substrate to occur,

leading to an oxidant capable of Tyr hydroxylation. This chemistry further suggests that MndD and HPCD may in fact differentially tune the redox potential of their active site metal centers *in the absence* of their catechol substrate. Moreover, since tyrosine hydroxylation is unlikely to be supported by the metal-superoxo oxidant implicated in the reaction mechanism of extradiol dioxygenases, we have proposed the involvement of a putative high-valent iron-oxo species. As the iron(II) form of FeMndD can nonetheless carry out extradiol catechol ring cleavage, the alternate mode of reactivity observed herein provides a striking illustration of the diverse O_2 activation processes that can be supported by the 2-His-1-carboxylate facial triad metal binding motif in a single enzyme.

Chapter 3.

XAS Studies of Co(II)-Substituted Homoprotocatechuate 2,3-Dioxygenase and Related Model Complexes

3.1 Introduction

In 1955, Hayaishi found that the nonheme iron-containing enzyme pyrocatechase (catechol 1,2-dioxygenase) could oxidize its substrate with incorporation of both atoms of molecular oxygen into the product.[121] This startling and unexpected discovery[122,123] laid the grounds for a explosive increase in our knowledge of the interaction of transition metal centers with molecular oxygen in biology over the past half-century. Recent years have seen growing interest in a superfamily of mononuclear nonheme iron oxygenases that bind iron(II) with two His residues and a carboxylate derived from either Asp or Glu (the 2-His-1-carboxylate facial triad)[28,124] have shown to be involved in a staggering array of oxidative transformations ranging from the biosynthesis of medicinally important antibiotics[3] and the regulation of the hypoxic response[67] to the bioremediation of environmentally damaging aromatic compounds.[125]

While many nonheme iron oxygenases are thought to employ a high-valent oxoiron oxidant to effect their substrate transformations,[81] extradiol catechol dioxygenases, which carry out oxidative cleavage of the aromatic C–C bond *cis* to the diol functionality of the catechol,[95] are of particular interest due in part to the fact that they are thought to employ a significantly different O_2 activation process.[7,96,97,126] Specifically, O_2 binding to the iron(II)-catecholate ES complex results in a putative iron(III)-superoxo-catecholate species, which then converts to an iron(II)-superoxo-semiquinone adduct via donation of an electron from the electron-rich aromatic substrate to the iron center. This diradical species is expected to undergo facile radical recombination to afford an iron(II)-alkylperoxo species that undergoes O–O bond heterolysis with concomitant oxygen atom incorporation and ring cleavage via a Criegee

rearrangement to give the resultant ring-cleavage product. Direct structural evidence for both the iron(II)-superoxo-semiquinone and iron(II)-alkylperoxo species has recently been obtained via elegant *in crystallo* X-ray crystallography trapping experiments by Kovaleva and Lipscomb with the iron(II)-dependent extradiol dioxygenase homoprotocatechuate 2,3-dioxygenase from *Brevibacterium fuscum* (HPCD) and the electron deficient substrate 4-nitrocatechol (4NC).[97] Interestingly, *B. fuscum* HPCD shares 83% sequency identity[104] and a remarkable degree of structural homology[105] with the homoprotocatechuate 2,3-dioxygenase from *Arthrobacter globiformis* (MndD), which exhibits a surprising dependence on manganese(II) to carry out the oxidative conversion of homoprotocatechuate (3,4-dihydroxyphenylalanine, HPCA) to 5-carboxymethyl-2-hydroxymuconic semialdehyde (5-CHMSA) (Scheme 3.1).[100-102] Why then has Nature chosen to employ Fe(II) for HPCD and Mn(II) in MndD to carry out the same chemical transformation? In the course of efforts to resolve this intriguing question, we found that substitution of the non-native metal cofactor in HPCD and MndD, affording MnHPCD and FeMndD, respectively, results in enzyme preparations that exhibit catalytic efficiencies (defined as k_{cat}/K_M^{HPCA} and k_{cat}/K_M^{O2}) towards HPCA cleavage that equal those of the native FeHPCD and MnMndD forms.[85] EPR spectroscopic studies established that the MnMndD/MnHPCD and FeMndD/FeHPCD enzyme pairs exhibit identical electronic structures in the presence of HPCA substrate, while the X-ray crystal structure of MnHPCD revealed that there was no alteration of active site structure upon metal substitution.[85] Furthermore both FeHPCD and FeMndD were susceptible to inactivation by oxidants such as H_2O_2, while the activities of the Mn(II)-substituted forms were unaffected. This observation suggests that the M(III)/M(II) reduction potential of

the Fe-substituted forms is lower than that those of the Mn-substituted enzymes, in line with a comparable reduction of the intrinsic aqueous reduction potentials (aqueous E^o for Fe(III/II) = +0.77 V, E^o for Mn(III/II) = +1.56 V)[116] for each metal in the HPCD and MndD active sites. We therefore proposed a mechanism in which facile electron transfer from the bound aromatic substrate to the metal center precludes a discrete metal(III)-superoxo species, the formation of which would be less favorable in the manganese case.[85] This proposal represents a radical departure from the mechanisms proposed for other mononuclear nonheme iron oxygenases, in which O_2 binding to the iron(II) center of the enzyme-substrate complex is thought to invariably result in an initial iron(III)-superoxo species.[80]

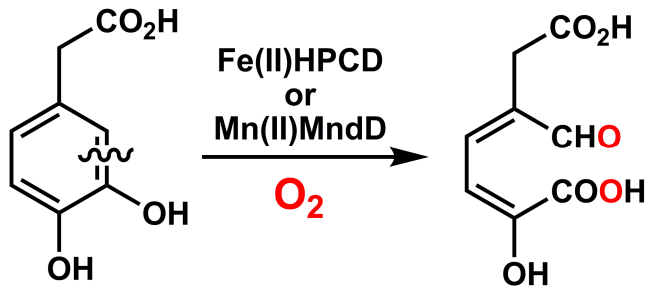

Scheme 3.1. Extradiol catechol cleavage reaction catalyzed by HPCD and MndD.

Rapid-freeze-quench EPR studies of the reaction of wild type MnHPCD-HPCA with O_2 by Hendrich and coworkers provided an initial experimental test of this remarkable proposal.[106] These experiments revealed that small quantities of an intermediate having EPR properties consistent with a Mn(III)-superoxo formulation were observed at very short timescales (*ca.* 10 ms).[106] This species then converts to a Mn(II) species that exhibited kinetics consistent with assignment to a Mn(II)-alkylperoxo

adduct[106] analogous to the Fe(II)-alkylperoxo species observed *in crystallo*.[97] Both intermediates observed by EPR occur prior to the irreversible and rate-limiting O–O bond cleavage step, and so the likelihood of their formation and decay would be expected to be sensitive to metal redox potential. That is, the transient M(III)-superoxo intermediate would be expected to form more slowly when Mn(II) is present in the HPCD active site, while electron donation from the substrate to return to the M(II) oxidation state of the second intermediate would be rapid for Mn(III) and slow for Fe(III) (Scheme 3.2). This self-compensation effect would therefore account for the identical overall steady-state kinetic reactivity for HPCD and MndD.[106]

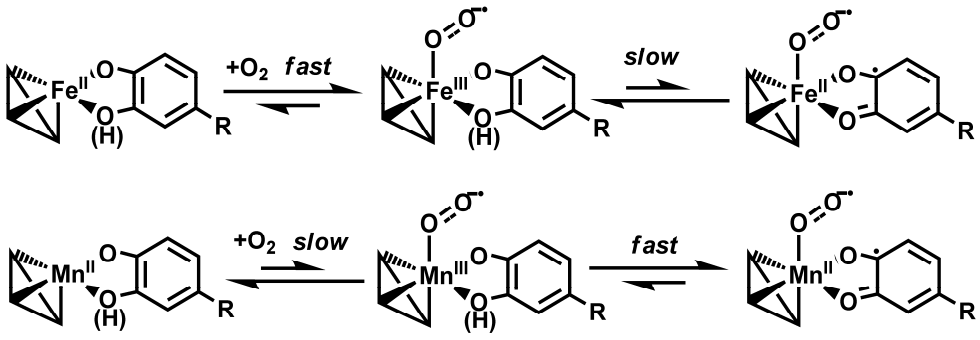

Scheme 3.2. Self-compensating effect of Mn(III/II) and Fe(III/II) redox potentials on the relative rates of two steps prior to rate-limiting O–O bond cleavage in MndD and HPCD.

The EPR studies of MnHPCD reported by Hendrich *et al.*, suggest that the metal redox potential may in fact play a role in modulating the relative rates of several steps in the reaction pathway of HPCD and MndD. One approach to testing this hypothesis is to employ a non-native metal cofactor that exhibits a different aqueous M(III/II) reduction potential than either manganese or iron, with cobalt (aqueous E^o for Co(III/II) = +1.92

V)[116] representing the most attractive option. We have recently found that Co(II) can be incorporated stoichiometrically into the HPCD active site by expression of the enzyme in *E. coli* in the presence of excess $Co(II)Cl_2$.[127] Remarkably, this Co-substituted HPCD exhibits a similar rate for steady-state turnover of its HPCA substrate as observed for both MnHPCD and FeHPCD, although its apparent affinity for O_2 appears to be significantly lower.[127] UV/Vis studies of as-isolated CoHPCD and the CoHPCD-HPCA complex reveal weak and broad visible Co(II) d-d transitions ($\varepsilon_{525} \sim 60\ M^{-1}cm^{-1}$ on a per Co basis) indicative of a distorted six-coordinate geometry for the Co(II) center, in agreement with intepretations from EPR spectroscopy.[127] Conversely, binding of the competitive inhibitor 3-hydroxyphenylacetic acid (3HPA) elicits a lavender-colored species with absorption features at 515 nm ($\varepsilon \sim 260\ M^{-1}cm^{-1}$) and 575 nm ($\varepsilon \sim 330\ M^{-1}cm^{-1}$), with the shape and intensity of these transitions being consistent with a distorted five-coordinate Co(II) site in CoHPCD-3HPA.[127] This appears to be the first example of an iron-dependent oxygenase that can still support oxygen activation chemistry with a non-native Co(II) center, in contrast to other oxygenases such as quercetin dioxygenase that may employ Co(II) as the native metal cofactor.[128,129] We have thus initiated a program to extensively characterize the reactivity of CoHPCD towards catechol substrates in conjunction with a variety of spectroscopic studies for comparison with the previously characterized Fe- and Mn-substituted HPCDs. As part of this effort, we have carried out initial X-ray absorption spectroscopic (XAS) studies of CoHPCD both in its as-isolated form (**CoHPCD**) and in complexes with HPCA (**CoHPCD-HPCA**), 4-nitrocatechol (**CoHPCD-4NC**), and 3HPA (**CoHPCD-3HPA**) substrates and inhibitors, the results of which are presented in this work. In order to provide a basis for

interpretation of the X-ray absorption near-edge (XANES) features of these enzymatic samples, we also present XANES studies of a series of five-coordinate Co(II) complexes containing a tris(pyrazolyl)hydroborate ligand and dithiocarbamate, organoxanthate, and acetylacetonate anicillary ligands. The results of our XAS study corroborate the structural hypotheses developed from UV/Vis and EPR studies of CoHPCD, and provide a framework for future studies of intermediates in the CoHPCD catalytic cycle that have been trapped by rapid-freeze-quench techniques.

3.2 Experimental

The Co(II) model complexes studied here were kindly provided by Prof. Michael Jensen (Ohio University). CoHPCD was grown and purified according to published procedures,[85,104] except that 25 mg/L $CoCl_2$ was added at the time of induction. All CoHPCD samples were prepared by Andrew Fielding.

3.2.1 XAS Sample Preparation

[($Tp^{Ph,Me}$)Co(S_2COEt)], 1-S_2COEt. A 14 mM solution of [($Tp^{Ph,Me}$)Co(S_2COEt)] was prepared in anaerobic toluene in a glove box and frozen immediately in an EXAFS sample cell. 7 XAS scans to $k = 6$ Å^{-1} were collected at NSLS beamline X3B.

[($Tp^{Ph,Me}$)Co(S_2CNPh_2)], 1-S_2CNPh_2. A 13 mM solution of [($Tp^{Ph,Me}$)Co(S_2CNPh_2)] was prepared in anaerobic toluene in a glove box and frozen immediately in an EXAFS sample cell. 6 XAS scans to $k = 6$ Å^{-1} were collected at NSLS beamline X3B.

[($Tp^{Ph,Me}$)Co(S_2CNEt_2)], 1-S_2CNEt_2. A 14 mM solution of [($Tp^{Ph,Me}$)Co(S_2CNEt_2)] was prepared in anaerobic toluene in a glove box and frozen immediately in an EXAFS sample cell. 8 XAS scans to $k = 6$ Å^{-1} were collected at SSRL beamline 7-3.

[($Tp^{Ph,Me}$)Co(acac)], 1-acac. An 11 mM solution of [($Tp^{Ph,Me}$)Co(acac)] was prepared in anaerobic toluene in a glove box and frozen immediately in an EXAFS sample cell. 8 XAS scans to $k = 6$ Å^{-1} were collected at SSRL beamline 7-3.

CoHPCD. As-isolated CoHPCD ($[Co]_T = 2.5$ mM) in 50 mM pH 7.5 MOPS buffer with 20% glycerol was frozen in an EXAFS sample cell. 9 XAS scans to $k = 13.5$ Å^{-1} were collected at SSRL beamline 7-3.

CoHPCD-HPCA. As-isolated CoHPCD ($[Co]_T = 2.5$ mM) in 50 mM pH 7.5 MOPS buffer with 20% glycerol was treated with 4 equiv. of HPCA in an anaerobic chamber and then immediately frozen in an EXAFS sample cell. No color change was evident upon sample freezing. 15 XAS scans to $k = 13.5$ Å^{-1} were collected at SSRL beamline 7-3.

CoHPCD-3HPA. As-isolated CoHPCD ($[Co]_T = 2.5$ mM) in 50 mM pH 7.5 MOPS buffer with 20% glycerol was treated aerobically with 5 equiv. of 3-HPA and then immediately frozen in an EXAFS sample cell. The sample exhibited the typical lavender color associated with this complex. 15 XAS scans to $k = 13.5$ Å^{-1} were collected at SSRL beamline 7-3.

3.2.2 X-ray Absorption Spectroscopy. Data Collection.

X-ray absorption data were collected on beamline 7-3 of the Stanford Synchrotron Radiation Light source (SSRL) of SLAC National Accelerator Laboratory with storage ring conditions of 3.0 GeV and 80 – 100 mA, or on beamline X3B of the National Synchrotron Light Source (NSLS) at Brookhaven National Laboratory with storage ring conditions of 2.8 GeV and 100 – 300 mA. At SSRL, Co K-edge XAS data were collected for frozen solutions maintained at a temperature of *ca.* 10 - 15 K over an energy

ranges of 7.48 – 8.42 keV (EXAFS data for **CoHPCD**, **CoHPCD-HPCA**, and **CoHPCD-3HPA**) or 7.48 – 7.87 keV (**1-S_2CNEt_2** and **1-acac**) using a Si(220) double crystal monochromator for energy selection and an Oxford Instruments CF1208 continuous flow liquid helium cryostat for temperature control. Harmonic rejection was achieved by a 9 keV cutoff filter. A 3μ Fe filter and Soller slits were used to attenuate background scattering. At NSLS, Fe K-edge XAS data were collected for frozen solutions maintained at *ca.* 25 – 30 K over an energy range of 7.5 – 7.9 keV (**1-S_2COEt** and **1-S_2CNPh_2**) using a Si(111) double crystal monochromator for energy selection and a Displex closed cycle cryostat for temperature control. A bent focusing mirror was used for harmonic rejection. A 3μ Fe filter was used to attenuate background scattering. Data were obtained as fluorescence excitation spectra with either a 30 element (SSRL) or 13-element (NSLS) solid-state germanium detector array (Canberra). A cobalt powder spectrum was recorded concomitantly for internal energy calibration and the first inflection point of the Co K-edge was assigned to 7709.5 eV.

3.2.3 Data Analysis.

Data reduction, averaging, and normalization were performed using the program EXAFSPAK.[130] Following calibration and averaging of the data, background absorption was removed by fitting a Gaussian function to the pre-edge region and then subtracting this function from the entire spectrum. A three-segment spline with fourth order components was then fit to the EXAFS region of the spectrum in order to extract $\chi(k)$. The program pySpline was used to identify optimal parameters for the spline function employed in EXAFSPAK.[131] Analysis of the pre-edge features was carried out with the program SSExafs[132] using a previously described protocol,[133] with the following

modification. Specifically, the ratios of the combined Gaussian/arctangent edge function were varied empirically, rather than being fixed in the 75%/25% proportion we have employed in previous Fe K-edge XANES studies.[133,134] This was necessary to obtain accurate fits for samples with extremely weak pre-edge features. The pre-edge fitting parameters reported are those providing the best match to both the experimental data and its second derivative.

Theoretical phase and amplitude parameters for a given absorber-scatterer pair were calculated using FEFF 8.40[135] and were utilized by the opt program of the EXAFSPAK package during curve-fitting. A truncated model of the CoHPCD active site was built from coordinates of the X-ray crystal structure of as-isolated Co(II)HPCD (E G. Kovaleva, unpublished observations). One bound His was removed, while for the remaining His, the Co–N_{His} distance was shortened to 2.10 Å and the His ring was rotated to be planar with the Co–N_{His} bond. Other Co-bound ligands were not modified from the crystal coordinates. The bound Glu was monodentate with a Co–O distance of 2.03 Å, while the three bound water ligands exhibited Co–O_{wat} bonds of 2.13 – 2.27 Å. A complete set of phase and amplitude parameter for all possible single-scattering paths and multiple-scattering paths involving the His ligand were calculated for this structure. The structure of a partially refined structure of a CoHPCD-4NC (4-NC = 4-nitrocatechol) complex (E G. Kovaleva, unpublished observations) was used for constructing Feff input models of **CoHPCD-HPCA** and **CoHPCD-3HPA**. One bound His was removed, and the nitro moiety of the 4NC was deleted. The remaining His and the bound catechol were rotated so that the rings were planar with the Co–O/N bonds. The Co–N_{His} bond length was shortened to 2.075 Å from 2.116 Å), while the Co–O_{Glu} bond length was shortened to

1.95 Å from 1.972 Å (the Glu was bound in a monodentate fashion). For the bound catechol, Co–O_3 = 2.025 Å, while Co–O_4 = 2.1595 Å. The remaining ligand was a bound water with Co–O_{wat} = 2.25 Å. This model was used for EXAFS analysis of **CoHPCD-HPCA**. The input model for **CoHPCD-3HPA** was identical to that of **CoHPCD-HPCA**, except that O_4 of the bound catechol was removed, while Co–O_3 was shortened slightly to 1.975 Å to better reflect a putative Co(II)-phenolate interaction. Only single-scattering paths were calculated for our models of **CoHPCD-HPCA** and **CoHPCD-3HPA**. In all analyses, the coordination number of a given shell was a fixed parameter, and was varied iteratively while bond lengths (r) and Debye-Waller factors (σ^2) were allowed to freely float. The amplitude reduction factor S_0 was fixed at 0.9, while the edge shift parameter E_0 was allowed to float as a single value for all shells (thus in any given fit, the number of floating parameters was typically equal to (2 × num shells) + 1). The goodness of fit F was defined simply as $\Sigma (\chi_{exptl}-\chi_{calc})^2$. For fits to unfiltered data, a second goodness of fit parameter, F-factor, was defined as $[\Sigma k^6(\chi_{exptl}-\chi_{calc})^2 / \Sigma k^6 \chi_{exptl}^2]^{1/2}$. In order to account for the effect that additional shells have on improving fit quality, an third goodness-of-fit metric *F*' was employed. $F' = F^2 / (N_{IDP} - N_{VAR})$, where N_{VAR} is the number of floated variables in the fit, while N_{IDP} is the number of independent data points and is defined as $N_{IDP} = 2\Delta k \Delta r / \pi$.[88] In the latter equation, Δk is the *k*-range over which the data is fit, while Δr is the back-transformation range employed in fitting Fourier-filtered data. *F*' is thus of principal utility in fitting Fourier-filtered data, but can also be employed for unfiltered data by assuming a large value of Δr.

3.3 Results

3.3.1 XANES Studies of CoHPCD and Related Models

The four five coordinate Co(II) model complexes studied in this work all exhibit fairly complex Co K-edge shapes, with a first intense inflection ranging from 7717.0 eV for **1-S_2COEt** to 7718.31 eV for **1-acac** and a less intense second inflection centered at *ca.* 7723 eV for all four complexes (Figure 3.1). The second energy is typical of that for Co(II), by analogy to previous studies of high-spin Co(II) model complexes[136-139] and Co(II) substituted enzymes.[140-142] The white line of the rising Co K-edge exhibits a single prominent absorption feature centered at *ca.* 7723 eV, which has been shown to be typical of Co(II) centers, whereas Co(III) complexes exhibit an additional intense peak at the absorption maximum centered at *ca.* 7736 eV,[138,139,141] a feature which is clearly not present for any of the **1-X** samples studied. The edge features of the three sulfur containing complexes **1-S_2COEt**, **1-S_2CNPh$_2$**, and **1-S_2CNEt$_2$** are remarkably similar to one another in both shape and intensity, suggesting that they exhibit very similar structures and electronic properties. **1-acac** exhibits a somewhat sharper and more intense Co K-edge absorption, which is not unexpected given the differences in Co(II) ligand set. Our analysis of the pre-edge features associated with a formally symmetry forbidden 1s to 3d transition show that all four complexes exhibit a single, fairly weak pre-edge feature centered at 7709.8 ± 0.1 eV, the energy of which is again consistent with a Co(II) oxidation state assignment.[136,137,141] The integrated areas of this feature vary substantially, ranging from 5.0 units for **1-S_2CNPh$_2$** to 12.1 units for **1-S_2COEt**, suggesting a fairly significant variation in the degree of distortion from centrosymmetry across the series. Given that X-ray crystallography studies indicate a fairly similar

structure for **1-S_2COEt**, **1-S_2CNPh$_2$**, and **1-S_2CNEt$_2$**,[143] and **1-acac** is expected to exhibit a similar structure as well, it is difficult to rationalize this variation in pre-edge intensities on structural grounds alone. The pre-edge values obtained for the **1-X** complexes fall in the midpoint of the few reported high-spin Co(II) pre-edge areas, which have ranged from 22 units and 11.2 units for a highly distorted five-coordinate Co(II)–NO adduct and a square pyramidal Co(II) site, respectively, in a porous organic host,[136,137] to 5.2 units for Co(II)-substituted hemerythrin, which contains a mixture of five-coordinate and distorted six-coordinate Co(II) sites.[141]

Figure 3.2 depicts a comparison of the XANES features of as-isolated **CoHPCD** the **CoHPCD-HPCA** substrate complex, and the **CoHPCD-3HPA** inhibitor complex. All three complexes exhibit edge spectra typical of enzymatic high-spin Co(II) sites,[141,142,144,145] with an average Co K-edge inflection energy of *ca.* 7722.8 ± 0.3 eV similar to that of the Co(II) model complexes examined in this work. Both **CoHPCD** and **CoHPCD-HPCA** exhibit Co K-edge absorption spectra that are sharper and more intense than those of the **1-X** model complexes, which is likely indicative of a higher coordination number in the enzyme samples. Consistent with this notion, the pre-edge features are extremely weak, with both **CoHPCD** and **CoHPCD-HPCA** exhibiting a single transition at *ca.* 7710.1 eV with integrated areas of 4.7 and 4.1 units, respectively. Conversely, **CoHPCD-3HPA** exhibits a less intense and broader rising Co K-edge absorption of similar appearance to the five-coordinate **1-X** model complexes, with two distinct inflections at 7719.20 eV and 7723.08 eV. The intensity of the pre-edge feature of **CoHPCD-3HPA** is significantly greater than for the other two CoHPCD samples studied here, with two distinct peaks split by 2.3 eV having a total integrated intensity of

18.2 units. This large pre-edge area is indicative of a substantial centrosymmetric distortion upon 3HPA binding to CoHPCD, and is consistent with the distorted five-coordinate Co(II) site suggested from the electronic absorption properties of this adduct.

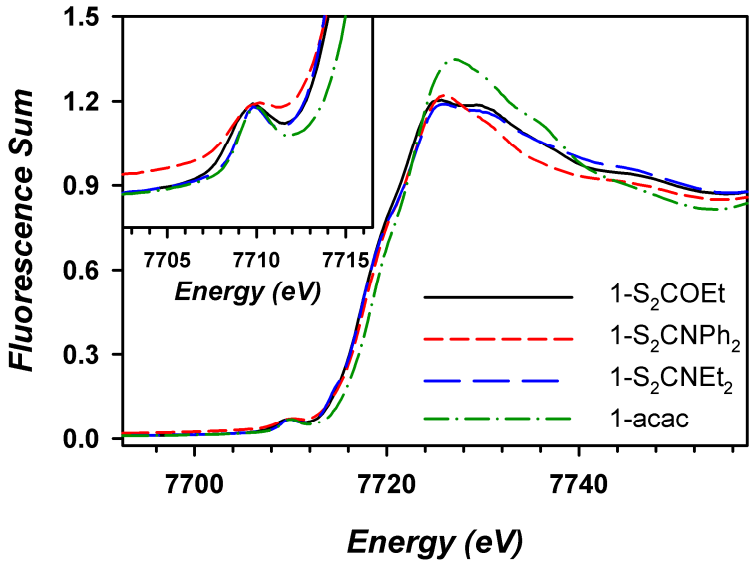

Figure 3.1. Comparison of the Co K-edge X-ray absorption edge and pre-edge (inset) features for several five-coordinate Co(II) model complexes. Key: **1-S_2COEt** (black, ——), **1-S_2CNPh$_2$** (red, – – –), **1-S_2CNEt$_2$** (blue, — — —), and **1-acac** (green, –·–·–).

Table 3.1. Pre-edge Analysis Parameters for Several 5C Co(II) Complexes.[a]

Species	E_{edge} (eV)[b]	$E_{pre\text{-}edge}$ (eV)	height	width	area
1-S_2COEt	7722.42 (7717.00)	7709.68(2)	0.0389(4)	2.91(4)	12.1(2)
1-S_2CNPh$_2$	7723.10 (7717.65)	7709.69(3)	0.0202(6)	2.31(10)	5.0(2)
1-S_2CNEt$_2$	7723.05 (7717.64)	7709.81(4)	0.035(1)	2.16(10)	8.1(4)
1-acac [c]	7722.92 (7718.31)	7709.92(5) 7712.32(20)	0.0406(7) 0.007(1)	2.33(9) 1.9(4)	10.1(4) 1.4(4)

[a] The fits presented are those that give the best agreement to the experimental data and its second derivative. Values in parentheses represent uncertainties of that parameter.
[b] Values in parentheses are those of a low energy inflection along the rising edge.
[c] The weak shoulder at 7712.32 eV is necessary to accurately model the dominant peak in the pre-edge

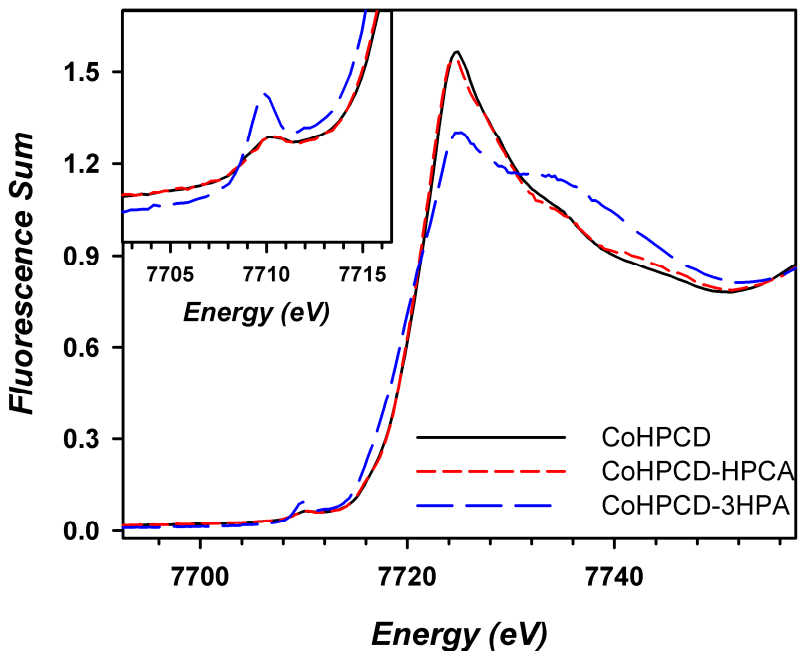

Figure 3.2. Comparison of the Co K-edge X-ray absorption edge and pre-edge (inset) features for CoHPCD samples. Key: **CoHPCD** (black, ——), **CoHPCD-HPCA** (red, – – –), and **CoHPCD-3HPA** (blue, — — —).

Table 3.2. Pre-edge Analysis Parameters for As-isolated CoHPCD and its Complexes.[a]

Species	E_{edge} (eV) [b]	$E_{pre\text{-}edge}$ (eV)	height	width	area
CoHPCD	7722.77	7710.13(7)	0.018(1)	2.42(17)	4.7(3)
CoHPCD-HPCA	7722.47	7710.13(8)	0.018(1)	2.18(21)	4.1(4)
CoHPCD-3HPA	7723.08 (7719.20)	7709.84(4) 7712.18(10)	0.061(1) 0.023(1)	1.99(8) 2.12(24)	13.0(6) 5.2(7)

[a] The fits presented are those that give the best agreement to the experimental data and its second derivative. Values in parentheses represent uncertainties of that parameter.
[b] Edge energy value in parentheses for the 3HPA complex is that of a low energy inflection along the rising edge.

3.3.2 Single-Scattering EXAFS Analysis of CoHPCD, CoHPCD-HPCA, and CoHPCD-3HPA

We turned to EXAFS analysis to obtain metrical parameters for **CoHPCD**, **CoHPCD-HPCA**, and **CoHPCD-3HPA** to gain a better understanding of what structural changes, if any, occur at the Co(II) site upon substrate or inhibitor binding. All three species exhibit well-defined $k^3\chi(k)$ EXAFS modulations out to the k = 13.5 Å^{-1} limit of data collection. Both **CoHPCD** and **CoHPCD-HPCA** exhibit very similar EXAFS spectra and Fourier transforms (Figure 3.3), with the Fourier transform exhibiting a single intense feature at r' = 1.6 Å^{-1} associated with first-shell ligands and a set of weak features distributed over r' = 2.2 – 4.0 Å^{-1} that can be assigned to single- and multiple-scattering pathways involving coordinated histidine ligands.[146-149] **CoHPCD-3HPA** exhibits a clearly different set of $k^3\chi(k)$ modulations, with the most apparent change being the shape of the feature at k = 4 Å^{-1}. Its Fourier transform is of similar appearance to those of **CoHPCD** and **CoHPCD-HPCA**, but with a downshift in the position of the primary first shell feature to r' ~ 1.5 Å that indicates some shortening in the metal-ligand bond lengths of the Co(II) center in **CoHPCD-3HPA**.

Analysis of the Fourier-filtered first-shell data for **CoHPCD** at the single-scattering level of theory (Table 3.3) indicates that the inner shell can be fit well to 5 - 6 N/O scatterers at 2.09 Å. Attempts to split this shell (fits 6-8) into two subshells consisting of a shell of Co–N/O scatterers and a shorter Co–O scatterer while retaining a total coordination number of 6 afforded modest improvements in fit quality, based on the magnitude of F and F'. However, the Debye-Waller factor associated with the short Co–O shell was typically quite large, and the difference in distance between the two shells of

0.13 Å is smaller than the resolution limitation of 0.14 Å (calculated as $2/(\pi \cdot k_{range})$)[87,90] of the EXAFS data collected for **CoHPCD**. Identical results are obtained for fits to unfiltered data (Table 3.3), with a splitting of the principal Co–N/O shell being unjustified based on the lack of improvement in *F'* (which corrects for the additional variables in the fit) and the difference in bond lengths being within the resolution of the data. We therefore conclude that splitting the principal Co–N/O shell into two subshells is not justified based on the available EXAFS data, and thus the best fit to the inner shell consists of 6 N/O scatterers at 2.09 Å (fits 6 and 14 in Table 3.3 and Figure 3.4). This fit is consistent with both our pre-edge analysis and data from UV/Vis and EPR spectroscopies, which favor a distorted 6C Co(II) site. Collection of Co K-edge XAS data for **CoHPCD** over a larger k_{range} to k = 15 Å^{-1} may allow us to more definitely address whether the principal Co–N/O shell can be split.

Addition of a shell of 4 Co•••C scatterers at *ca.* 3.1 Å leads to a minor additional improvement in fit quality (fit 20 in Table 3.3 and Figure 3.4), although σ^2 for this shell is quite high for chemically reasonable numbers of carbon scatterers (arising from two bound His and a Glu), presumably reflecting disorder in the positions of these carbon atoms. Adding a second shell of carbon scatterers results in decreased fit quality, with the refined bond distance being quite sensitive to coordination number, suggesting that a single-scattering analysis of majority of the outer-shell features is not justified. This observation is not surprising given that these features arise principally from multiple-scattering effects (*vide infra*), with earlier studies of His-containing metalloproteins showing that these features cannot be accurately reproduced by single-scattering EXAFS alone.[146,148]

Single-scattering EXAFS analysis of Fourier-filtered inner-shell data for **CoHPCD-HPCA** revealed a best fit consisting of 5 Co–N/O scatterers at 2.06 Å (fit 3, Table 3.4 and Figure 3.5), indicating some possible shortening in the average Co(II)-ligand bond lengths compared to as-isolated **CoHPCD** and consistent with the small difference in FT maxima forthe two samples (Figure 3.3). We initially expected to be able to uniquely resolve one or more short Co–O distances arising from the bound catecholate substrate, on the basis that the Co–O bond lengths associated with the deprotonated catechol oxygens will be significantly shorter than those of other Co(II) ligands. However, attempts to split the principal Co–N/O shell and resolve two different sets of scatterers were unsuccessful (fits 6-9, Table 3.4), as chemically unreasonable σ^2 values were obtained and the additional shells were not justified by the lack of improvement in fit quality. As was the case in our analysis of **CoHPCD**, analysis of unfiltered EXAFS data for **CoHPCD-HPCA** afforded an identical best fit for the first shell, with a shell of 5 Co–N/O scatters at 2.07 Å (fit 12, Table 3.4) that cannot be separated into two subshells. The quality of the fit to unfiltered data can be improved by addition of a disordered shell of 3-4 Co•••C scatters at *ca.* 2.97 Å (fit 20, Table 3.4 and Figure 3.5). The apparent change in coordination number for **CoHPCD-HPCA** is surprising, given that XANES analysis indicates that it has very similar symmetry to the six-coordinate **CoHPCD**, while UV/Vis and EPR spectroscopies are also consistent with a distorted octahedral geometry. However, given the typical error of 25% in coordination number and the accuracy of ±0.02 Å in bond lengths determined by EXAFS,[87,90] it is in fact the case that our EXAFS analyses of **CoHPCD** and **CoHPCD-HPCA** are identical to one another within experimental error.

As we anticipated, EXAFS analysis of **CoHPCD-3HPA** indicates more substantial structural changes occur at the Co(II) center of CoHPCD upon 3HPA binding. The best fit to the Fourier-filtered inner shell is obtained for 4 to 5 Co–N/O scatterers at 1.99 Å (fit 2, Table 3.5 and Figure 3.6), which is an experimentally significant reduction in average bond length of ~0.1 Å compared to **CoHPCD**. The reduction in coordination number is in agreement with the large pre-edge area for **CoHPCD-3HPA**, as well as the enhanced intensity of the Co(II) d–d transitions observed by UV/Vis spectroscopy. It was not possible to obtain meaningful fits when this shell was split into two subshells with a total coordination number of 5 or 6 (fits 6-8, 11 in Table 3.5). While two-shell fits with a total coordination number of 4 (fits 10, 12 in Table 3.5) gave chemically reasonably Debye-Waller factors and an experimentally significant improvement in fit quality, the difference in absorber-scatterer distances of 0.12 Å between the two subshells for these fits is smaller than the intrinsic resolution limitation of 0.14 Å associated with the data collected for **CoHPCD-3HPA** (k_{range} = 2 – 13.5 Å^{-1}). An analogous sequence of fits is obtained for the EXAFS analysis of unfiltered data (Table 3.5). We therefore cannot justify a two-shell fit, and conclude that the first coordination sphere for **CoHPCD-3HPA** is best modeled with a single shell of 4 to 5 Co–N/O scatterers at 1.99 Å. As we suggested earlier for **CoHPCD**, the collection of Co K-edge XAS data for **CoHPCD-3HPA** over a larger k_{range} to k = 15 Å^{-1} should provide further insight into whether the principal Co–N/O shell can be split into two subshells. Finally, fits to unfiltered data also support the presence of 3-4 Co•••C scatters at *ca.* 3.0 Å (fit 23, Table 3.5 and Figure 3.6), with the addition of this shell affording a substantial improvement in the quality of the fit.

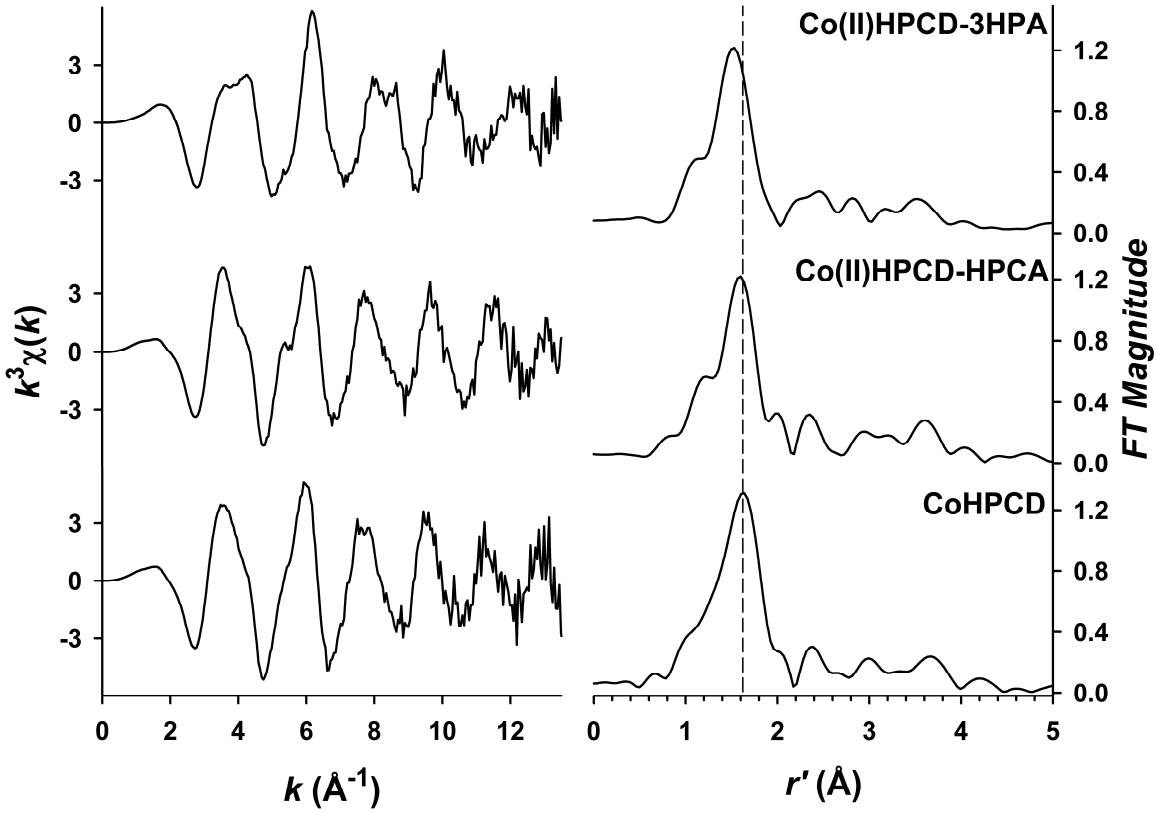

Figure 3.3. (left) Comparison of the $k^3\chi(k)$ weighted EXAFS data for **CoHPCD** (bottom), **CoHPCD-HPCA** (middle), and **CoHPCD-3HPA** (top) The y-axis scaling is identical for all plots. (right) Comparison of the Fourier transforms of **CoHPCD** (bottom), **CoHPCD-HPCA** (middle), and **CoHPCD-3HPA** (top). The FT range used for all samples was k = 2 – 13.5 Å^{-1}. The vertical dashed line highlights changes in the position of the most intense feature in the Fourier transforms.

Table 3.3. Single-Scattering EXAFS Analysis of **CoHPCD**.[a]

Fourier-filtered EXAFS fits

	Co-N/O			Co-O				
fit	**n**	**r**	**σ^2**	**n**	**r**	**σ^2**	**F** [b]	***F'*** [b]
1	3	2.10	2.0				63.2	482
2	4	2.10	3.4				25.3	77
3	5	2.09	4.8				9.6	11
4	***6***	***2.09***	***6.1***				***10.3***	***13***
5	7	2.09	7.4				22.6	61
6	5	2.09	4.6	1	1.96	7.8	8.4	11
7	4	2.11	2.6	1	1.98	1.4	6.2	6
8	4	2.10	3.9	2	1.99	9.9	8.6	12
9	6	2.08	5.6	1	1.88	15.1	12.8	26
10[c]	2	2.28	47.8	4	2.07	4.7	12.3	24

Unfiltered EXAFS fits

	Co-N/O			Co•••C					
fit	**n**	**r**	**σ^2**	**n**	**r**	**σ^2**	**F** [b]	***F*-factor** [b]	***F'*** [b]
11	3	2.10	1.8				273	0.457	0.346
12	4	2.10	3.3				192	0.384	0.172
13	5	2.10	4.6				159	0.349	0.118
14	*6*	*2.09*	*5.9*				*160*	*0.350*	*0.119*
15	7	2.09	7.3				186	0.377	0.160
16	5 1	2.10 1.95	3.8 4.3				157	0.346	0.126
17	4 1	2.11 1.98	2.1 1.1				152	0.341	0.118
18	4 2	2.10 2.00	3.7 10.6				161	0.351	0.133
19	6	2.10	6.0	2	3.10	3.1	142	0.329	0.103
20	***6***	***2.10***	***6.0***	***4***	***3.08***	***9.7***	***148***	***0.336***	***0.112***
21	6	2.10	6.0	6	3.07	17.6	160	0.350	0.131
22	6	2.10	6.0	4 4	3.08 4.03	10.2 5.1	154	0.343	0.136

[a] *k*-range = 2 – 13.5 Å^{-1}, back-transformation range for Fourier-filtered data = 0.7 – 2.25 Å, resolution = 0.137 Å, r is in units of Å, σ^2 is in units of 10^{-3} Å^2. Fits of the N/O shell used parameters for a N scatterer. EXAFS cannot distinguish between scatterers differing by Z = 1.

[b] Goodness-of-fit parameter F defined as $\Sigma(\chi_{exptl}-\chi_{calc})^2$. *F-factor* = $[\Sigma k^6(\chi_{exptl}-\chi_{calc})^2 / \Sigma k^6\chi_{exptl}^2]^{1/2}$. A third parameter, *F'*, is defined as $F' = F^2 / \nu$, where $\nu = N_{IDP} - N_{VAR}$. N_{IDP} is the number of independent data points, while N_{VAR} is the number of floated variables in each optimization step. The values of *F'* shown have been divided by a factor of 10^4 for convenience. *F'* is a measure of whether an added shell significantly improves the fit.

[c] Fit 10 represents an attempt to fit two shells consisting of two long Fe–N and 4 shorter Fe–O/N scatterers.

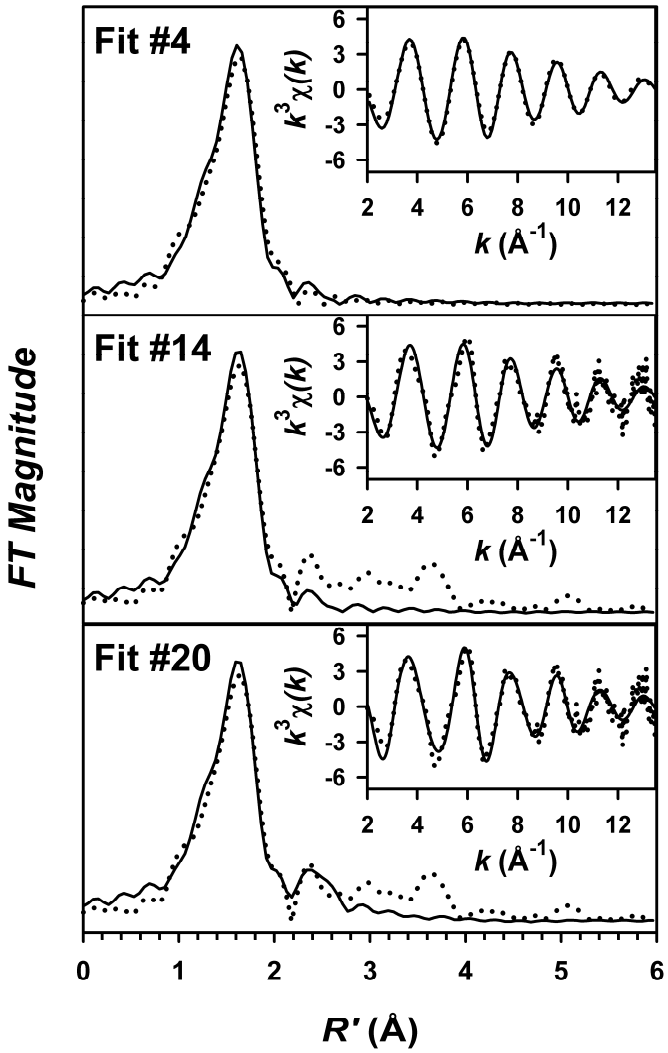

Figure 3.4. Fits to the Fourier transforms of the Fe K-edge EXAFS data ($k^3\chi(k)$) and unfiltered EXAFS spectra ($k^3\chi(k)$, insets) for **CoHPCD**. Experimental data is shown with dotted lines (•••) and fits are shown with solid lines (——). Fourier transformation range: k = 2 – 13.5 Å^{-1}; back-transformation range = 0.7 – 2.25 Å (fit 4 only). Fit parameters associated with the stated fit are shown in Table 3.3.

Table 3.4. Single-Scattering EXAFS Analysis of **CoHPCD-HPCA**.[a]

Fourier-filtered EXAFS fits

	Co-N/O			Co-O				
fit	**n**	**r**	**σ^2**	**n**	**r**	**σ^2**	**F** [b]	**F'** [b]
1	3	2.06	2.2				42.6	227
2	4	2.06	3.6				16.8	35
3	***5***	***2.06***	***5.0***				***10.7***	***14***
4	6	2.06	6.4				18.2	41
5	7	2.06	7.8				34.9	152
6	5	2.06	4.8	1	1.89	18.2	11.5	22
6a	5	2.07	4.8	1	2.24	14.0	9.5	15
7	4	2.06	3.9	1	2.10	16.5	10.0	17
8	3	2.06	3.1	2	2.04	12.3	10.5	18
9	3	2.10	1.9	1	1.98	0.1	14.2	34

Unfiltered EXAFS fits

	Co-N/O			Co•••C					
fit	**n**	**r**	**σ^2**	**n**	**r**	**σ^2**	**F** [b]	***F*-factor** [b]	***F'*** [b]
10	3	2.07	2.1				220	0.442	0.214
11	4	2.07	3.6				166	0.384	0.122
12	*5*	*2.07*	*5.0*				*152*	*0.368*	*0.102*
13	6	2.06	6.3				167	0.385	0.123
14	7	2.06	7.8				202	0.424	0.180
15	5 1	2.07 2.29	4.7 8.0				142	0.355	0.098
16	4 1	2.07 2.19	3.5 14.0				148	0.363	0.107
17	3 1	2.06 2.11	2.6 4.8				165	0.383	0.131
18	5	2.07	5.0	2	2.96	7.4	132	0.342	0.084
19	5	2.07	5.0	3	2.96	9.9	129	0.339	0.081
20	***5***	***2.07***	***5.0***	***4***	***2.96***	***12.6***	***129***	***0.338***	***0.080***
21	5	2.07	5.0	4 4	2.96 4.44	12.9 6.4	103	0.303	0.057
22	5 1	2.07 2.25	4.5 8.0	4	2.99	12.1	124	0.333	0.083
23	5 0.5	2.08 2.27	4.7 3.0	4	2.99	11.9	123	0.331	0.081

[a] *k*-range = 2 – 13.5 $Å^{-1}$, back-transformation range for Fourier-filtered data = 0.7 – 2.2 Å, resolution = 0.138 Å, r is in units of Å, σ^2 is in units of 10^{-3} $Å^2$. Fits of the N/O shell used parameters for a N scatterer. EXAFS cannot distinguish between scatterers differing by Z = 1.

[b] Goodness-of-fit parameter F defined as $\Sigma(\chi_{exptl}-\chi_{calc})^2$. *F-factor* = $[\Sigma k^6(\chi_{exptl}-\chi_{calc})^2 / \Sigma k^6\chi_{exptl}^2]^{1/2}$. A third parameter, *F'*, is defined as $F' = F^2 / \nu$, where $\nu = N_{IDP} - N_{VAR}$. N_{IDP} is the number of independent data points, while N_{VAR} is the number of floated variables in each optimization step. The values of *F'* shown have been divided by a factor of 10^4 for convenience. *F'* is a measure of whether an added shell significantly improves the fit.

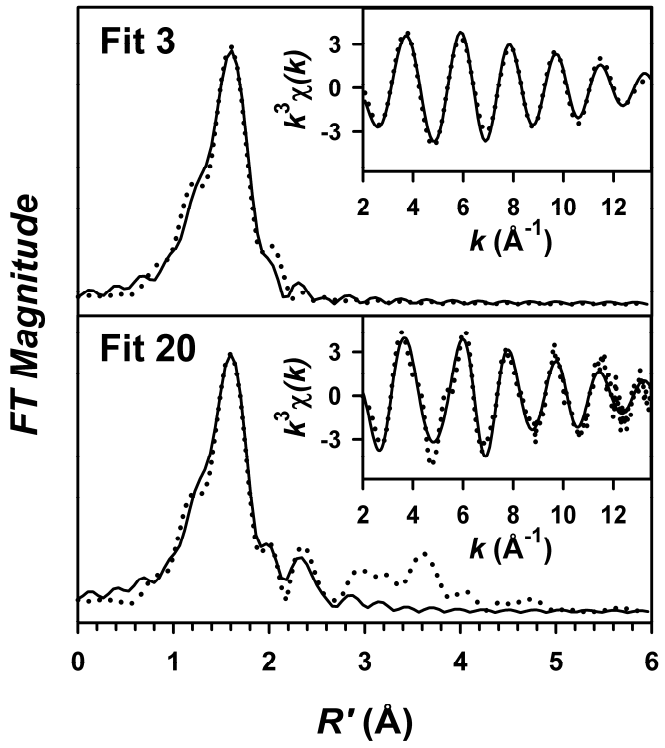

Figure 3.5. Fits to the Fourier transforms of the Fe K-edge EXAFS data ($k^3\chi(k)$) and unfiltered EXAFS spectra ($k^3\chi(k)$, insets) for **CoHPCD-HPCA**. Experimental data is shown with dotted lines (•••) and fits are shown with solid lines (——). Fourier transformation range: k = 2 – 13.5 Å^{-1}; back-transformation range = 0.7 – 2.2 Å (fit 3 only). Fit parameters associated with the stated fit are shown in Table 3.4.

Table 3.5. Single-Scattering EXAFS Analysis of **CoHPCD-3HPA**.[a]

Fourier-filtered EXAFS fits

	Co-N/O			Co-O				
fit	**n**	**r**	**σ^2**	**n**	**r**	**σ^2**	**F [b]**	**F' [b]**
1	3	1.99	2.8				24.6	84
2	***4***	***1.99***	***4.4***				***11.0***	***17***
3	5	1.99	5.9				16.9	40
4	6	1.98	7.4				36.4	184
5	7	1.98	9.0				64.0	570
6	5	1.99	5.9	1	2.40	13.9	10.5	21
7	4	1.99	4.4	1	2.46	15.4	7.4	11
8	4	1.99	4.4	2	2.49	29.0	7.3	10
9	3	1.99	2.8	1	2.51	15.7	22.7	99
10	3	2.03	2.0	1	1.91	0.0	6.3	8
11	3	1.99	3.4	2	1.91	14.2	17.0	56
12	2	2.05	1.4	2	1.93	1.9	7.3	10

Unfiltered EXAFS fits

	Co-N/O			Co•••C					
fit	**n**	**r**	**σ^2**	**n**	**r**	**σ^2**	**F [b]**	***F*-factor [b]**	***F'* [b]**
13	3	1.99	2.7				181	0.419	0.150
14	*4*	*1.99*	*4.3*				*150*	*0.381*	*0.102*
15	5	1.99	5.8				160	0.394	0.117
16	6	1.99	7.4				199	0.439	0.181
17	7	1.99	9.0				256	0.498	0.298
18	4 1	1.99 2.46	4.3 11.0				143	0.372	0.103
19	3 1	1.99 2.48	2.66 9.50				177	0.414	0.157
20	3 1	2.03 1.91	2.08 0.32				145	0.375	0.106
21	2 2	2.04 1.93	1.95 2.68				151	0.383	0.115
22	4	1.99	4.3	2	2.99	1.2	101	0.312	0.051
23	***4***	***2.00***	***4.3***	***3***	***2.99***	***3.1***	***99***	***0.310***	***0.049***
24	4	2.00	4.3	4	3.00	5.0	102	0.315	0.052
25	4	1.99	4.3	3 4	2.99 4.42	3.2 4.8	84	0.286	0.040
26	2 2	2.05 1.94	2.3 2.2	2	2.99	1.0	96	0.305	0.051
27	2 2	2.05 1.94	2.7 2.4	3	2.99	3.0	93	0.300	0.048
28	2 2	2.05 1.94	2.8 2.4	4	2.99	4.7	94	0.302	0.049

[a] *k*-range = 2 – 13.5 $Å^{-1}$, back-transformation range for Fourier-filtered data = 0.7 – 2.1 Å, resolution = 0.138 Å, r is in units of Å, σ^2 is in units of 10^{-3} $Å^2$. Fits of the N/O shell used parameters for a N scatterer. EXAFS cannot distinguish between scatterers differing by Z = 1.

[b] Goodness-of-fit parameter F defined as $\Sigma(\chi_{exptl}-\chi_{calc})^2$. *F-factor* = $[\Sigma k^6(\chi_{exptl}-\chi_{calc})^2 / \Sigma k^6\chi_{exptl}^2]^{1/2}$. A third parameter, *F'*, is defined as $F' = F^2 / \nu$, where $\nu = N_{IDP} - N_{VAR}$. N_{IDP} is the number of independent data points, while N_{VAR} is the number of floated variables in each optimization step. The values of *F'* shown have been divided by a factor of 10^4 for convenience. *F'* is a measure of whether an added shell significantly improves the fit.

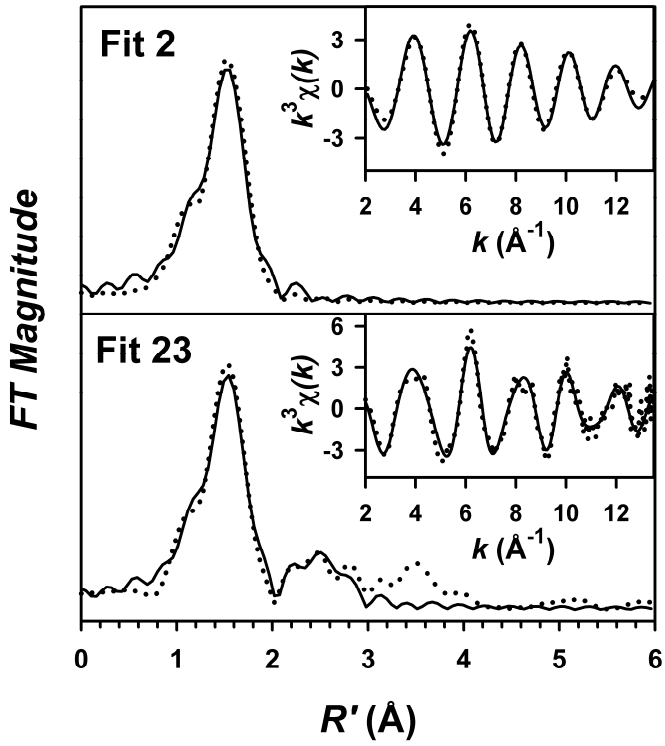

Figure 3.6. Fits to the Fourier transforms of the Fe K-edge EXAFS data ($k^3\chi(k)$) and unfiltered EXAFS spectra ($k^3\chi(k)$, insets) for **CoHPCD-3HPA**. Experimental data is shown with dotted lines (•••) and fits are shown with solid lines (——). Fourier transformation range: k = 2 – 13.5 $Å^{-1}$; back-transformation range = 0.7 – 2.1 Å (fit 2 only). Fit parameters associated with the stated fit are shown in Table 3.5.

3.3.3. Preliminary Multiple-Scattering EXAFS Analysis of CoHPCD

The EXAFS analyses of **CoHPCD**, **CoHPCD-HPCA**, and **CoHPCD-3HPA** presented in this work provide useful insight into the metrical parameters of Co(II) coordination in these samples. However, simple two-shell fits consisting of Co–N/O and Co•••C scatterers do not accurately reproduce the experimental $k^3\chi(k)$ EXAFS, particularly at low k, or the Fourier transforms at high r' (Figures 3.4 – 3.6). A number of seminal EXAFS studies of metalloproteins and related model complexes have shown that these high r' features arise from multiple scattering from coordinated imidazoles.[146-149] We therefore extended our analysis of as-isolated **CoHPCD** to include multiple-scattering effects, and the results of this study provide a basis for treatment of multiple scattering effects in our ongoing EXAFS studies of CoHPCD complexes and intermediates.

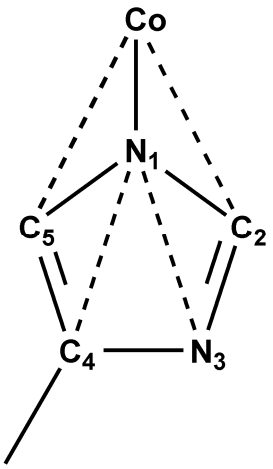

Scheme 3.3. Schematic of relevant scattering pathways in for a Co-bound imidazole ligand. Single scattering pathways involving N_1, C_2, and C_5 contribute, as do 3 and 4 body multiple scattering pathways involving N_1/N_3 and N_1/C_4. Other possible single and multiple-scattering paths do not contribute significantly to the observed EXAFS.

The basis for accurate EXAFS simulations of multiple scattering from coordinated imidazoles was first developed by Strange and co-workers in their EXAFS studies of Cu,Zn-superoxide dismutase,[146,150] with further improvements by both Scott[147,149] and Penner-Hahn.[148] In this approach, the coordinated imidazole is treated as a rigid body with fixed bond lengths and angles for the ring system. As shown in Scheme 3.3, there will be simple single-scattering paths that involve the coordinated N_1 nitrogen, as well as single-scattering paths involving C_2 and C_5, both of which are accounted for in the single-scattering EXAFS analyses of **CoHPCD**, **CoHPCD-HPCA**, and **CoHPCD-3HPA** that we have presented. Additionally, the Co–N_1–N_3 and Co–N_1–C4 angles are typically *ca.* 165 – 170°, and this nearly linear arrangement significantly increases the likelihood that the excited photoelectron will continue from N_1 to either N_3 or C_4 before returning to the Co center. This multiple-scattering interaction takes the form of degenerate pairs of three body (Co–N_1–N_3–Co and Co–N_3–N_1–Co are identical and have equal probabilities of occurring) and single four body (e.g. Co–N_1–N_3–N_1–Co) paths that have been found to contribute significantly to the observed EXAFS based on model studies.[146,148] Conversely, multiple-scattering paths involving Co–N_1–C_2/C_5 do not contribute significantly, given the typical Co–N_1–C_2/C_5 bond angle of 125°, and the fact that multiple scattering effects are generally insignificant for atomic arrangements having bond angles less than 150°.[151] The intensity of these multiple scattering pathways ties in closely with both the number of bound His residues and their angular relationship to the metal center. In the multiple-scattering EXAFS analysis of CoHPCD carried out here, we assumed that the imidazole ring was bound to Co(II) in a perfectly symmetric fashion, with the imidazole ring being collinear with the M–N_{His} bond. We note that available

crystal structures of FeHPCD[97,105] and MnHPCD[85] show a bond angle of ca. 160° for the M(II)–N_{His}–His_{ring} moiety.

Analysis of the $k^3\chi(k)$ EXAFS data for **CoHPCD** using multiple scattering reveals that the fit quality is significantly improved by inclusion of paths for coordinated His residues. Much of the improvement stems from better agreement of the model with experimental EXAFS data at low k (Figure 3.7), where multiple scattering effects are most dominant. The best fit is obtained for two Co(II)-bound His moieties, as this fit gives the most reasonable Debye-Waller factor (fit 23a, Table 3.6 and Figure 3.7). In this fit, the parameters associated with the His moiety are floated independently of those of the first shell. We carried out several additional fits in which the both the His multiple scattering paths were correlated to the length and coordination number of the Co–N_{His} scatterer. This is a useful approach to tease out inner-shell scattering interactions that arise solely from coordinated His, as opposed to bound carboxylates or solvent ligands.[144,145,147,149,152,153] Again, fits involving two His provide the best agreement to experimental data, with a five-coordinate Co(II) model (fit 23g, Table 3.6 and Figure 3.7) providing the best overall fit. This analysis reveals an average Co–N_{His} bond length of 2.13 Å, with the remainder of the Co(II) coordination sphere being modeled as 3 – 4 Co–O scatterers at *ca.* 2.04 Å. The visual agreement with outer-sphere components of the Fourier transform improves noticeably relative to the fitting approach represented by fit 23a (Figure 3.7).

Table 3.6. Multiple-Scattering EXAFS Analysis of **CoHPCD**.[a]

	Co-N/O			Co•••C			Co•••His [b]					
fit	**n**	**r**	**σ^2**	**n**	**r**	**σ^2**	**n**	**r**	**σ^2**	**F [c]**	***F*-factor [c]**	***F'* [c]**
14	6	2.93	5.9							160	0.350	0.119
20	6	2.10	6.0	4	3.08	9.7				148	0.336	0.112
23a	***6***	***2.09***	***6.0***	***4***	***3.08***	***11.0***	***8 4 4***	***4.31 4.33 4.29***	***6.8***	***116***	***0.298***	***0.055***
23b	6	2.09	6.0	2	3.10	3.4	4 2 2	4.31 4.33 4.28	2.7	113	0.295	0.052
23c	6	2.09	6.0	4	3.08	11.3	12 6 6	4.32 4.34 4.29	10.6	117	0.300	0.056
23d	***4 2***	***2.04 2.12***	***8.2 3.1***	***4***	***3.05***	***10.3***	***8 4 4***	***4.26 4.29 4.24***	***3.1***	***136***	***0.323***	***0.076***
23e	5 1	2.05 2.12	9.2 0.3	2	3.06	4.9	4 2 2	4.26 4.28 4.24	0.3	131	0.317	0.070
23f	3 3	2.04 2.12	6.6 5.3	6	3.05	18.3	12 6 6	4.26 4.28 4.24	5.3	166	0.356	0.112
23g	***3 2***	***2.05 2.13***	***5.2 3.5***	***4***	***3.06***	***9.6***	***8 4 4***	***4.28 4.31 4.26***	***3.5***	***114***	***0.295***	***0.053***
23h	4 1	2.05 2.13	6.5 0.8	4	3.06	8.9	4 2 2	4.28 4.31 4.26	0.8	108	0.288	0.048
23i	2 3	2.03 2.13	4.0 4.4	6	3.06	16.0	12 6 6	4.27 4.29 4.25	4.3	157	0.347	0.101

[a] *k*-range = 2 – 13.5 Å^{-1}, resolution = 0.138 Å, r is in units of Å, σ^2 is in units of 10^{-3} Å^2.

[b] For each His residue, there are four three-body paths , two four-body paths, and two single-scattering two-body paths involving the most distant C_3/N_4 atoms. For example, fits with an 8,4,4 arrangement assume two equivalent His residues.

[c] Goodness-of-fit parameter F defined as $\Sigma(\chi_{exptl}-\chi_{calc})^2$. *F-factor* = $[\Sigma k^6(\chi_{exptl}-\chi_{calc})^2 / \Sigma k^6\chi_{exptl}^2]^{1/2}$. A third parameter, *F'*, is defined as $F' = F^2 / \nu$, where $\nu = N_{IDP} - N_{VAR}$. N_{IDP} is the number of independent data points, while N_{VAR} is the number of floated variables in each optimization step. The values of *F'* shown have been divided by a factor of 10^4 for convenience. *F'* is a measure of whether an added shell significantly improves the fit.

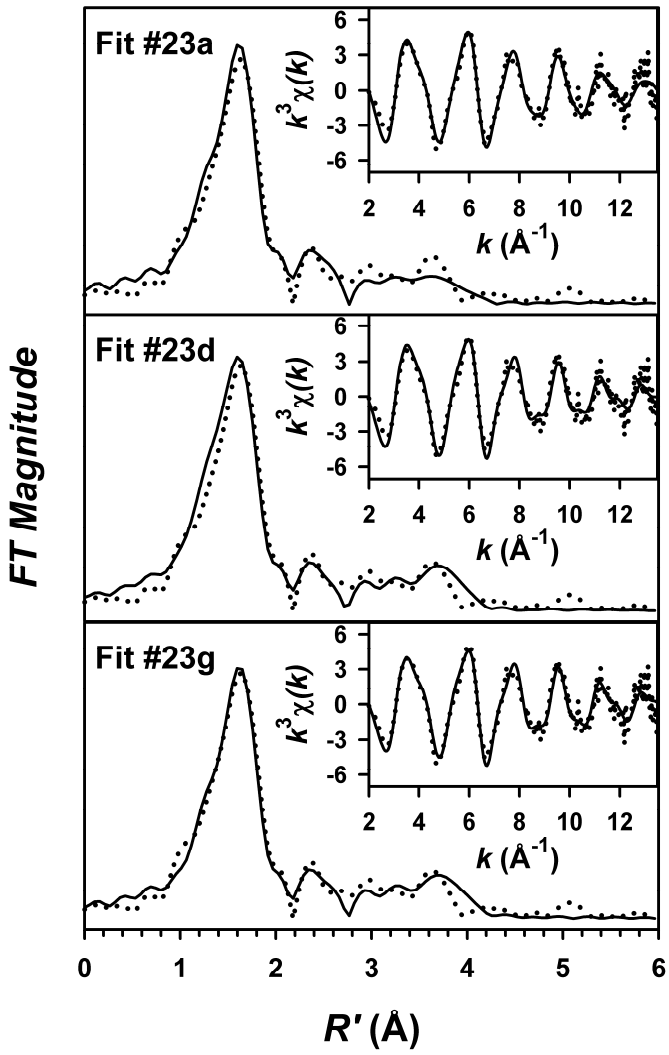

Figure 3.7. Multiple-scattering fits to the Fourier transforms of the Fe K-edge EXAFS data ($k^3\chi(k)$) and unfiltered EXAFS spectra ($k^3\chi(k)$, insets) for **CoHPCD**. Experimental data is shown with dotted lines (•••) and fits are shown with solid lines (——). Fourier transformation range: k = 2 – 13.5 Å^{-1}. Fit parameters associated with the stated fit are shown in Table 3.6.

3.4 Discussion

We have previously demonstrated that metal-substitution studies of the very similar pair of Mn(II) and Fe(II)-dependent extradiol dioxygenases, MndD and HPCD, can provide unique insights into the role of the metal center in modulating oxygen activation.[85,86,106] Our recent discovery that Co(II) may be substituted into the active site of HPCD to afford a Co(II)-dependent O_2 activating dioxygenase[127] represents a significant extension of this effort, as we can now test whether the trends observed for the Fe(II)- and Mn(II)-substituted enzymes also hold for the Co(II) form. In the work presented in this chapter, we have made the first steps towards developing a picture of the Co(II) coordination environment in CoHPCD through X-ray absorption spectroscopy, which allows us to rationalize available spectroscopic data for this enzyme and lays the groundwork for future studies of oxygenated intermediates.

Our XAS studies of the Co(II) model complexes **1-S_2COEt**, **1-S_2CNPh$_2$**, **1-S_2CNEt$_2$**, and **1-acac** were intended to provide a grounding for understanding the edge and pre-edge features of CoHPCD using structurally well-defined model complexes. Structural parameters for **1-S_2COEt**, **1-S_2CNPh$_2$**, and **1-S_2CNEt$_2$** obtained via X-ray crystallography are summarized in Table 3.7, along with details of two Co(II) complexes similar to **1-acac** (a crystal structure of **1-acac** is not available at present). The three complexes with sulfur-containing co-ligands all exhibit fairly similar distorted trigonal bipyramidal geometries (τ = 0.544 – 0.646) having a significant distortion imposed by the long Co(II)–S bond lengths, and we would have thus expected fairly similar pre-edge areas for each complex given their similar distortions from centrosymmetry. The fact that the areas vary significantly, from 5 units for **1-S_2CNPh$_2$** to 12.1 units for **1-S_2COEt**,

suggests that some factor other than geometric structure modulates the pre-edge intensity, or else that there is some alteration of structure in solution relative to the crystal structures. Additional insight into the electronic structures of these complexes from either EPR or NMR studies may shed light into this intriguing question. We emphasize that the pre-edge areas of the **1-X** model complexes, with the exception of **1-S_2CNPh_2**, are significantly larger than that of the distorted six-coordinate Co(II) site in Co-substituted hemerythrin,[141] consistent with their lower degree of centrosymmetry.

Table 3.7. Structural Parameters for the **1-X** Co(II) Complexes.[a]

1-S_2COEt		**1-S_2CNPh_2**		**1-S_2CNEt_2**	
Co(1)-N(5)	2.066 Å	Co(1)-N(4)	2.068 Å	Co(1)-N(7)	2.099 Å
Co(1)-N(7)	2.165 Å	Co(1)-N(6)	2.177 Å	Co(1)-N(9)	2.196 Å
Co(1)-N(9)	2.063 Å	Co(1)-N(8)	2.110 Å	Co(1)-N(11)	2.083 Å
Co(1)-S(2)	2.339 Å	Co(1)-S(2)	2.356 Å	Co(1)-S(3)	2.363 Å
Co(1)-S(3)	2.543 Å	Co(1)-S(3)	2.460 Å	Co(1)-S(4)	2.426 Å
τ	0.544	τ	0.646	τ	0.644

[Tp(CHPh_2)]Co(II)(acac)		**[Tp(Ph)]Co(II)(acac)**	
ITAWIJ		**TULDOT**	
Co(1)-N(6)	2.187 Å	Co(1)-N(6)	2.258 Å
Co(1)-N(8)	2.069 Å	Co(1)-N(8)	2.078 Å
Co(1)-N(10)	2.077 Å	Co(1)-N(10)	2.072 Å
Co(1)-O(4)	2.016 Å	Co(1)-O(3)	1.949 Å
Co(1)-O(5)	1.967 Å	Co(1)-O(4)	1.987 Å
τ	0.270	τ	0.704

[a] Structural data for **1-S_2COEt**, **1-S_2CNPh_2**, and **1-S_2CNEt_2** was kindly provided in advance of publication by Dr. Michael Jensen (Ohio University). No crystal structure for **1-acac** is available at present. Structural parameters for two other Co(II) complexes with both Tp and acac ligands are shown, and the 6 letter Cambridge Crystallographic Database accession codes are given. ITAWIJ was originally published in reference 154, while TULDOT was published in reference 155. τ values were calculated according to reference 156. The atom labeling scheme are those employed in the respective structures.

Our XAS studies reveal a distorted six-coordinate site with two bound histidines for as-isolated **CoHPCD**, based on the smaller pre-edge area relative to the **1-X** models and our analysis of the EXAFS. Interestingly, the EXAFS analysis at the single-scattering level of theory suggests the presence of a single shorter Co(II)–O/N bond, which we attribute to a monodentately-bound carboxylate amino acid ligand, in line with suggestions made in the EXAFS analyses of the extradiol dioxygenase 2,3-dihydroxybiphenyl 1,2-dioxygenase (DHBD)[157] and more recently for the pterin-dependent oxygenases phenylalanine hydroxylase[158,159] and tyrosine hydroxylase.[160] More importantly, it appears that the Co(II) substitution does not alter the geometric structure of the resting state, as both FeHPCD[97,105] and MnHPCD[85] have been shown to contain six-coordinate metal sites in the resting state. Indeed, the mechanistic proposals postulated for the majority of nonheme oxygenases with a 2-His-1-carboxylate metal binding motif involve solvent-derived ligands occupying the open coordination sites of the metal center in the resting state.[1,2,28]

In line with the mechanistic model for 2-His-1-carboxylate containing oxgenases and the proposed reaction schemes for extradiol dioxygenases in particular,[95,96] we would expect binding of HPCA to result in a five-coordinate structure for **CoHPCD-HPCA**. However, the pre-edge intensity is identical to that of **CoHPCD**, which suggests a similar degree of distortion from centrosymmetry at the Co(II) centers of both the as-isolated form and the enzyme-substrate complex. This is in line with the nearly identical intensities of the Co(II) d-d transitions for **CoHPCD** and **CoHPCD-HPCA**; if the latter was indeed five-coordinate, one would expect significantly more intense visible features similar in shape to those of **CoHPCD-3HPA**. While our EXAFS analysis is most

consistent with a five-coordinate Co(II) center in **CoHPCD-HPCA**, a six-coordinate model cannot be excluded, given the 25% error in coordination numbers associated with EXAFS analysis.[87,90] Bond-valence sum (BVS) analysis of EXAFS results offers a mechanism for distinguishing between the five- and six-coordinate possibilities,[161-163] as illustrated by our studies of catechol 2,3-dioxygenase (2,3-CTD),[164] but reliable BVS parameters have not been reported for Co(II) centers, suggesting a rationale for why the technique has been not employed in other XAS studies of Co(II)-substituted proteins.[141,144,145,152,153] While we expected to be able to resolve one or more short Co–O distances attributable to deprotonated bound HPCA, we were unable to split the principal inner shell into two subshells. Previous EXAFS studies of both 2,3-CTD and DHBD showed evidence for a short Fe–O bond attributable to binding of catechol as a monoanion,[164] with the monoanionic binding of the catechol substrate in extradiol dioxygenases being thought to promote O_2 activation by the iron center via a redox tuning process.[95,96,164-166] At present, there is no experimental data available regarding the binding mode of the HPCA substrate in any of the metal-substituted forms of HPCD or MndD. However, crystal structures of the FeHPCD-HPCA and MnMndD-HPCA complexes suggest that M(II)–O_{3HPCA} is significantly shorter than M(II)–O_{4HPCA}, consistent with deprotonation of the O_3 oxygen of HPCA and binding as a monoanion.[105] While it is tempting to suggest that the absence of a short Co–O bond in our EXAFS analysis of **CoHPCD-HPCA** points towards an altered substrate binding mode in this metal-substituted form, it is more likely to be a consequence of a comparatively small difference in Co–ligand bond lengths that we are unable to resolve using the presently available **CoHPCD-HPCA** EXAFS data. We are presently endeavoring to address the

nature of HPCA binding to CoHPCD by collecting new higher quality Co K-edge EXAFS data on **CoHPCD-HPCA**, as well as directly determining the protonation state of the bound substrate through UV resonance Raman studies of CoHPCD.

The XANES and EXAFS data for the **CoHPCD-3HPA** inhibitor complex suggests a four-coordinate or distorted five-coordinate environment for this species, in excellent agreement with the intense Co(II) d-d transitions observed by UV/Vis spectroscopy. The average Co(II)–N/O bond length shortens by *ca.* 0.07 – 0.1 Å compared to either **CoHPCD-HPCA** or **CoHPCD**, consistent with a lower total coordination number in this species. There is some evidence for the presence of one or two shorter Co–O scatterers at approximately 1.91 Å. These short distances can likely be assigned to the coordinated glutamate and/or the coordinated phenolate of 3HPA, with a $Co–O_{3HPA}$ bond length of *ca.* 1.91 Å falling on the lower edge of the 1.89 – 2.10 Å range of bond lengths reported for several other $Co(II)–O_{phenolate}$ adducts.[167-171] As with **CoHPCD**, we cannot justify two-shell fits to **CoHPCD-3HPA** based on the differences in bond lengths being smaller than the resolution of the EXAFS data, but we anticipate that collection of additional higher-quality EXAFS data will confirm our conclusions. The lower coordination number observed in **CoHPCD-3HPA** presumably reflects the fact that 3HPA binds in a fashion that precludes binding of exogenous solvent to the Co(II) center, therefore enforcing a highly distorted Co(II) site. Although EXAFS analysis can only supply metal-ligand distances and not angular data, we suggest that the second-sphere residue Arg293, which has been shown to interact with the carboxylate tail of HPCA,[105] enforces similar binding geometries for 3HPA and HPCA, and that the site ordinarily occupied by O_4 in the ES complex remains vacant in **CoHPCD-3HPA** by

reason of the proximity of the ring to the Co(II) center. The absence of ring expansion chemistry with 3HPA can be attributed to the fact that 3HPA is considerably less likely to donate an electron to the incipient Co–O_2 adduct, compared with the native catechol substrate HPCA.

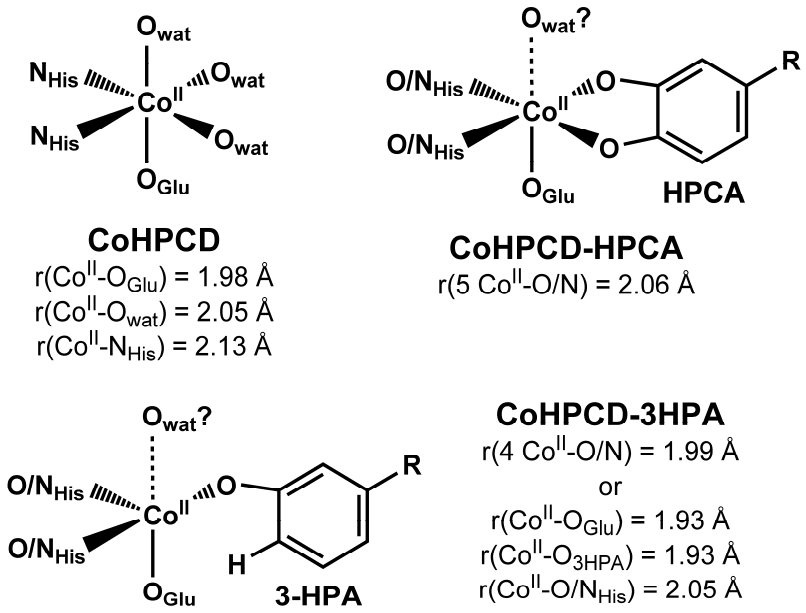

Scheme 3.4. Proposed structures for **CoHPCD**, **CoHPCD-HPCA**, and **CoHPCD-3HPA** derived from EXAFS analysis. A solvent water ligand (O_{wat}) may remain weakly bound in both **CoHPCD-HPCA** and **CoHPCD-3HPA**, but was not detected in our analysis.

To summarize, our XAS studies of CoHPCD have served principally to validate the structures of **CoHPCD**, **CoHPCD-HPCA** and **CoHPCD-3HPA** inferred from electronic absorption studies (Scheme 3.4), as well as develop methods for the interpretation of multiple-scattering features in the EXAFS, the analysis of which is presently ongoing. In addition, the XANES and EXAFS parameters obtained for these three species provide a baseline for understanding the changes in the electronic and geometric structure that occur upon oxygenation of CoHPCD-substrate intermediates, as

we have recently obtained evidence for several such oxygenated intermediates via transient kinetic and rapid-freeze quench EPR methods (Andrew Fielding, unpublished observations). Our kinetic and spectroscopic studies of CoHPCD should further extend our understanding of the role played by the metal center in modulating O_2 reactivity in extradiol dioxygenases.

Chapter 4.

XAS Studies of Oxoiron(IV) Complexes of Tetramethylcyclam with Additional Pendant Donors

4.1 Introduction

It has been suggested that many mononuclear nonheme oxygenases containing a 2-His-1-carboxylate facial triad metal binding motif employ high-valent oxoiron oxidants to carry out a wide array of metabolically and environmentally relevant transformations on substrates containing strong C–H bonds.[1-3,28] Some enzymes in this superfamily employ a cofactor, such as α-ketoglutarate (αKG) or pterin, that functions to supply two additional electrons to the initial Fe–O_2 adduct (frequently described as an iron(III)-superoxo), hence promoting heterolytic O–O bond cleavage and formation of an oxoiron(IV) oxidant.[2,4,28] Direct evidence for this oxoiron(IV) species in the catalytic cycle of nonheme dioxygenases has recently been obtained through thoughtfully designed transient kinetic studies by Krebs, Bollinger, and their collaborators for the αKG-dependent dioxygenases taurine/αKG dioxygenase (TauD)[11-14] and prolyl 4-hydroxylase,[18] the αKG-dependent halogenases CytC3[19,20] and SyrB2,[21] and the pterin-dependent oxygenase tyrosine hydroxylase.[23].

Much information of great value can be obtained from the transient kinetics and rapid-freeze-quench approaches employed to good effect by Krebs, Bollinger, and their coworkers,[11,18,20,21,23,81] but such studies are technically challenging, and the extent to which the enzyme active site can be varied chemically is somewhat limited. Studies of model complexes represent an attractive strategy to significantly broaden the scope of possible structures and donor atoms, and it is therefore not surprising that model complexes have contributed significantly to our understanding of the properties of these biologically relevant oxidants.[172] Of these, the most comprehensive work has been carried out on pseudo-octahedral oxoiron(IV) complexes employing a tetramethylcyclam

(TMC) ligand that provides four amine nitrogen donors in the equatorial plane (Scheme 4.1), the first example of which was reported in 2003 ($[Fe^{IV}(O)(TMC)(NCMe)]^{2+}$, (**1**, TMC = 1,4,8,11-tetramethyl-1,4,8,11-tetraazacyclododecane).[173] The substitutionally labile axial site *trans* to the oxo can accommodate a variety of neutral and anionic donors, the basicity of which has been shown to greatly affect the electronic structure and reactivity of the oxoiron(IV) center.[174-177] However, this approach is less amenable to the employment of large, sterically bulky donors such as pyridine, or highly reactive ligands of biological relevance, such as thiolates.[91] A useful strategy to remedy this deficiency and further extend the range of possible *trans* ligands in the TMC family is to tether the *trans* donor to a nitrogen atom of the TMC macrocycle. This approach has previously been employed in the study of thiolate-ligated oxoiron(IV) complexes by Que and coworkers[91,178] and in studies of a variety of high-valent iron complexes by Wieghardt and coworkers.[179-183]

We have recently embarked on efforts to characterize the electronic structures and reactivity of a number of new oxoiron(IV) complexes obtained using TMC complexes with pendant carboxylate (TMCAc), amide (TMCdma, TMCdmpa), pyridine (TMCpy), and pyridine N-oxide (TMCpyO) functionalities, as shown in Scheme 4.1. As part of this undertaking, we employed X-ray absorption spectroscopy (XAS) to obtain a more detailed understanding of the structural features of this series of complexes, principally via extended X-ray absorption fine structure (EXAFS) analysis to obtain metrical parameters for the first coordination sphere. A number of these complexes, including $[Fe^{IV}(O)(TMCpy)]^{2+}$ (**1-py**), $[Fe^{IV}(O)(TMCdma)]^{2+}$ (**1-dma**), and $[Fe^{IV}(O)(TMCdmpa)]^{2+}$ (**1-dmpa**), proved amenable to crystallization and structural solution by X-ray

crystallography,[184,185] thus affording an unprecedented opportunity to compare structural parameters for an oxoiron(IV) center obtained in the solid state by crystallography with those obtained in solution via EXAFS analysis. Our EXAFS results demonstrate that the structure of the first coordination sphere in this series of oxoiron(IV) complexes is not significantly affected by the identity of the pendant *trans* ligand, in line with similarities in electronic environment suggested by Mössbauer spectroscopy.[186]

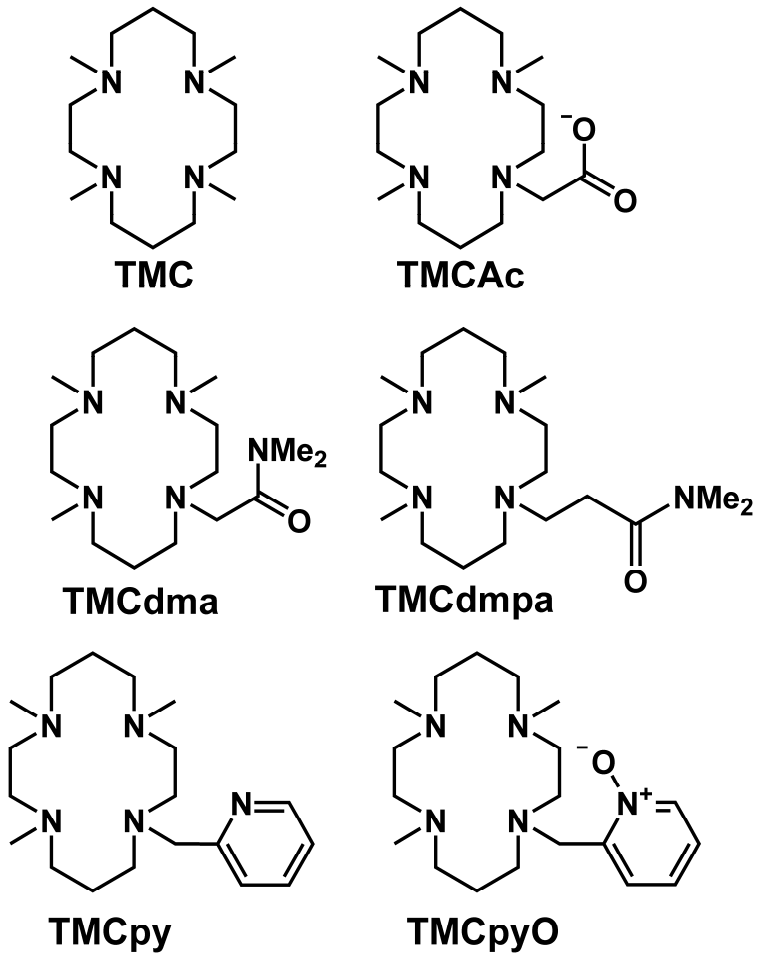

Scheme 4.1. TMC and TMC-derived ligands with pendant functionalities.

4.2 Experimental

4.2.1 XAS Sample Preparation

All oxoiron(IV) complexes were prepared by Dr. Jason England via treatment of a solution of the appropriate Fe(II) precursor with solid iodosylbenzene (PhIO), followed by transfer to an XAS solution cell and immediate freezing in liquid nitrogen. The concentration and yield of each sample are as follows.

$[Fe^{IV}(O)(TMCAc)]^{+}$, 1-Ac. A 12 mM sample of $[Fe^{IV}(O)(TMCAc)](BPh_4)$ in CD_3CN was prepared and frozen in an SSRL solution cell. The yield of the Fe(IV) complex was >95%, based on UV/Vis absorption.

$[Fe^{IV}(O)(TMCpyO)]^{2+}$, 1-pyO. A 16 mM sample of $[Fe^{IV}(O)(TMCPyO)](OTf)_2$ in CD_3CN was prepared and frozen in an SSRL solution cell. The yield of the Fe(IV) complex was >95%, based on UV/Vis absorption.

$[Fe^{IV}(O)(TMCpy)]^{2+}$, 1-py. A 16 mM solution of $[Fe^{IV}(O)(TMCPy)](OTf)_2$ in CD_3CN was prepared and frozen in an SSRL solution cell. The yield of the Fe(IV) complex was >95%, based on UV/Vis absorption.

$[Fe^{IV}(O)(TMCdma)]^{2+}$, 1-dma. A 16 mM solution of $[Fe^{IV}(O)(TMCDma)](OTf)_2$ in CD_3CN was prepared and frozen in an SSRL solution cell. The yield of the Fe(IV) complex was quantitative, based on UV/Vis absorption.

$[Fe^{IV}(O)(TMCdmpa)]^{2+}$, 1-dmpa. An 18.4 mM solution of $[Fe^{IV}(O)(TMCdmpa)](OTf)_2$ in CH_3CN was prepared and frozen in an SSRL solution cell. The yield of the Fe(IV) complex was ~95%, based on UV/Vis absorption.

$[Fe^{IV}(O)(TMC)(OAc)]^{+}$, 1-(OAc). A 9.4 mM solution of $[Fe^{IV}(O)(TMC)(OAc)]^{+}$ in CH_3CN was prepared by Jason England and frozen in a tandem Mössbauer/XAS cup. The yield of the Fe(IV) complex was ~95%, based on UV/Vis absorption.

$[Fe^{IV}(O)(TMCdma)]^{2+}$ + base, 1-Bl.S. A 6.94 mM solution of **1-dma** was prepared in butyronitrile at -60 °C, to which 2.5 equiv of tetraoctylammonium hydroxide was added, affording a vivid blue species. The desired species was obtained in *ca.* 90% yield on the basis of UV/Vis absorption.

4.2.2 X-ray Absorption Spectroscopy. Data Collection.

X-ray absorption data was collected on beamlines 9-3 (**1-Ac**, **1-pyO**, **1-py**, **1-dma**, **1-dmpa**, **1-(OAc)**) and 7-3 (**1-Bl.S.**) of the Stanford Synchrotron Radiation Light source (SSRL) of SLAC National Accelerator Laboratory with storage ring conditions of 3.0 GeV and 80 – 100 mA. Fe K-edge XAS data were collected for frozen solutions maintained at a temperature of *ca.* 15 K over an energy range of 6.9 – 8.0 keV using a Si(220) double crystal monochromator for energy selection and an Oxford Instruments CF1208 continuous flow liquid helium cryostat for temperature control. Harmonic rejection was achieved using a Rh-coated focusing mirror upstream of the monochromator at beamline 9-3, and by a 9 keV cutoff filter at beamline 7-3. Data were obtained as fluorescence excitation spectra with 30 element (SSRL) solid-state germanium detector arrays (Canberra). An iron foil spectrum was recorded concomitantly for internal energy calibration and the first inflection point of the K-edge was assigned to 7112.0 eV. The Fe concentration and number of scans acquired for each XAS sample were as follows: **1-Ac**, 12 mM Fe, 6 scans; **1-pyO**, 16 mM Fe, 6 scans; **1-**

py, 16 mM Fe, 6 scans; **1-dma**, 16 mM Fe, 7 scans; **1-dmpa**, 18.4 mM Fe, 4 scans; **1-(OAc)**, 9.4 mM Fe, 10 scans; **1-Bl.S.**, 6.94 mM Fe, 21 scans.

4.2.3 Data Analysis.

Data reduction, averaging, and normalization were performed using the program EXAFSPAK.[130] Following calibration and averaging of the data, background absorption was removed by fitting a Gaussian function to the pre-edge region and then subtracting this function from the entire spectrum. A three-segment spline with fourth order components was then fit to the EXAFS region of the spectrum in order to extract $\chi(k)$. Analysis of the pre-edge features was carried out with the program SSExafs[132] using a previously described protocol.[133] Theoretical phase and amplitude parameters for a given absorber-scatterer pair were calculated using FEFF 8.40[135] at the single-scattering level of theory, and were utilized by the opt program of the EXAFSPAK package during curve-fitting. In all analyses, the coordination number of a given shell was a fixed parameter, and was varied iteratively while bond lengths (*r*) and Debye-Waller factors (σ^2) were allowed to freely float. The amplitude reduction factor S_0 was fixed at 0.9, while the edge shift parameter E_0 was allowed to float as a single value for all shells (thus in any given fit, the number of floating parameters = (2 × num shells) + 1). The goodness of fit F was defined simply as $\Sigma\ (\chi_{exptl}-\chi_{calc})^2$. In order to account for the effect that additional shells have on improving fit quality, an additional goodness-of-fit metric *F*' was employed. $F' = F^2 / (N_{IDP} - N_{VAR})$, where N_{VAR} is the number of floated variables in the fit, while N_{IDP} is the number of independent data points and is defined as $N_{IDP} = 2\Delta k\Delta r / \pi$.[88] In the latter equation, Δk is the *k*-range over which the data is fit, while Δr is the back-transformation range employed in fitting Fourier-filtered data. *F*' is thus of

principal utility in fitting Fourier-filtered data, but can also be employed for unfiltered data by assuming a large value of Δr.

4.3 Results

4.3.1 XANES

We first examined the edge and pre-edge properties of this collection of pendant-TMC oxoiron(IV) complexes. All complexes studied exhibit XANES spectra of similar shape and intensity (Figure 4.1), suggesting that variation of the pendant axial ligand does not greatly affect the electronic and structural environment of the iron(IV) center. The one exception to this is **1-py**, which exhibits a distinctive bump along the rising edge at *ca.* 7121 eV and a slightly broadened rising white-line absorption compared to complexes containing amide or carboxylate pendant groups. The average edge energy of 7124.95 ± 0.7 eV is typical of previously reported nonheme oxoiron(IV) model complexes,[133,177,187] with the edge inflection energy ranging from 7124.00 eV for **1-py** to 7125.91 eV for **1-dma**. All seven complexes studied here exhibit a single intense pre-edge transition centered at 7114.1 ± 0.1 eV arising from 1s-to-3d transitions that gain intensity via distortions from centrosymmetry that promote 4p mixing into the 3d orbitals of the Fe(IV) center. In contrast to the results of Jackson *et al.* for *trans* substituted oxoiron(IV) complexes of the TMC ligand with free non-pendant anionic axial ligands,[177] the pre-edge areas vary only modestly, with weighted pre-edge areas ranging from 28 for **1-pyO** to 36 for **1-Ac**. The one exception to this trend is **1-Bl.S.** (Figure 4.2), which exhibits a weighted pre-edge area of 23 that is significantly smaller than that of its oxoiron(IV) precursor **1-dma**. The smaller pre-edge area of **1-Bl.S.** is consistent with the significant

electronic and structural changes at the Fe(IV) center that are implied by the smaller quadrupole splitting for this complex in comparison with its **1-dma** precursor.[186] It is intriguing that the normalized XAS spectra for **1-dma** and **1-Bl.S.** overlay almost perfectly, as shown in Figure 4.2, suggesting that the differences in Fe(IV) environment that affect both pre-edge area and ΔE_Q apparently do not significantly impact the transitions comprising both the rising K-edge and the near-edge regions of the XAS spectrum.

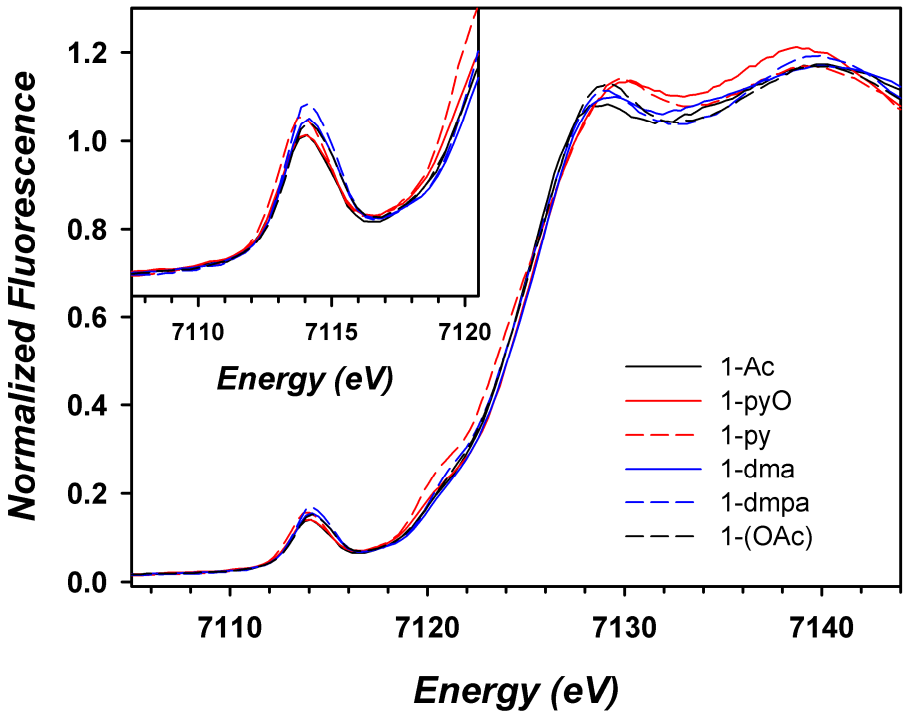

Figure 4.1. Comparison of the Fe K-edge X-ray absorption edge and pre-edge (inset) features of species **1-Ac** (black line, ——), **1-pyO** (red line, ——), **1-py** (red dashes, – – –), **1-dma** (blue line, ——), **1-dmpa** (blue dashes, – – –), and **1-(OAc)** (black dashes, – – –).

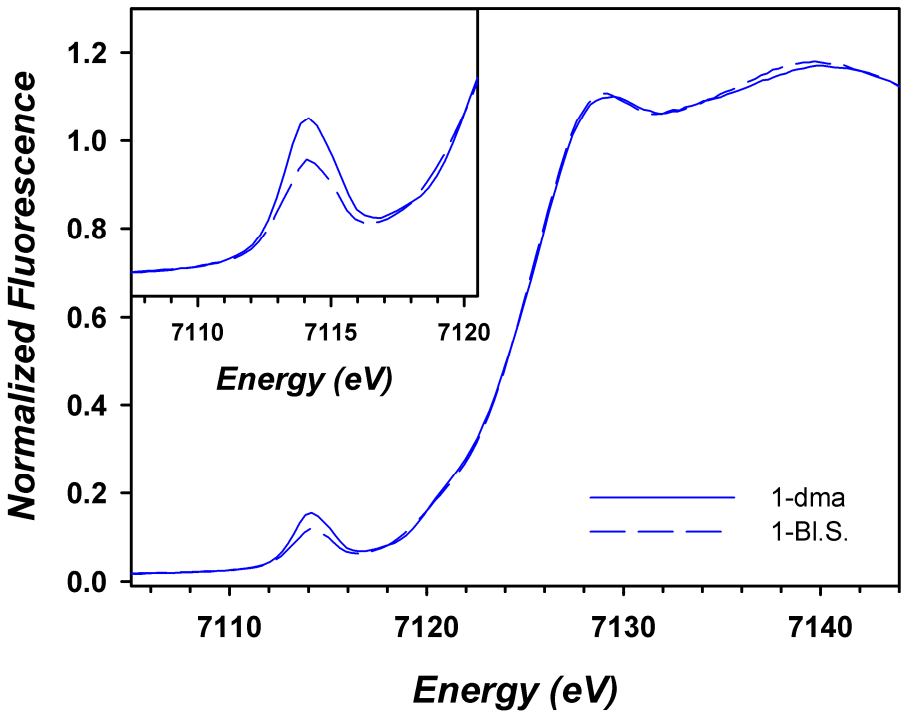

Figure 4.2. Comparison of the Fe K-edge X-ray absorption edge and pre-edge (inset) features of species **1-dma** (blue line, ——) and **1-Bl.S.** (blue dashes, — — —).

Table 4.1. Pre-edge Analysis Parameters for Pendant TMC Oxoiron(IV) Complexes.[a]

Species	yield	E_{edge} (eV)	$E_{preedge}$ (eV)	height	width	area[b]
1-py	95%	7124.00	7113.96(1)	0.121(1)	2.51(3)	32.4(3) [34]
1-pyO	95%	7124.58	7114.03(1)	0.102(1)	2.45(3)	26.5(3) [28]
1-dma	100%	7125.91	7114.18(1)	0.116(1)	2.45(2)	30.4(3)
1-Bl.S.	90%	7125.83	7114.14(1)	0.079(1)	2.44(2)	20.6(2) [23]
1-dmpa	95%	7124.72	7114.20(1)	0.132(1)	2.42(2)	34.1(4) [36]
1-Ac	95%	7124.64	7114.07(1)	0.103(1)	2.48(2)	27.2(3) [29]
1-(OAc)	95%	7125.00	7114.21(1)	0.113(1)	2.45(2)	29.6(3) [31]

[a] The fits presented are those that give the best agreement to the experimental data and its second derivative. Values in parentheses represent uncertainties in the final digit of that parameter.
[b] The values given in square brackets are the weighted pre-edge areas that would be expected for a sample that was quantitative in the given oxoiron(IV) complex, and assume that any other species present in the measured sample do not contribute significantly to observed pre-edge intensity.

4.3.2 EXAFS

The principal objective of our EXAFS analysis of the **1-X** series of complexes was to obtain metrical parameters for the first coordination sphere, including evidence for the presence of a short Fe=O interaction. We were especially interested in what differences, if any, there were between **1-Bl.S.** and its precursor **1-dma**, since the former exhibits a significantly altered set of Mössbauer parameters.[186] The $k^3\chi(k)$ EXAFS spectra and their respective Fourier transforms of the seven **1-X** complexes studied here are shown in Figures 4.3 and 4.4. All seven complexes exhibit very similar oscillations and EXAFS amplitudes for values of $k < 10$ Å^{-1}, and the oscillations are almost entirely damped for $k > 10$ Å^{-1}, with the exception of **1-dma** and perhaps **1-py**. Indeed, the only readily apparent difference amongst the spectra is the shape and intensity of the shoulder centered at $k = 5.5$ Å^{-1}. As might be expected, the Fourier transforms of the EXAFS spectra also quite similar, with an intense asymmetric feature centered at $r' = 1.6$ Å, attributable to donor atoms in the first coordination sphere, and a set of weak, overlapping signals ranging over $r' = 2 - 3$ Å that can be assigned to outer shell scattering from carbon atoms of the TMC framework (Figure 4.4). The magnitude of the $r' = 1.6$ Å^{-1} feature is also fairly similar for all species, consistent with the similarity in the $k^3\chi(k)$ EXAFS amplitudes, thus suggesting that both coordination number and the extent of disorder in the first shell are largely invariant across the **1-X** series. **1-dma** and **1-Bl.S.** represent a noteworthy exception (Figure 4.5), as the amplitude of the $k^3\chi(k)$ EXAFS of **1-Bl.S.** is somewhat less than that of **1-dma**, and this manifests as a somewhat less intense and narrower $r' = 1.6$ Å feature in the FT.

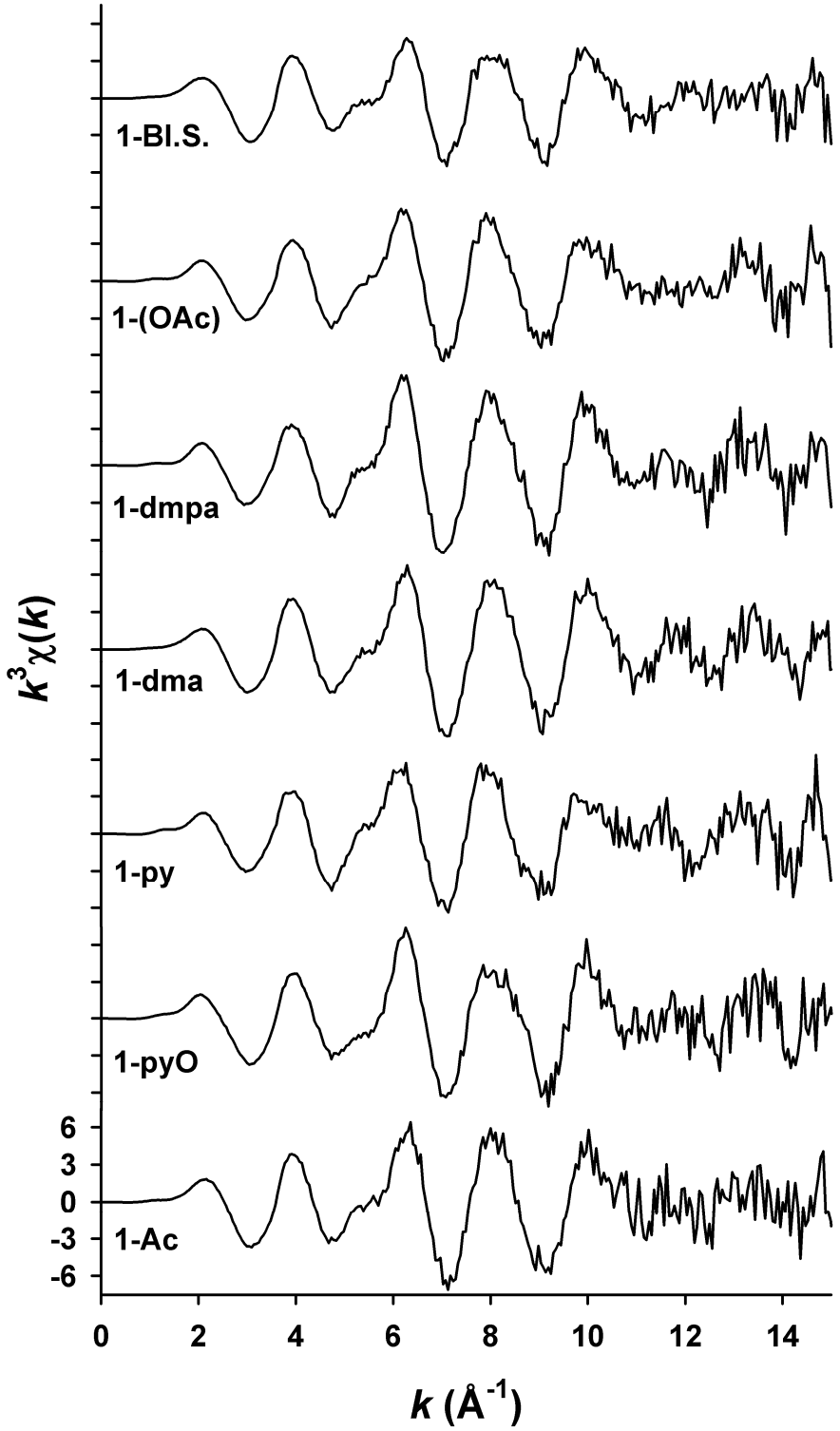

Figure 4.3. Comparison of $k^3\chi(k)$ EXAFS data for **1-Ac**, **1-pyO**, **1-py**, **1-dma**, **1-dmpa**, **1-(OAc)**, and **1-Bl.S.** The y-axis scaling is identical for all plots.

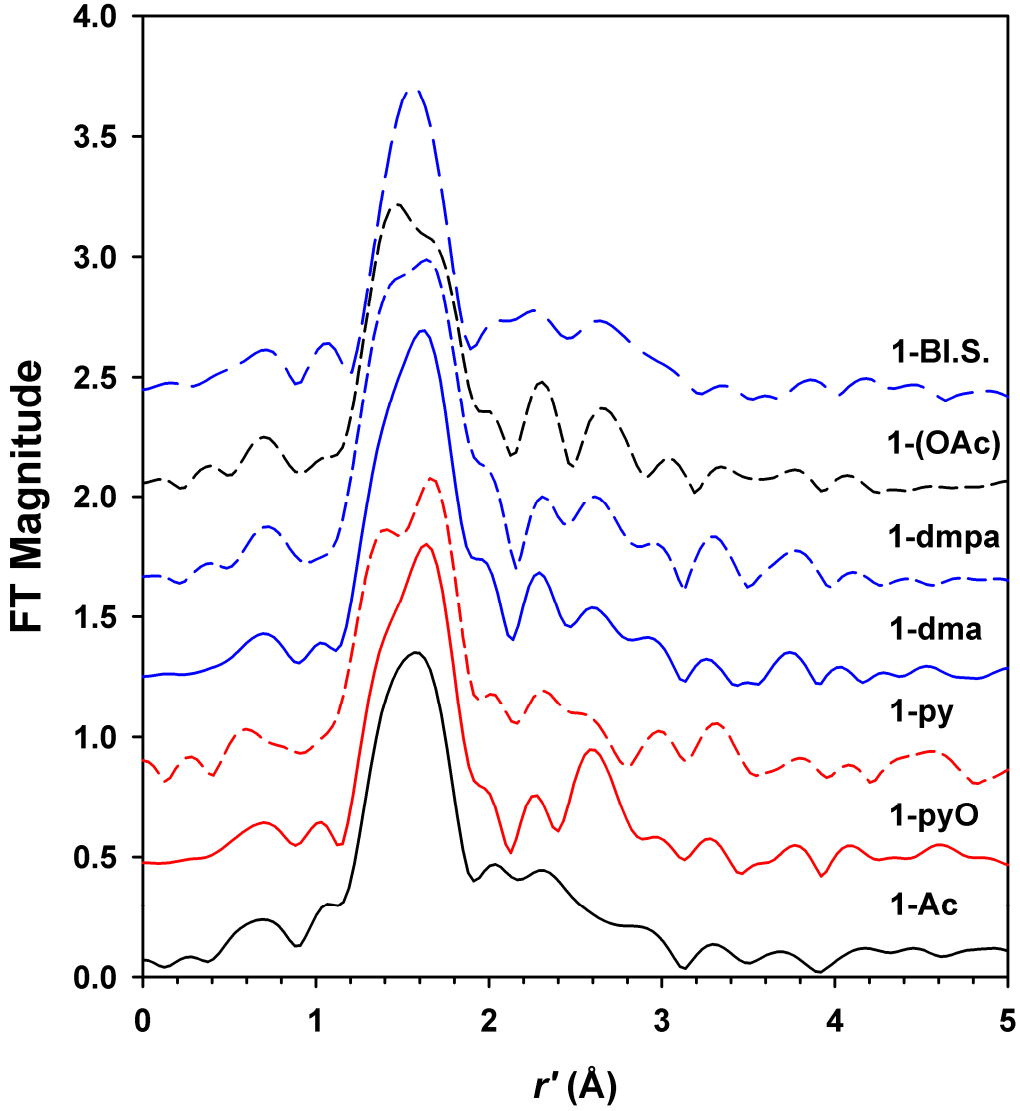

Figure 4.4. Comparison of the Fourier transforms of **1-Ac** (black line, ——), **1-pyO** (red line, ——), **1-py** (red dashes, – – –), **1-dma** (blue line, ——), **1-dmpa** (blue dashes, – – –), and **1-(OAc)** (black dashes, – – –), and **1-Bl.S.** (blue em dashes, — — —). FT ranges were as follows: **1-Ac**, $k = 2 – 14.5$ Å^{-1}; **1-pyO**, $k = 2 – 14.9$ Å^{-1}; **1-py**, $k = 2 – 14.5$ Å^{-1}; **1-dma**, $k = 2 – 15.0$ Å^{-1}; **1-dmpa**, $k = 2 – 14.9$ Å^{-1}; **1-(OAc)**, $k = 2 – 14.9$ Å^{-1}; **1-Bl.S.**, $k = 2 – 14.0$ Å^{-1}. The spectra are offset by 0.4 units for ease of comparison, but are otherwise scaled identically.

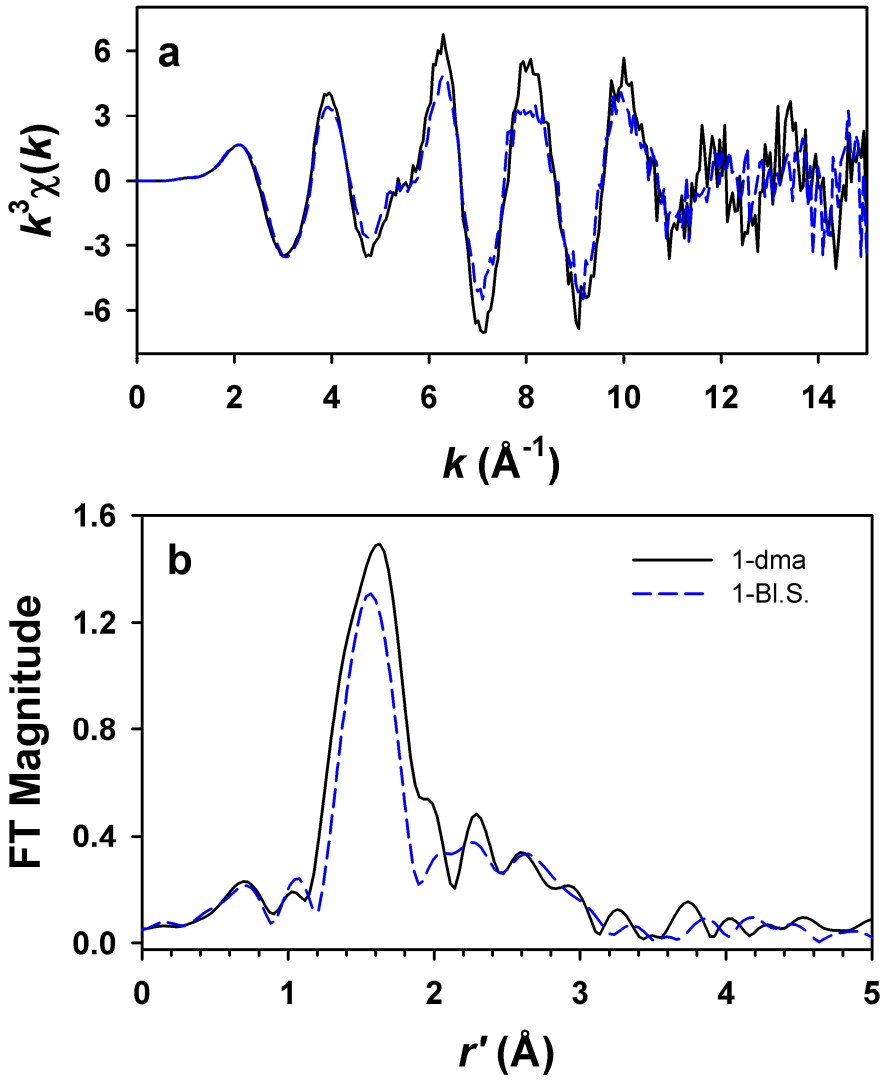

Figure 4.5. Overlay comparison of (a) $k^3\chi(k)$ EXAFS data for **1-dma** (black line, ——) with **1-Bl.S.** (blue dashes, – – –) and (b) the Fourier transforms thereof. FT ranges were as follows: **1-dma**, $k = 2 – 15.0$ Å^{-1} and **1-Bl.S.**, $k = 2 – 14.0$ Å^{-1}.

Given the near-identity of their EXAFS spectra, it should not be surprising that the EXAFS analyses of the **1-X** species were also quite similar (Tables 4.3 – 4.10 and Figures 4.6 – 4.12). Table 4.2 summarizes the best three shell fits for the **1-X** series, with a shell of 4-5 Fe–N scatterers at 2.03 – 2.07 Å and a single Fe–O scatterer at 1.63 Å, except for **1-Bl.S.**, which exhibits an Fe–O bond length of 1.67 Å. Addition of the oxo scatterer shell to the fit resulted in profound improvements in fit quality, suggesting that it constituted an integral component of the EXAFS modulations. These observations are similar to those made for the $[Fe^{IV}(O)(TMC)(X)]^{+/2+}$ complexes reported by Jackson *et al.*, in which X is a free, non-appended ligand.[177] In general, it was not possible to split the primary shell of Fe–N scatterers into two subshells of $Fe–N_{eq}$ and $Fe–O/N_{ax}$ scatterers. This is nicely illustrated by first shell fits of **1-Ac** (Table 4.3), **1-pyO** (Table 4.4), **1-py** (Table 4.5), and **1-dma** (Table 4.9), in which fits including the $Fe–O/N_{ax}$ scatterer resulted in chemically unreasonable bond lengths and Debye-Waller factors for that scatterer. In some instances, the difference in bond lengths between the $Fe–N_{eq}$ and $Fe–O/N_{ax}$ shells was smaller than the resolution limitation of 0.12 – 0.13 Å (e.g. fit 10 of Table 4.3 for **1-Ac**) of the available data, and it would therefore not be possible to independently resolve the axial and equatorial scatterers by EXAFS analysis. The variation of 0.04 Å in Fe–N bond lengths is within the error of ±0.02 Å associated with metal-ligand bond lengths in EXAFS, and in conjunction with the invariant Fe=O bond length, we may conclude that all **1-X** complexes exhibit identical first shell coordination parameters. **1-Bl.S.**, obtained via treatment of **1-dma** with base, represents an interesting exception. The base is thought to deprotonate the methylenic carbon linking the amide functionality with the TMC nitrogen (*c.f.* Scheme 4.1), and DFT studies suggested that

this alteration in the electronic environment would lead to a modest lengthening in the Fe=O bond to *ca.* 1.67 Å along with a shortening of the *trans* Fe–O_{amide} bond to 1.944 Å (from values of 1.646 Å and 2.024 Å, respectively, for **1-dma** via DFT).[186] While attempts to split the principal Fe–N/O shell for **1-Bl.S.** did not prove fruitful (fits 34 – 40 in Table 4.10) on the basis of a poorer overall goodness of fit, it is notable that the Debye-Waller factor associated with this shell is considerably larger than that of its **1-dma** precursor, or indeed those obtained for all other complexes with an attached pendant arm. This presumably reflects greater static disorder in the range of bond lengths comprising this shell in **1-Bl.S.**, as the purity is quite similar to other complexes studied here. In addition, **1-Bl.S.** does exhibit an experimentally significant lengthening in the Fe=O bond length obtained by EXAFS, indicating that its electronic environment is clearly altered relative to the other pendant **1-X** complexes.

There is a considerably greater variation in the *r'* and σ^2 values associated with the Fe•••C shell in the three shell fits shown in Table 4.2. This may perhaps reflect subtle structural variations across the series, or else the fact that weakness of the Fe•••C contribution to the EXAFS makes identification of a clear global minimum more problematic. Examination of the crystal structures of complexes containing the TMC ligand reveal the presence of two distinct populations of Fe•••C distances over the range of 2.8 – 3.1 Å, as well as several long range Fe•••C interactions of *ca.* 3.5 Å in length involving the most distant propylene carbons of the TMC macrocycle.[173,184] In our analysis of the first samples examined chronologically (**1-Ac**, **1-pyO**, and **1-py** in December 2007), addition of a single shell of Fe•••C scatterers afforded significant improvements in fit quality as judged by the improvement in the goodness-of-fit metric

F'. The visual agreement to the Fourier transform (Figures 4.6 – 4.8) is also excellent, but the $k^3\chi(k)$ EXAFS is less accurately modeled, particularly around k = 5.5 Å^{-1}. For **1-(OAc)**, **1-dmpa**, and **1-dma**, we also found that, although three shell fits containing a single Fe•••C component provided a perfectly adequate simulation of the data, more elaborate fits involving two or three Fe•••C shells led generally to further modest improvements in fit quality. We do note that the increase in *F'* for fits to unfiltered data (see fits 24-30 in Table 4.6 for **1-(OAc)**, fits 24-28 in Table 4.7 for **1-dmpa**, and fits 30-36 in Table 4.9 for **1-dma**) suggests that these additional Fe•••C shells contribute only minimally to the observed EXAFS. There is an obvious improvement in the match of the experimental and calculated Fourier transforms for fits with three Fe•••C shells compared to those with one Fe•••C shell for **1-(OAc)**, (Figure 4.9), whereas the same comparison for **1-dma** shows that the three and five shell fits do not appear appreciably different (Figure 4.11). The most striking results for the outer shell were obtained for **1-Bl.S.** Fits to a single shell of Fe•••C scatterers at 2.95 Å afforded exceptionally large Debye-Waller factors even for low numbers of scatterers, indicative of significant disorder in this shell (fits 41-43, Table 4.10) and a poor match to the experimental data (Figure 4.12). Splitting this shell into two sub-shells of Fe•••C scatterers at 2.85 Å and 3.0 Å did not result in a significant improvement in fit quality (fits 44-47, Table 4.10) or agreement to experimental data (Figure 4.12). However, the addition of a shell of Fe•••C scatterers at *ca.* 3.44 Å (fits 48 – 53 , Table 4.10) significantly improved the fit quality, and this can be primarily attributed to a better match between the modeled and calculated EXAFS for the k = 5.5 Å^{-1} feature, which is not accurately reproduced for other combinations of Fe•••C shells (Figure 4.12). We do not have an explanation at present for why a shell of

Fe•••C scatterers at long range can only be justifiably included for **1-Bl.S.**, and not for **1-(OAc)**, **1-dmpa**, or **1-dma**, but it likely reflects subtle differences in the carbon atom arrangements in the respective complexes. It should be emphasized that the parameters associated with the inner shell scatterers are not affected by the combination of shells used to fit outer shell features, which clearly indicates that the EXAFS of the **1-X** series predominantly arises from atoms directly coordinated to the iron(IV) center, and not those farther afield.

Table 4.2. Best Three-shell Fits to Pendant-TMC Oxoiron(IV) Complexes.

	Fe–N/O			Fe–O/N			Fe•••C		
Species	**n**	**r(Å)**	**σ^2**	**n**	**r(Å)**	**σ^2**	**n**	**r(Å)**	**σ^2**
1-py	4	2.07	2.8	1	1.63	1.8	4	2.96	6.8
1-pyO	4	2.04	2.3	1	1.63	2.8	4	3.01	2.9
1-dma	5	2.04	2.9	1	1.63	2.1	5	2.97	7.9
1-Bl.S.	5	2.03	5.4	0.9	1.67	2.5	4	2.93	11.5
1-dmpa	5	2.05	3.1	1	1.63	1.2	4	3.01	4.9
1-Ac	4	2.04	3.0	1	1.63	1.5	6	2.96	10.0
1-(OAc)	5	2.06	4.8	1	1.64	1.3	3	3.01	3.2

Table 4.3. EXAFS Analysis of **1-Ac**.[a]

	Fe-O/N			Fe-N/O			Fe•••C				
fit	**n**	**r**	**σ^2**	**n**	**r**	**σ^2**	**n**	**r**	**σ^2**	**F [b]**	***F'* [b]**
1				3	2.04	2.0				258.4	0.824
2				4	2.04	3.2				238.5	0.702
3				5	2.04	4.4				255.7	0.807
4				6	2.04	5.6				304.2	1.142
5	1	1.63	1.6	4	2.04	3.1				76.1	0.095
6	0.9	1.63	1.1	4	2.04	3.0				74.5	0.091
7	*1*	*1.63*	*1.8*	*5*	*2.04*	*4.3*				*73.4*	*0.088*
8	0.9	1.63	1.2	5	2.04	4.2				74.8	0.092
9	1	1.63	1.4	4 1	2.04 2.41	2.7 -0.4				42.2	0.043
10	1	1.63	1.9	4 1	2.07 1.96	2.2 -0.4				73.6	0.132
11				4	2.04	3.2				321.6	0.642
12				5	2.04	4.4				340.5	0.720
13	1	1.64	1.5	4	2.04	3.0				155.1	0.171
14	1	1.63	1.6	5	2.04	4.3				153.8	0.168
15	1	1.63	1.6	4	2.04	3.0	3	2.97	6.1	101.3	0.085
16	1	1.63	1.6	4	2.04	3.0	4	2.97	7.4	94.7	0.074
17	1	1.63	1.6	4	2.04	3.0	5	2.96	8.7	91.6	0.069
18	*1*	*1.63*	*1.6*	*4*	*2.04*	*3.0*	*6*	*2.96*	*9.9*	*91.2*	*0.069*
19	1	1.63	1.6	4	2.04	3.0	7	2.96	11.3	93.1	0.072
20	1	1.63	1.7	5	2.04	4.3	3	2.96	6.0	104.5	0.090
21	1	1.63	1.7	5	2.04	4.3	4	2.96	7.3	99.4	0.082
22	*1*	*1.63*	*1.7*	*5*	*2.04*	*4.2*	*5*	*2.96*	*8.7*	*97.8*	*0.079*
23	1	1.63	1.7	5	2.04	4.2	6	2.96	10.0	98.8	0.081
24	1	1.63	1.7	5	2.04	4.2	7	2.96	11.4	102.0	0.086
25				4	2.04	3.2				878.8	4.797
26				5	2.04	4.4				918.3	5.238
27	1	1.63	1.5	4	2.04	3.0				540.2	2.070
28	1	1.63	1.7	5	2.04	4.2				534.3	2.025
29	1	1.63	1.6	5	2.04	4.2	5	2.96	8.6	426.7	1.505
30	***1***	***1.63***	***1.5***	***4***	***2.04***	***3.0***	***6***	***2.96***	***10.0***	***417.2***	***1.438***

[a] Fourier transform range k = 2.0 - 14.5 Å^{-1} (resolution = 0.13 Å). r is in units of Å; σ^2 is in units of 10^{-3} Å^2. Fits to filtered data employed back transformation ranges of 0.7-2.1 Å (fits 1-10) and 0.7-3.1 Å (fits 11-24). Fits 25-30 are on unfiltered data.

[b] Goodness-of-fit parameter F defined as $\Sigma(\chi_{exptl}-\chi_{calc})^2$. A second parameter, *F'*, is defined as $F' = F^2 / \nu$, where $\nu = N_{IDP} - N_{VAR}$. N_{IDP} is the number of independent data points, while N_{VAR} is the number of floated variables in each optimization step. The values of *F'* shown have been divided by a factor of 10^4 for convenience. *F'* is a measure of whether an added shell significantly improves the fit.

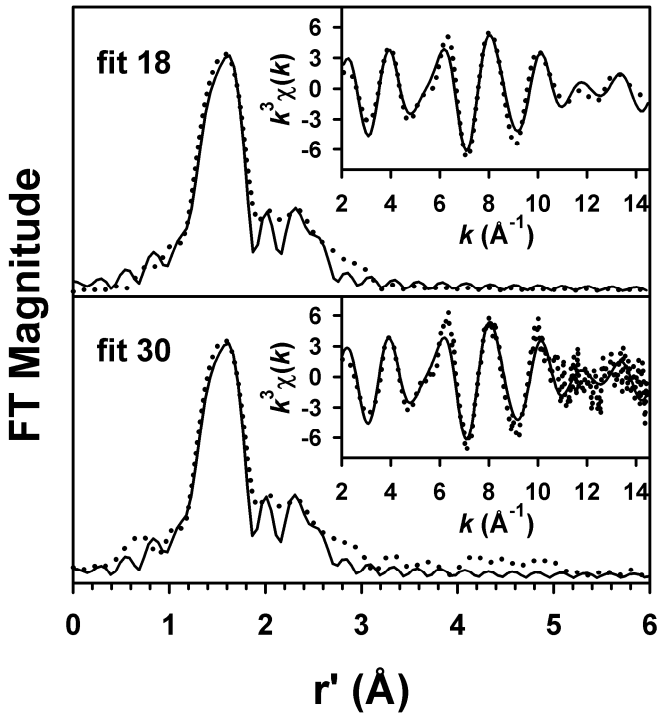

Figure 4.6. Fits to the Fourier transforms of the Fe K-edge EXAFS data ($k^3\chi(k)$) and either Fourier-filtered or unfiltered EXAFS spectra ($k^3\chi(k)$, insets) for **1-Ac**. Experimental data is shown with dotted lines (•••), while fits are shown with solid lines (——). Fourier transformation range: $k = 2 – 14.5$ Å^{-1}; back-transformation range: 0.7 – 3.1 Å. Fit parameters associated with the stated fit are shown in Table 4.3.

Table 4.4. EXAFS Analysis of **1-pyO**.[a]

	Fe-O/N			Fe-N/O			Fe•••C				
fit	**n**	**r**	**σ^2**	**n**	**r**	**σ^2**	**n**	**r**	**σ^2**	**F** [b]	***F'*** [b]
1				3	2.04	1.3				157.3	0.266
2				4	2.04	2.5				137.2	0.202
3				5	2.04	3.6				156.2	0.262
4				6	2.04	4.8				211.9	0.483
5	*1*	*1.63*	*3.2*	*4*	*2.04*	*2.4*				*46.4*	*0.030*
6	0.9	1.63	2.6	4	2.04	2.4				43.4	0.026
7	*1*	*1.63*	*3.5*	*5*	*2.04*	*3.6*				*45.6*	*0.028*
8	0.9	1.63	2.8	5	2.04	3.6				45.3	0.028
9	1	1.63	3.6	4 1	2.02 2.11	2.3 -0.4				38.1	0.027
10				4	2.04	2.4				245.0	0.359
11				5	2.04	3.6				267.6	0.429
12	1	1.63	3.0	4	2.04	2.3				149.1	0.151
13	1	1.63	3.3	5	2.04	3.5				151.2	0.156
14	1	1.63	3.2	5	2.04	3.5	3	3.01	1.7	74.7	0.044
15	1	1.63	3.2	5	2.04	3.5	4	3.01	2.8	73.1	0.042
16	1	1.63	3.2	5	2.04	3.5	5	3.01	3.9	76.5	0.046
17	1	1.63	3.1	5	2.04	3.5	6	3.01	5.0	83.9	0.055
18	1	1.63	3.0	4	2.04	2.3	3	3.02	1.6	67.1	0.035
19	*1*	*1.63*	*3.0*	*4*	*2.04*	*2.3*	*4*	*3.02*	*2.8*	*63.8*	*0.032*
20	1	1.63	3.0	4	2.04	2.3	5	3.02	3.9	65.7	0.034
21	1	1.63	2.9	4	2.04	2.3	6	3.02	5.0	71.7	0.040
22				4	2.05	2.4				757.1	3.432
23				5	2.04	3.6				801.2	3.844
24	1	1.63	2.8	4	2.04	2.3				559.5	2.130
25	1	1.63	3.1	5	2.04	3.5				556.9	2.110
26	1	1.63	3.0	5	2.04	3.5	4	3.01	2.9	412.5	1.340
27	***1***	***1.63***	***2.8***	***4***	***2.04***	***2.3***	***4***	***3.01***	***2.9***	***401.7***	***1.271***

[a] Fourier transform range k = 2.0 - 14.9 Å^{-1} (resolution = 0.12 Å). r is in units of Å; σ^2 is in units of 10^{-3} Å^2. Fits to filtered data employed back transformation ranges of 0.7-2.2 Å (fits 1-9) and 0.7-3.1 Å (fits 10-21). Fits 22-27 are on unfiltered data.

[b] Goodness-of-fit parameter F defined as $\Sigma(\chi_{exptl}-\chi_{calc})^2$. A second parameter, *F'*, is defined as $F' = F^2 / \nu$, where $\nu = N_{IDP} - N_{VAR}$. N_{IDP} is the number of independent data points, while N_{VAR} is the number of floated variables in each optimization step. The values of *F'* shown have been divided by a factor of 10^4 for convenience. *F'* is a measure of whether an added shell significantly improves the fit.

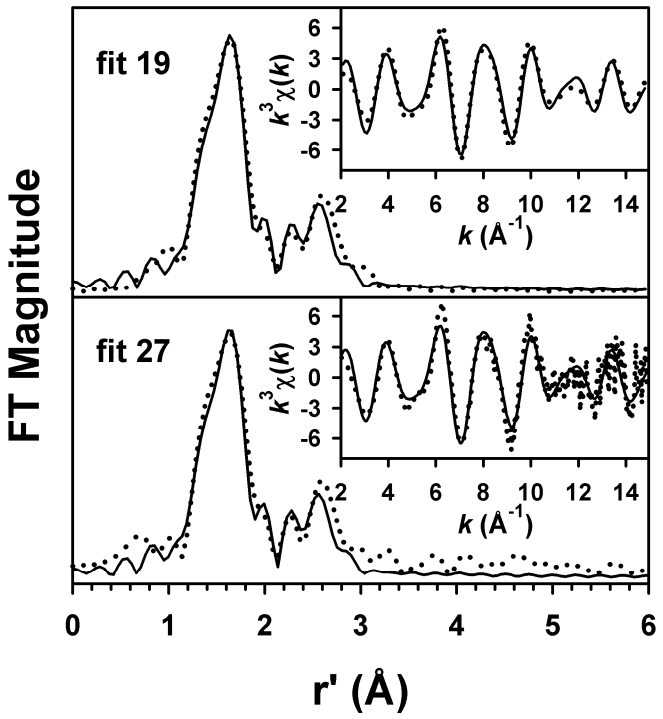

Figure 4.7. Fits to the Fourier transforms of the Fe K-edge EXAFS data ($k^3\chi(k)$) and either Fourier-filtered or unfiltered EXAFS spectra ($k^3\chi(k)$, insets) for **1-pyO**. Experimental data is shown with dotted lines (•••), while fits are shown with solid lines (——). Fourier transformation range: k = 2 – 14.9 Å^{-1}; back-transformation range: 0.7 – 3.1 Å. Fit parameters associated with the stated fit are shown in Table 4.4.

Table 4.5. EXAFS Analysis of **1-py**.[a]

	Fe-O/N			Fe-N/O			Fe•••C				
fit	**n**	**r**	**σ^2**	**n**	**r**	**σ^2**	**n**	**r**	**σ^2**	**F**	***F'***
1				3	2.07	1.6				185.0	0.469
2				4	2.07	2.9				173.7	0.413
3				5	2.06	4.1				193.4	0.512
4				6	2.07	5.4				242.0	0.802
5	*1*	*1.63*	*2.2*	*4*	*2.07*	*2.9*				*29.1*	*0.016*
6	0.9	1.63	1.7	4	2.07	2.9				28.5	0.015
7	1	1.63	2.2	5	2.07	4.2				36.0	0.024
8	0.9	1.63	1.7	5	2.07	4.1				37.0	0.026
9	1	1.63	2.2	4 1	2.07 2.34	2.9 31.8				27.7	0.023
10				4	2.07	2.9				239.7	0.376
11				5	2.07	4.1				259.9	0.441
12	1	1.63	2.2	5	2.07	4.2				98.9	0.074
13	1	1.63	2.2	4	2.07	2.9				92.5	0.064
14	1	1.63	2.1	4	2.07	2.9	3	2.96	5.3	49.8	0.022
15	*1*	*1.63*	*2.1*	*4*	*2.07*	*2.9*	*4*	*2.97*	*7.1*	*47.3*	*0.020*
16	1	1.63	2.1	4	2.07	2.9	5	2.97	8.7	47.8	0.020
17	1	1.63	2.1	4	2.07	2.9	6	2.97	10.4	50.4	0.022
14a	1	1.63	2.2	5	2.07	4.2	3	2.96	5.2	59.6	0.031
15a	1	1.63	2.1	5	2.07	4.2	4	2.96	6.9	58.6	0.030
16a	1	1.63	2.1	5	2.07	4.2	5	2.96	8.8	60.1	0.032
17a	1	1.63	2.1	5	2.07	4.2	6	2.96	10.4	63.7	0.036
18				4	2.07	2.8				676.2	2.989
19				5	2.07	4.1				723.6	3.422
20	1	1.63	1.9	4	2.07	2.8				362.7	0.989
21	1	1.63	2.0	5	2.07	4.1				375.1	1.058
22	***1***	***1.63***	***1.8***	***4***	***2.07***	***2.8***	***4***	***2.96***	***6.8***	***274.9***	***0.669***
23	1	1.63	1.9	5	2.07	4.1	4	2.96	6.6	297.3	0.782

[a] Fourier transform range k = 2.0 - 14.5 Å^{-1} (resolution = 0.13 Å). r is in units of Å; σ^2 is in units of 10^{-3} Å^2. Fits to filtered data employed back transformation ranges of 0.7-2.0 Å (fits 1-9) and 0.7-3.0 Å (fits 10-17a). Fits 18-23 are on unfiltered data.

[b] Goodness-of-fit parameter F defined as $\Sigma(\chi_{exptl}-\chi_{calc})^2$. A second parameter, *F'*, is defined as $F' = F^2 / \nu$, where $\nu = N_{IDP} - N_{VAR}$. N_{IDP} is the number of independent data points, while N_{VAR} is the number of floated variables in each optimization step. The values of *F'* shown have been divided by a factor of 10^4 for convenience. *F'* is a measure of whether an added shell significantly improves the fit.

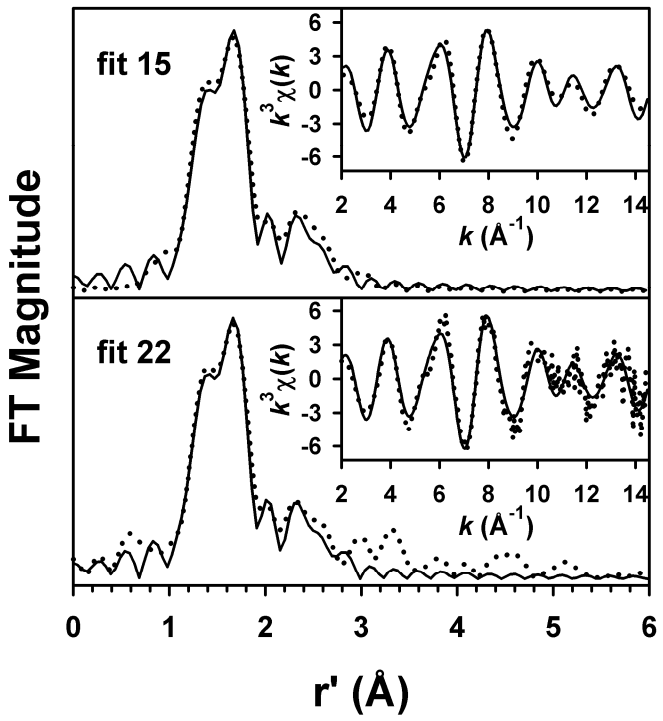

Figure 4.8. Fits to the Fourier transforms of the Fe K-edge EXAFS data ($k^3\chi(k)$) and either Fourier-filtered or unfiltered EXAFS spectra ($k^3\chi(k)$, insets) for **1-py**. Experimental data is shown with dotted lines (•••), while fits are shown with solid lines (——). Fourier transformation range: $k = 2 – 14.5$ Å^{-1}; back-transformation range: 3.0 – 0.7 Å. Fit parameters associated with the stated fit are shown in Table 4.5.

Table 4.6. EXAFS Analysis of **1-(OAc)**.[a]

	Fe-N/O			Fe-O/N			Fe•••C				
fit	**n**	**r**	**σ^2**	**n**	**r**	**σ^2**	**n**	**r**	**σ^2**	**F [b]**	***F'* [b]**
1	2	2.06	1.0							279.9	0.922
2	3	2.06	2.4							216.2	0.550
3	4	2.05	3.7							199.6	0.469
4	5	2.05	4.9							214.0	0.539
5	6	2.06	6.2							256.4	0.773
6	4	2.06	3.5	1	1.64	1.4				42.6	0.028
7	*5*	*2.05*	*4.8*	*1*	*1.64*	*1.6*				*39.9*	*0.024*
8	4	2.06	3.6							287.2	0.494
9	5	2.06	4.8							296.1	0.525
10	4	2.06	3.4	1	1.64	1.1				109.1	0.081
11	5	2.06	4.7	1	1.64	1.3				109.8	0.082
12	5	2.06	4.8	1	1.64	1.3	2	3.01	1.3	73.2	0.042
13	*5*	*2.06*	*4.7*	*1*	*1.64*	*1.3*	*3*	*3.01*	*3.4*	*72.9*	*0.042*
14	5	2.06	4.7	1	1.64	1.3	4	3.00	5.6	75.7	0.045
15	5	2.06	4.7	1	1.64	1.2	5	3.00	7.8	80.4	0.051
16	5	2.05	4.7	1	1.64	1.3	2 2	2.89 3.02	3.3 -0.3	62.1	0.036
17	5	2.04	4.7	1	1.64	1.4	2 3	2.86 3.01	2.4 1.0	64.8	0.039
18	5	2.05	4.7	1	1.64	1.3	3 2	2.90 3.03	6.1 0.0	69.1	0.045
19	*5*	*2.05*	*4.6*	*1*	*1.64*	*1.3*	*2* *2* *2*	*2.89* *3.03* *3.47*	*3.8* *-0.1* *3.6*	*53.7*	*0.033*
20	4	2.06	3.6							704.6	2.973
21	5	2.06	4.9							745.4	3.327
22	4	2.06	3.4	1	1.64	1.2				353.7	0.851
23	5	2.05	4.8	1	1.64	1.3				351.3	0.840
24	5	2.06	4.8	1	1.64	1.4	2	3.01	1.1	279.2	0.614
25	*5*	*2.06*	*4.8*	*1*	*1.64*	*1.3*	*3*	*3.01*	*3.2*	*280.1*	*0.618*
26	5	2.06	4.8	1	1.64	1.3	4	3.00	5.4	286.9	0.648
27	5	2.05	4.8	1	1.64	1.3	2 2	2.88 3.02	3.9 -0.3	267.0	0.666
28	5	2.05	4.8	1	1.64	1.3	3 2	2.90 3.03	7.4 0.3	276.0	0.712
29	5	2.05	4.8	1	1.64	1.3	2 3	2.86 3.02	3.2 1.3	273.4	0.699
30	**5**	**2.05**	**4.7**	**1**	**1.64**	**1.3**	**2** **2** **2**	**2.89** **3.02** **3.45**	**3.5** **-0.3** **2.6**	**244.2**	**0.685**

[a] Fourier transform range k = 2.0 - 14.9 Å^{-1} (resolution = 0.12 Å). r is in units of Å; σ^2 is in units of 10^{-3} Å^2. Fits to filtered data employed back transformation ranges of 0.8-2.2 Å (fits 1-7) and 0.8-3.2 Å (fits 8-19). Fits 20-30 are on unfiltered data.

[b] Goodness-of-fit parameter F defined as $\Sigma(\chi_{exptl}-\chi_{calc})^2$. A second parameter, *F'*, is defined as $F' = F^2 / \nu$, where $\nu = N_{IDP} - N_{VAR}$. N_{IDP} is the number of independent data points, while N_{VAR} is the number of floated variables in each optimization step. The values of *F'* shown have been divided by a factor of 10^4 for convenience. *F'* is a measure of whether an added shell significantly improves the fit.

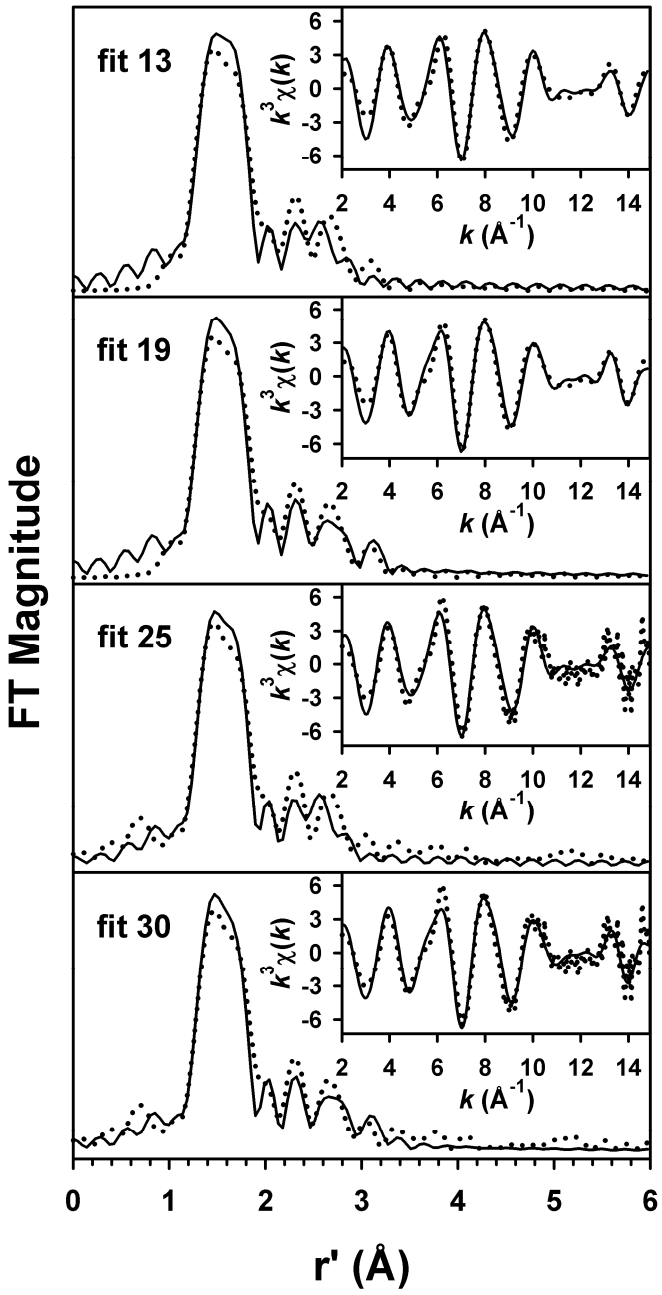

Figure 4.9. Fits to the Fourier transforms of the Fe K-edge EXAFS data ($k^3\chi(k)$) and either Fourier-filtered or unfiltered EXAFS spectra ($k^3\chi(k)$, insets) for **1-(OAc)**. Experimental data is shown with dotted lines (•••), while fits are shown with solid lines (——). Fourier transformation range: k = 2 – 14.9 Å^{-1}; back-transformation range: 3.2 – 0.8 Å. Fit parameters associated with the stated fit are shown in Table 4.6.

Table 4.7. EXAFS Analysis of **1-dmpa**.[a]

	Fe-N/O			Fe-O/N			Fe•••C				
fit	**n**	**r**	**σ^2**	**n**	**r**	**σ^2**	**n**	**r**	**σ^2**	**F [b]**	***F'* [b]**
1	2	2.05	-0.2							385.3	1.747
2	3	2.05	1.1							291.2	0.998
3	4	2.05	2.2							254.7	0.763
4	5	2.05	3.2							257.7	0.781
5	6	2.04	4.2							290.4	0.992
6	4	2.05	2.1	1	1.63	1.2				64.3	0.064
7	*5*	*2.05*	*3.1*	*1*	*1.63*	*1.4*				*54.6*	*0.046*
8	4	2.05	2.1							338.2	0.685
9	5	2.05	3.2							344.8	0.712
10	4	2.05	2.0	1	1.64	1.1				138.1	0.130
11	5	2.05	3.0	1	1.63	1.2				131.7	0.118
12	5	2.05	3.0	1	1.63	1.2	3	3.01	3.4	80.9	0.051
13	*5*	*2.05*	*3.0*	*1*	*1.63*	*1.2*	*4*	*3.01*	*4.7*	*79.7*	*0.050*
14	5	2.05	3.0	1	1.63	1.2	5	3.01	6.0	82.4	0.053
15	5	2.05	3.0	1	1.63	1.2	6	3.00	7.4	87.8	0.061
16	5	2.05	3.0	1	1.63	1.2	4 1	3.01 3.46	4.8 1.4	70.7	0.047
17	5	2.05	3.0	1	1.63	1.2	4 2	3.01 3.48	4.8 4.2	66.6	0.041
18	5	2.05	3.0	1	1.63	1.2	4 3	3.01 3.49	4.8 6.8	64.3	0.039
19	5	2.05	3.0	1	1.63	1.2	4 4	3.01 3.50	4.8 9.4	63.0	0.037
20	4	2.06	2.1							900.7	4.858
21	5	2.05	3.2							924.3	5.116
22	4	2.05	2.0	1	1.64	1.1				475.5	1.538
23	5	2.05	3.1	1	1.63	1.2				462.1	1.453
24	5	2.05	3.1	1	1.63	1.2	3	3.01	3.5	364.8	1.048
25	***5***	***2.05***	***3.1***	***1***	***1.63***	***1.2***	***4***	***3.01***	***4.9***	***363.4***	***1.040***
26	5	2.05	3.0	1	1.63	1.1	5	3.01	6.2	369.4	1.074
27	5	2.05	3.0	1	1.63	1.1	6	3.00	7.6	381.3	1.145
28	5	2.05	3.1	1	1.63	1.1	4 2	3.01 3.55	4.9 9.6	338.7	1.072

[a] Fourier transform range k = 2.0 - 14.9 Å^{-1} (resolution = 0.12 Å). r is in units of Å; σ^2 is in units of 10^{-3} Å^2. Fits to filtered data employed back transformation ranges of 0.8-2.2 Å (fits 1-7) and 0.8-3.2 Å (fits 8-19). Fits 20-28 are on unfiltered data.

[b] Goodness-of-fit parameter F defined as $\Sigma(\chi_{exptl}-\chi_{calc})^2$. A second parameter, *F'*, is defined as $F' = F^2 / \nu$, where $\nu = N_{IDP} - N_{VAR}$. N_{IDP} is the number of independent data points, while N_{VAR} is the number of floated variables in each optimization step. The values of *F'* shown have been divided by a factor of 10^4 for convenience. *F'* is a measure of whether an added shell significantly improves the fit.

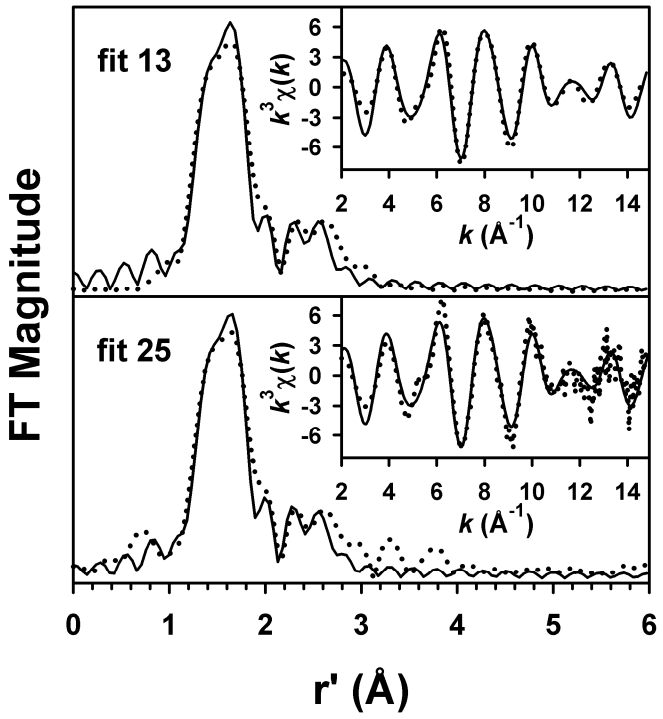

Figure 4.10. Fits to the Fourier transforms of the Fe K-edge EXAFS data ($k^3\chi(k)$) and either Fourier-filtered or unfiltered EXAFS spectra ($k^3\chi(k)$, insets) for **1-dmpa**. Experimental data is shown with dotted lines (•••), while fits are shown with solid lines (——). Fourier transformation range: k = 2 – 14.9 Å^{-1}; back-transformation range: 3.2 – 0.8 Å. Fit parameters associated with the stated fit are shown in Table 4.7.

Table 4.8. Fourier-filtered EXAFS Analysis of **1-dma**.[a]

	Fe-N/O			Fe-O/N			Fe•••C				
fit	**n**	**r**	**σ^2**	**n**	**r**	**σ^2**	**n**	**r**	**σ^2**	**F [b]**	***F'* [b]**
1	2	2.03	-0.2							327.9	1.250
2	3	2.04	1.0							230.8	0.619
3	4	2.04	2.1							197.2	0.452
4	5	2.03	3.1							206.7	0.497
5	6	2.04	4.1							255.9	0.761
6	4	2.04	1.9	1	1.63	2.3				63.0	0.060
7	*5*	*2.04*	*3.0*	*1*	*1.63*	*2.5*				*55.3*	*0.046*
8	4 1	2.06 1.96	1.0 -1.3	1	1.63	2.7				50.4	0.055
9	4	2.04	2.0							286.1	0.484
10	5	2.04	3.0							299.3	0.530
11	4	2.04	1.8	1	1.63	2.1				144.2	0.140
12	5	2.04	2.9	1	1.63	2.3				139.9	0.131
13	5	2.04	2.9	1	1.63	2.3	3	2.98	4.8	89.6	0.062
14	5	2.04	2.9	1	1.63	2.3	4	2.98	6.4	85.4	0.057
15	*5*	*2.04*	*2.9*	*1*	*1.63*	*2.3*	*5*	*2.98*	*7.9*	*84.4*	*0.055*
16	5	2.04	2.9	1	1.63	2.2	6	2.97	9.2	85.9	0.057
17	5	2.04	2.9	1	1.63	2.2	7	2.97	10.8	89.6	0.062
18	5	2.04	2.9	1	1.63	2.2	5 1	2.97 3.44	8.0 0.9	74.9	0.051
19	5	2.04	2.9	1	1.63	2.2	5 2	2.97 3.45	8.0 3.7	71.4	0.047
20	5	2.04	2.9	1	1.63	2.2	5 3	2.98 3.47	8.0 6.6	69.5	0.044
21	5	2.04	2.9	1	1.63	2.3	5 4	2.97 3.48	8.1 9.4	68.4	0.043
22	5	2.04	2.8	1	1.63	2.1	3 2	2.91 3.04	4.3 0.6	76.8	0.054
23	5	2.04	2.8	1	1.63	2.1	3 3	2.89 3.03	4.2 1.9	78.2	0.056
24	5	2.04	2.8	1	1.63	2.1	2 3	2.88 3.02	2.0 1.6	76.6	0.054
25	***5***	***2.03***	***2.8***	***1***	***1.63***	***2.0***	***2*** ***3*** ***2***	***2.88*** ***3.02*** ***3.44***	***1.9*** ***1.6*** ***3.2***	***61.3***	***0.042***

[a] Fourier transform range k = 2.0 – 15.0 Å^{-1} (resolution = 0.12 Å). r is in units of Å; σ^2 is in units of 10^{-3} Å^2. All fits shown here were to Fourier-filtered data employing back transformation ranges of 0.7-2.1 Å (fits 1-8) and 0.7-3.1 Å (fits 9-25).

[b] Goodness-of-fit parameter F defined as $\Sigma(\chi_{exptl}-\chi_{calc})^2$. A second parameter, *F'*, is defined as $F' = F^2 / \nu$, where $\nu = N_{IDP} - N_{VAR}$. N_{IDP} is the number of independent data points, while N_{VAR} is the number of floated variables in each optimization step. The values of *F'* shown have been divided by a factor of 10^4 for convenience. *F'* is a measure of whether an added shell significantly improves the fit.

Table 4.9. Unfiltered EXAFS Analysis of **1-dma**.[a]

	Fe-N/O			Fe-O/N			Fe•••C				
fit	**n**	**r**	**σ^2**	**n**	**r**	**σ^2**	**n**	**r**	**σ^2**	**F [b]**	***F'* [b]**
26	4	2.04	2.0							710.6	2.988
27	5	2.04	3.0							737.1	3.215
28	4	2.04	1.8	1	1.63	1.9				425.0	1.212
29	5	2.04	2.9	1	1.63	2.1				407.8	1.116
30	5	2.04	2.9	1	1.63	2.1	4	2.98	6.5	303.6	0.715
31	*5*	*2.04*	*2.9*	*1*	*1.63*	*2.1*	*5*	*2.97*	*7.9*	*302.2*	*0.708*
32	5	2.04	2.9	1	1.63	2.1	6	2.97	9.4	306.0	0.726
33	5	2.04	2.8	1	1.63	2.0	3 2	2.91 3.04	4.1 0.9	291.4	0.779
34	5	2.04	2.8	1	1.63	2.0	2 3	2.88 3.02	2.4 2.2	291.7	0.781
35	5	2.04	2.8	1	1.63	2.0	3 3	2.89 3.03	4.6 2.5	294.8	0.797
36	***5***	***2.04***	***2.8***	***1***	***1.63***	***2.0***	***2*** ***3*** ***2***	***2.88*** ***3.02*** ***3.49***	***2.4*** ***2.2*** ***7.0***	***269.0***	***0.813***

[a] Fourier transform range k = 2.0 – 15.0 Å^{-1} (resolution = 0.12 Å). r is in units of Å; σ^2 is in units of 10^{-3} Å^2. All fits shown are for unfiltered EXAFS data.

[b] Goodness-of-fit parameter F defined as $\Sigma(\chi_{exptl}-\chi_{calc})^2$. A second parameter, *F'*, is defined as $F' = F^2 / \nu$, where $\nu = N_{IDP} - N_{VAR}$. N_{IDP} is the number of independent data points, while N_{VAR} is the number of floated variables in each optimization step. The values of *F'* shown have been divided by a factor of 10^4 for convenience. *F'* is a measure of whether an added shell significantly improves the fit.

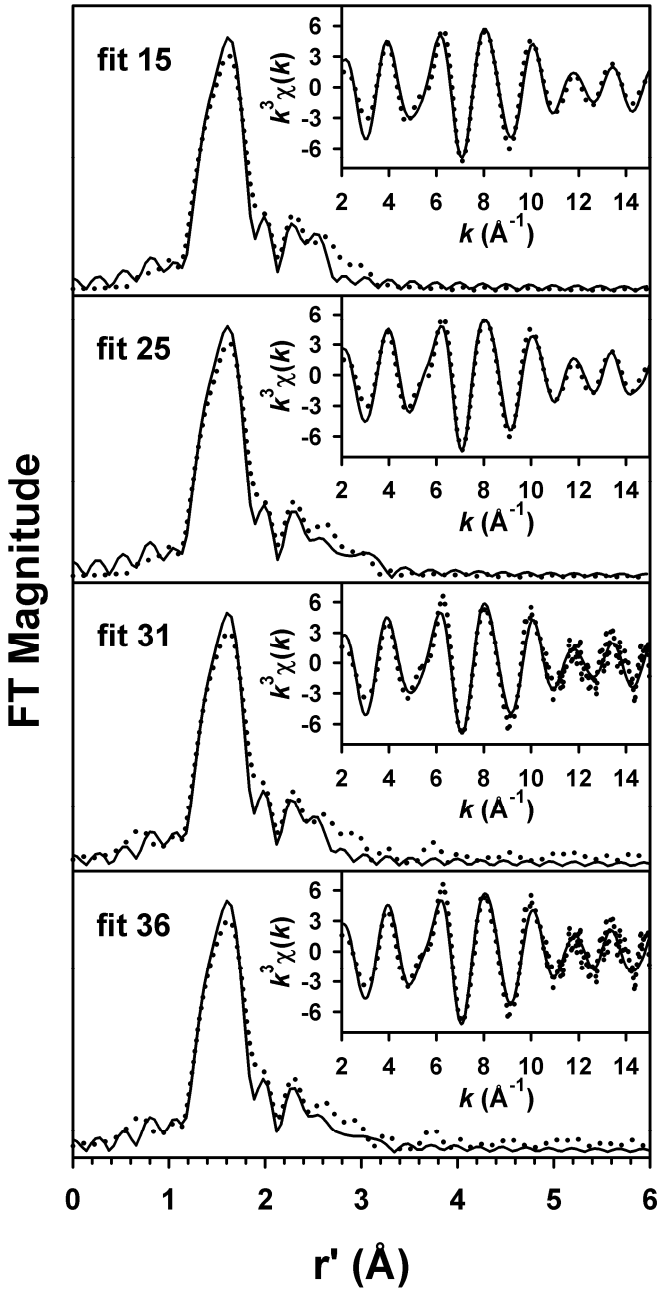

Figure 4.11. Fits to the Fourier transforms of the Fe K-edge EXAFS data ($k^3\chi(k)$) and either Fourier-filtered or unfiltered EXAFS spectra ($k^3\chi(k)$, insets) for **1-dma**. Experimental data is shown with dotted lines (•••), while fits are shown with solid lines (——). Fourier transformation range: k = 2 – 15 Å^{-1}; back-transformation range: 3.1 – 0.7 Å. Fit parameters associated with the stated fit are shown in Table 4.8 (filtered) or Table 4.9 (unfiltered).

Table 4.10. Unfiltered EXAFS Analysis of **1-Bl.S.**.[a]

	Fe-N/O			Fe-O/N			Fe•••C			Fe•••C				
fit	n	r	σ^2	n	r	σ^2	n	r	σ^2	n	r	σ^2	F	*F'*
27	3	2.04	2.5										421.5	1.110
28	4	2.04	3.9										406.5	1.033
29	5	2.04	5.3										445.9	1.243
30	6	2.04	6.8										524.4	1.719
31	3	2.04	2.3	1	1.66	2.4							302.6	0.654
31a	3	2.04	2.2	0.9	1.66	1.7							285.1	0.581
32	4	2.04	3.9	1	1.66	2.8							233.1	0.388
32a	4	2.04	3.9	0.9	1.66	2.2							224.7	0.361
33	5	2.03	5.4	1	1.67	3.0							213.6	0.326
33a	5	2.04	5.4	0.9	1.67	2.4							213.2	0.325
34	4 1	2.04 2.22	3.9 27.2	0.9	1.67	2.2							210.1	0.368
35	3 1	2.00 2.09	2.1 -0.3	0.9	1.66	2.8							221.3	0.408
36	3 2	2.03 2.02	3.1 14.0	0.9	1.66	2.1							229.4	0.439
37	4 1	2.07 1.98	5.7 0.6										440.8	1.388
38	4 1	2.04 2.22	3.9 27.9	0.9	1.66	2.2							210.1	0.368
39	3 1	2.08 1.96	0.9 -1.8										387.4	1.072
40	3 1	2.05 1.98	3.5 4.5	0.9	1.66	2.3							232.5	0.450
41	5	2.03	5.4	0.9	1.67	2.4	3	2.95	9.1				178.6	0.266
42	*5*	*2.03*	*5.4*	*0.9*	*1.67*	*2.5*	*4*	*2.94*	*11.5*				*179.9*	*0.270*
43	5	2.03	5.4	0.9	1.67	2.4	5	2.93	13.5				184.7	0.284

44	5	2.03	5.4	0.9	1.67	2.6	4 2	2.85 3.02	9.5 1.8				180.1	0.324
45	5	2.03	5.4	0.9	1.67	2.6	4 3	2.83 3.01	8.4 3.3				185.7	0.345
46	*5*	*2.03*	*5.4*	*0.9*	*1.67*	*2.5*	*3* *3*	*2.82* *3.00*	*6.0* *3.3*				*179.7*	*0.323*
47	5	2.03	5.4	0.9	1.67	2.5	3 2	2.85 3.02	7.0 1.6				172.5	0.298
48	5	2.03	5.4	0.9	1.67	2.4	4	2.94	11.7	2	3.42	1.8	140.5	0.197
49	5	2.03	5.4	0.9	1.67	2.4	4	2.95	11.7	3	3.42	3.5	133.0	0.177
50	5	2.03	5.4	0.9	1.67	2.4	4	2.95	11.5	4	3.43	5.0	128.8	0.166
51	*5*	*2.03*	*5.4*	*0.9*	*1.67*	*2.4*	*4*	*2.95*	*11.5*	*5*	*3.43*	*6.6*	*127.1*	*0.162*
52	5	2.03	5.4	0.9	1.67	2.4	4	2.96	11.4	6	3.44	8.3	127.2	0.162
53	5	2.03	5.4	0.9	1.67	2.5	4	2.96	11.2	7	3.44	10.2	128.7	0.166
54	5	2.03	5.4	0.9	1.67	2.6	4 2	2.87 3.03	10.1 2.0	5	3.42	6.0	116.7	0.170
55	5	2.03	5.4	0.9	1.67	2.5	3 2	2.86 3.02	7.2 1.5	5	3.43	5.9	115.0	0.165
56	***5***	***2.03***	***5.4***	***0.9***	***1.67***	***2.5***	***3*** ***3***	***2.84*** ***3.01***	***6.1*** ***3.2***	***5***	***3.42***	***6.1***	***116.0***	***0.168***

[a] Fourier transform range k = 2.0 - 14.0 Å^{-1} (resolution = 0.13 Å). r is in units of Å; σ^2 is in units of 10^{-3} Å^2. All fits shown are for unfiltered EXAFS data.

[b] Goodness-of-fit parameter F defined as $\Sigma(\chi_{exptl}-\chi_{calc})^2$. A second parameter, F', is defined as $F' = F^2 / \nu$, where $\nu = N_{IDP} - N_{VAR}$. N_{IDP} is the number of independent data points, while N_{VAR} is the number of floated variables in each optimization step. The values of F' shown have been divided by a factor of 10^4 for convenience. F' is a measure of whether an added shell significantly improves the fit.

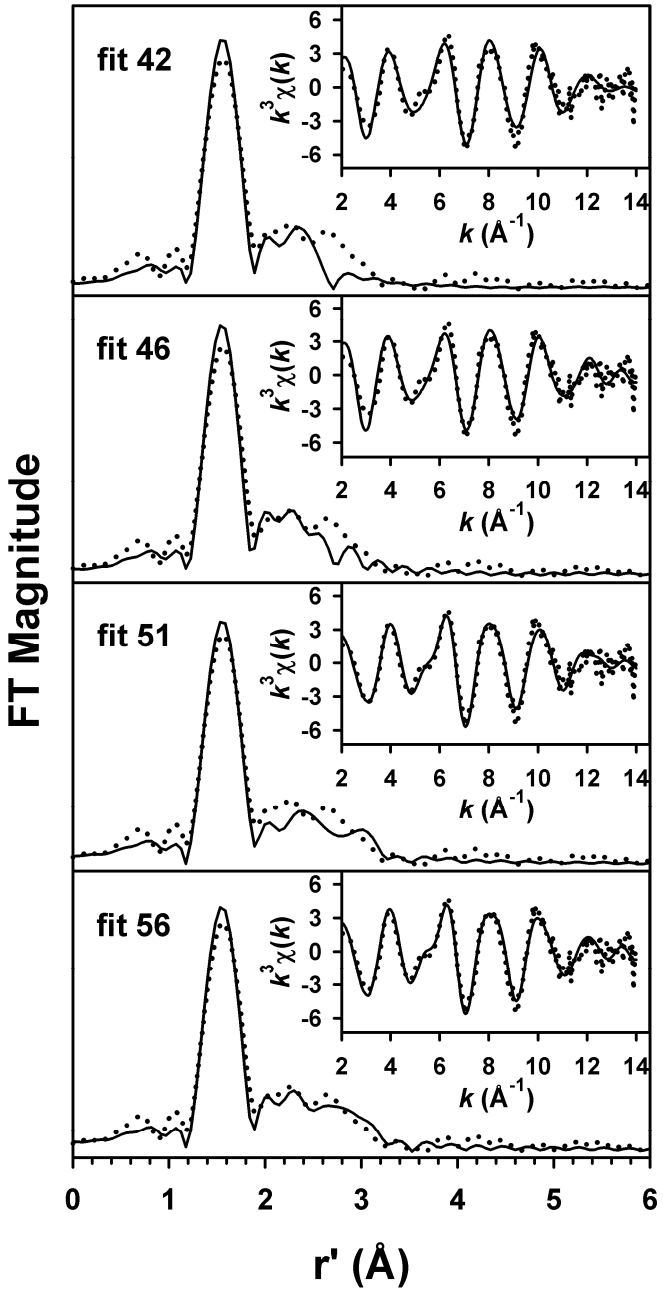

Figure 4.12. Fits to the Fourier transforms of the Fe K-edge EXAFS data ($k^3\chi(k)$) and unfiltered EXAFS spectra ($k^3\chi(k)$, insets) for **1-Bl.S.**. Experimental data is shown with dotted lines (•••), while fits are shown with solid lines (——). Fourier transformation range: k = 2 – 14 Å^{-1}. Fit parameters associated with the stated fit are shown in Table 4.10.

4.4 Discussion

We have presented results from a complete X-ray absorption spectroscopic characterization of a series of oxoiron(IV) complexes employing a tetramethylcyclam ligand with an attached pendant *trans* nitrogen or oxygen donor. The pre-edge areas associated with the 1s-to-3d transition obtained by XANES analysis and the metrical parameters for the first coordination sphere obtained by EXAFS analysis show that the geometric and electronic properties of the oxoiron(IV) unit are not significantly affected by the identity of the *trans* ligand in this series (Table 4.11). The structural parameters obtained by EXAFS are largely in good agreement with available X-ray diffraction and computational parameters, within the error of ±0.02 Å associated with metal-ligand bond lengths determined by EXAFS. We note that the bond lengths obtained via EXAFS for the Fe=O moiety are generally slightly shorter by 0.03 – 0.04 Å than those obtained via X-ray crystallography. This could reflect some subtle alteration of the environment of the complex in solution compared to the solid state, or else represents a systematic error in our EXAFS analysis, the origins of which we are unable to identify at the moment. For example, the Fe=O bond length of 1.68 Å obtained via EXAFS[133] for $[Fe^{IV}(O)(N4py)]^{2+}$ is significantly longer than the crystallographic value of 1.639 Å.[188]

The absence of any significant electronic or structural changes over this series of **1-X** complexes based on our XAS analysis is in reasonably good agreement with previous results reported by Jackson *et al.* for $[Fe^{IV}(O)(TMC)(X)]^{+/2+}$ complexes in which X was a non-pendant ligand *trans* to the oxo moiety.[177] In that study, the Fe=O bond was slightly longer and the electronic structure of the overall complex was greatly perturbed when X was hydroxide or thiolate.[177] A consideration of the available resonance Raman

and Mössbauer data (Table 4.11) reveals that the electronic distortion of the oxoiron(IV) center is much more modest for the **1-X** complexes examined here than was the case in earlier work, based on the relatively small changes in quadrupole splitting value, ν(Fe=O), and pre-edge area, as well as the correlation of the latter two values with the former (Figure 4.13). Indeed, given the relatively limited range of chemical functionalities in the present study, this should not be surprising. The most interesting comparison can be made between the related complexes **1-Bl.S.** and **1-dma. 1-Bl.S.** exhibits a much smaller Mössbauer quadrupole splitting of 0.51 mm s^{-1} compared to the value of 1.10 mm s^{-1} obtained for its **1-dma** precursor, suggesting that the hypothesized deprotonation of the pendant amide arm affords a significant alteration of the Fe(IV) electronic environment. The smaller pre-edge area and somewhat longer Fe=O bond of **1-Bl.S.** indicate a greater degree of centrosymmetry at the iron(IV) center of **1-Bl.S.** compared to **1-dma**, and this pair of complexes thus strengthens the standing hypothesis that the nature of the ligand *trans* to the oxo moiety greatly affects the electronic properties and reactivity of nonheme oxoiron(IV) centers.[176,177] We also characterized a complex, **1-OAc**, which represents an addition to the series of oxoiron(IV) TMC complexes with a free X ligand. Both the pre-edge area and Fe=O stretching frequency are in line with the correlation with quadrupole splitting parameters reported previously (Figure 4.13).[177] However, despite its apparent structural and electronic similarities to **1-Ac**, **1-(OAc)** is more than two orders of magnitude more reactive than **1-Ac** towards either triphenylphosphine or dihydroanthracene substrates, and exhibits a half-life towards self-decay at 25 °C of only 45 minutes, compared to 2 days for **1-Ac**.[186] This reactivity trend is unexpected in light of reactivity trends observed previously for related

complexes,[176] and suggests that additional properties such as the electrochemical characteristics of the oxoiron(IV) center or steric factors may play a significant role on modulating reactivity, particularly for the series of pendant TMC complexes discussed here. In summary, we have structurally characterized several additional examples of growing family of nonheme oxoiron(IV) complexes, the study of which is providing new insight into the factors which govern the structure and reactivity of nonheme oxoiron(IV) centers in biology.

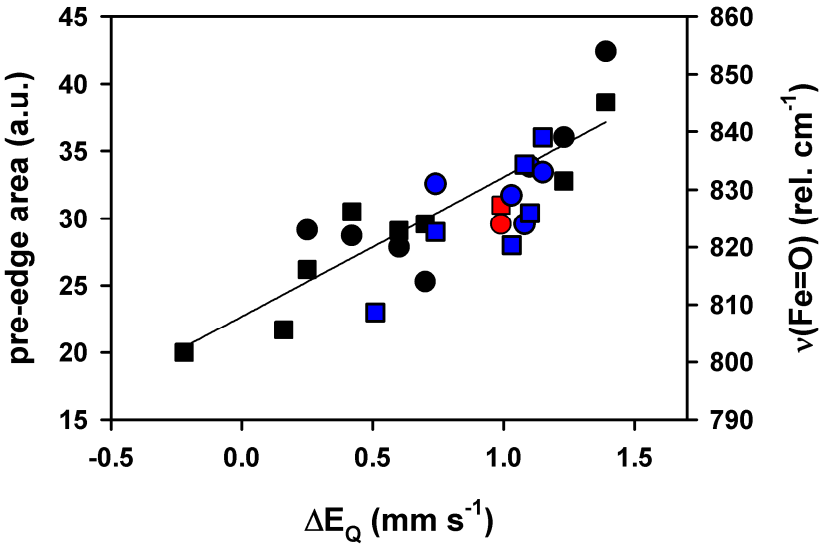

Figure 4.13. Comparision of the pre-edge area (red square for **1-(OAc)** and blue square for other **1-X** complexes) and ν(Fe=O) (cm^{-1}, red circle for **1-(OAc)** and blue cicle for other **1-X** complexes) of **1-X** complexes studied herein with other *trans*-substituted $[Fe^{IV}(O)(TMC)(X)]^{+/2+}$ complexes described by Jackson *et al.* in reference 177 (pre-edge areas given as black squares and ν(Fe=O) as black circles).

Table 4.11. Structural and Spectroscopic Properties of Pendant **1-X** Complexes.[a]

Species		Fe-N/O		Fe=O			Mössbauer		
		n	r(Å)	n	r(Å)	ν(Fe=O) (cm^{-1})	δ (mm s^{-1})	ΔE_Q (mm s^{-1})	pre-edge area
1-py	**EXAFS**	4	2.07	1	1.63				
	XRD	$4N_{eq}$ $1N_{py}$	2.083 2.117	1	1.667	824	0.18	1.08	34
1-pyO	**EXAFS**	4	2.04	1	1.63	829	0.17	1.03	28
1-dma	**EXAFS**	5	2.04	1	1.63				
	XRD	$4N_{eq}$ $1O_{amide}$	2.061 1.981	1	1.658	834	0.13	1.10	30.4
	DFT	$4N_{eq}$ $1O_{amide}$	2.102 2.024	1	1.646				
1-Bl.S.	**EXAFS**	5	2.03	0.9	1.67				
	DFT	$4N_{eq}$ $1O_{amide}$	2.102 1.944	1	1.667	--	0.13	0.51	23
1-dmpa	**EXAFS**	5	2.05	1	1.63				
	XRD	$4N_{eq}$ $1O_{amide}$	2.084 1.987	1	1.666	833	0.18	1.15	36
1-Ac	**EXAFS**	4	2.04	1	1.63				
	DFT	$4N_{eq}$ $1O_{ac}$	2.103 1.945	1	1.666	831	0.13	0.74	29
1-(OAc)	**EXAFS**	5	2.06	1	1.64	824	0.19	0.99	31

[a] EXAFS parameters are those given in Table 4.2, while pre-edge areas are the weighted values given in Table 4.1. All data for **1-py** is from reference 184. XRD structural parameters for **1-dma** and **1-dmpa** are from J. England, V. G. Young, Jr., unpublished observations, while DFT structural parameters for **1-dma** and **1-Bl.S.** are from M. Martinho, unpublished observations. DFT structural parameters for **1-Ac** are from reference 182. All ν(Fe=O) values are from reference 189, while Mössbauer parameters are from M. Martinho, E. Münck, unpublished observations.

Chapter 5.

XAS Studies of Sulfinate-Ligated Iron Complexes

Portions of this work have been submitted for publication to *J. Am. Chem. Soc.* as: "Sulfur versus Iron Oxidation in an Iron-Thiolate Model Complex." Aidan R. McDonald, Michael R. Bukowski, Erik R. Farquhar, Timothy A. Jackson, Kevin D. Koehntop, Mi Sook Seo, Raymond F. De Hont, Audria Stubna, Jason A. Halfen, Eckard Münck, Wonwoo Nam, and Lawrence Que, Jr.

5.1 Introduction

Enzymes that activate dioxygen in the presence of a thiolate ligand have received considerable attention over the years, principally as a result of their unique electronic properties and reactivity. The heme-containing oxygenase cytochrome P450 represents a classic example which has received considerable attention over a period of decades.[8,10] In the O_2 activation pathway of P450, the *trans* effect exerted by a cysteine thiolate ligand is thought to promote heterolytic O–O bond cleavage leading to a potent oxidant best described as an oxoiron(IV) center coupled to a porphyrin radical cation (compound I). [8,10] While the exceptional reactivity and instability of P450 compound I has precluded extensive spectroscopic study of its properties,[190] Green and coworkers have recently described the characterization of the less reactive compound I of another heme thiolate enzyme, chloroperoxidase (CPO),[191] as part of their studies of the role of the thiolate ligand in modulating the properties of heme-derived iron-oxo moieties,[192-195] with X-ray absorption spectroscopic studies suggesting a short Fe=O bond of 1.65 Å and a weak Fe–S interaction of 2.48 Å in CPO compound I.[191] Intriguingly, density functional theory (DFT) calculations on CPO compound I and the structurally analogous compound I of P450 show delocalization of the porphryin radical cation onto the bound thiolate, indicative of partial sulfur oxidation.[191,195] However, a decisive elucidation of the role of the *trans* thiolate in P450 and CPO remains elusive, in part due to the lack of porphyrin-containing model complexes with an oxoiron(IV)-thiolate adduct.

With the notable exception of the superoxide detoxifying enzyme superoxide reductase, which contains an N_4S iron binding motif consisting of four histidines in the equatorial plane and an axial cysteine thiolate,[196-199] *nonheme* iron sites that react with O_2

or its reduced analogues *and* contain thiolate ligation are quite rare. Indeed, the best characterized examples act on substrates that contain a thiolate sulfur atom. For example, the nonheme oxidase isopenicillin N synthase (IPNS) carries out conversion of a linear tripeptide substrate containing a cysteine to the bicyclic ring system of isopenicillin, the precursor of all biologically known penicillin antibiotics.[119,200] IPNS is thought to employ iron(III)-superoxo and oxoiron(IV) oxidants to effect this unique tandem oxidative desaturation/ring closure chemistry, with binding of the substrate thiolate to the iron(II) center acting as a trigger for O_2 binding and activation.[3,201] Cysteine dioxygenase (CDO) carries out oxidation of cysteine (Cys) to cysteinesulfinate, an important step in the biosynthesis of taurine.[202] A variety of plausible mechanisms for this conversion have been described, all of which involve binding of the Cys thiolate to Fe(II)CDO[203] followed by oxidation of the thiolate to sulfinate by some as yet unidentified Fe–O_2 derived oxidant.[204] Finally, the hydrolytic enzyme nitrile hydratase contains a nonheme iron(III) (or occasionally cobalt(III)) center with Cys-derived thiolate, sulfenate, and sulfinate ligands.[197] This novel active site is believed to arise from post-translational oxidation of Cys thiolate residues, possibly via a metal-assisted oxidation pathway, although details of the conversion remain scarce. It is apparent that an understanding of the factors that control sulfur oxidation at heme and nonheme iron sites is of considerable interest given the role that thiolate moieties appear to play in directing O_2 activation and in turn potentially being the target of oxidation. This is reflected by the numerous studies of thiolate oxidation to oxidized sulfur species in nickel, iron, and cobalt model complexes. [197,205,206]

Several years ago, Bukowski *et al.* described the generation and characterization of a thiolate-ligated oxoiron(IV) complex using a nonheme macrocyclic tetramethylcyclam ligand that models the high-valent oxoiron oxidants (compounds I and II) proposed for both P450 and CPO.[178] This species was generated by treatment of the Fe(II) precursor, $[Fe^{II}(TMCS)](PF_6)$ (**1**) with the peracid *m*-chloroperoxybenzoic acid (*m*-CPBA) in the presence of base to afford $[Fe^{IV}(O)(TMCS)]^+$ (**2**) (Scheme 5.1). A combination of mass spectrometry, Mössbauer, and X-ray absorption spectroscopic studies indicated that **2** contained an iron(IV) center with a relatively long Fe=O bond of 1.70 Å and a thiolate sulfur that had not been oxidized—the oxidation process appeared to be exclusively metal-centered.

Subsequent studies revealed that treatment of **1** with *m*-CBPA in the *absence* of base afforded a new iron(IV) center having Mössbauer parameters distinct from those of **2**, and moreover that more than one equivalent of oxidant was needed to generate this new species (Scheme 5.1).[91] Specifically, addition of either 1 or 2 equivalents of *m*-CPBA to **1** resulted in generation of a new Fe(II) species, **3**, exhibiting Mössbauer parameters (δ = 1.06 mm/s, ΔE_Q = 3.77 mm/s) different from those of **1** (δ = 0.90 mm/s, ΔE_Q = 3.06 mm/s). Mass spectrometry studies of **3** revealed isotope patterns indicative of the addition of 2 oxygen atoms to **1**, suggesting oxidation of the thiolate sulfur to a sulfinate ($-SO_2$) had occurred and leading to the formulation of **3** as $[Fe^{II}(TMCSO_2)]^+$. Addition of a third equivalent of *m*-CPBA to **3** resulted in development of near-IR features in the electronic absorption spectrum that have been shown to be characteristic of oxoiron(IV) centers.[172,207,208] Mössbauer studies revealed that the oxidation in this step was exclusively metal centered (δ = 0.19 mm/s, ΔE_Q = 1.28 mm/s), with mass

spectrometry studies suggesting that this new oxoiron(IV) species can be formulated as $[Fe^{IV}(O)(TMCSO_2]^+$, (**4**) and resonance Raman studies providing evidence for an Fe(IV)=O moiety. Table 5.1 summarizes available physical data for **1**, **3**, and **4** in comparison with previously published values for **2**.

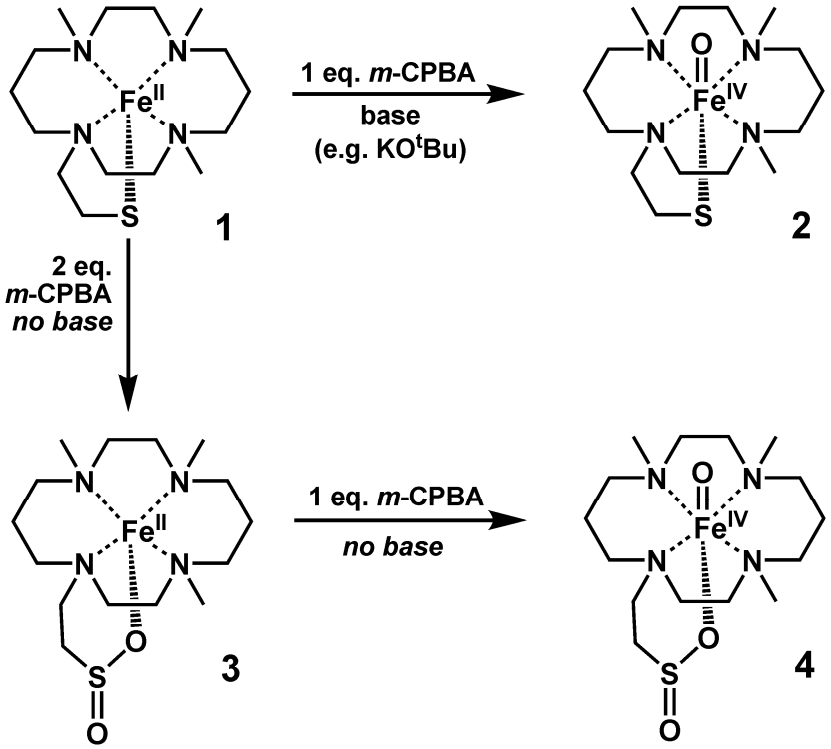

Scheme 5.1. Reactions of **1** with *m*-CPBA.

Table 5.1. Physical Properties of **1** – **5**.[a]

Species	λ_{max} (nm) (ε ($M^{-1}cm^{-1}$))	δ (mm/s)	ΔE_Q (mm/s)	$\nu_{Fe=O}$ (cm^{-1})
1	320 (1500)	0.90	3.06	-
2	460 (1300), 570 (1200), 860 (200), 990 (150)	0.18	0.21	n.d.
3	280 (3000)	1.01	3.77	-
4	830 (170), 990 (170)	0.19	1.28	834
5	n.d.	1.13	3.92	-

[a] δ is the Mössbauer isomer shift, while ΔE_Q is the Mössbauer quadrupole splitting parameter. No ν(Fe=O) vibration has been detected for **2** to date by any vibrational technique. All data is from reference 91, except that for **2**, which is from reference 209.

In order to understand changes in the iron environment inferred from our spectroscopic measurements during the oxidation process, we were interested in obtaining structural parameters for the new species generated in this work. **3** and **4** did not prove amenable to crystallization and structural characterization by X-ray diffraction methods, and we therefore turned to extended X-ray absorption fine structure (EXAFS) analysis to provide metrical details of the iron coordination environment in these complexes. We present details of a complete X-ray absorption characterization of **1**, **3**, and **4**, as well as $[Fe^{II}(TMC)(O_2SPh)](O_2SPh)$ (**5**), an independently synthesized Fe(II)-sulfinate complex.

5.2 Experimental

5.2.1 XAS Sample Preparation

[Fe^{II}(TMCS)](PF_6), 1. A 40 mM solution of **1** was prepared in anhydrous, degassed MeCN in an anaerobic chamber, transferred to a sample cell wrapped in Kapton tape, and frozen immediately in liquid nitrogen.

[Fe^{II}($TMCSO_2$)]$^+$, 3. A 14 mM MeOH solution of **1** was treated with two equivalents of 3-chloroperoxybenzoic acid (*m*-CPBA), transferred to a tandem Mössbauer/XAS cup, and frozen in liquid nitrogen. Mössbauer analysis showed that the sample contained 75% **3**, 14% of an unidentified Fe(III) species, and 11% of an Fe(IV) species.

[Fe^{IV}(O)($TMCSO_2$)]$^+$, 4. An 8 mM MeCN solution of **1** was treated with three equiv. of *m*-CPBA, with an 80% yield of **4** measured by UV/Vis spectroscopy.

[Fe^{II}(TMC)(O_2SPh)](O_2SPh), 5. A 30 mM solution of 5 was prepared in anhydrous, degassed THF in an anaerobic chamber, transferred to a sample cell wrapped in Kapton tape, and frozen immediately in liquid nitrogen.

5.2.2 X-ray Absorption Spectroscopy. Data Collection.

X-ray absorption data for **3** was collected on beamline X9B of the National Synchrotron Light Source (NSLS) at Brookhaven National Laboratory, with storage ring conditions of 2.8 GeV and 100 – 300 mA, while data for **1**, **4**, and **5** were collected on beamline 7-3 of the Stanford Synchrotron Radiation Light source (SSRL) of SLAC National Accelerator Laboratory with storage ring conditions of 3.0 GeV and 80 – 100 mA. At NSLS, Fe K-edge XAS data were collected for a frozen solution of **3** (in MeOH, 6 complete scans) maintained at ca. 15 K over an energy range of 6.9 – 8.0 keV using a Si(111) double crystal monochromator for energy selection and a Displex closed cycle cryostat for

temperature control. A bent focusing mirror was used for harmonic rejection. At SSRL, Fe K-edge XAS data were collected for frozen solutions of **1**, **4**, and **5** maintained at a temperature of *ca.* 10 K over an energy range of 6.9 – 8.0 keV using a Si(220) double crystal monochromator for energy selection and an Oxford Instruments CF1208 continuous flow liquid helium cryostat for temperature control. Harmonic rejection was achieved by a 9 keV cutoff filter. Data were obtained as fluorescence excitation spectra with either a 13 element (NSLS) or 30 element (SSRL) solid-state germanium detector array (Canberra). An iron foil spectrum was recorded concomitantly for internal energy calibration and the first inflection point of the K-edge was assigned to 7112.0 eV.

5.2.3 Data Analysis.

Data reduction, averaging, and normalization were performed using the program EXAFSPAK.[130] Following calibration and averaging of the data, background absorption was removed by fitting a Gaussian function to the pre-edge region and then subtracting this function from the entire spectrum. A three-segment spline with fourth order components was then fit to the EXAFS region of the spectrum in order to extract $\chi(k)$. Analysis of the pre-edge features was carried out with the program SSExafs[132] using a previously described protocol.[133] Theoretical phase and amplitude parameters for a given absorber-scatterer pair were calculated using FEFF 8.40 at the single-scattering level of theory, and were utilized by the opt program of the EXAFSPAK package during curve-fitting. Parameters for **1** were calculated using the coordinates of the reported crystal structure.[210] Parameters for **3** were calculated for a modification of the starting complex structure in which an O-bound sulfinate was introduced, such that the Fe•••S distance was increased to 3.3 Å from the 2.3 Å distance in **1** and an O atom bound to the

sulfur was placed at a distance of 2.0 Å from the Fe center. The Fe–O–S bond angle was ~130°. These parameters are consistent with other iron-sulfinate moieties that have been described in the literature.[211-213] Parameters for **4** were calculated for a modification of the DFT structure published for **2**[178] in which an O-bound sulfinate was introduced, such that the Fe•••S distance was increased to 3.3 Å and an O atom bound to the sulfur was placed at a distance of 2.0 Å from the Fe center. The Fe–O–S bond angle was ~130°. The Fe=O bond length was adjusted to 1.64 Å. A path for a Fe–S interaction at 2.3 Å (as seen in the crystal structure of **1** and the EXAFS analysis of **2**) was also considered in order to test a wider range of possible Fe•••S distances. Finally, parameters for **5** were calculated using the coordinates of the crystal structure reported for this species. Structures of the models for **3**, **4**, and **5** are shown in Scheme 5.2. In all analyses, the coordination number of a given shell was a fixed parameter, and was varied iteratively while bond lengths (r) and Debye-Waller factors (σ^2) were allowed to freely float. The amplitude reduction factor S_0 was fixed at 0.9, while the edge shift parameter E_0 was allowed to float as a single value for all shells (thus in any given fit, the number of floating parameters = (2 × num shells) + 1). The goodness of fit, F (or F-factor) was defined as $[\Sigma k^6(\chi_{exptl}-\chi_{calc})^2 / \Sigma k^6 \chi_{exptl}^2]^{1/2}$.

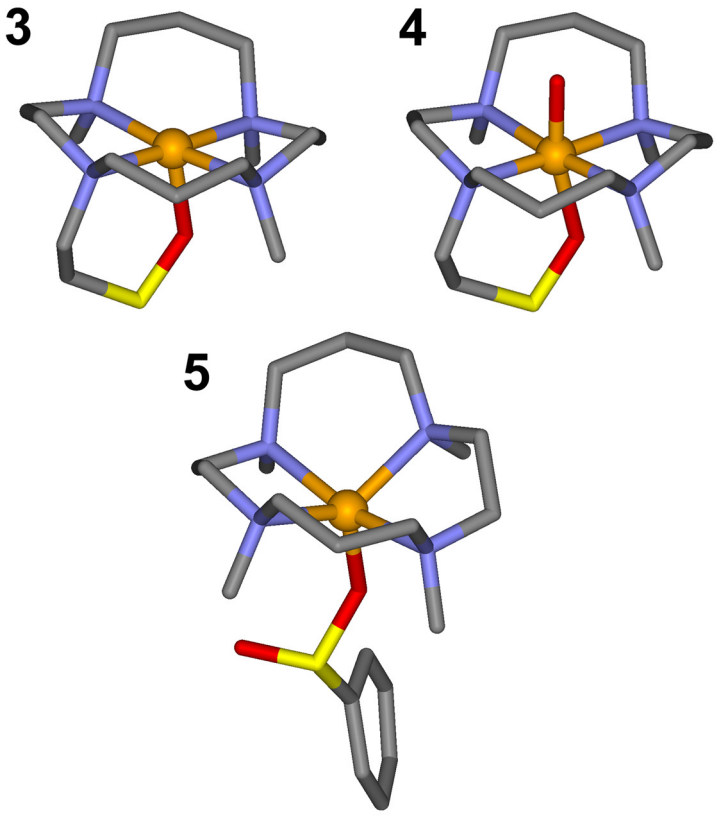

Scheme 5.2. FEFF input models for **3**, **4**, and **5**. The structures were generated using ChemBio 3D Ultra 11.0 (Cambridgesoft) and Accelrys DS Visualizer 2.5 (Accelrys Software Inc.). The central iron atom is shown as an orange sphere, while other atoms are shown as sticks (carbon = grey, nitrogen = blue, oxygen = red, sulfur = yellow). The structure of **5** is described in reference 91.

5.3 Results

5.3.1 XANES

The Fe(II) complexes **1**, **3**, and **5** exhibit edge and pre-edge X-ray absorption properties typical of high-spin Fe(II) complexes (Figure 5.1). The first inflection point of the rising edge, tabulated in Table 5.2, ranges from 7122.35 eV for **1** to 7123.10 eV for **5**. The modest differences in edge energy can be attributed to variation in the effective nuclear charge on the Fe(II) center, as would be expected given the highly basic thiolate ligated to **1** and the more weakly basic sulfinates bound to **3** and **5**. All three complexes exhibit a moderately intense pre-edge transition centered at *ca.* 7112.5 eV, a value typical of Fe(II) complexes.[214] Both the thiolate-containing complex **1** and the sulfinate-containing complex **5** exhibit a splitting of 1.8 – 1.9 eV in the pre-edge feature, with the peak at higher energy being the less intense of the two, and integrated pre-edge intensities of 17.5 and 9.8 units, respectively. Conversely, **3** exhibits a more symmetric pre-edge feature with a total intensity of 13.4 units. There is some indication of a shoulder on the high energy face of the pre-edge peak, but it was not possible to accurately fit this feature. This observation likely reflects the lower resolution of the Si(111) crystal monochromator used at NSLS X9B to measure data for **3**, in comparison with the Si(220) monochromator in use at SSRL 7-3, where XAS data for **1** and **5** were measured. Similar observations have been made in earlier XAS studies of methane monooxygenase.[215] Our observations are consistent with studies of other high spin square pyramidal Fe(II) complexes of the form $[Fe^{II}(TMC)(X)]^{2+/+}$, where X = N_3^-, Cl^-, Br^-, or CH_3CN, all of which exhibited a pre-edge feature containing two peaks split by 1.8 – 2.0 eV and a total intensity of 11 – 13.4 units.[214] Although **1** does exhibit an unusually high total pre-edge

intensity for a 5-coordinate complex, the splitting of 1.8 eV is in line with the 5-coordinate site observed via X-ray crystallography and MCD.[210]

The Fe(IV) complex **4**, on the other hand, exhibits a substantial blue-shift of greater than 2 eV in the rising K-edge relative to **1** and **3**, with an edge inflection at 7125.66 eV. This is consistent with the metal-centered oxidation observed by Mössbauer spectroscopy for this species, and is at the upper end of the range of values measured for other trans substituted oxoiron(IV) complexes using the TMC ligand, which range from 7124.0 eV for $[Fe^{IV}(O)(TMC)(O_2CCF_3)]^+$ to 7125.4 eV for $[Fe^{IV}(O)(TMC)(NCS)]^+$.[177] The pre-edge transition of **4** also exhibits a blue-shift of *ca.* 1.5 eV relative to the Fe(II) precursors **1** and **3**, and can be simulated as a single Gaussian having a normalized area of 24.9 units. Weighting of this area for the composition of the sample (80% in Fe(IV)) gives a weighted pre-edge area of 31 units, a value that is considerably larger than the area of 20 units obtained for the thiolate-ligated Fe(IV) complex **2**.[178] The pre-edge intensity of **4** is more comparable to those of *trans*-substituted oxoiron(IV) complexes with weakly basic ligands such as $^-O_2CCF_3$ (38.6 units) or NCMe (32.8 units).[177] This observation is consistent with the large ΔE_Q value obtained for **4**, reflecting extensive distortion in the electronic environment of the Fe(IV) center.

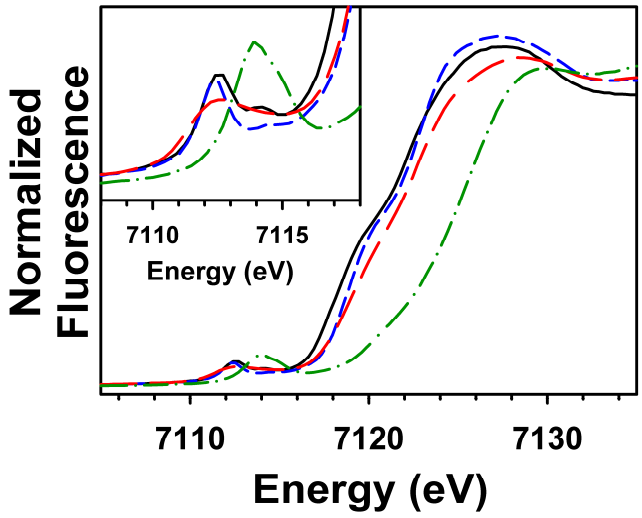

Figure 5.1. Comparison of the Fe K-edge X-ray absorption edge and pre-edge (inset) features of species **1** (black, ——), **3** (red, — — —), **4** (green, –·–·–), and **5** (blue, – – –).

Table 5.2. Pre-edge Analysis Parameters for **1**, **3**, **4**, and **5**.[a]

Species	E_{edge} *(eV)*	$E_{preedge}$ *(eV)*	*height*	*width*	*area*
1	7122.35	7112.52(3) 7114.35(6)	0.069(1) 0.027(2)	1.86(7) 1.25(12)	13.6(5) 3.6(5)
3[b,c]	7123.03	7112.59(2)	0.043(2)	2.93(9)	13.4(9)
4[b]	7125.66	7114.08(1)	0.0932(7)	2.508(23)	24.9(2)
5	7123.10	7112.36(1) 7114.25(7)	0.0550(9) 0.0098(8)	1.42(3) 1.44(19)	8.3(2) 1.5(2)

[a] The fits presented are those that give the best agreement to the experimental data and its second derivative. Values in parentheses represent uncertainties in the final digit of that parameter.
[b] The XAS sample of **3** was shown by Mössbauer analysis to contain 75% **3**, 11% **4**, and 14% of an unidentified Fe(III) species. The XAS sample of **4** was 80% in **4**, based on UV/Vis spectroscopy. The peak areas given have not been weighted for the purity of the respective samples.
[c] There is evidence for a very weak shoulder in the pre-edge feature of **3**. However we were not able to accurately model this shoulder peak with our analysis protocol.

5.3.2 EXAFS.

We next turned to EXAFS analysis to develop an understanding of the structural changes occurring at the Fe site during treatment of **1** with oxidants. **1** exhibits $k^3\chi(k)$ EXAFS oscillations which exhibit unchanged amplitude over the energy range collected (Figure 5.2), while the Fourier transform of this data affords a spectrum in *r*-space consisting of an intense feature at *r'* = 1.9 Å associated with the donor atoms of the TMCS ligand and considerably weaker features spread over *r'* = 2.3 – 3.2 Å that can be assigned to outer-shell scattering from carbon atoms (Figure 5.3). **3**, on the other hand, exhibits a considerable diminution of EXAFS amplitude compared to **1**, particularly for $k > 4$ Å^{-1}. Similarly, the Fourier transform of **3** is considerably more complex, and the magnitude of the most intense feature is only half that of **1**. This presumably reflects a considerably different arrangement of atoms in **3** that results in significant destructive interference between shells of scattering atoms and a consequent decrease in EXAFS intensity. **5** exhibits EXAFS and FT spectra that are nearly identical in appearance to those of **3**, suggesting that it is indeed an excellent structural model for **3** (*vide infra*). Finally, **4** exhibits moderately intense $k^3\chi(k)$ EXAFS in which the phase of the modulations has lengthened relative to the precursors **1** and **3**. This observation is indicative of a shortening in the iron-ligand bond lengths that dominate the EXAFS, and has been observed in previous studies of mononuclear oxoiron(IV) species.[133,216] This is readily apparent in the Fourier transform of **4**, in which the most intense feature has broadened slightly and shifted to *r'* = 1.6 Å. The weak features associated with outer-shell carbon scatterers have also downshifted to r' ~ 2.4 Å. This shift is consistent with the shortening of bond lengths that would be expected in the low spin Fe(IV) complex **4**, relative to its

high-spin Fe(II) precursors **1** and **3**. The $k^3\chi(k)$ EXAFS and its Fourier transform for **4** are similar to appearance to those obtained for other *trans*-substituted $[Fe^{IV}(O)(TMC)(X)]^{2+/+}$ complexes by Jackson *et al.*[177]

Analysis of the EXAFS data for an acetonitrile solution of **1** demonstrates that the structure obtained in the solid state using X-ray crystallography is retained in solution (Table 5.3, Figure 5.4). The inner shell can be modeled with 4 Fe–N at 2.19 Å and 1 Fe–S at 2.29 Å, values which are identical, within the error of ±0.02 Å associated with metal-ligand distances measured by EXAFS,[88,89] to the crystallographic values of $Fe–N_{ave}$ = 2.201 Å and Fe–S = 2.297 Å.[210] The Fe–N and Fe–S shells may be added in either order and fit quality improves significantly with the addition of the second shell, indicating that each shell is an integral component of the fit. Attempts to fit the outer shell with a single shell of Fe•••C scatterers at 3.07 Å afforded moderate improvements in goodness-of-fit (fits 9-13, Table 5.3), but the magnitude of the Debye-Waller factor associated with the Fe•••C shell is quite large and both the $k^3\chi(k)$ EXAFS and Fourier transform are not adequately modeled using this simple three shell fit (Fit 11, Figure 5.4). Attempts to split this shell into two sub-shells of Fe•••C scatterers resulted in insignificant improvement in fit quality (fits 14-17, Table 5.3). Conversely, addition of a shell of carbon scatterers at *ca.* 3.5 Å gave a more tangible improvement in fit quality, though again the visual agreement with experimental data is less satisfactory (fit 19, Figure 5.4). The best fits are obtained for a combination of 3 distinct sets of Fe•••C scatterers at 2.99 Å, 3.16 Å, and 3.54 Å, exemplified by fit 22 in Table 5.3. The shorter distances are readily assigned to carbons of the ethylene linkers as well as the methyl carbons which are distributed over a range of distances between 2.8 Å and 3.1 Å, while the longest distance is associated with

the most distant carbons on the propylene linkers. This combination is necessary to accurately fit the weak bump at $k = 5$ Å^{-1} in the EXAFS, and the significant improvement in the fit quality metric F to 0.312 compared to the F values of ~0.39 obtained for fits with a single shell of carbon scatterers (*e.g.* fit 11) indicates that the complexity of these five shell best fits is justified. The relatively small Debye-Waller factors associated with the two shorter Fe•••C shells can be attributed to destructive interference between the two shells.

We next turned to analysis of **3**, bearing in mind the results of mass spectrometry experiments that suggested oxidation of the thiolate sulfer of **1** to a sulfinate. Fits of the inner shell to a single set of Fe–N scatterers resulted in unreasonably large σ^2 values (fits 1-4, Table 5.4), suggesting the presence of iron ligands at a distinctly different distance from the refined value of 2.2 Å. Indeed, addition of a shell for a single Fe–O scatterer results in a significant improvement in fit quality and chemically reasonable Debye-Waller factors for both shells of first coordination sphere atoms. The best fits of the inner shell are obtained for 3 Fe–N at 2.19 Å and 1 Fe–O at *ca.* 1.97 Å (fit 5, Table 5.4). The total coordination number is underestimated, which may reflect either a relatively large distribution of bond lengths for the equatorial nitrogens of the TMCS ligand, or else destructive interference by other components of the comparatively heterogeneous sample of **3** examined here. Addition of a sulfur scatterer results in significant improvement in fit quality and a refined Fe•••S distance of 3.27 Å. The remainder of the EXAFS can be simulated nicely with a set of 4-5 Fe•••C scatterers at 2.97 Å. The Fe•••S and Fe•••C shells can be added in either order to arrive at the same best fit, and both components are necessary for a good fit to the data, as demonstrated by a visual comparison of fits 9 and

15 (Figure 5.5) with the best fit, fit 11. Indeed, it was possible to start fits with the Fe•••S scatterer at 3.27 Å and add the other three shells sequentially (fits 19-22, Table 5.4), demonstrating that the sulfur scatterer at this distance is an integral component of the fit. We were not able to fit Fe–S interactions at the shorter distances that would be expected for either a bound thiolate or an S-bound sulfinate ligand. The EXAFS analysis therefore supports the presence of an O-bound sulfinate moiety composed of the 1.95 Å Fe–O and 3.27 Å Fe•••S scatterers observed in our fits.

In order to test the validity of our fitting model for **3**, we carried out an EXAFS analysis of the structurally characterized complex **5**, which contains an O-bound sulfinate with Fe–O = 1.995 Å and Fe•••S = 3.175 Å. As might be expected from the similarities in the EXAFS of **3** and **5**, the analysis of **5** proceeded in a similar fashion. Fits to a single shell of Fe–N scatterers at ~2.2 Å gave large Debye-Waller factors indicative of substantial static disorder in the bond lengths in the inner shell. Indeed, as with **3**, introduction of a short Fe–O scatterer significantly improved fit quality, with the best fit to the inner shell consisting of 4 Fe–N at 2.20 Å and 1 Fe–O at 1.96 Å (fit 6, Table 5.5). While the Fe–N distance is consistent with the crystallographic value of 2.21 Å obtained for $Fe–N_{ave}$, the Fe–O distance is shorter than the bond length of 1.995 Å obtained for $Fe–O_{sulfinate}$ in the X-ray crystal structure of **5**. Similarly, fits of the outer-shell features revealed an unexpectedly longer Fe•••S distance of 3.28 Å, compared to the crystallographic distance of 3.175 Å. The fit can be completed with a shell of 4-5 Fe•••C scatterers centered at 2.99 Å assignable to carbons of the TMC macrocycle. As was the case for **3**, the Fe•••S and Fe•••C shells can be added in either order (fits 8-11 and 12-17 in Table 5.5), and the fit can be initiated from the Fe•••S shell (fits 18-22, Table 5.5),

indicating that this is a required component of the fit. Furthermore, fits in which the outer shell features are simulated with two shells of carbon scatterers give a significantly poorer fit quality and worse agreement to the experimental data (fit 23, Figure 5.6). We were unable to fit the Fe•••S distance to values other than the refined distance of 3.28 Å, including the crystallographic value of 3.175 Å. The EXAFS analysis of **5** thus supports the retention in solution of the sulfinate moiety observed by X-ray crystallography, and importantly provides strong support for the presence of an O-bound sulfinate in the structure of **3** that we have advanced. The discrepancy in Fe–O and Fe•••S distances obtained from X-ray crystallography and EXAFS analysis for **5** suggests a change in sulfinate binding geometry occurs in solution, but we are unable to advance a rational explanation for why this occurs.

Having established structures for the several Fe(II) species examined in this study, we next analyzed the EXAFS of the oxoiron(IV) complex **4**. The EXAFS analysis of **4** is quite similar to those reported by Jackson *et al.*, for other trans substituted oxoiron(IV) complexes with the TMC ligand,[177] consistent with the similarities in the EXAFS and Fourier transform noted previously. The inner shell can be fit to a shell of 5 Fe–N at 2.07 Å and a single short Fe–O scatterer, assignable to an oxo moiety, at 1.64 Å, the addition of which affords a substantial improvement in fit quality (fit 8, Table 5.6). Numerous attempts were made to split the primary Fe–N shell in order to ascertain whether an O-bound sulfinate was present, as we anticipated based on the structure of **3** and the mass spectrometry and Mössbauer properties of **4**. While it was possible to fit a putative Fe–$O_{sulfinate}$ interaction at *ca.* 1.95 Å, the refined bond length was fairly variable, and the fit quality either worsened or improved insignificantly (fits 9-15, Table 5.6), suggesting that

this shell was not a required component of the fit. This contrasts strongly with results for both **3** and **5**, where addition of this shell led to profound improvements in fit quality. The outer shell features can be adequately simulated with a single shell of 4 Fe•••C scatterers at 2.96 Å (fit 17, Table 5.6). Attempts to fit multiple Fe•••C shells did not afford appreciable improvements in fit quality. More importantly, it was not possible to fit an Fe•••S interaction at any distance as part of our EXAFS refinement of **4**. The weakness of the outer-shell features and their similarity to those of other $[Fe^{IV}(O)(TMC)(X)]^{2+/+}$ complexes that lack a heavy atom scatterer (*e.g.* X = NCMe, NCO^-, or OH^-) strongly suggests that a Fe•••S interaction does not contribute significantly to the EXAFS of **4**. Coupling this observation to the absence of the well-defined Fe–O interaction at *ca.* 1.9 Å that would be expected for an O-bound sulfinate forces us to conclude that our EXAFS analysis of **4** does not provide any insight into the question of whether the sulfinate moiety binds to the Fe(IV) center of **4**. However, we do note that our EXAFS analysis provides convincing evidence for the presence of a short Fe=O interaction at 1.64 Å, supporting results from resonance Raman and Mössbauer spectroscopies that suggested that **4** was an oxoiron(IV) complex.

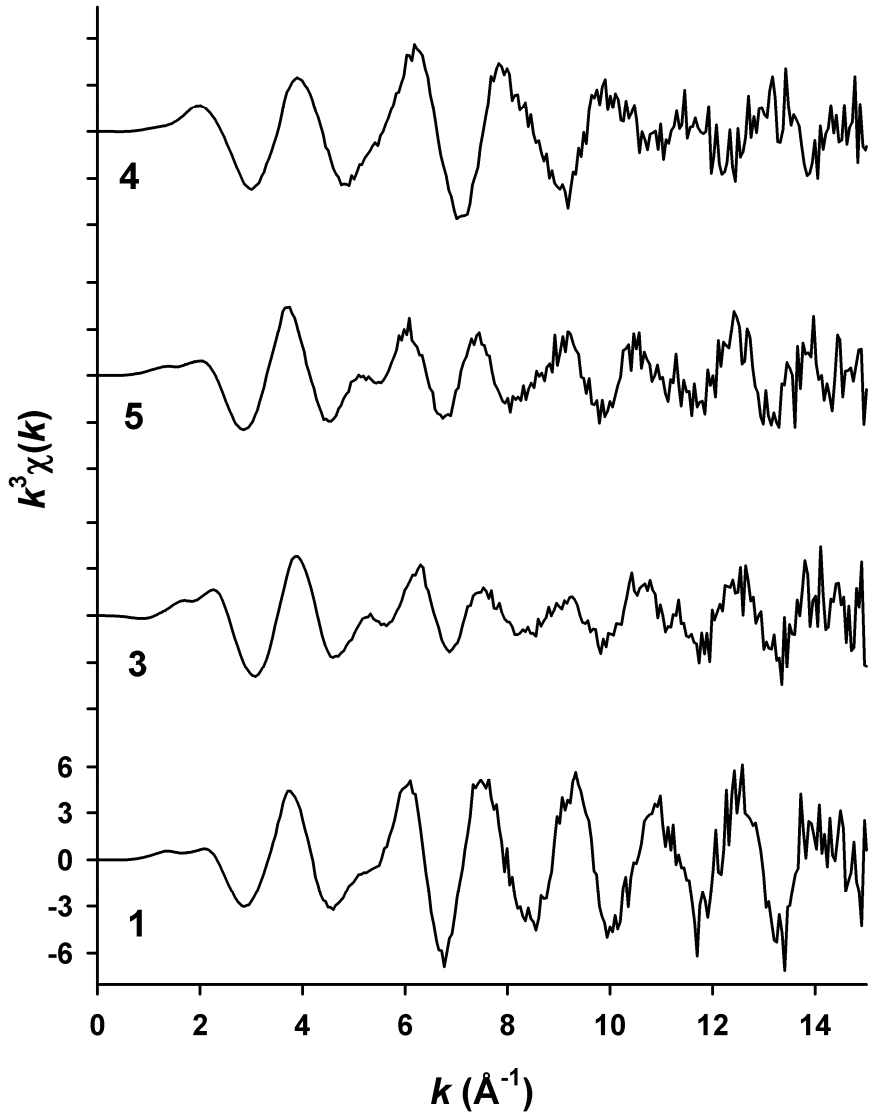

Figure 5.2. Comparison of $k^3\chi(k)$ weighted EXAFS data for **1**, **3**, **4**, and **5**. The y-axis scaling is identical for all plots.

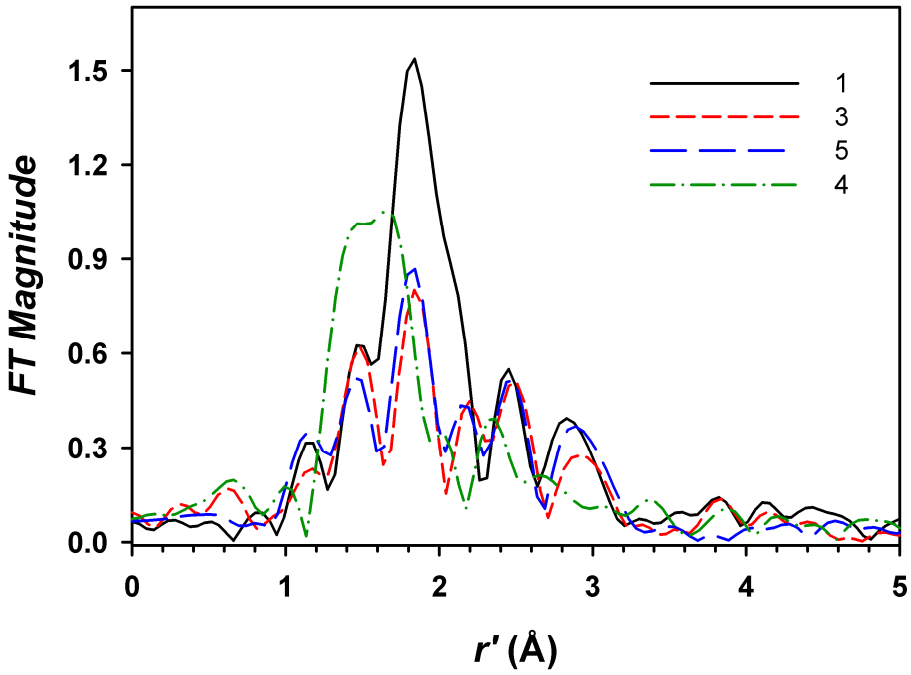

Figure 5.3. Comparison of the Fourier transforms of **1** (black, ——), **3** (red, – – –), **4** (green, –·–·–), and **5** (blue, — — —). FT ranges were as follows: **1**, $k = 2 – 15$ Å^{-1}; **3**, $k = 2 – 14.3$ Å^{-1}; **4**, $k = 2 – 14.95$ Å^{-1}; **5**, $k = 2 – 14.85$ Å^{-1}.

Table 5.3. EXAFS Fitting Results for **1**.[a]

	Fe-N/O			Fe-S			Fe•••C			
fit	n	*r*	σ^2	n	*r*	σ^2	n	*r*	σ^2	F
1	4	2.19	0.7							0.480
2	5	2.18	1.6							0.506
3	6	2.18	2.6							0.558
4	4	2.19	2.2	1	2.29	2.6				0.436
5	5	2.20	2.6	1	2.27	2.6				0.446
6				1	2.27	-0.6				0.572
7	4	2.19	2.3	1	2.29	2.4				0.436
8	5	2.20	3.5	1	2.28	1.6				0.445
9	4	2.19	2.1	1	2.29	2.6	3	3.07	7.5	0.396
10	4	2.19	2.1	1	2.29	2.6	4	3.07	8.5	0.391
11	*4*	*2.19*	*2.1*	*1*	*2.29*	*2.7*	*5*	*3.07*	*9.7*	*0.389*
12	4	2.19	2.3	1	2.29	2.4	6	3.06	10.8	0.390
13	4	2.19	2.4	1	2.29	2.3	7	3.06	11.9	0.393
14	4	2.19	2.0	1	2.28	2.3	3 3	2.99 3.14	0.9 -0.0	0.355
15	4	2.19	2.2	1	2.28	2.0	3 4	2.98 3.13	0.8 1.3	0.360
16	*4*	*2.19*	*2.0*	*1*	*2.28*	*2.7*	*4* *4*	*2.98* *3.14*	*2.1* *1.2*	*0.366*
17	4	2.19	2.0	1	2.28	2.5	4 5	2.97 3.13	2.0 2.3	0.375
18	4	2.19	2.7	1	2.29	2.0	5 4	3.07 3.55	9.8 6.4	0.357
19	*4*	*2.19*	*2.6*	*1*	*2.29*	*2.0*	*5* *6*	*3.07* *3.55*	*9.9* *8.4*	*0.354*
20	4	2.19	2.6	1	2.29	2.0	5 8	3.08 3.56	9.7 10.7	0.356
21	4	2.19	2.4	1	2.29	1.9	4 4 4	2.99 3.15 3.54	2.1 0.9 5.5	0.320
22	***4***	***2.19***	***2.2***	***1***	***2.29***	***2.2***	***4*** ***4*** ***6***	***2.99*** ***3.16*** ***3.54***	***2.3*** ***1.0*** ***8.1***	***0.312***
23	4	2.19	2.3	1	2.29	2.0	4 4 8	2.99 3.15 3.54	2.5 1.1 11.1	0.310

[a] Fourier transform range k = 2.0 – 15.0 Å^{-1} (resolution = 0.121 Å). r is in units of Å; σ^2 is in units of 10^{-3} Å^2. All fits are to unfiltered data. Goodness-of-fit parameter F defined as $[\Sigma k^6(\chi_{exptl}-\chi_{calc})^2 / \Sigma k^6 \chi_{exptl}^2]^{1/2}$.

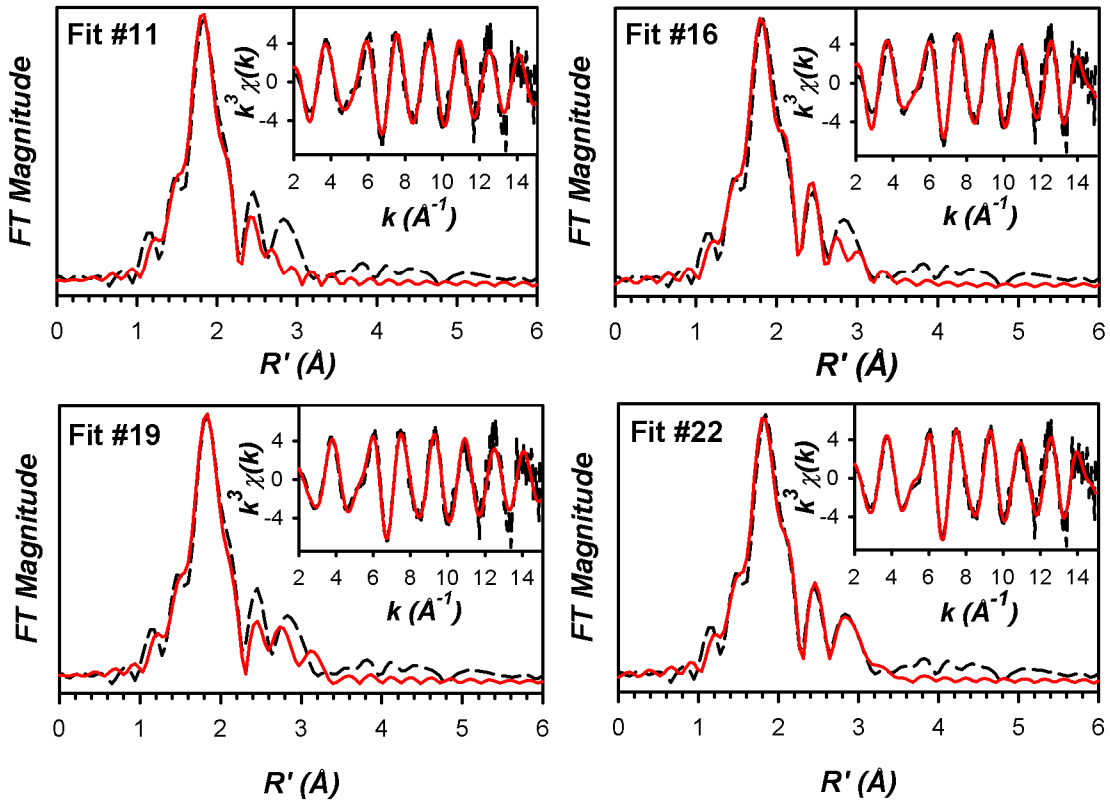

Figure 5.4. Fits to the Fourier transforms of the Fe K-edge EXAFS data ($k^3\chi(k)$) and unfiltered EXAFS spectra ($k^3\chi(k)$, inset) for **1**. Experimental data is shown with dashed lines (- - - -), while fits are shown with solid red lines (——). Fourier transformation range: k = 2 – 15 Å^{-1}. Fit parameters associated with the stated fit are shown in Table 5.3.

.

Table 5.4. EXAFS Fitting Results for **3**.[a]

	Fe-N/O			Fe-O/N			Fe•••S			Fe•••C			
fit	n	*r*	σ^2	n	*r*	σ^2	n	*r*	σ^2	n	*r*	σ^2	F
1	3	2.21	5.1										0.722
2	4	2.21	11.8										0.754
3	5	2.22	24.5										0.770
4	6	2.22	32.3										0.786
5	3	2.19	3.1	1	1.97	1.1							0.582
6	3	2.20	2.2	2	1.98	6.4							0.615
7	4	2.19	5.8	1	1.95	0.7							0.605
8	5	2.19	8.7	1	1.94	0.6							0.646
9	*3*	*2.19*	*3.3*	*1*	*1.96*	*1.2*	*1*	*3.27*	*5.5*				*0.507*
10	3	2.18	3.5	1	1.95	0.9	1	3.26	3.0	3	2.97	2.9	0.376
11	***3***	***2.18***	***3.5***	***1***	***1.95***	***0.8***	***1***	***3.27***	***2.9***	***4***	***2.97***	***4.6***	***0.378***
12	3	2.18	3.4	1	1.95	0.7	1	3.27	2.9	5	2.97	6.2	0.390
13	3	2.18	3.2	1	1.96	0.7				3	2.99	5.7	0.474
14	3	2.18	3.1	1	1.96	0.6				4	3.00	7.7	0.463
15	*3*	*2.18*	*3.2*	*1*	*1.96*	*0.6*				*5*	*3.00*	*9.5*	*0.459*
16	3	2.18	3.2	1	1.96	0.5				6	3.00	11.0	0.462
18	3	2.18	3.5	1	1.95	0.8	1	3.27	2.9	4	2.97	4.6	0.379
19							1	3.27	3.3				0.947
20	3	2.21	5.3				1	3.29	3.6				0.663
21	3	2.19	3.2	1	1.96	1.2	1	3.26	5.3				0.506
22	3	2.18	3.5	1	1.95	0.8	1	3.27	2.8	4	2.97	4.6	0.379

[a] Fourier transform range $k = 2.0 – 14.0$ Å^{-1} (resolution = 0.131 Å). *r* is in units of Å; σ^2 is in units of 10^{-3} Å^2. All fits are to unfiltered data. Goodness-of-fit parameter F defined as $[\Sigma k^6(\chi_{exptl}-\chi_{calc})^2 / \Sigma k^6 \chi_{exptl}^2]^{1/2}$.

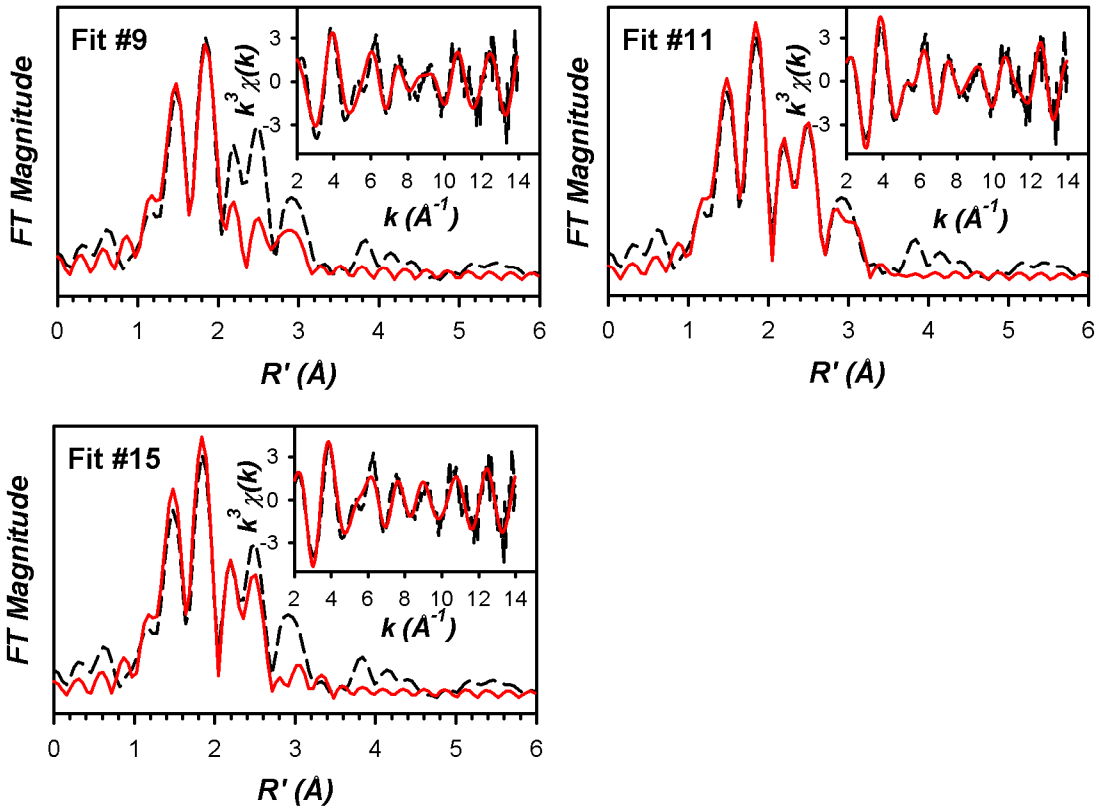

Figure 5.5. Fits to the Fourier transforms of the Fe K-edge EXAFS data ($k^3\chi(k)$) and unfiltered EXAFS spectra ($k^3\chi(k)$, inset) for **3**. Experimental data is shown with dashed lines (- - - -), while fits are shown with solid red lines (——). Fourier transformation range: k = 2 – 14 Å^{-1}. Fit parameters associated with the stated fit are shown in Table 5.4.

Table 5.5. EXAFS Fitting Results for **5**.[a]

	Fe-N/O			Fe-O/N			Fe•••S			Fe•••C			
fit	n	*r*	σ^2	n	*r*	σ^2	n	*r*	σ^2	n	*r*	σ^2	F
1	3	2.22	2.9										0.650
2	4	2.21	5.6										0.680
3	5	2.20	10.4										0.717
4	6	2.19	17.4										0.740
5	3	2.21	2.0	1	1.99	4.0							0.598
6	4	2.20	4.2	1	1.96	2.3							0.593
7	5	2.19	6.4	1	1.95	1.5							0.609
8	*4*	*2.20*	*4.4*	*1*	*1.96*	*1.9*	*1*	*3.29*	*1.4*				*0.492*
9	4	2.18	4.5	1	1.95	1.3	1	3.28	0.9	3	2.98	2.7	0.400
10	***4***	***2.18***	***4.5***	***1***	***1.95***	***1.3***	***1***	***3.28***	***0.7***	***4***	***2.99***	***4.3***	***0.402***
11	4	2.18	4.5	1	1.95	1.3	1	3.28	0.7	5	2.99	6.1	0.410
12	4	2.19	4.3	1	1.96	1.9				3	3.04	9.3	0.533
13	4	2.19	4.3	1	1.96	1.9				4	3.04	10.5	0.524
14	*4*	*2.19*	*4.3*	*1*	*1.96*	*2.0*				*5*	*3.04*	*11.8*	*0.521*
15	4	2.19	4.3	1	1.96	2.1				6	3.04	13.0	0.523
17	4	2.18	4.5	1	1.95	1.3	1	3.28	0.8	4	2.99	4.3	0.402
18							1	3.28	1.5				0.932
19							1	3.27	1.0	4	2.97	4.3	0.846
20	4	2.21	5.9				1	3.30	1.8				0.603
21	1	2.20	4.4	1	1.96	1.9	1	3.29	1.4				0.492
22	4	2.18	4.5	1	1.95	1.3	1	3.28	0.7	4	2.99	4.4	0.402
23	*4*	*2.18*	*4.7*	*1*	*1.95*	*1.7*				*4* *4*	*2.98* *3.16*	*1.6* *1.4*	*0.467*
24	4	2.18	4.6	1	1.95	1.6				4 2	3.00 3.17	2.8 -1.6	0.445
25	4	2.18	4.7	1	1.95	1.7				4 6	2.97 3.14	0.1 2.2	0.461

[a] Fourier transform range $k = 2.0 – 14.3$ Å^{-1} (resolution = 0.128 Å). *r* is in units of Å; σ^2 is in units of 10^{-3} Å^2. All fits are to unfiltered data. Goodness-of-fit parameter F defined as $[\Sigma k^6(\chi_{exptl}-\chi_{calc})^2 / \Sigma k^6 \chi_{exptl}^2]^{1/2}$

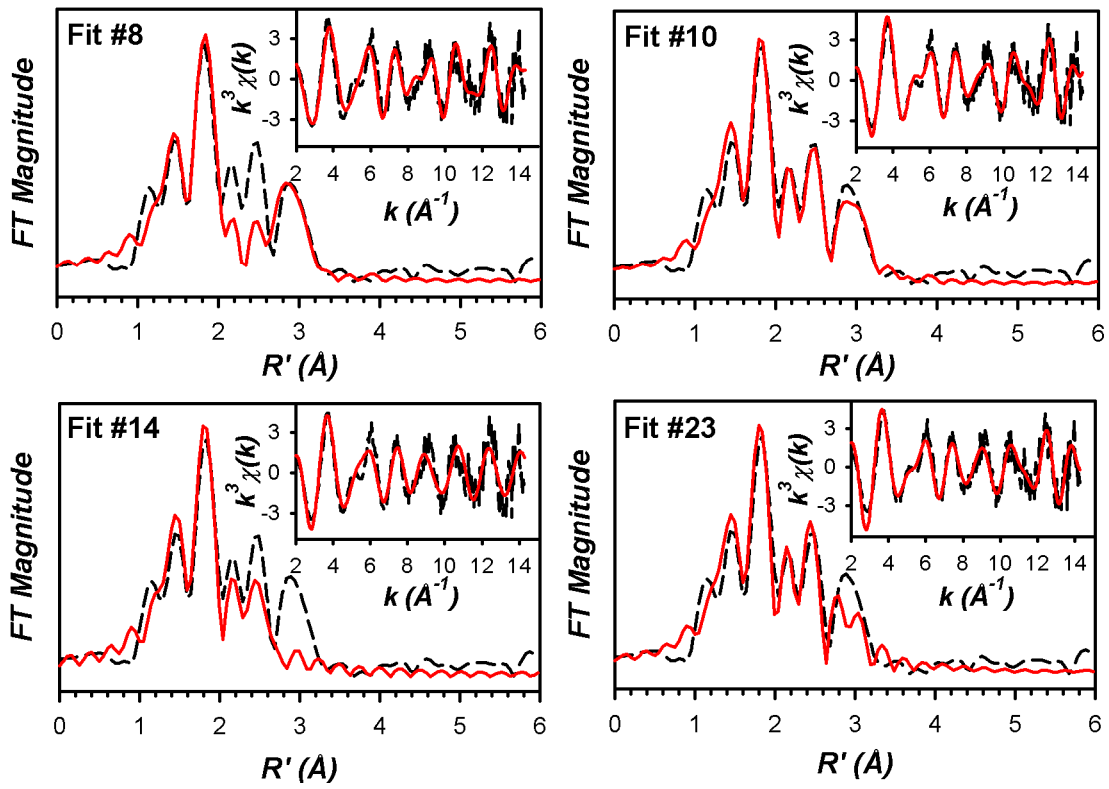

Figure 5.6. Fits to the Fourier transforms of the Fe K-edge EXAFS data ($k^3\chi(k)$) and unfiltered EXAFS spectra ($k^3\chi(k)$, inset) for **5**. Experimental data is shown with dashed lines (- - - -), while fits are shown with solid red lines (——). Fourier transformation range: $k = 2 – 14.3$ Å^{-1}. Fit parameters associated with the stated fit are shown in Table 5.5.

Table 5.6. EXAFS Fitting Results for **4**.[a]

	Fe-N/O			Fe-O/N			Fe•••C			
fit	n	*r*	σ^2	n	*r*	σ^2	n	*r*	σ^2	F
1	3	2.07	2.4							0.562
2	4	2.07	3.8							0.529
3	5	2.07	5.1							0.531
4	6	2.06	6.4							0.559
5	4	2.07	3.9	1	1.64	4.0				0.466
6	4	2.07	3.8	0.8	1.64	2.6				0.447
7	5	2.06	5.3	1	1.64	4.2				0.443
8	*5*	*2.06*	*5.2*	*0.8*	*1.64*	*2.7*				*0.430*
9	*4*	*2.08*	*2.6*	*0.8* *1*	*1.64* *1.93*	*3.60* *1.98*				*0.423*
10	3	2.09	0.7	0.8 1	1.63 1.96	3.92 -0.30				0.435
11	3	2.08	2.7	0.8 2	1.64 1.97	3.06 7.08				0.428
12	4	2.08	1.8	1	1.94	0.0				0.519
13	4	2.09	3.3	2	1.96	4.8				0.570
14	3	2.09	0.0	1	1.95	-1.4				0.499
15	3	2.10	1.2	2	1.97	2.4				0.529
16	5	2.06	5.2	0.8	1.64	2.6	3	2.96	7.5	0.407
17	***5***	***2.06***	***5.2***	***0.8***	***1.64***	***2.7***	***4***	***2.96***	***9.3***	***0.411***
18	5	2.06	5.1	0.8	1.64	2.6	5	2.96	11.3	0.419
19	5	2.06	5.1	0.8	1.64	2.6	2 3	2.87 3.01	1.7 2.4	0.407
20	5	2.06	5.1	0.8	1.64	2.5	2 2	2.88 3.02	1.2 0.1	0.399
21	5	2.06	5.2	0.8	1.63	2.6	2 4	2.85 3.00	1.5 3.6	0.418
22	5	2.06	5.2	0.8	1.63	2.6	3 3	2.87 3.02	3.9 2.5	0.417
23	*5*	*2.06*	*5.2*	*0.8*	*1.64*	*2.7*	*4* *4*	*2.98* *3.42*	*9.5* *6.4*	*0.381*
24	5	2.06	5.2	0.8	1.64	2.7	4 5	2.98 3.42	9.4 8.7	0.381
25	5	2.06	5.2	0.8	1.64	2.7	4 3	2.97 3.42	9.4 4.6	0.382

[a] Fourier transform range k = 2.0 – 14.95 Å^{-1} (resolution = 0.121 Å). r is in units of Å; σ^2 is in units of 10^{-3} Å^2. All fits are to unfiltered data. Goodness-of-fit parameter F defined as $[\Sigma k^6(\chi_{exptl}-\chi_{calc})^2 / \Sigma k^6 \chi_{exptl}^2]^{1/2}$.

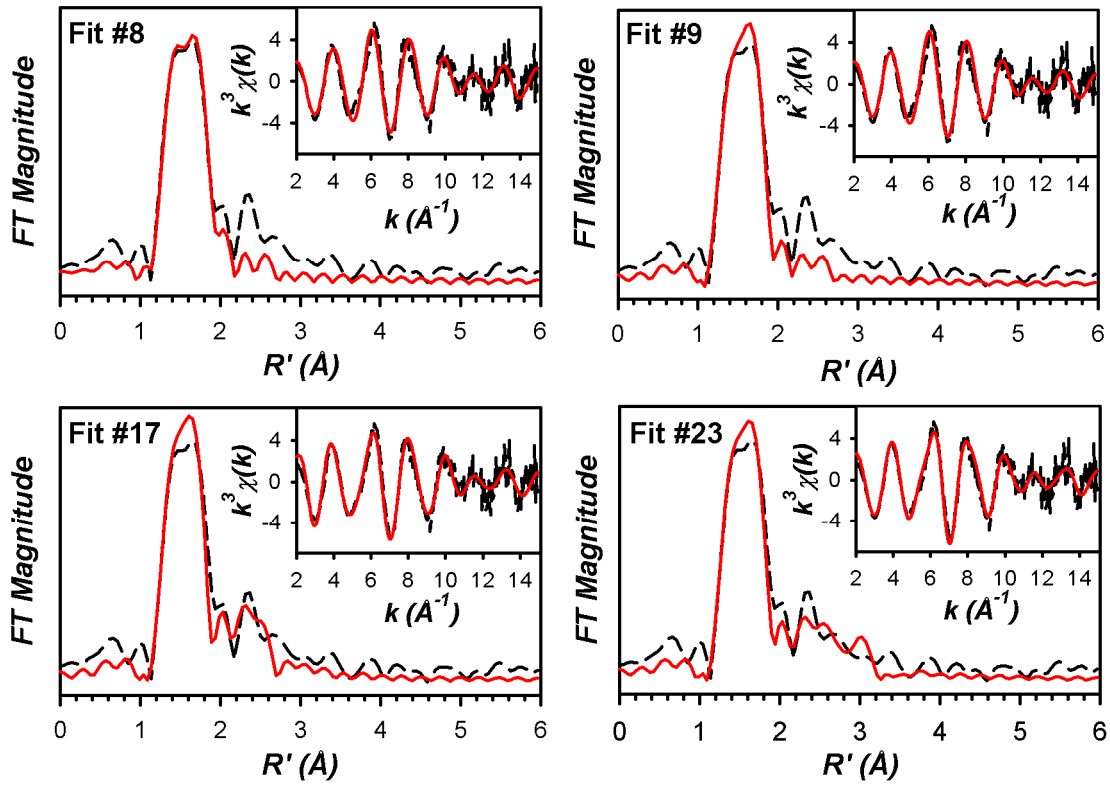

Figure 5.7. Fits to the Fourier transforms of the Fe K-edge EXAFS data ($k^3\chi(k)$) and unfiltered EXAFS spectra ($k^3\chi(k)$, inset) for **4**. Experimental data is shown with dashed lines (- - - -), while fits are shown with solid red lines (——). Fourier transformation range: $k = 2 – 14.95$ Å^{-1}. Fit parameters associated with the stated fit are shown in Table 5.6.

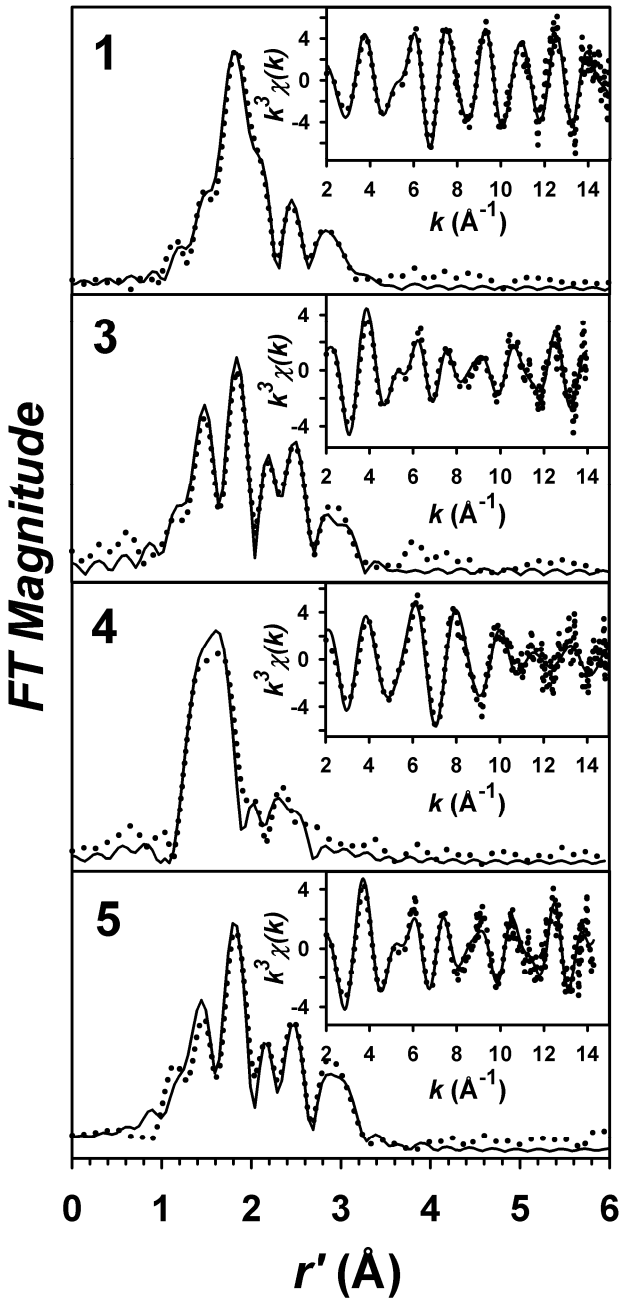

Figure 5.8. Fourier transforms of the Fe K-edge EXAFS data ($k^3\chi(k)$) and unfiltered EXAFS spectra ($k^3\chi(k)$, inset) obtained for **1**, **3**, **4**, and **5**. Experimental data is shown with dotted lines (•••••), while fits are shown with solid lines (——). Fourier transformation ranges are as follows: k = 2 – 15 Å^{-1} (**1**), k = 2 – 14 Å^{-1} (**3**), k = 2 – 14.95 Å^{-1} (**4**), k = 2 – 14.3 Å^{-1} (**5**). Fit parameters for **1**, **3**, **4**, and **5** are those shown in bold italics in Tables 5.3, 5.4, 5.6, and 5.5, respectively.

5.4 Discussion

We have described herein a comprehensive Fe K-edge X-ray absorption spectroscopy study of an iron(II)-thiolate precursor complex **1**, two novel iron(II) complexes **3** and **5**, and a new oxoiron(IV) species **4** that was derived from metal-based oxidation of **3**. EXAFS analyses of these complexes, summarized in Table 5.7, reveal that oxidation of **1** to form **3** affords changes in the EXAFS consistent with formation of a O-bound sulfinate Fe(II) complex. The remarkable similarity of the EXAFS of **3** with that of a structurally characterized iron(II)-sulfinate complex **5** lends credence to our structural hypothesis for **3**. Finally, Fe K-edge EXAFS analysis of **4** indicates the presence of a short Fe–O bond associated with an oxo moiety, but cannot clearly identify the axial ligand.

Table 5.7. Metrical Parameters for Complexes **1 – 5**.[a]

	Fe-N/O			Fe-O/N			Fe•••S			Fe•••C		
Species	**n**	**r**	**σ^2**	**n**	**r**	**σ^2**	**n**	**r**	**σ^2**	**n**	**r**	**σ^2**
										4	2.99	2.3
1 (XAS)	4	2.19	2.2				1	2.29	2.2	4	3.16	1.0
										6	3.54	8.1
1 (XRD)	4	2.201					1	2.297				
2 (XAS)	3	2.09	2.0	1	1.70	1.0	1	2.33	0.6	4	2.95	6.3
2 (DFT)	4	2.13		1	1.68		1	2.39				
3 (XAS)	3	2.18	3.5	1	1.95	0.8	1	3.27	2.9	4	2.97	4.6
4 (XAS)	5	2.06	5.2	1	1.64	2.7				4	2.96	9.3
5 (XAS)	4	2.18	4.5	1	1.95	1.3	1	3.28	0.7	4	2.99	4.3
5 (XRD)	4	2.215		1	1.996		1	3.175				

[a] *r* is in units of Å; σ^2 is in units of 10^{-3} Å^2 and is given only for EXAFS-derived structures. All EXAFS fits are to unfiltered data, except for **2**. The EXAFS fits given for **1**, **3**, **4**, and **5** are those shown in bold italics in Tables 5.3, 5.4, 5.6, and 5.5, respectively, while the EXAFS fit for **2** is from reference 178. X-ray diffraction structural parameters for **1** are from reference 210, while those of **5** were described in reference 91. The DFT structure for **2** was described in reference 178.

Our assignment of an O-bound sulfinate in **3** rests principally on two related observations from the EXAFS analysis. First, the Fe•••S distance lengthens considerably to *ca.* 3.27 Å relative to the 2.3 Å distance observed in **1**. The detection of this long Fe•••S interaction by EXAFS indicates that the sulfur must comprise part of a rigid body that remains bound to the Fe(II) center. This is coupled to the appearance of a new Fe–O interaction at *ca.* 1.95 Å, the inclusion of which is required to obtain high quality fits. In conjunction with the mass spectrometry results that show **3** contains two more oxygen atoms than **1**, it was most reasonable to hypothesize that **3** contains a sulfinate ($-SO_2$) in which an oxygen atom is bound to iron. Transition metal complexes containing an S-bound sulfinate have been extensively characterized, most notably for Ni(II), Fe(III), and Co(III),[197,205,206] but systematic studies in comparison with thiolate-containing precursors have shown that the metal-sulfur bond length is not significantly affected by sulfur oxidation to a sulfinate, and indeed tends to shorten somewhat.[205] Conversely, iron complexes containing an O-bound sulfinate ligand appear to be considerably rarer, as a search of the Cambridge Crystallographic Database reveals only three examples, all of which are Fe(III) complexes.[211-213] The structures of these three complexes are shown in Figure 5.8, and metrical parameters associated with the Fe(III) coordination environment are summarized in Table 5.8 in comparison with those of **5**, the Fe(II)-$O_{sulfinate}$ complex studied in this work. All three complexes exhibit Fe–O_1 bond lengths ranging from 1.91 Å to 2.00 Å and Fe•••S separations of 3.05 Å to 3.24 Å, similar to the Fe-O_1 and Fe•••S distances of 1.995 Å and 3.175 Å, respectively, obtained for **5** via X-ray crystallography. These values are also in agreement with the Fe–O_1 distance of 1.95 Å and Fe•••S distance of 3.27 Å obtained in our EXAFS analysis of **3**, further supporting the presence of an O-

bound sulfinate. Assuming a S–O_1 bond length of 1.53 Å (average of the four S–O_1 bond lengths given in Table 5.8), the bond angle of the Fe–O_1–S moiety in **3** would be approximately 140°, on the upper end of the reported values of 119.9° – 137.5° (Table 5.8). We suggest that the observed O-bound sulfinate in **3** is thermodynamically favored, as opposed to the more frequently observed S-bound linkage isomer, reflecting a combination of steric constraints imposed by the TMC ligand itself and the short ethylenic linker. Mascharak and co-workers have advanced a similar argument to account for the O-bound sulfinate in [Fe^{III}(PyP{S$\underline{O}_2$}$_2$)] (XICVOI in Figure 5.8).[213] Additional evidence for an O-bound sulfinate formulation for **3** is obtained from the nearly identical EXAFS spectra and analysis obtained for **5**. Indeed, it was with some consternation that we found that the distances associated with the Fe–O_1–S moiety in **5** were nearly identical to those of **3**, and clearly different from the values obtained in the crystal structure determination (Table 5.7). While the change in the Fe–O_1 bond length to 1.95 Å from the crystallographically determined 1.995 Å value is almost within the error of ±0.02 Å in bond lengths determined by EXAFS,[88,89] the shortening of this bond in conjunction with a lengthening in the Fe•••S interaction does suggest that the sulfinate binding geometry is altered in solution. No obvious explanation for this variation presents itself, though we do note that the crystal structure was obtained from crystals grown in CH_2Cl_2, whereas the EXAFS was carried out on a THF solution of **5**, with solvent perhaps playing some role in crystal packing. Similarly, it is notable that the sulfinate geometry obtained via EXAFS for **5** is quite similar to that of a reported iron(III)-heme-$O_{sulfinate}$ adduct, [Fe^{III}(tpp)(O_2SPh)] (CETWON in Figure 5.8), particularly for the putative Fe–O_1–S bond angle.[211] We emphasize that notwithstanding the apparent

structural differences for **5** in solution as indicated by our EXAFS analysis, we have shown that the ligand set observed by X-ray crystallography for **5** is retained, and that the similarity of the EXAFS features of **5** to those of **3** strongly support a $N_4O_{sulfinate}$ structure for **3**.

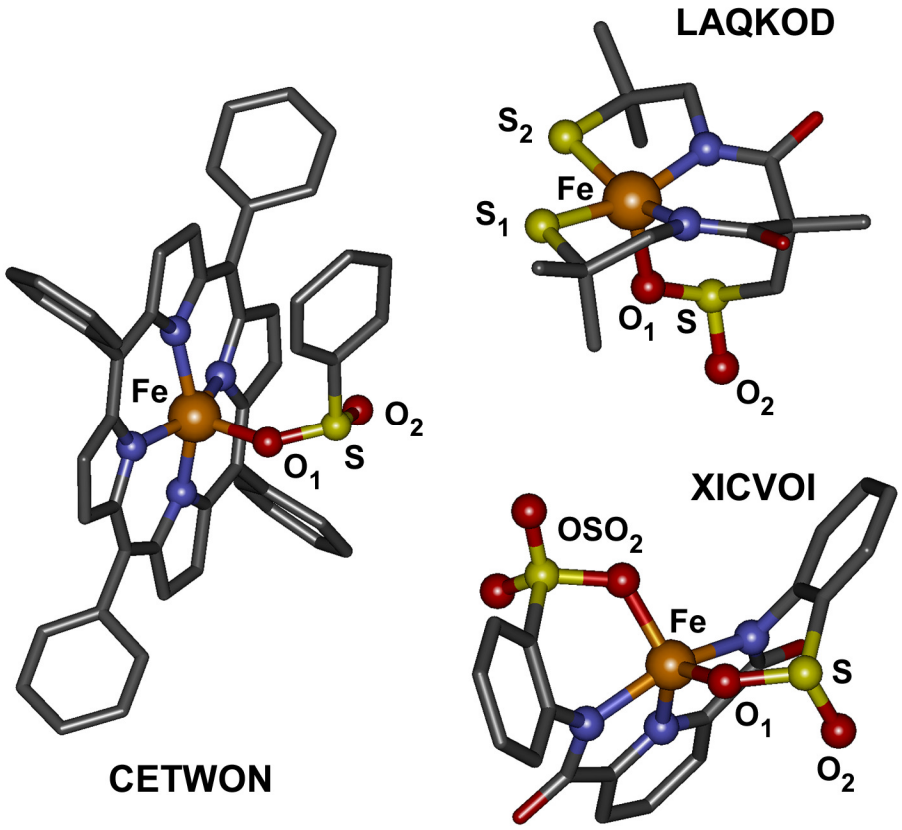

Figure 5.8. Structures of three crystallographically characterized Fe(III)-$O_{sulfinate}$ complexes. The structures were generated using the published coordinates in Accelrys DS Visualizer 2.5 (Accelrys Software Inc.). The central iron atom is shown as an orange sphere, atoms binding the iron center or associated with the sulfinate are shown as spheres, and all other atoms are shown as sticks (carbon = grey, nitrogen = blue, oxygen = red, sulfur = yellow). The labels of atoms associated with the bound sulfinate correspond to the designations given in Table 5.8. The 6 letter codes associated with each structure correspond to their accession codes in the Cambridge Crystallographic Database.

Table 5.8. Metrical Parameters for Iron Complexes Containing O-bound Sulfinates.[a]

$[Fe^{III}(tpp)(O_2SPh)]$		$Fe(III)(N_2S_2(O_2S))$		$Fe(III)(PyP\{SO_2\}_2)$[b]	
CETWON		**LAQKOD**		**XICVOI**	
$Fe\text{-}O_1$	1.924 Å	$Fe\text{-}O_1$	2.004 Å	$Fe\text{-}O_1$	1.910 Å
Fe···S	3.242 Å	Fe···S	3.046 Å	Fe···S	3.106 Å
$S\text{-}O_1$	1.553 Å	$S\text{-}O_1$	1.503 Å	$S\text{-}O_1$	1.563 Å
$S\text{-}O_2$	1.456 Å	$S\text{-}O_2$	1.477 Å	$S\text{-}O_2$	1.479 Å
$Fe\text{-}O_1\text{-}S$	137.5 °	$Fe\text{-}O_1\text{-}S$	119.9 °	$Fe\text{-}O_1\text{-}S$	126.6 °
$Fe\text{-}N_{eq1}$	2.047 Å	$Fe\text{-}S_1$	2.223 Å	$Fe\text{-}N_{eq1}$	2.020 Å
$Fe\text{-}N_{eq2}$	2.064 Å	$Fe\text{-}S_2$	2.213 Å	$Fe\text{-}N_{eq2}$	2.071 Å
$Fe\text{-}N_{eq3}$	2.056 Å	$Fe\text{-}N_{eq1}$	1.946 Å	$Fe\text{-}N_{eq3}$	2.018 Å
$Fe\text{-}N_{eq4}$	2.032 Å	$Fe\text{-}N_{eq2}$	1.957 Å	$Fe\text{-}OSO_2$	1.913 Å

$[Fe^{II}(TMC)(O_2SPh)]^+$, **5**	
$Fe\text{-}O_1$	1.995 Å
Fe···S	3.175 Å
$S\text{-}O_1$	1.515 Å
$S\text{-}O_2$	1.486 Å
$Fe\text{-}O_1\text{-}S$	129 °
$Fe\text{-}N_{eq1}$	2.231 Å
$Fe\text{-}N_{eq2}$	2.175 Å
$Fe\text{-}N_{eq3}$	2.257 Å
$Fe\text{-}N_{eq4}$	2.196 Å

[a] The 6 letter Cambridge Crystallographic Database accession codes are given for each of the three structures. The labeling scheme is that given in Figure 5.8. Data for **5** is from reference 91.
[b] This structure is described as containing two sulfinates in the original paper,[213] but the structure from the CCDC (XICVOI) reveals the presence of one sulfinate (-OSO) and one sulfonate ($-OSO_2$). The metrical parameters presented are for the sulfinate only, and not the average of both oxidized sulfur species.

XAS analysis of **4** revealed the presence of an oxo moiety at a distance of 1.64 Å from the Fe(IV) center, but we were unable to identify any contribution deriving from an O- or S-bound sulfinate adduct. This was unexpected given the ease with which we identified the sulfinate moiety in **3** and **5**, but perhaps should not have been surprising given the weakness of the outer-shell features of **4** compared with **3** and **5** (Figure 5.3). Mass spectrometry demonstrates that **4** can be formulated as $[Fe^{IV}(TMCS)(O)_3]^+$, and as one oxygen atom can be assigned to the oxo moiety that we detected by EXAFS, **4** clearly should contain a sulfinate. Similarly, vibrational spectroscopic studies on **4** reveal the presence of features associated with the symmetric and asymmetric stretching modes of a sulfinate ($\nu_s(SO_2)$ = 1003 cm^{-1}, $\nu_{as}(SO_2)$ = 1150 cm^{-1}).[91] A simple explanation for our EXAFS observations is that the Fe–O_1–S body is no longer rigid in **4**, due either to dissociation of the sulfinate ligand from the Fe(IV) center or else sampling of multiple conformations by the sulfinate, all of which would destructively interact with one another in the EXAFS, precluding their observation. Jackson *et al.* have previously reported a systematic study of a series of $[Fe^{IV}(O)(TMC)(X)]^{2+/+}$ complexes in which they noted that the quadrupole splitting (ΔE_Q) associated with the Fe(IV) center correlated roughly linearly with normalized pre-edge area and ν(Fe=O).[177] The normalized pre-edge area of 31 units and ν(Fe=O) value of 834 cm^{-1} correlate well with the ΔE_Q value of 1.28 mm s^{-1} obtained for **4** (Figure 5.9), and are consistent with a weakly basic *trans* ligand such as sulfinate, as opposed to the more basic thiolate in **2**. The sulfinate dissociation postulated previously may be accompanied by binding of solvent (MeCN) or *m*-chlorobenzoic acid, which would be obtained from heterolytic O–O bond cleavage of the *m*-CBPA oxidant as **4** is generated in solution.[91] Unfortunately, both of these possibilities are also weakly

basic ligands and would be expected to give large pre-edge areas, ν(Fe=O), and ΔE_Q values, as exemplified by the parameters obtained by Jackson *et al.* for $[Fe^{IV}(O)(TMC)(NCMe)]^{2+}$ and $[Fe^{IV}(O)(TMC)(O_2CCF_3)]^{+}$ (both of these complexes occupy the upper right quadrant in Figure 5.9),[177,208,217] and we therefore cannot glean any additional insight into the identity of the *trans* ligand in **4** from this XANES correlation. It is noteworthy that of the *trans*-substituted oxoiron(IV) complexes reported in this family, the identity of the *trans* ligand has only been uniquely identified via EXAFS analysis in two cases: a.) **2**, in which a sulfur atom was required in the fit;[178] and b.) $[Fe^{IV}(O)(TMC)(NCS)]^{+}$, in which multiple scattering interactions involving the thiocyanate ligand were clearly evident,[177] though this presumably reflects the fact that many of the *trans* ligands consist exclusively of light atoms. One attractive mechanism to further test whether sulfinate binding is detectable at an oxoiron(IV) center by Fe K-edge XAS would be to prepare the oxoiron(IV) analogue of **5**, presumably by direct oxo-atom transfer to **5** or else the ligand substitution experiments which proved fruitful in earlier studies.[177] However, neither of these approaches has succeeded to date.[91] An alternate, and perhaps more appealing, approach would involve carrying out sulfur K-edge XAS studies of **4**, in order to directly probe the sulfur oxidation state and the nature of its interaction, if any, with the iron center via both XANES and EXAFS analysis. This technique has recently proven of great utility in characterizing the mixed thiolate/sulfenate/sulfinate site of nitrile hydratase.[218] While beyond the scope of the present work, S K-edge XAS would be expected to provide a number of complementary insights into the electronic structure of the sulfinate-ligated iron complexes **3**, **4**, and **5** described herein.

In closing, we wish to emphasize that, while we were unable to specifically identify the axial ligand in **4**, our EXAFS analysis convincingly demonstrates that it is indeed an oxoiron(IV) complex that is clearly distinct from the thiolate-ligated oxoiron(IV) complex **2** based on the shorter Fe=O bond and absence of an inner-shell Fe–S bond in **4**. We have also employed XAS to provide the first structural characterization of Fe(II)-$O_{sulfinate}$ adducts (**3** and **5**) reported in the literature, leading to the identification of a spectroscopic signature for O–bound sulfinates in the Fe-K edge EXAFS spectra. In sum, this study has further fleshed out the complex landscape of iron and sulfur oxidation chemistry that can occur at an iron(II)-thiolate site in the presence of an oxidant, providing a structural basis for interpretation of similar chemistry in nonheme iron enzymes that bind protein-derived thiolates or react with thiolate-containing substrates.[119,120,197,201-204]

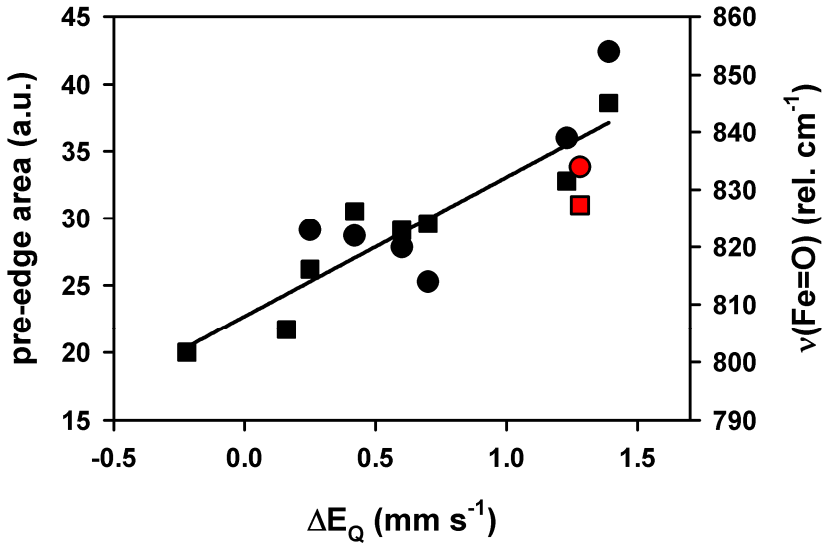

Figure 5.9. Comparision of the pre-edge area (red square) and ν(Fe=O) (cm^{-1}, red circle) of **4** with other *trans*-substituted $[Fe^{IV}(O)(TMC)(X)]^{+/2+}$ complexes described by Jackson *et al.* in reference 177 (pre-edge areas given as black squares and ν(Fe=O) as black circles).

Chapter 6.

XAS Studies of Trigonal Bipyramidal Iron Complexes, Including the First High-Spin Oxoiron(IV) Complex

Portions of this work have been previously published as:

1. Jason England, Marlène Martinho, Erik R. Farquhar, Jonathan R. Frisch, Emile L. Bominaar, Eckard Münck, and Lawrence Que, Jr. "A Synthetic High-Spin Oxoiron(IV) Complex. Generation, Spectroscopic Characterization and Reactivity." *Angew. Chem. Int. Ed.* **2009**, *48*, 3622-3626.
2. Jason England, Yisong Guo, Erik R. Farquhar, Victor J. Young, Jr., Eckard Münck, and Lawrence Que, Jr. "The Crystal Structure of a High-Spin Oxoiron(IV) Complex and Characterization of Its Self-Decay Pathway." *J. Am. Chem. Soc.* **2010**, *132*, 8635-8644..

6.1 Introduction

Recent years have seen a growing appreciation of the role of a large superfamily of mononuclear nonheme iron oxygenases in carrying out a variety of vitally important biochemical oxidative transformations.[2-4,81] By analogy to the heme paradigm, several subfamilies of these enzymes are thought to employ high-valent oxoiron species to activate the strong C–H bonds of their target substrate. In 2003, Krebs, Bollinger, and coworkers obtained the first direct evidence for a mononuclear nonheme oxoiron(IV) oxidant in their studies of the α-ketoglutarate (αKG) dependent enzyme taurine/aKG dioxygenase (TauD),[11] and they have subsequently isolated and characterized additional examples for prolyl 4-hydroxylase,[18] the αKG-dependent halogenases CytC3[20] and SyrB2,[21] and the pterin-dependent oxygenase tyrosine hydroxlase.[23] Concurrent with the TauD discovery, Que and coworkers reported the spectroscopic and crystallographic characterization of the first nonheme oxoiron(IV) model complex, $[Fe^{IV}(O)(TMC)(NCMe)]^{2+}$ (**1**, TMC = 1,4,8,11-tetramethyl-1,4,8,11-tetraazacyclododecane),[173] igniting a veritable explosion in the number of isolated and characterized oxoiron(IV) model complexes over the past several years.[172] However, nearly all oxoiron model complexes isolated to date have been found to contain low spin $S = 1$ oxoiron(IV) centers, while all five enzymatic intermediates studied by Krebs and Bollinger have contained high spin $S = 2$ oxoiron(IV) centers. Furthermore, the vast majority of these model complexes employ tetra- or pentadentate nitrogen-rich ligands that afford a pseudo-octahedral ligand set to the iron center in which the principal distortion from octahedral geometry is induced by the oxo ligand.[172], whereas computational studies of the oxoiron(IV) intermediate of TauD suggest that either a five-

coordinate trigonal bipyramidal geometry or a distorted six-coordinate geometry obtained via bidentate carboxylate coordination are most consistent with available spectroscopic data.[219,220] Theoretical predictions also suggest that $S = 2$ oxoiron(IV) centers will be considerably more reactive than their S = 1 counterparts.[208,221-223] Although it is clear that studies of $S = 1$ oxoiron(IV) model complexes have contributed greatly to our understanding of this chemical moiety, the preparation and characterization of high spin $S = 2$ oxoiron(IV) model complexes should allow us to develop a better understanding of the geometric and electronic structures and reactivities of analogous biological oxoiron(IV) centers. Unfortunately, the only $S = 2$ oxoiron(IV) model complex isolated to date, $[Fe^{IV}(O)(H_2O)_5]^{2+}$, was far too unstable to permit extensive study of its structural and reactivity properties.[224,225]

Magnetic circular dichroism (MCD) studies of **1** and other $S = 1$ oxoiron(IV) complexes suggest that the ligand field splitting diagram of these pseudo-octahedral complexes can be thought of as a C_{4v} distortion of O_h geometry (Scheme 6.1).[207,208] In this case, the spin state is controlled by the splitting of the d_{xy} and d_{x2-y2} orbitals that interact with the equatorial ligands. The lack of any $S = 2$ oxoiron(IV) complexes other than the aforementioned $[Fe^{IV}(O)(H_2O)_5]^{2+}$ species in this geometry suggests that the equatorial ligand field is larger than the spin-pairing energy for the majority of ligands employed to date, hence favoring the $S = 1$ state. The enzyme active sites are thought to employ weak-field carboxylate ligands in the equatorial plane to promote the high-spin $S = 2$ state.[220-222] Alternatively, one could employ a five-coordinate C_{3v} trigonal bipyramidal (TBP) geometry in which there are two pairs of energetically degenerate orbitals (d_{xy}/d_{x2-y2} and d_{xz}/d_{yz}) and thus an $S = 2$ state is strongly favored over the low-

spin S = 0 case. Indeed, this geometry has been suggested for the oxoiron(IV) intermediate of TauD, with the three protein-derived ligands enforcing a TBP arrangement.[219,220,226] However, there are remarkably few examples of well-characterized high-valent trigonal bipyramidal iron complexes that might provide insight into this question. Cummins and Schrock have described the characterization of a TBP S = 0 $[Fe^{IV}(CN)(t\text{-}BuMe_2SiNCH_2CH_2)_3N]^0$ adduct via Mössbauer spectroscopy,[227] but direct structural confirmation has not been forthcoming. Similarly, in 2000, Borovik reported the structural characterization of the unique TBP oxoiron(III) complex $[Fe^{III}(O)(H_3buea)]^{2-}$ (H_3buea = tris[(*N*'-tert-butylureaylato)-*N*-ethylene]aminato) generated via treatment of its Fe(II) precursor with O_2.[228] However, evidence for the putative oxoiron(IV) intermediate that precedes the oxoiron(III) product has not been obtained in the intervening decade.

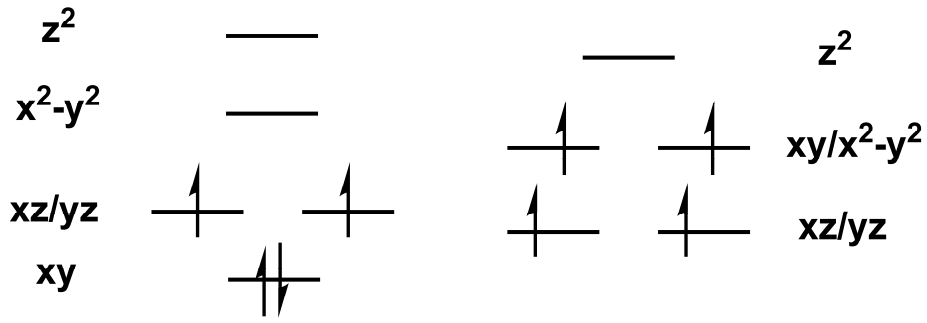

Scheme 6.1. Ligand field splitting diagrams for d^4 iron(IV) in (left) S = 1 C_{4v} pseudo-octahedral symmetry and (right) S = 2 C_{3v} trigonal bipyramidal symmetry.

In an effort to generate a high-spin oxoiron(IV) center in a trigonal bipyramidal geometry, we employed the sterically encumbered ligand TMG_3tren (Scheme 6.2, TMG_3tren = 1,1,1-tris{2-[N^2-(1,1,3,3-tetramethylguanidino)]ethyl}amine)),[229] which was

recently successfully utilized to isolated and characterize an end-on copper(II)-superoxo species.[230-232] Treatment of $[Fe^{II}(NCMe)(TMG_3tren)]^{2+}$ (**2-NCMe**) in acetonitrile with the oxo transfer reagent 2-(tert-butylsulfonyl)iodosylbenzene[233] afforded a new species that was shown by mass spectrometry and Mössbauer studies to be the oxoiron(IV) complex $[Fe^{IV}(O)(TMG_3tren)]^{2+}$ (**4-O**), with high-field Mössbauer experiments suggesting that **4-O** contained a high-spin $S = 2$ iron(IV) center.[92] This complex, while unexpectedly inert towards the oxidation of hydrocarbons, perhaps as a consequence of steric congestion imposed by the bulky tetramethylguanidinium arms, exhibits a considerably faster rate of self-decay compared to other well-characterized $S = 1$ oxoiron(IV) model complexes.[234] The self-decay process was subsequently shown to be intramolecular, and mass spectrometry and Mössbauer studies revealed that self-decay of **4-O** resulted in the generation of a mixture of high-spin $S = 5/2$ Fe(III) complexes consisting of both self-hydroxylated ligand and a putative iron(III)-hydroxide adduct.[93] Treatment of **4-O** with the substrate 1,4-cyclohexadiene (1,4-CHD) resulted in exclusive formation of the iron(III)-hydroxide species $[Fe^{III}(OH)(TMG_3tren)]^{2+}$ (**3-OH**), , presumably via H-atom abstraction from 1,4-CHD.

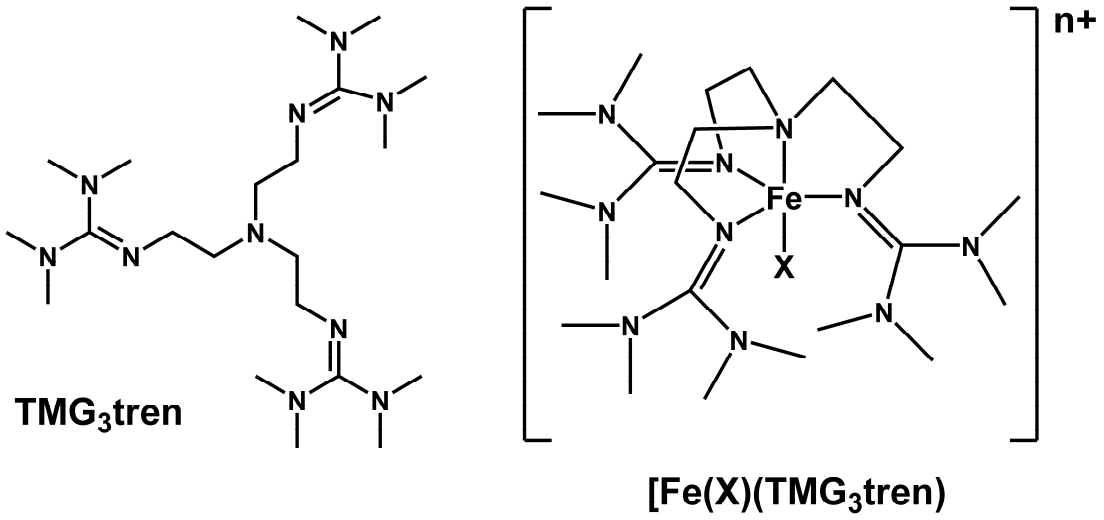

Scheme 6.2. (left) Structure of the ligand TMG_3tren. (right) Generalized structure of the trigonal bipyamidal iron complexes studied in this work (X = O^{2-}, OH^-, NCMe, F^-, N_3^-, and CN^-).

In this chapter, we describe an X-ray absorption spectroscopy (XAS) study of the high-spin oxoiron(IV) complex **4-O** and its H-atom abstraction product **3-OH**. The results presented herein corroborate the proposed structures of both **4-O** and **3-OH**, and are in excellent agreement with the recently reported crystal structure of **4-O**. We also describe the comprehensive characterization by XAS of a series of iron-TMG_3tren complexes with NCMe, F^-, N_3^-, and CN^- ancillary ligands in iron(II), iron(III), and in one case, iron(IV) oxidation states (**2-X**, **3-X**, and **4-X**). This includes structural characterization of the novel diamagnetic S = 0 iron(IV) complex $[Fe^{IV}(CN)(TMG_3tren)]^{3+}$ (**4-CN**). This latter work is part of an effort to provide a basis for interpretation of the electronic and structural properties of the trigonal bipyramidal complexes **3-OH** and **4-O**, and by extension, those of the S = 2 oxoiron(IV) enzyme intermediates.

6.2 Experimental

6.2.1 XAS Sample Preparation

All samples were prepared by Dr. Jason England, using either an oxo transfer reagent or bulk electrolysis methods, as outlined below.

$[Fe^{II}(TMG_3tren)(NCMe)](OTf)_2$, 2-NCMe-A. A 12.6 mM MeCN solution of $[Fe^{II}(TMG_3tren)(NCMe)](OTf)_2$ was prepared and frozen in a tandem Mössbauer/XAS cup. 12 XAS scans to $k = 15$ Å^{-1} were collected at NSLS beamline X3B.

$[Fe^{II}(TMG_3tren)(NCMe)]^{2+}$, 2-NCMe-B. A 6.04 mM MeCN solution of $[Fe^{II}(TMG_3tren)(NCMe)](ClO_4)_2$ was prepared and frozen in a tandem Mössbauer/XAS cup. 10 XAS scans to $k = 6$ Å^{-1} were collected at SSRL beamline 7-3.

$[Fe^{II}(TMG_3tren)(F)]^{+}$, 2-F. 5.19 mM $[Fe^{II}(TMG_3tren)(F)](OTf)$ was dissolved in MeCN and frozen in a tandem Mössbauer/XAS cup. 12 XAS scans to $k = 6$ Å^{-1} were collected at SSRL beamline 7-3.

$[Fe^{II}(TMG_3tren)(N_3)]^{+}$, 2-$N_3$. 6.77 mM $[Fe^{II}(TMG_3tren)(N_3)](OTf)$ was dissolved in MeCN and frozen in a tandem Mössbauer/XAS cup. 8 XAS scans to $k = 6$ Å^{-1} were collected at SSRL beamline 7-3.

$[Fe^{II}(TMG_3tren)(CN)]^{+}$, 2-CN. 18.3 mM $[Fe^{II}(TMG_3tren)(CN)](OTf)$ was dissolved in MeCN and frozen in a SSRL XAS solution cell. 4 XAS scans to $k = 15$ Å^{-1} were collected at SSRL beamline 7-3.

$[Fe^{III}(TMG_3tren)(NCMe)]^{3+}$, 3-NCMe. A 1.16 mM CH_3CN solution of **2-NCMe** was subjected to an applied potential of +500 mV vs Fc^{+}/Fc^{0}V in the presence of 0.1 M NBu_4BF_4 at -40 °C. The sample was frozen in a tandem Mössbauer/XAS cup, and the

yield of **3-NCMe** was taken to be quantitative based on UV/Vis. 8 XAS scans to k = 6 Å^{-1} were collected at SSRL beamline 7-3.

[Fe^{III}(TMG$_3$tren)(F)]$^{2+}$, 3-F. A 2.29 mM CH_3CN solution of **2-F** was subjected to an applied potential of -200 mV vs Fc^+/Fc^0 in the presence of 0.1 M NBu_4BF_4 at -40 °C. The sample was frozen in a tandem Mössbauer/XAS cup, and the yield of **3-F** was taken to be quantitative based on UV/Vis. 8 XAS scans to k = 6 Å^{-1} were collected at SSRL beamline 7-3.

[Fe^{III}(TMG$_3$tren)(N$_3$)]$^{2+}$, 3-N$_3$. A 2.04 mM CH_3CN solution of **2-N$_3$** was subjected to an applied potential of +500 mV vs Fc^+/Fc^0 in the presence of 0.1 M NBu_4BF_4 at -40 °C. The sample was frozen in a tandem Mössbauer/XAS cup, and the yield of **3-N$_3$** was taken to be quantitative based on UV/Vis. 10 XAS scans to k = 6 Å^{-1} were collected at SSRL beamline 7-3.

[Fe^{III}(TMG$_3$tren)(CN)]$^{2+}$, 3-CN. A 5.36 mM CH_3CN solution of **3-CN** was subjected to an applied potential of +500 mV vs Fc^+/Fc^0 in the presence of 0.1 M NBu_4BF_4 at -40 °C. The sample was frozen in a tandem Mössbauer/XAS cup, and the yield of **3-CN** was taken to be quantitative based on UV/Vis. 14 XAS scans to k = 15 Å^{-1} were collected at SSRL beamline 7-3.

[Fe^{III}(TMG$_3$tren)(OH)]$^{2+}$, 3-OH. A sample of [$^{n.a./57}$Fe^{IV}(O)(TMG$_3$tren)]$^{2+}$ (**4-O**) was prepared by addition of 1 equiv. 2-(tert-butylsulfonyl)iodosylbenzene[233] dissolved in CH_2Cl_2 to an CH_3CN solution of the ^{57}Fe-enriched **2-NCMe** precursor at -30 °C. The solution was then treated with 1,4-cyclohexadiene (1,4-CHD) and frozen in a tandem Mössbauer/XAS cup. The final Fe complex concentration was 5.49 mM (1.76 mM $^{57}Fe_T$) and the sample contained 9.1% v/v CH_2Cl_2, which was expected to attenuate

observed X-ray fluorescence. Mössbauer analysis revealed that 88% of the sample was an S = 5/2 Fe(III) species, which is assumed to be the desired **3-OH** species. 13 XAS scans to $k = 15$ Å^{-1} were collected at NSLS beamline X3B.

$[Fe^{IV}(O)(TMG_3tren)]^{2+}$, 4-O. Solutions of **2-MeCN** in MeCN were treated with 2-(tert-butylsulfonyl)iodosylbenzene dissolved in CH_2Cl_2. The iron(IV) complex was obtained ~90% yield based on its absorbance. The samples contained *ca.* 13 % v/v CH_2Cl_2, which was expected to attenuate the observed fluorescence signal.

$[Fe^{IV}(TMG_3tren)(CN)]^{3+}$, 4-CN. A 2.83 mM CD_3CN solution of **2-CN** was subjected to an applied potential of +2100 mV vs. Fc^+/Fc^0 in the presence of 0.1 M NBu_4BF_4 at -40 °C. The sample was frozen in a tandem Mössbauer/XAS cup, with Mössbauer analysis indicating a yield for **4-CN** of 90%. 19 XAS scans to $k = 15$ Å^{-1} were collected at SSRL beamline 7-3.

$Fe^{IV}(TMG_3tren)(CN)]^{3+}$, 4-CN-B. A duplicate sample of **4-CN** was prepared as follows. A 2.09 mM CD_3CN solution of **2-CN** was subjected to an applied potential of +2100 mV vs. Fc^+/Fc^0 in the presence of 0.1 M NBu_4BF_4 at -40 °C. The sample was frozen in a tandem Mössbauer/XAS cup, with an estimated yield for **4-CN** of 90% based on UV/Vis. 11 XAS scans to $k = 6$ Å^{-1} were collected at SSRL beamline 7-3.

6.2.2 X-ray Absorption Spectroscopy. Data Collection.

X-ray absorption data for all **2-X**, **3-X**, and **4-X** samples (except for **2-NCMe** and **3-OH**) were collected on beamline 7-3 of the Stanford Synchrotron Radiation Light source (SSRL) of SLAC National Accelerator Laboratory with storage ring conditions of 3.0 GeV and 80 – 100 mA. Data for **2-NCMe-A** and **3-OH** were obtained on beamline X3B of the National Synchrotron Light Source (NSLS) at Brookhaven National Laboratory,

with storage ring conditions of 2.8 GeV and 100 – 300 mA. At SSRL, Fe K-edge XAS data were collected for frozen solutions maintained at a temperature of *ca.* 10 - 15 K over an energy ranges of 6.9 – 8.0 keV (EXAFS data for **2-**, **3-**, **4-CN**, **4-O**) or 6.9 – 7.3 keV (**2-**, **3-F/N_3/NCMe**, and **4-CN-B**) using a Si(220) double crystal monochromator for energy selection and an Oxford Instruments CF1208 continuous flow liquid helium cryostat for temperature control. Harmonic rejection was achieved by a 9 keV cutoff filter. At NSLS, Fe K-edge XAS data were collected for frozen solutions maintained at *ca.* 25 – 30 K over an energy range of 6.9 – 8.0 keV (**2-NCMe-A** and **3-OH**) using a Si(111) double crystal monochromator for energy selection and a Displex closed cycle cryostat for temperature control. A bent focusing mirror was used for harmonic rejection. Data were obtained as fluorescence excitation spectra with either a 30 element (SSRL) or 13-element (NSLS) solid-state germanium detector array (Canberra). An iron foil spectrum was recorded concomitantly for internal energy calibration and the first inflection point of the K-edge was assigned to 7112.0 eV. The edge energies were routinely monitored during data collection for red-shifts indicative of sample photoreduction; no significant photoreduction was observed for any of the species studied here.

6.2.3 Data Analysis.

Data reduction, averaging, and normalization were performed using the program EXAFSPAK.[130] Following calibration and averaging of the data, background absorption was removed by fitting a Gaussian function to the pre-edge region and then subtracting this function from the entire spectrum. A three-segment spline with fourth order components was then fit to the EXAFS region of the spectrum in order to extract $\chi(k)$.

The program pySpline was used to identify optimal parameters for the spline function employed in EXAFSPAK.[131] Analysis of the pre-edge features was carried out with the program SSExafs[132] using a previously described protocol.[133] The pre-edge fitting parameters reported are those providing the best match to both the experimental data and its second derivative.

Theoretical phase and amplitude parameters for a given absorber-scatterer pair were calculated using FEFF 8.40[135] and were utilized by the opt program of the EXAFSPAK package during curve-fitting. Parameters for **4-O** were calculated using the coordinates of the structure obtained by DFT calculations.[92] Parameters for **3-OH** were calculated for a modification of the reported crystal structure of **4-O**[93] in which the Fe=O distance was lengthened to 1.825 Å and the Fe–N_{ax} bond length was lengthened to 2.25 Å. The coordinates of all other atoms were left unchanged. Parameters for **2-CN** were calculated using the coordinates of the crystal structure without further modification.[185] Parameters for **3-CN** were calculated for a modification of the **2-CN** structure in which Fe–N_{eq} and Fe–$C_{C\equiv N}$ were shortened to 2.00 Å, and Fe–N_{ax} was shortened to 2.25 Å. Parameters for **4-CN** were calculated for a further modification for the foregoing structure in which Fe–N_{eq} and Fe–$C_{C\equiv N}$ were shortened to 1.80 Å, and Fe–N_{ax} was shortened to 2.00 Å. The Fe–C≡N bond angle of 179.5° and the C≡N distance of 1.14 Å in **2-CN** were assumed to be unchanged in our EXAFS models of **3-CN** and **4-CN**, which we believe to be a reasonable assumption given the steric bulk of the TMG_3tren ligand and the near linearity of the Fe–N=N bond angle in the crystal structures of **2-N_3** and **3-N_3**.[185] Phase and amplitude parameters for multiple-scattering pathways involving the Fe–C≡N were explicitly calculated and employed in our EXAFS analyses. A number of

possible multiple-scattering pathways involving the TMG_3tren ligand atoms were also considered, but were not deemed to contribute significantly to the observed EXAFS, and therefore these were not included in our EXAFS analyses of **3-OH**, **4-O**, **2-CN**, **3-CN**, and **4-CN**. In all analyses, the coordination number of a given shell was a fixed parameter, and was varied iteratively while bond lengths (r) and Debye-Waller factors (σ^2) were allowed to freely float. The amplitude reduction factor S_0 was fixed at 0.9, while the edge shift parameter E_0 was allowed to float as a single value for all shells (thus in any given fit, the number of floating parameters was typically equal to (2 × num shells) + 1). The goodness of fit F was defined simply as $\Sigma\ (\chi_{exptl}-\chi_{calc})^2$. For fits to unfiltered data, a second goodness of fit parameter, F-factor, was defined as $[\Sigma k^6(\chi_{exptl}-\chi_{calc})^2\ /\ \Sigma k^6\chi_{exptl}{}^2]^{1/2}$. In order to account for the effect that additional shells have on improving fit quality, an third goodness-of-fit metric *F*' was employed. $F' = F^2\ /\ (N_{IDP} - N_{VAR})$, where N_{VAR} is the number of floated variables in the fit, while N_{IDP} is the number of independent data points and is defined as $N_{IDP} = 2\Delta k\Delta r\ /\ \pi$.[88] In the latter equation, Δk is the *k*-range over which the data is fit, while Δr is the back-transformation range employed in fitting Fourier-filtered data. *F*' is thus of principal utility in fitting Fourier-filtered data, but can also be employed for unfiltered data by assuming a large value of Δr.

6.3 Results

6.3.1. XANES of 4-O and 3-OH

2-NCMe-A exhibits edge and pre-edge parameters typical of high-spin Fe(II) compounds, with a first inflection point along the rising Fe K-edge of 7121.1 eV and a single pre-edge transition centered at 7112.5 eV with a total area of 15.1 units. This area lies on the high side of the tabulated areas for five-coodinate Fe(II) complexes.[134,214] The Fe K-edge absorption spectra collected for **4-O** reveal a significantly different edge-shape, with a blue-shift of *ca.* 2 eV in the edge inflection energy to ~7123.2 eV, consistent with two-electron oxidation of the iron center upon conversion of **2-NCMe-A** to **4-O**. Similarly, the pre-edge feature also exhibits a 1.5 eV blue-shift to ca. 7114 eV, with a total integrated area of 27 units. This area is significantly lower than the value of 60 – 70 units estimated for the $S = 2$ aqueous oxoiron(IV) complex, $[Fe^{IV}(O)(H_2O)_5]^{2+}$, although the pre-edge feature of that species is extremely broad.[225] Both the energy and intensity of the pre-edge feature of **4-O** are consistent with values reported for a number of $S = 1$ oxoiron(IV) model compounds to date.[133,177,187,216] Unlike all $S = 1$ oxoiron(IV) models reported to date, the pre-edge feature of **4-O** cannot be simulated with a single Gaussian peak (Figure 6.2), with the best fit consisting of two peaks at 7113.8 eV and 7115.56 eV with peak areas of 24 units and 3 units, respectively. The **4-O** pre-edge feature is similar in appearance to that reported for the $S = 2$ oxoiron(IV) intermediate of the αKG-dependent halogenase SyrB2.[21] The presence of two peaks in the pre-edge features of $S = 2$ oxoiron(IV) complexes can be rationalized by spin-polarization of the α and β d_{z2} orbitals that results in a large splitting of these orbitals in the $S = 2$ case such that it is experimentally detectable, as suggested by a recent computational study.[235]

While this spin-polarization effect is also present for S = 1 oxoiron(IV) centers, the orbital splitting is presumably too small to be detected at the resolution of a typical Fe K-edge XAS experiment.

The iron(III) species **3-OH,** generated by treatment of **4-O** with 1,4-CHD, exhibits an edge shape similar to that of **4-O**. The edge energy of 7122.62 eV represents a modest red-shift relative to **4-O** of *ca.* 0.6 eV, but is 1.5 eV higher in energy than 2-**NCMe-A**, consistent with the iron(III) assignment from Mössbauer and EPR spectroscopy. 3-OH exhibits a single symmetric pre-edge transition at 7113.9 eV with a total area of 21 units. This area compares favorably to the values of 21 and 25 units reported for the five-coordinate trigonal bipyramidal oxoiron(III) complex $[Fe^{III}(O)(H_3buea)]^{2-}$ and its hydroxoiron(III) analog $[Fe^{III}(OH)(H_3buea)]^{-}$.[236]

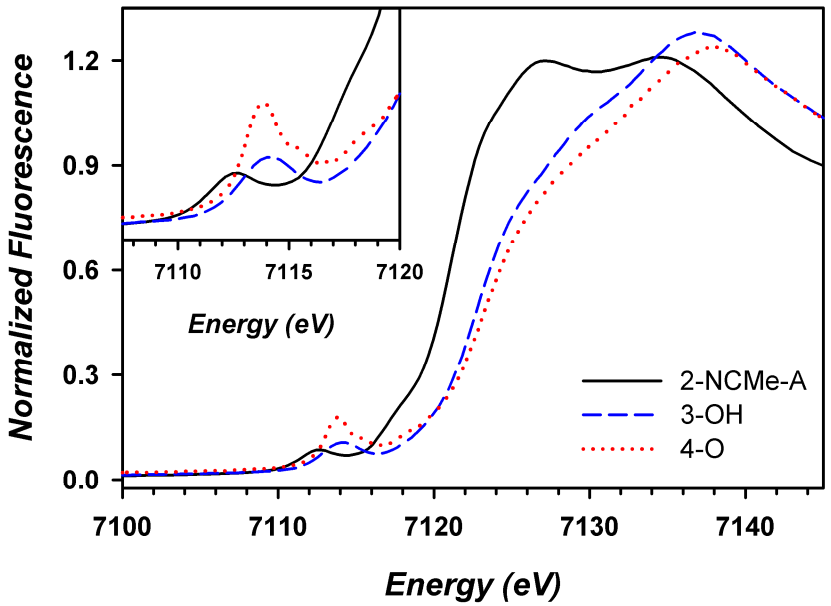

Figure 6.1. Comparison of the Fe K-edge X-ray absorption edge and pre-edge (inset) features of **2-NCMe-A** (black, ——), **3-OH** (blue, – – –), and **4-O** (red, ·····).

Table 6.1. Pre-edge Analysis Parameters for **2-NCMe-A**, **3-OH**, and **4-O**.[a]

Species	Purity	E_{edge} (eV)	$E_{pre\text{-}edge}$ (eV)	height	width	area
2-NCMe-A	--	7121.14	7112.50	0.0502(6)	2.82(4)	15.1(2)
3-OH	88%	7122.62	7113.99	0.0669(7)	2.92(4)	20.8(3)
4-O [b]	93%	7123.18	7113.89	0.111(1)	2.18(3)	25.8(5)
			7113.80 7115.56	0.119(1) 0.028(2)	1.878(28) 1.05(7)	23.9(4) 3.1(3)

[a] The fits presented are those that give the best agreement to the experimental data and its second derivative. Values in parentheses represent uncertainties in the final digit of that parameter. Purity was asessed by Mössbauer analysis of the samples prepared for XAS.
[b] Fits with either one or two Gaussian pre-edge functions are given for **4-O**.

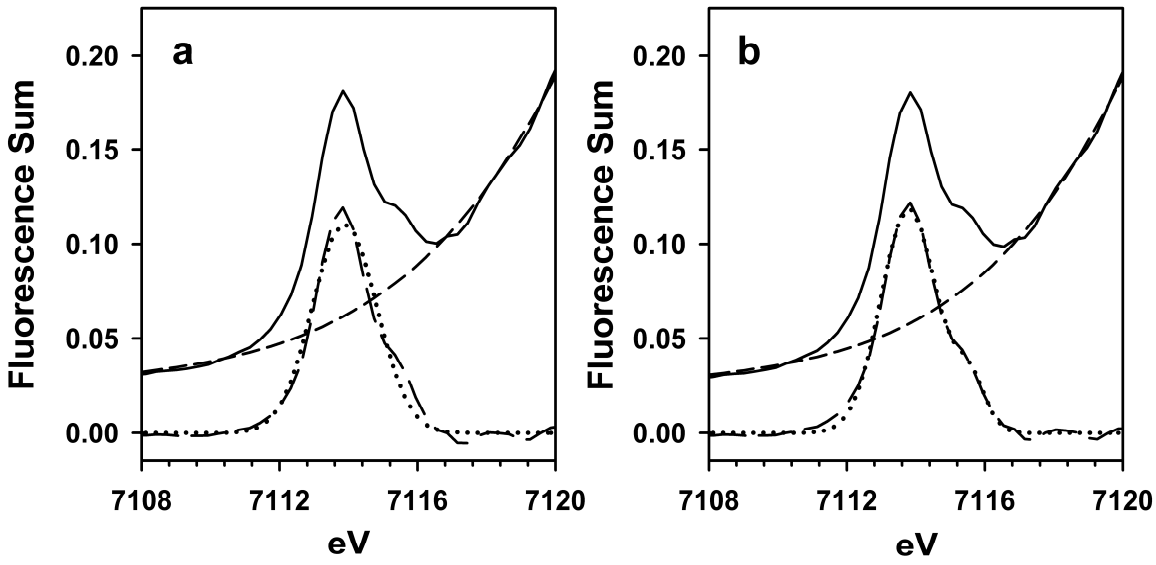

Figure 6.2. Comparison of (a) one peak and (b) two peak refinements of the pre-edge feature of **4-O**, clearly illustrating the presence of a shoulder. Parameters are those given in Table 6.1 for **4-O**. Lines are defined as follows: experimental data (——), edge function (– – –), data – edge function (— — —), peak fit (····).

6.3.2. EXAFS Analysis of 4-O and 3-OH

We were able to collect good quality EXAFS data for both **4-O** and **3-OH** (Figure 6.3), despite the fact that both samples contain significant quantities of the strong X-ray absorbing solvent CH_2Cl_2. While the $k^3\chi(k)$ EXAFS modulations of **4-O** are clearly distinct from those of S = 1 oxoiron(IV) complexes,[133,177,187] the Fourier transform is similar in shape and appearance to those obtained using TMC as a supporting ligand.[91,177] The FT of **4-O** exhibits a sharp peak centered at r' = 1.6 Å^{-1} associated with scattering interactions from first-shell ligands, along with a broad lower-intensity feature spread over r' = 2.2 – 3.2 Å^{-1} associated with outer-shell scattering from carbon and nitrogen atoms of the ligand. The EXAFS modulations of **3-OH** have much smaller amplitudes than those of **4-O**, and there are several subtle changes in the beat pattern, principally at k = 8 Å^{-1}. This manifests more clearly in the **3-OH** FT, in which the r' = 1.6 Å peak is only half as intense as **4-O**, and has broadened slightly (Figure 6.3). This observation is indicative of a greater degree of destructive overlap in the EXAFS oscillations associated with the inner shell of **3-OH**, due to either the specific combination of bond lengths or greater static disorder in the range of bond lengths.[216] Interestingly, the intensity of the outer-shell feature centered at r' = 2.6 Å is invariant for **4-O** and **3-OH**.

EXAFS curve-fitting analysis of **4-O** reveals that the inner shell is best fit to 4 Fe–N scatterers at 1.99 Å assigned to the equatorial and axial nitrogen donors of the TMG_3tren ligand and a single Fe–O scatterer at 1.65 Å associated with the bound oxo (fit 9, Table 6.2). These values are in excellent agreement with the X-ray crystal structure obtained recently for **4-O**, in which Fe–$N_{eq(ave)}$ and Fe=O bond lengths were found to be 2.005 Å and 1.661 Å, respectively.[93] The quality of the fit to the inner shell is fairly

insensitive to the total coordination number of the principal Fe–N shell, with fits to either a five-coordinate (fits 8 and 9, Table 6.2) or six-coordinate site (fits 10 and 11, Table 6.2) giving identical goodness-of-fit parameters. We favor a five-coordinate site based principally on the premise that the steric encumbrance of the supporting TMG_3tren ligand[229] would preclude binding of exogenous solvent ligands, which is supported by the lack of evidence from other techniques such as mass spectrometry for such an event.[92] It was also not possible to split the principal Fe–N shell into two subshells of Fe–N_{eq} and Fe–N_{ax} scatterers (fits 5 and 12, Table 6.2), as implausibly small or negative Debye-Waller factors were obtained in these fits, and the improvement in fit quality was modest. It is noteworthy, however, that the Fe– N_{ax} distance of *ca.* 2.1 Å obtained in these fits agrees nicely with the crystallographic value of 2.112 Å.[93] Finally, the outer shell can be modeled with a shell of 3-4 Fe•••C at 2.93 Å and a second shell of 6-7 Fe•••C/N at 3.36 Å (fit 22, Table 6.2 and Figure 6.4). Consideration of the crystal structures of **4-O** and its **2-NCMe** precursor suggests that the former is associated with carbons of the tren backbone of the ligand, while the latter can be assigned to carbon and nitrogen atoms on the guanidinium pendant arms.[92,93,229]

We anticipated from mass spectrometry studies that **3-OH** was likely a hydroxide adduct formed by H-atom abstraction from 1,4-CHD by **4-O**. EXAFS analysis indicates that the inner shell can be modeled as 3 Fe–N scatterers located at 2.00 Å corresponding to the equatorial nitrogen donors of the TMG_3tren ligand. We attribute the absence of any significant lengthening in the Fe–N_{eq} bond length from that of **4-O** to steric constraints imposed by the ligand. More importantly, addition of a short Fe–O/N scatterer leads to a refined bond length of 1.77 Å assignable to the hydroxide ligand (fits

5 and 5a, Table 6.3), concurrent with significant improvements in fit quality. The Debye-Waller factor associated with the Fe–O shell is large, which we attribute to static disorder introduced by the presence of multiple iron(III) species in samples of **3-OH**, as shown by EPR studies.[93] In contrast to **4-O**, the coordination number of the principal Fe–N shell appears to be significantly underestimated, with fits to 4 Fe–N giving a significantly poorer visual agreement to the experimental data. It was not possible to fit a unique Fe–N_{ax} distance for **3-OH**, as these fits exhibited markedly poorer fit quality and unreasonably large σ^2 values (fits 7a and 7b, Table 6.3). The outer-shell features can be modeled with two distinct shells of Fe•••C/N scatterers at 2.99 Å and 3.37 Å attributable to the backbone of the TMG_3tren ligand, and consistent with our observations for **4-O**. The requirement for a short Fe–OH distance to obtain good fits to the **3-OH** EXAFS data is nicely illustrated by a series of fits in which this shell was added as the last component of the fit (fits 19-22, Table 6.3). Fit 21, in which all components of our best fit (fit 14, Table 6.3 and Figure 6.4) are present except for the short Fe–O shell, exhibits a significant mismatch to both the inner-shell feature in the Fourier transform and the $k^3\chi(k)$ EXAFS data (Figure 6.5). Addition of the short Fe–O scatterer to this fit leads to profound improvements in fit quality and the match to experimental data. This observation is analogous to ones we have made elsewhere for a pair of Fe(II) complexes containing an O-bound sulfinate, in which addition of a short Fe–O distance to a nearly complete fit leads to significant improvements in fit quality.[91]

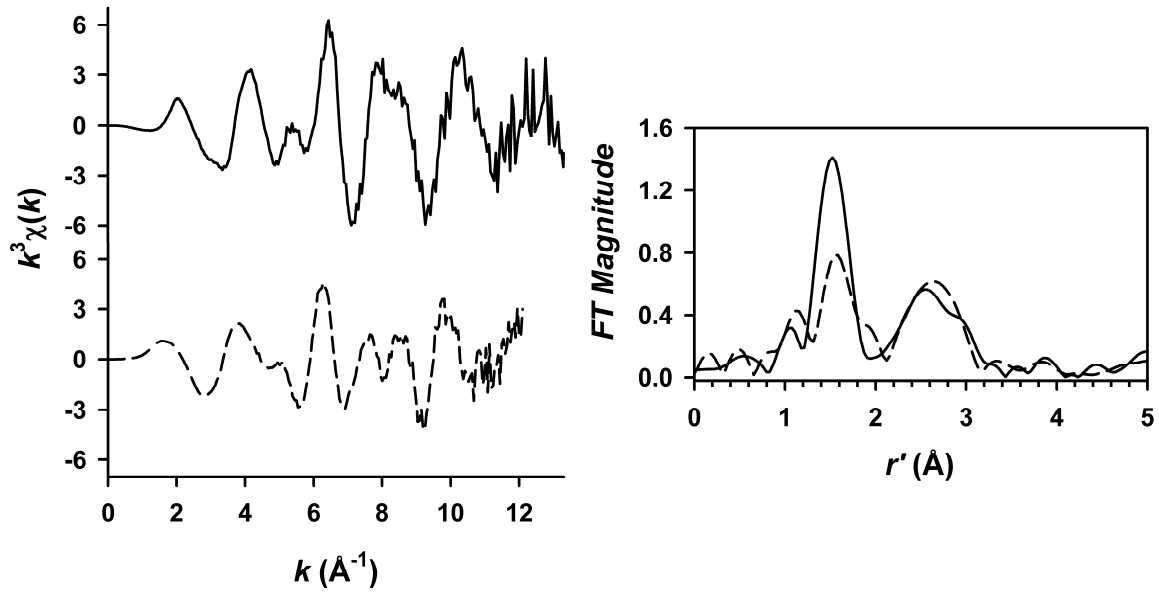

Figure 6.3 (left) Comparison of the $k^3\chi(k)$ EXAFS spectra of **3-OH** (– – –) with its precursor **4-O** (——). The spectra are scaled identically. (right) Overlay of the Fourier transforms of $k^3\chi(k)$ EXAFS data for **3-OH** (– – –) and its precursor **4-O** (——). Fourier transformation ranges are as follows: k = 2-12.15 Å^{-1} (**3-OH**); k = 2-13.3 Å^{-1} (**4-O**).

Table 6.2. EXAFS Analysis for **4-O**.[a]

	Fe-N/O			Fe-O/N			Fe•••C			Fe•••C/N			
fit	**n**	**r**	**σ^2**	**n**	**r**	**σ^2**	**n**	**r**	**σ^2**	**n**	**r**	**σ^2**	***F-factor*** [b]
1	3	1.99	2.3										0.654
2	4	1.99	3.9										0.668
3	5	1.99	5.5										0.708
4	6	1.99	7.2										0.761
5	3 1	1.97 2.11	-1.2 -4.6										0.624
6	3	1.99	2.7	1	1.64	2.2							0.565
7	3	1.99	2.7	0.9	1.64	1.4							0.556
8	4	1.99	4.3	1	1.65	2.0							0.527
9	4	1.99	4.4	0.9	1.65	1.3							0.524
10	5	1.98	5.9	1	1.65	1.6							0.522
11	5	1.98	6.0	0.9	1.65	1.1							0.523
12	3 1	1.96 2.09	0.2 -3.1	0.9	1.66	2.3							0.514
13	4	1.99	4.4	0.9	1.64	1.5	3	2.92	2.5				0.473
14	4	1.98	4.4	0.9	1.64	1.6	4	2.91	4.1				0.479
15	4	1.98	4.3	0.9	1.65	1.6	5	2.91	5.5				0.489
16	5	1.98	5.9	0.9	1.65	1.2	3	2.91	2.6				0.481
17	5	1.98	5.8	0.9	1.65	1.2	4	2.91	3.9				0.487
18	4	1.99	4.4	0.9	1.65	1.6	3	2.93	2.0	5	3.36	2.2	0.331
19	4	1.99	4.4	0.9	1.65	1.5	3	2.93	2.1	6	3.36	3.1	0.324
20	4	1.99	4.4	0.9	1.65	1.5	3	2.93	2.2	7	3.36	4.0	0.321
21	4	1.99	4.4	0.9	1.65	1.5	3	2.93	2.3	8	3.36	4.9	0.321
22	***4***	***1.99***	***4.4***	***0.9***	***1.65***	***1.4***	***4***	***2.93***	***3.8***	***7***	***3.36***	***4.2***	***0.319*** [c]
23	4	1.99	4.4	0.9	1.65	1.4	4	2.93	3.6	6	3.36	3.3	0.324
24	5	1.99	6.0	0.9	1.65	1.2	3	2.92	2.2	7	3.35	4.1	0.322

25	5	1.99	6.1	0.9	1.65	1.1	4	2.95	3.9	7	3.35	4.5	0.324

[a] Fourier transform range $k = 2.0 – 13.3$ Å^{-1} (resolution = 0.139 Å). r is in units of Å; σ^2 is in units of 10^{-3} Å^2. All fits are to unfiltered data. The first shell was fit using scatterers with nitrogen parameters, the second shell with oxygen parameters, and the fourth shell with carbon parameters, based on the expected backscatterers at each distance. However, EXAFS cannot distinguish between backscatterers differing by $Z = 1$.

[b] Goodness-of-fit parameter *F-factor* defined as $[\Sigma k^6(\chi_{exptl}-\chi_{calc})^2 / \Sigma k^6 \chi_{exptl}^2]^{1/2}$.

Table 6.3. EXAFS Analysis for **3-OH**.[a]

	Fe-N/O			Fe-O			Fe•••C			Fe•••C/N			
fit	**n**	**r**	**σ^2**	**n**	**r**	**σ^2**	**n**	**r**	**σ^2**	**n**	**r**	**σ^2**	***F-factor*** [b]
1	2	2.03	1.9										0.711
2	3	2.02	4.8										0.731
3	4	2.02	7.9										0.771
4	5	2.01	11.7										0.812
5	3	2.00	3.2	1	1.78	6.3							0.692
5a	3	2.00	3.2	0.9	1.77	5.5							0.692
6	4	1.99	5.4	1	1.75	4.4							0.699
6a	4	1.99	5.6	0.9	1.74	3.7							0.698
7a	3 1	2.01 2.36	3.3 13.2	0.9	1.78	6.4							0.688
7b	3 1	2.03 2.35	4.8 8.1										0.712
8	3	2.02	3.4	0.9	1.78	7.2	4	3.02	0.5				0.438
9	3	2.02	3.3	0.9	1.78	7.3	5	3.02	1.6				0.431
10	3	2.02	3.4	0.9	1.78	7.3	6	3.02	2.6				0.434
11	3	2.02	3.4	0.9	1.78	7.3	7	3.02	3.6				0.443
12	3	2.01	3.3	0.9	1.77	5.8	5	3.00	2.3	5	3.38	3.1	0.299
13	3	2.00	3.3	0.9	1.77	5.4	5	3.00	2.4	6	3.38	4.1	0.297
14	***3***	***2.00***	***3.3***	***0.9***	***1.77***	***5.1***	***5***	***2.99***	***2.6***	***7***	***3.37***	***5.0***	***0.295***
15	3	2.00	3.2	0.9	1.77	4.6	5	2.99	2.8	8	3.37	5.7	0.295
16	3	2.01	3.4	0.9	1.77	5.9	6	3.00	3.6	6	3.38	4.6	0.298
17	3	2.01	3.3	0.9	1.77	5.7	6	3.00	3.7	7	3.38	5.6	0.296
18	3	2.00	3.3	0.9	1.77	5.4	6	3.00	3.7	8	3.37	6.4	0.296
19	3	2.03	4.8				5	3.03	1.6				0.467
20	3	2.02	3.4	0.9	1.78	7.4	5	3.02	1.6				0.431
21	*3*	*2.02*	*4.9*				*5*	*3.03*	*2.0*	*7*	*3.41*	*7.9*	*0.385*

22	3	2.00	3.3	0.9	1.77	5.1	5	2.99	2.6	7	3.37	5.0	0.295

[a] Fourier transform range $k = 2.0 – 12.15$ Å^{-1} (resolution = 0.156 Å). r is in units of Å; σ^2 is in units of 10^{-3} Å^2. All fits are to unfiltered data.
[b] Goodness-of-fit parameter *F-factor* defined as $[\Sigma k^6(\chi_{exptl}-\chi_{calc})^2 / \Sigma k^6 \chi_{exptl}^2]^{1/2}$.

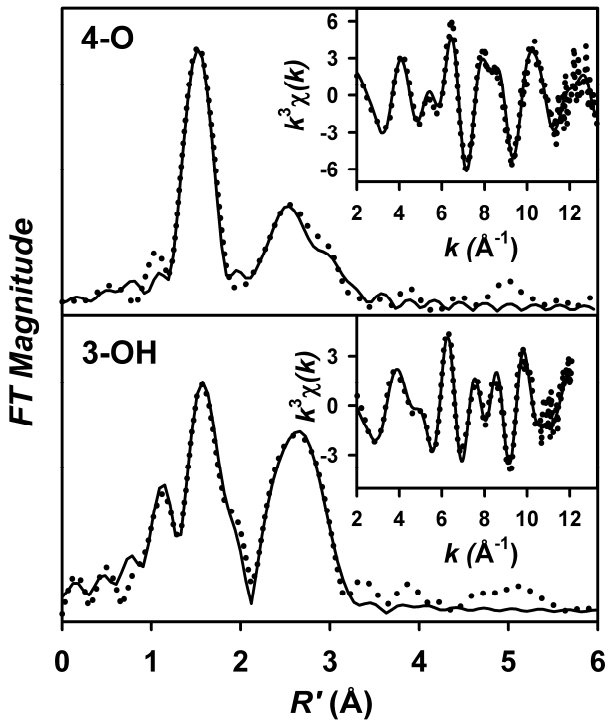

Figure 6.4. Fourier transforms of the Fe K-edge EXAFS data ($k^3\chi(k)$) and unfiltered EXAFS spectra ($k^3\chi(k)$, inset) obtained for **4-O** and **3-OH**. Experimental data is shown with dotted lines (•••••), while fits are shown with solid lines (——). Fourier transformation ranges are as follows: k = 2 – 13.3 Å^{-1} (**4-O**), k = 2 – 12.15 Å^{-1} (**3-OH**) Fit parameters for **4-O** and **3-OH** are those shown in bold italics in Tables 6.2 and 6.3, respectively.

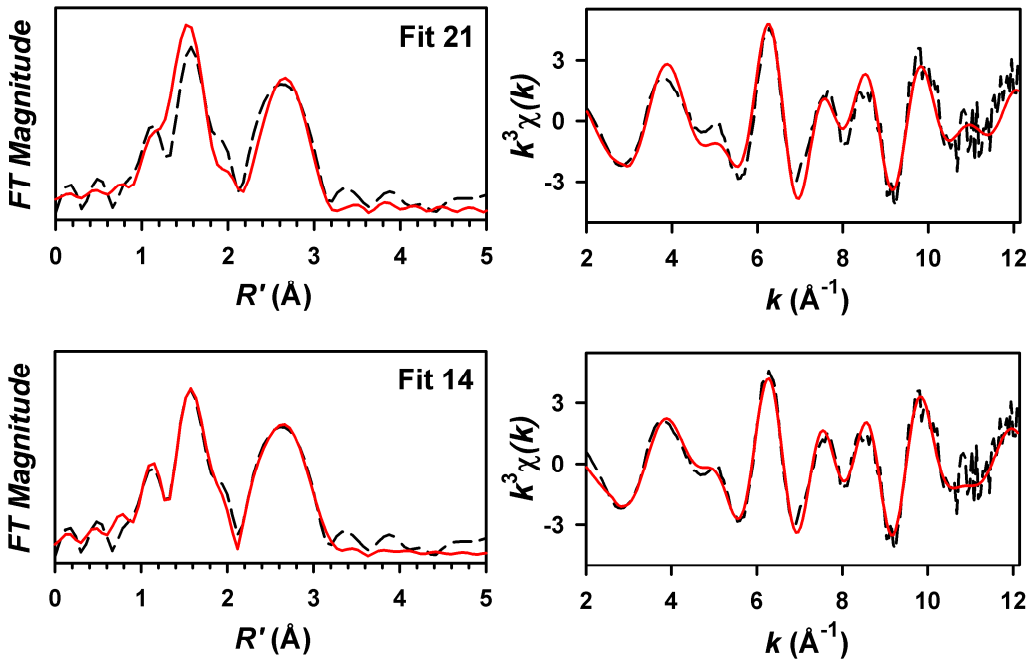

Figure 6.5. Comparison of EXAFS fits to **3-OH** either without (fit 21, top) or with (fit 14, bottom) a short Fe–O scatterer. Experimental data is shown with dashed lines (- - - -), while fits are shown with solid red lines (——). Fourier transformation range: k = 2 – 12.15 Å^{-1}. Fit parameters associated with the stated fit are shown in Table 6.3.

6.3.3. XANES Analysis of Psuedohalide Adducts

In order to obtain a better understanding of the XANES features of **3-OH**, and **4-O**, we carried out a comprehensive XANES study of a series of iron(II), iron(III), and one iron(IV) complexes with the TMG_3tren ligand and several ancillary ligands (NCMe, N_3^-, F^-, and CN^-). The **2-X** series of complexes all exhibit fairly similar XANES spectra consistent with high-spin iron(II) centers (Figure 6.6), with a first inflection energy for the rising K-edge of 7121.2 – 7121.5 eV for **2-F**, **2-NCMe-B**, and **2-N_3** and a somewhat higher edge energy of 7122.25 eV for **2-CN**. All four complexes exhibit a pre-edge feature with two peaks in which the more intense peak is centered at *ca.* 7112.6 eV and the shoulder lies some 1.7 – 1.8 eV higher in energy at approximately 7114.35 eV (Table 6.4). The total integrated pre-edge areas lie in a fairly narrow range of 13 – 15 units, which would be expected from the very similar structures of the **2-X** complexes determined by X-ray crystallography.[185] These intensities are on the high end of values reported previously for five-coordinate high-spin iron(II) complexes, most of which have exhibited square pyramidal C_{4v} geometries.[134,214] Indeed, published XANES parameters for comparable trigonal bypyramidal iron(II) sites appear to be rare in the literature, and unlike other coordination geometries, a theoretical treatment of the factors contributing to the pre-edge transitions has not been forthcoming. The trigonal bipyamidal IPNS model complex $[Fe^{II}(TPA)(SC_6H_2\text{-}2,4,6\text{-}Me_3)]$ ($\tau = 0.90$), has a pre-edge area of 8.9, although it is not clear whether this complex exhibits two peaks in its pre-edge.[134,201,237] As a second example, the trigonal bipyramidal high-spin Fe(II)–O_5 site in the mineral grandidierite[238] exhibits two pre-edge peaks with a total integrated intensity of 13 units.[239,240] The grandidierite pre-edge feature is quite similar to those of **2-X**, with an intense primary

peak and a less intense shoulder with a splitting of 1.7 eV. We suggest that the intensity of the **2-X** pre-edges may in part reflect the distortion from idealized trigonal bipyramidal geometry imposed by the long apical Fe–N_{ax} bond from the TMG_3tren ligand. Both **2-CN** and **2-NCMe-B** also exhibit a well-defined shoulder along the rising edge centered at 7118 eV, which must be included in the pre-edge peak analysis in order to provide a good fit. This shoulder is considerably weaker for **2-F** and **2-N_3** and is not a critical component of the fitting process. Similar shoulders have been observed for other cyanide-containing iron complexes such as $K_3[Fe(CN)_6]$[214] or cyanide-bound metmyogloblin[241], and likely represent a transition involving an interaction of the π* orbitals of cyanide with the iron 3d orbitals.[241,242]

One electron oxidation of **2-X** is accompanied by blue-shifts of the edge and pre-edge energies of approximately +2 eV, consistent with metal-centered oxidation and the **3-X** complexes being ferric (Table 6.4, Figure 6.8 for **X** = **CN**). The edge energies range from 7123.0 eV for **3-NCMe** to 7124.4 eV for **3-CN**. The pre-edge region of all **3-X** complexes exhibits a single peak centered at 7114.2 eV with a greater integrated intensity than encountered for their **2-X** congeners, as would be expected from the additional electron hole for the **3-X** series. In addition, there is a very weak and poorly resolved shoulder on the low-energy side of the primary pre-edge transition for all **3-X** complexes other than **3-N_3**, which must be included to obtain a good fit.. The integrated pre-edge intensities, which range from 16 for **3-N_3** to 20 for **3-CN**, are similar to the value of 21 we obtained for **3-OH**, but appear to be somewhat smaller than the areas of 21-27 reported previously for Borovik's trigonal bipyramidal $[Fe^{III}(H_3buea)(X)]^{2-/-}$ ($X = O^{2-}$, S^{2-}, OH^-) complexes.[236] The trigonal bipyramidal Fe(III) site in the mineral yoderite exhibits

a single sharp pre-edge transition with an intensity of *ca.* 17 units, in good agreement with the values obtained for **3-X**.[239] Interestingly, the feature observed on the rising edge of **2-X** is of much lower intensity in the analogous **3-X** complexes and is only clearly discernible for **3-CN** and **3-N_3**, suggesting that the nature of this edge transition may be closely tied to an effect of iron oxidation state on the probability of the transition.

Of the possible **4-X** complexes, we were able to isolate only the $S = 0$ iron(IV) complex **4-CN** in high yield for characterization by XAS. The one-electron oxidation of **3-CN** to **4-CN** elicits a further +2 eV blue-shift of the Fe K-edge inflection energy (Figure 6.8) from 7124.4 eV to 7126.75 eV, supporting the posited metal-centered oxidation to iron(IV). Remarkably, the edge energy of **4-CN** is more than +3 eV higher in energy than its $S = 2$ congener **4-O** (7123.2 eV), an effect which likely reflects a much greater effective nuclear charge for the diamagnetic **4-CN** complex that is partially mitigated in **4-O** by the highly covalent Fe=O bond.[243] **4-CN** exhibits an extremely sharp pre-edge transition centered at 7112.9 eV with a total integrated intensity of 29 units, along with a poorly resolved shoulder peak at *ca.* 7114.5 eV that has an area of approximately 4.5 units (average of **4-CN** and **4-CN-B**, Table 6.5) The area of the principal feature is similar to those obtained for **4-O** and an assortment of $S = 1$ oxoiron(IV) complexes.[133,177,187] However, the energy of the **4-CN** pre-edge transition is *red-shifted* by *ca.* -1.5 eV relative to **3-CN** (Figure 6.8) and by -1 eV relative to **4-O** (Figure 6.9), suggesting a significant contraction of the d orbitals relative to both its high-spin precursor **3-CN** and high-spin congener **4-O**. This phenomenon was previously observed by Wieghardt and co-workers in studies of dinuclear complexes with a $[Fe^{III}(\mu\text{-}O)(\mu\text{-carboxylato})_2M^{III}]^{2+}$ (M = Fe, Cr) core in which the $S = 5/2$ iron(III) center is

oxidized to $S = 1$ iron(IV),[244] as well as more recent studies of three-coordinate iron(III)-imido complexes in comparison to iron(II)-amido precursors.[243] **4-CN** also exhibits two distinct weak edge transitions at 7117.3 eV and 7119.0 eV, neither of which is present in **4-O**, suggesting a relationship to some combination of the $S = 0$ spin state of **4-CN** and the cyanide ligand itself.

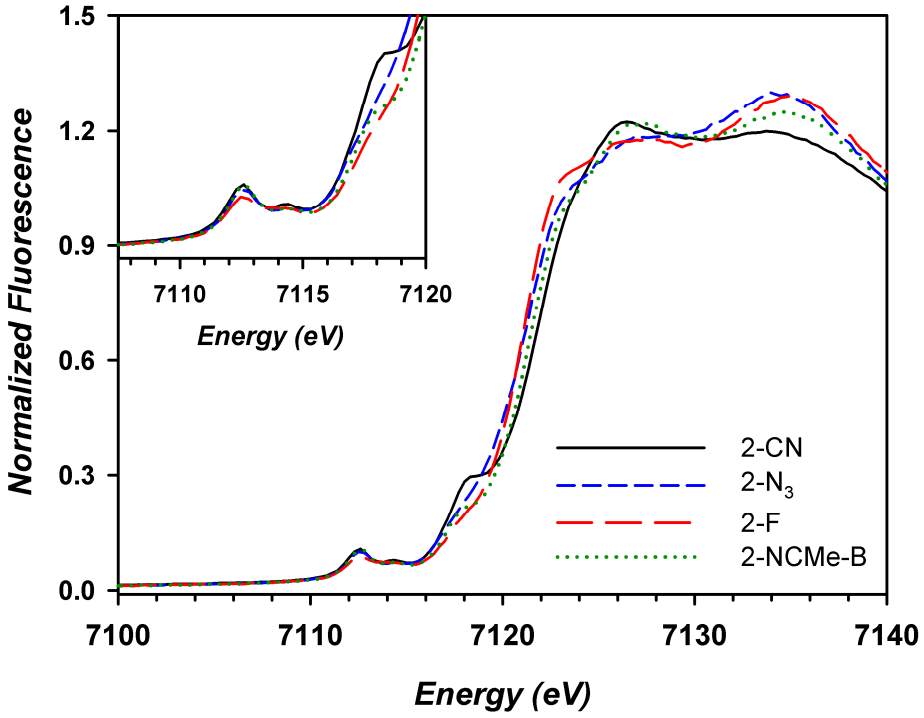

Figure 6.6. Comparison of the Fe K-edge X-ray absorption edge and pre-edge (inset) features of the **2-X** series. Key: **2-CN** (black, ——), **2-N$_3$** (blue, – – –), **2-F** (red, — — —), and **2-NCMe-B** (green, ·····).

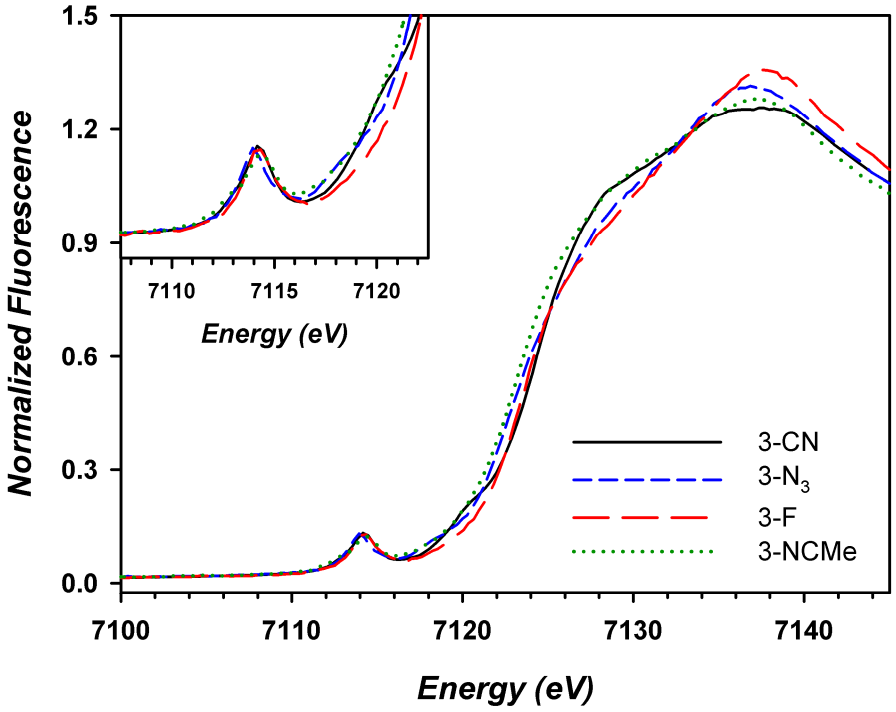

Figure 6.7. Comparison of the Fe K-edge X-ray absorption edge and pre-edge (inset) features of the **3-X** series. Key: **3-CN** (black, ——), **3-N$_3$** (blue, – – –), **3-F** (red, — — —), and **3-NCMe** (green, ·····).

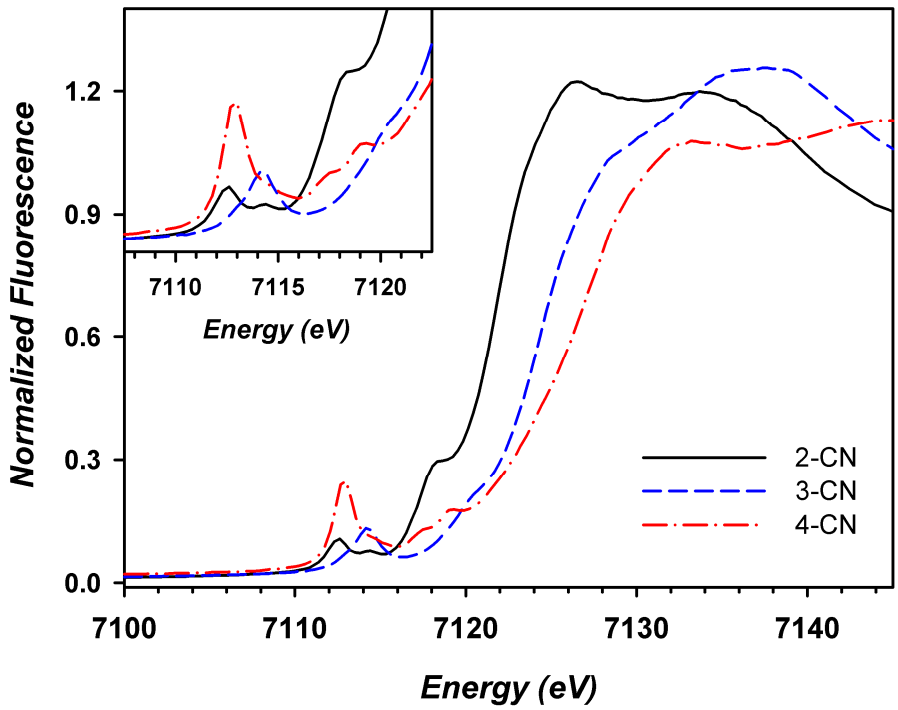

Figure 6.8. Comparison of the Fe K-edge X-ray absorption edge and pre-edge (inset) features of **2-CN** (black, ——), **3-CN** (blue, – – –) and **4-CN** (red, ·–·–·–).

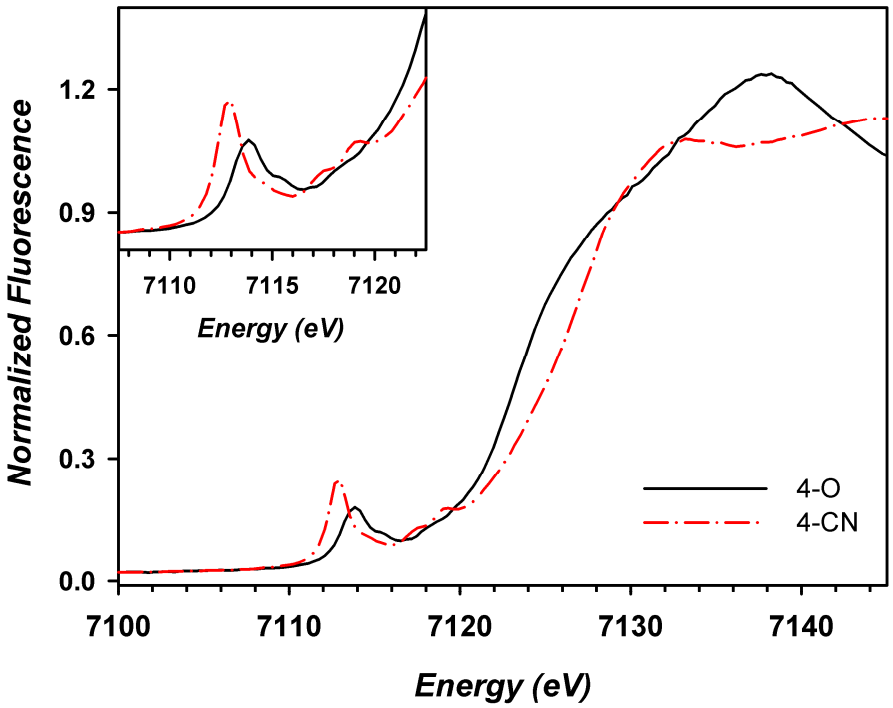

Figure 6.9. Comparison of the Fe K-edge X-ray absorption edge and pre-edge (inset) features of **4-O** (black, ——) and **4-CN** (red, ·–·–·–).

Table 6.4. Pre-edge Analysis Parameters for **2-, 3-, 4-X** (X = CN^-, NCMe, F^-, N_3^-).[a]

Species	E_{edge} (eV)	$E_{pre\text{-}edge}$ (eV)	height	width	area	edge peaks (eV) [b]
2-CN	7122.25	7112.51(1) 7114.31(3)	0.0675(9) 0.025(1)	1.71(4) 1.08(8)	12.3(2) 2.8(2)	7118.02
2-N_3	7121.53	7112.57(1) 7114.39(3)	0.0643(7) 0.021(1)	1.80(3) 1.10(8)	12.3(2) 2.4(2)	7117.38
2-F	7121.22	7112.58(1) 7114.32(4)	0.0540(7) 0.023(1)	1.92(5) 1.26(8)	11.0(3) 3.0(3)	7117.75
2-NCMe-B	7121.25	7112.56(1) 7114.36(3)	0.065(1) 0.020(1)	1.57(3) 1.13(9)	10.8(3) 2.4(2)	7118.04
3-CN	7124.40	7114.25(5) 7112.60(30)	0.087(5) 0.018(3)	1.77(7) 2.0(4)	16.4(1.4) 3.8(1.4)	7120.25
3-N_3	7123.60	7113.96(1)	0.0799(9)	1.886(26)	16.0(2)	7118.23
3-F	7123.65	7112.01(9) 7114.25(1)	0.0092(9) 0.0869(5)	1.41(22) 1.97(3)	1.4(2) 18.3(3)	--
3-NCMe	7123.00	7114.35(4) 7112.60(10)	0.084(2) 0.021(2)	1.76(8) 1.47(23)	15.6(8) 3.3(7)	--
4-CN	7126.84	7112.87(2) 7114.53(8)	0.189(3) 0.038(3)	1.44(4) 1.26(17)	29.0(8) 5.1(7)	7117.27 7119.02
4-CN-B	7126.64	7112.91(2) 7114.55(8)	0.193(4) 0.034(3)	1.44(4) 1.11(17)	29.5(9) 4.0(7)	7117.35 7119.00

[a] The fits presented are those that give the best agreement to the experimental data and its second derivative, which in all cases were fits in which the pre-edge peak widths were allowed to vary independently, instead of being constrained to a single common value. Values in parentheses represent uncertainties in the final digit of that parameter.

[b] Energy associated with the edge transition. For all complexes other than **4-CN** and **4-CN-B**, this was obtained from the peak-fitting analysis.

6.3.4. EXAFS Analysis of 2-, 3-, and 4-CN

The unique diamagnetic nature of **4-CN** prompted interest in its geometric structure and how that structure compares to its **2-CN** and **3-CN** precursors, and we have therefore carried out an EXAFS analysis of all three complexes. All three complexes exhibit $k^3\chi(k)$ EXAFS spectra and Fourier transforms of comparable intensities, with the most interesting property being the progressive shift in the positions of peaks in the FT spectra going from **2-CN** to **3-CN** to **4-CN** (Figures 6.10, 6.11). Specifically, the principal inner-shell feature at r' = 1.7 Å for **2-CN** downshifts to 1.6 Å for **3-CN** and even further to 1.4 Å for **4-CN**, which is indicative of shortening in bond lengths as the iron center becomes progressively more oxidized. A similar progressive downshift is also apparent for the outer-shell feature from r' = 2.8 Å for **2-CN** to r' = 2.4 Å for **4-CN**.

The postulated reduction in metal-ligand bond lengths is corroborated by analysis of Fourier-filtered EXAFS data at the single scattering level of theory for **2-CN**, **3-CN**, and **4-CN** (Table 6.5, Figure 6.12). The inner-shell feature of **2-CN** can be simulated with a shell of 3 Fe–N scatterers at 2.09 Å (fit **2-CN**-B, Table 6.5 and Figure 6.12), a value that is in good agreement with the average Fe–N_{eq} bond length of 2.1097(12) Å obtained by X-ray crystallography for **2-CN**.[185] We were unable to deconvolve a unique Fe–C_{CN} scatterer by single-scattering EXAFS analysis alone (fits F and G to **2-CN**, Table 6.5); the crystallographic Fe–C_{CN} bond length of 2.1293(15) Å in **2-CN** is very similar to those of Fe–N_{eq}, and as EXAFS cannot distinguish between scatterers differing by Z = 1,[87,90] we would not expect to be able to specifically resolve cyanide-derived carbon scattering against the more intense Fe–N_{eq} EXAFS modulations. Although the X-ray crystal structure of **2-CN** indicates that the Fe–N_{ax} bond length (2.3017(12) Å) associated

with the capping nitrogen of the TMG_3tren ligand is very different from those of Fe–N_{eq}, it was not possible to resolve a long Fe–N_{ax} scatterer, as the fit quality was significantly poorer relative to one-shell fits and the Debye-Waller factor associated with the Fe–N_{ax} shell was quite large. This observation is identical to those made earlier in this work for **3-OH** and **4-O**, and presumably reflect destructive interactions between the EXAFS modulations for the principal Fe–N_{eq} shell and those of the Fe–N_{ax} shell.

First-shell fits to **3-CN** afford a best fit with a single shell of 3 to 4 Fe–N scatterers at 2.01 Å, with the shortening in this distance relative to **2-CN** being consistent with the smaller ionic radius of iron(III). Although a crystal structure of **3-CN** is not presently available, the refined bond lengths for this shell compare favorably to the average Fe–N_{eq} distances of 2.028 Å and 2.021 Å obtained for **3-N_3** and **3-F**.[185] It was not possible to uniquely refine either Fe–C_{CN} or Fe–N_{ax} distances for **3-CN**, since the fits obtained generally exhibited either poorer fit quality or chemically implausible Debye-Waller factors, or both. We favor fit **3-CN**-C (Table 6.5, Figure 6.12) with 4 Fe–N scatterers as the best fit as it more closely reflects the presumed coordination number of five for this species (we expect *r*(Fe–C_{CN}) to be similar to r(Fe–N_{eq}) by analogy to **2-CN**) without a significant loss of fit quality, in contrast to the result obtained for **2-CN**.

Unexpectedly, we were able to resolve two distinct shells of scatterers for **4-CN**, with the best fit consisting of 3 Fe–N scatterers at 1.81 Å assigned to the three equatorial N_{eq} donors and 1 Fe–N at 2.03 Å that can be assigned to the axial capping nitrogen (fit I, Table 6.5 and Figure 6.12). The difference of 0.22 Å for the Fe–N_{eq} and Fe–N_{ax} shells is in good agreement with the difference of 0.192 Å for these bond lengths in **2-CN**, and other crystallographically characterized **2-X** and **3-X** complexes exhibit differences of

similar magnitude.[185,229] The *ca.* 0.2 Å compression in the Fe–N_{eq} distance compared to **3-CN** is consistent with conversion from the high-spin $S = 5/2$ Fe(III) center in **3-CN** to a low-spin $S = 0$ iron(IV) center for **4-CN** in which the d-orbitals have contracted significantly, affording a dramatic shortening of the average bond length. We are unable to offer an explanation at present for why the axial nitrogen can be uniquely resolved in **4-CN** alone, and not in **2-CN**, **3-CN**, **3-OH**, or **4-O**.

We then turned to an analysis of the unfiltered EXAFS data for **2-CN**, **3-CN**, and **4-CN**, and obtained an identical set of best fits to the first shell (see Tables A6.1 – A6.3 in the Appendix). However, fits to the outer-shell feature analogous to those for **3-OH** and **4-O** with a combination of two shells of single-scattering Fe•••C and Fe•••C/N interactions did not accurately reproduce the experimental $k^3\chi(k)$ EXAFS data, particularly at low k. This is nicely illustrated for **2-CN**, in which a fit with 6 Fe•••C at 3.06 Å and 7 Fe•••C/N at 3.42 Å, although matching the Fourier transform quite nicely, exhibits a clear mismatch to the experimental $k^3\chi(k)$ EXAFS with a clear pattern of oscillations in the residual (fit 8b, Table 6.6 and Figure 6.13. Similar conclusions can be drawn for **3-CN** (Table 6.7, Figure 6.14) and **4-CN** (Table 6.8, Figure 6.15). This suggests that multiple-scattering effects involving the linearly coordinated Fe–C≡N moiety may contribute significantly to the EXAFS of the **CN** series of complexes.

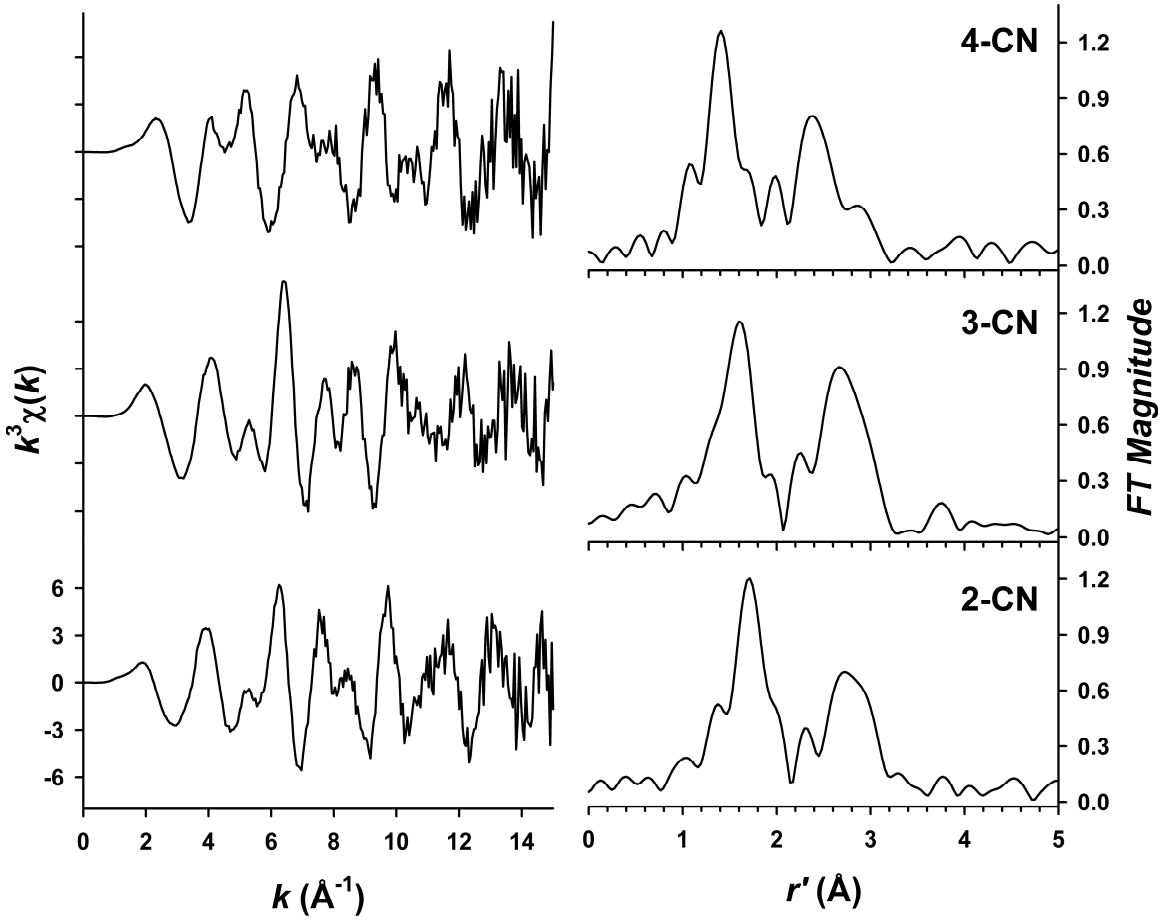

Figure 6.10. (left) Comparison of the $k^3\chi(k)$ weighted EXAFS data for **2-CN** (bottom), **3-CN** (middle), and **4-CN** (top) The y-axis scaling is identical for all plots. (right) Comparison of the Fourier transforms of **2-CN** (bottom), **3-CN** (middle), and **4-CN** (top). FT ranges were as follows: **2-CN**, $k = 2 - 14.8$ Å^{-1}; **3-CN**, $k = 2 - 14.5$ Å^{-1}; **4-CN**, $k = 2 - 14.8$ Å^{-1}.

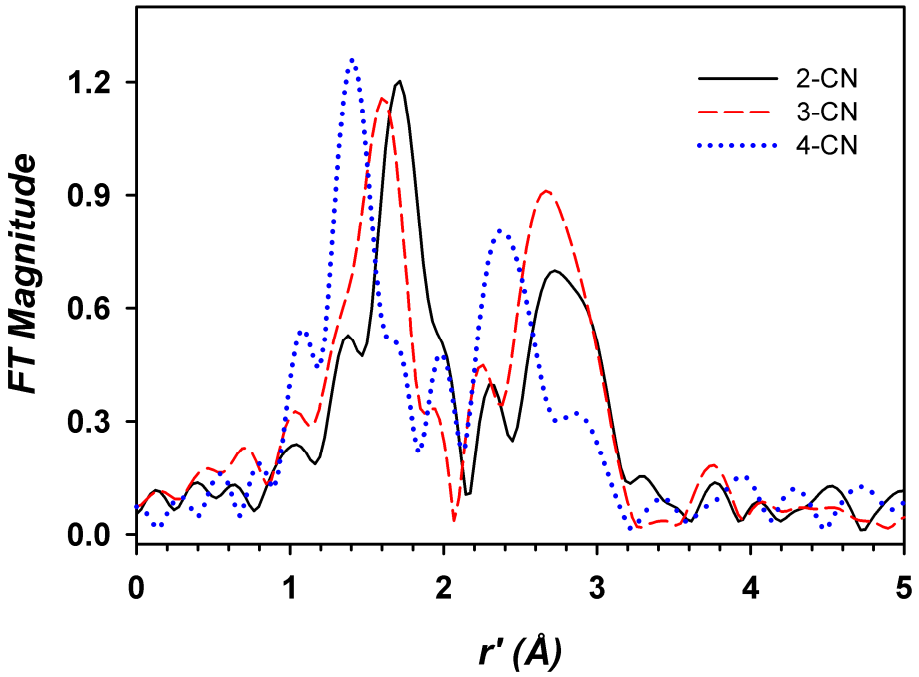

Figure 6.11. An overlay plot comparison of the Fourier transforms of **2-CN**, **3-CN**, and **4-CN**, identical to those shown in Figure 6.10. FT ranges were as follows: **2-CN**, k = 2 – 14.8 Å^{-1} (black, ——); **3-CN**, k = 2 – 14.5 Å^{-1} (red, – – –); **4-CN**, k = 2 – 14.8 Å^{-1} (blue, ·····).

Table 6.5. Analyses of Fourier-filtered EXAFS Data for **2-CN**, **3-CN**, and **4-CN**.[a]

		Fe-N			Fe-C/N				
Species	**fit**	**n**	**r**	**σ^2**	**n**	**r**	**σ^2**	**F [b]**	***F'* [b]**
	A	2	2.09	-0.4				36.4	138
	B	***3***	***2.09***	***1.1***				***15.2***	***24***
	C	4	2.09	2.4				33.5	117
	D	5	2.08	3.8				77.1	619
2-CN	F[c]	2	2.07	0.0	1	2.15	-1.1	12.7	21
	G[c]	3	2.09	4.3	1	2.10	-1.2	20.5	55
	H[c]	2	2.10	0.3	1	2.06	2.9	14.5	28
	I[c]	3	2.09	1.1	1	2.35	20.8	13.7	25
	J[c]	4	2.09	2.5	1	2.36	4.2	20.5	56
	A	2	2.01	0.7				48.4	276
	B	*3*	*2.01*	*2.4*				*14.2*	*24*
	C	***4***	***2.01***	***4.0***				***17.2***	***35***
	D	5	2.01	5.6				44.3	230
3-CN	F[c]	2	1.99	0.6	1	2.10	-0.8	17.0	44
	G[c]	3	2.01	2.5	1	2.18	39.5	13.4	28
	H[c]	2	2.04	0.7	1	1.95	0.5	11.8	21
	I[c]	3	2.02	2.5	1	2.12	24.4	13.0	26
	J[c]	4	2.02	3.9	1	2.29	9.9	13.4	27
	A	2	1.81	0.6				11.6	19
	B	3	1.80	2.3				26.6	98
	C	4	1.80	3.9				80.5	900
	D	5	1.80	5.9				151.6	3192
4-CN	F[c]	2	1.83	5.8	1	1.82	-1.7	8.2	13
	G[c]	3	1.81	11.7	1	1.82	-2.1	16.4	51
	H[c]	2	1.81	0.6	1	1.94	13.1	7.6	11
	I [c]	***3***	***1.81***	***2.2***	***1***	***2.03***	***3.5***	***13.5***	***35***
	J[c]	4	1.81	4.1	1	2.04	0.8	40.7	319

[a] *r* is in units of Å; σ^2 is in units of 10^{-3} Å^2. All fits are to Fourier-filtered data, as follows: **2-CN**, Fourier transform range of k = 2.0 – 14.8 Å^{-1} (resolution = 0.123 Å), back-transformation range = 0.7 – 2.25 Å; **3-CN**, k = 2.0 – 14.5 Å^{-1} (resolution = 0.126 Å), back-transformation range = 0.7 – 2.15 Å; **4-CN**, k = 2.0 – 14.8 Å^{-1} (resolution = 0.123 Å), back-transformation range = 0.7 – 1.95 Å.

[b] Goodness-of-fit parameter F defined as $\Sigma(\chi_{exptl}-\chi_{calc})^2$. A second parameter, *F'*, is defined as $F' = F^2 / \nu$, where $\nu = N_{IDP} - N_{VAR}$. N_{IDP} is the number of independent data points, while N_{VAR} is the number of floated variables in each optimization step. The values of *F'* shown have been divided by a factor of 10^4 for convenience. *F'* is a measure of whether an added shell significantly improves the fit.

[c] For **2-CN**, **3-CN**, and **4-CN**, the Fe-C/N shell was fit with parameters for a Fe–C scatterer arising from coordinated cyanide (fits F and G) or parameters for a Fe–N scatterer arising from the long Fe–N_{ax} scatterer (fits H, I, J). EXAFS cannot distinguish between backscatterers differing by Z = 1.

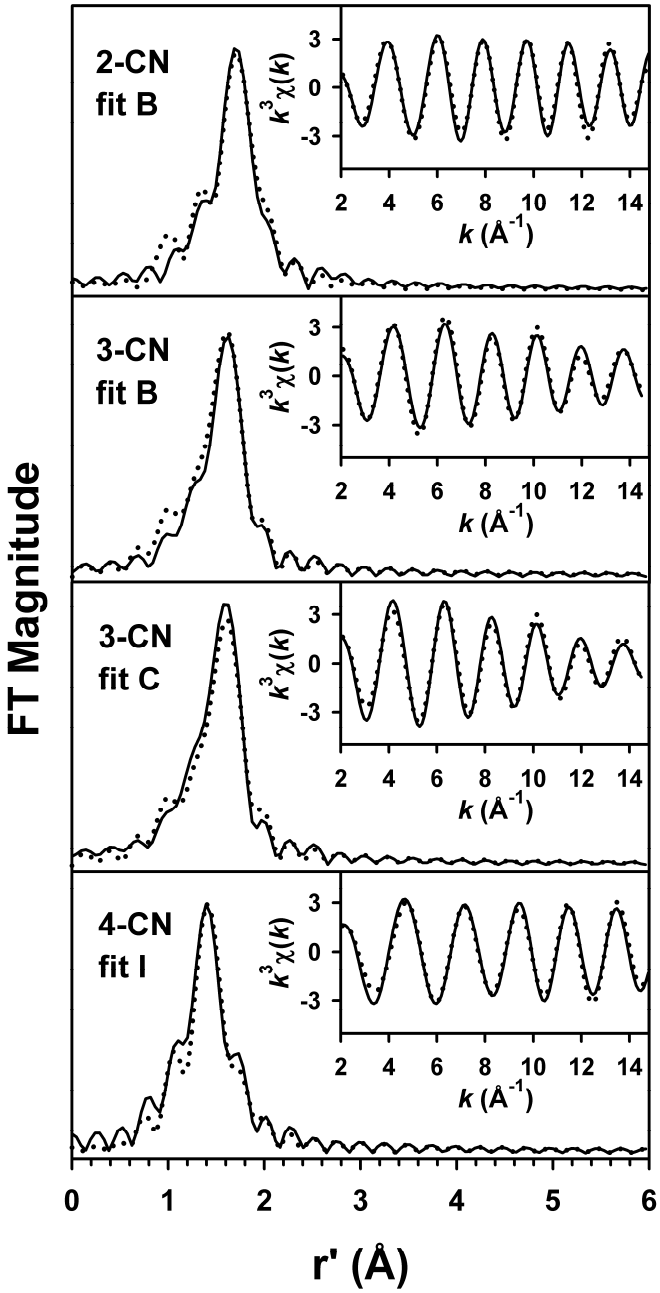

Figure 6.12. Fits to the Fourier transforms of the Fe K-edge EXAFS data ($k^3\chi(k)$) and Fourier-filtered EXAFS spectra ($k^3\chi(k)$, insets) for **2-CN**, **3-CN**, and **4-CN**. Experimental data is shown with dotted lines (•••), while fits are shown with solid lines (——). **2-CN**, Fourier transform range of k = 2.0 – 14.8 Å^{-1}, back-transformation range = 0.7 – 2.25 Å; **3-CN**, k = 2.0 – 14.5 Å^{-1}, back-transformation range = 0.7 – 2.15 Å; **4-CN**, k = 2.0 – 14.8 Å^{-1}, back-transformation range = 0.7 – 1.95 Å. Fit parameters associated with the stated fit are shown in Table 6.5.

The treatment of multiple-scattering contributions from linearly coordinated diatomic ligands such as CN[245-247] or NO[248-254] in EXAFS analysis is fairly well developed.[255] A typical Fe–C≡N moiety would be expected to exhibit a weak two-body Fe–N single-scattering path, a degenerate pair of three-body paths involving all three atoms, and a single four-body path (Scheme 6.3), in addition to a single-scattering Fe–C path. When the Fe–C≡N bond angle is approximately 180°, as is the case for **2-CN**, the lengths of all these paths will be identical, while the path lengths for the respective two-, three-, and four-body paths will obviously differ for bent Fe–CN moieties. In our analysis of **2-CN**, **3-CN**, and **4-CN** for multiple-scattering effects from coordinated cyanide, we assumed that there was only a single cyanide ligand with an Fe–C≡N bond angle of 180°, on the premise that the steric congestion of the supporting TMG_3tren ligand would preclude a bent binding mode *in solution*. We also assumed that the C≡N bond length (1.15 Å) in **2-CN** was unchanged in **3-CN** or **4-CN**.

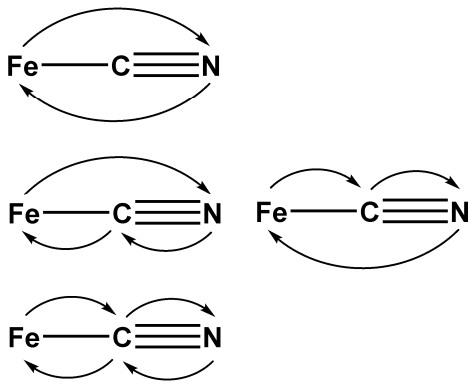

Scheme 6.3. Photoelectron scattering paths for a linear Fe–C≡N moiety, all of which will have equal pathlengths. There are two degenerate three body paths.

Addition of scattering contributions from a cyanide ligand to our fits of **2-CN** lead to a significant improvement in fit quality to fits with either one or two shells of Fe•••C/N scatterers, suggesting that the cyanide multiple-scattering paths contribute significantly to the observed EXAFS (Table 6.6). The best fit, consisting of 3 Fe–N at 2.09 Å, 4 Fe•••C at 3.05 Å, 5 Fe•••C/N at 3.42 Å, and a linearly coordinated cyanide with path lengths of 3.28 Å, exhibits an excellent agreement to experimental data with a flat residual (fit 9j, Table 6.6 and Figure 6.13). The cyanide path length is in excellent agreement with the Fe•••N_{CN} distance of 3.279 Å obtained in the **2-CN** crystal structure. We note that the fit quality is not especially sensitive to the total numbers of Fe•••C/N scatterers. Several fits were also carried out in which the Fe–C_{CN} path was included in the fit and the length of this path linked to the multiple scattering paths of the cyanide ligand. This approach is analogous to that employed in Chapter 3 of this thesis and elsewhere[144,145,147,149,152,153] to obtain metal–N_{His} bond lengths distinct from other first-shell ligands. For **2-CN**, this approach results in fits similar in quality to those presented above, with a refined Fe–N_{eq} distance of 2.08 Å and an Fe–C_{CN} distance of 2.11 Å, both of which are in good agreement with the crystallographic values of 2.1097(12) Å and 2.1293(15) Å, respectively (fit 10a, Table 6.6 and Figure 6.13). However, the Debye-Waller factor for the Fe–C_{CN} shell is unusually negative, suggesting a far more ordered and rigid Fe–C bond than theoretically predicted for this distance, and fits in which the Debye-Waller factor was fixed at a small positive value were not possible. We thus conclude that the data does not support independent refinement of the Fe–C_{CN} bond length in **2-CN**.

Multiple scattering EXAFS analysis of **3-CN** revealed a similar sequence of fits as encountered for **2-CN**. The cyanide-derived multiple-scattering pathways significantly

improved the agreement of fits with experimental data, with the best fit consisting of 4 Fe–N scatterers at 2.01 Å, 5 Fe•••C scatterers at 2.99 Å, 7 Fe•••C/N at 3.39 Å, and a linearly coordinated cyanide with path lengths of 3.22 Å (fit 9j, Table 6.7 and Figure 6.14). The shortening of the outer-shell scatterer distances by *ca.* 0.05 - 0.1 Å is consistent with the shortening in Fe(III)-ligand distances observed in our earlier fits. Unlike our experience with **2-CN**, it was possible to independently refine an Fe–C_{CN} distance linked to the cyanide multiple-scattering paths for **3-CN**, provided that the Debye-Waller factor for this path was constrained to a chemically reasonable value (compare fit 10a with fits 10, 10b, 10c in Table 6.7). This approach yields 3 Fe–N_{eq} at 2.01 Å and 1 Fe–C_{CN} at 2.07 Å (fit 10, Table 6.7 and Figure 6.14), although we note that the refined Fe–C_{CN} distance is predicated on identical C≡N bond lengths in **2-CN** and **3-CN**.

EXAFS analysis of the outer-shell features of **4-CN** suggested differences in the progression of best fits relative to **2-CN** and **3-CN**. For example, the improvement in single-scattering fits when the second Fe•••C/N shell is added is much more modest, although the visual agreement with the Fourier transform and the $k^3\chi(k)$ EXAFS at low k is much improved when it is included (compare fits 6b and 8b in Table 6.8 and Figure 6.15). In addition, inclusion of multiple-scattering paths from a coordinated cyanide ligand led to relatively small improvements in fit quality as measured by the goodness-of-fit parameters F and F-factor relative to fits employing only single-scattering paths. Indeed, the fit parameter *F'*, which corrects for the effect of additional shells,[88,89] increases when the cyanide paths are including, indicating that this inclusion is not justified on quality-of-fit grounds alone (compare fits 8b and 9m in Table 6.8). However,

^{13}C NMR studies of **4-^{13}CN** reveal a ^{13}CN resonance that exhibits coupling to the S = ½ nucleus of ^{57}Fe when ^{57}Fe-labeled **4-^{13}CN** is employed in the NMR experiment, providing direct evidence for cyanide binding in **4-CN** (Jason England, unpublished observations). Similarly, EXAFS fits that include the cyanide ligand exhibit a significantly better agreement to experimental data than those without (Figures 6.15, 6.16). It is possible that the cyanide ligand exhibits a different binding geometry than that assumed in our structural model for EXAFS analysis, and studies on this point are presently ongoing. The best fit to the data for 4-CN consists of 3 Fe–N scatterers at 1.81, 3 Fe–N at 2.03 Å, 5 Fe•••C scatterers at 2.85 Å, 4 Fe•••C/N at 3.45 Å, and a linearly coordinated cyanide with path lengths of 3.08 Å (fit 9l, Table 6.8 and Figure 6.16). The shortening of the distances for the first Fe•••C shell and the cyanide moiety is in good agreement with the compression in inner-shell distances relative to **3-CN**. Independent refinement of the Fe–C_{CN} distance resulted in fits in which it was not necessary to fix the Debye-Waller factor for the Fe–C_{CN} shell to obtain chemically reasonable fit parameters (unlike **2-CN** and **3-CN**), with the principal inner shell being split into 2-3 Fe–N_{eq} at *ca.* 1.81 Å and 1 Fe–C_{CN} at 1.88 Å (fits 10 and 10a, Table 6.8 and Figure 6.16). Notably, a significantly better fit to the inner-shell feature is obtained when the Fe–N_{eq} coordination number is underestimated, suggesting significant destructive interference between the Fe–N_{eq} and Fe–C_{CN} shells. We emphasize that these fits implicitly assume a C≡N distance of 1.15 Å, which may in fact not be the case for **4-CN**. We conclude that our EXAFS analysis of **2-CN**, **3-CN**, and **4-CN** has provided strong supporting evidence for the coordination of cyanide to the iron center in a linear fashion, leading to enhanced

intensity of the outer-shell features in the Fourier transform that we were able to associate solely with single scattering paths in **3-OH** and **4-O**.

Table 6.6. Multiple-Scattering Analysis of Unfiltered EXAFS Data for **2-CN**.[a]

	Fe-N/C			Fe•••C			Fe•••C=N					
fit	**n**	**r**	**σ^2**	**n**	**r**	**σ^2**	**n**	**r**	**σ^2**	**F [b]**	***F*-factor [b]**	***F'* [b]**
2	3	2.09	0.8							640	0.615	2.07
6a	3	2.09	0.8	4	3.06	1.9				486	0.535	1.32
7a	3	2.09	0.9	5	3.41	1.4				488	0.536	1.34
8b	*3*	*2.09*	*0.9*	*6* *7*	*3.06* *3.42*	*3.0* *2.6*				*250*	*0.384*	*0.39*
9	3	2.09	0.6				2,1,1	3.27	0.9	328	0.440	0.61
9a	3	2.09	0.8	3	3.03	-0.1	2,1,1	3.29	-0.1	250	0.384	0.40
9b	3	2.09	0.7	4	3.03	1.4	2,1,1	3.28	0.4	272	0.401	0.47
9c	3	2.09	0.7	5	3.03	4.4	2,1,1	3.27	1.1	302	0.422	0.58
9d	3	2.09	0.7	6	3.03	5.3	2,1,1	3.27	1.2	329	0.441	0.69
9e	3	2.09	0.6	3	3.44	-0.1	2,1,1	3.25	0.5	274	0.402	0.47
9f	3	2.09	0.6	4	3.44	1.0	2,1,1	3.25	0.6	283	0.408	0.51
9g	3	2.09	0.6	5	3.44	2.9	2,1,1	3.26	1.0	293	0.416	0.54
9h	3	2.09	0.6	6	3.44	4.8	2,1,1	3.26	1.2	306	0.425	0.59
9i	3	2.09	0.8	4 4	3.05 3.43	3.3 2.3	2,1,1	3.27	2.3	199	0.343	0.29
9j	***3***	***2.09***	***0.8***	***4*** ***5***	***3.05*** ***3.42***	***2.8*** ***5.0***	***2,1,1***	***3.28***	***2.0***	***196***	***0.340***	***0.28***
9k	3	2.09	0.8	5 5	3.05 3.42	4.7 3.7	2,1,1	3.27	0.3	199	0.343	0.29
9l	3	2.09	0.8	4 6	3.05 3.42	2.1 8.2	2,1,1	3.29	1.3	193	0.338	0.27
9m	3	2.09	0.8	5 6	3.05 3.42	4.3 5.5	2,1,1	3.28	2.8	197	0.341	0.28
9n	3	2.09	0.8	6 7	3.06 3.42	5.7 6.7	2,1,1	3.28	2.9	199	0.343	0.29
10	3 1	2.09 2.10	1.2 7.3	4 5	3.06 3.41	1.9 1.4	2,1,1	3.24	7.3	222	0.362	0.36
10a	*3* *1*	*2.08* *2.11*	*6.2* *-2.6*	*4* *5*	*3.06* *3.43*	*4.8* *2.9*	*2,1,1*	*3.25*	*1.9*	*189*	*0.334*	*0.28*
10b	2 1	2.08 2.12	1.6 -1.6	4 5	3.04 3.42	3.7 4.4	2,1,1	3.27	1.8	185	0.331	0.27
10c	3 1	2.08 2.12	1.9 0.9				2,1,1	3.26	0.9	356	0.459	0.71
10d	3 1	2.06 2.11	6.3 -3.0				2,1,1	3.25	0.6	309	0.427	0.54
10e	2 1	2.07 2.12	2.6 -2.6				2,1,1	3.26	0.5	306	0.425	0.53

[a] *r* is in units of Å; σ^2 is in units of 10^{-3} Å^2. All fits are to unfiltered data. Fourier transform range k = 2.0 – 14.8 Å^{-1} (resolution = 0.123 Å).

[b] Goodness-of-fit parameter F defined as $\Sigma(\chi_{exptl}-\chi_{calc})^2$. *F-factor* = $[\Sigma k^6(\chi_{exptl}-\chi_{calc})^2 / \Sigma k^6\chi_{exptl}^2]^{1/2}$. A third parameter, *F'*, is defined as $F' = F^2 / \nu$, where $\nu = N_{IDP} - N_{VAR}$. N_{IDP} is the number of independent data points, while N_{VAR} is the number of floated variables in each optimization step. The values of *F'* shown have been divided by a factor of 10^4 for convenience. *F'* is a measure of whether an added shell significantly improves the fit.

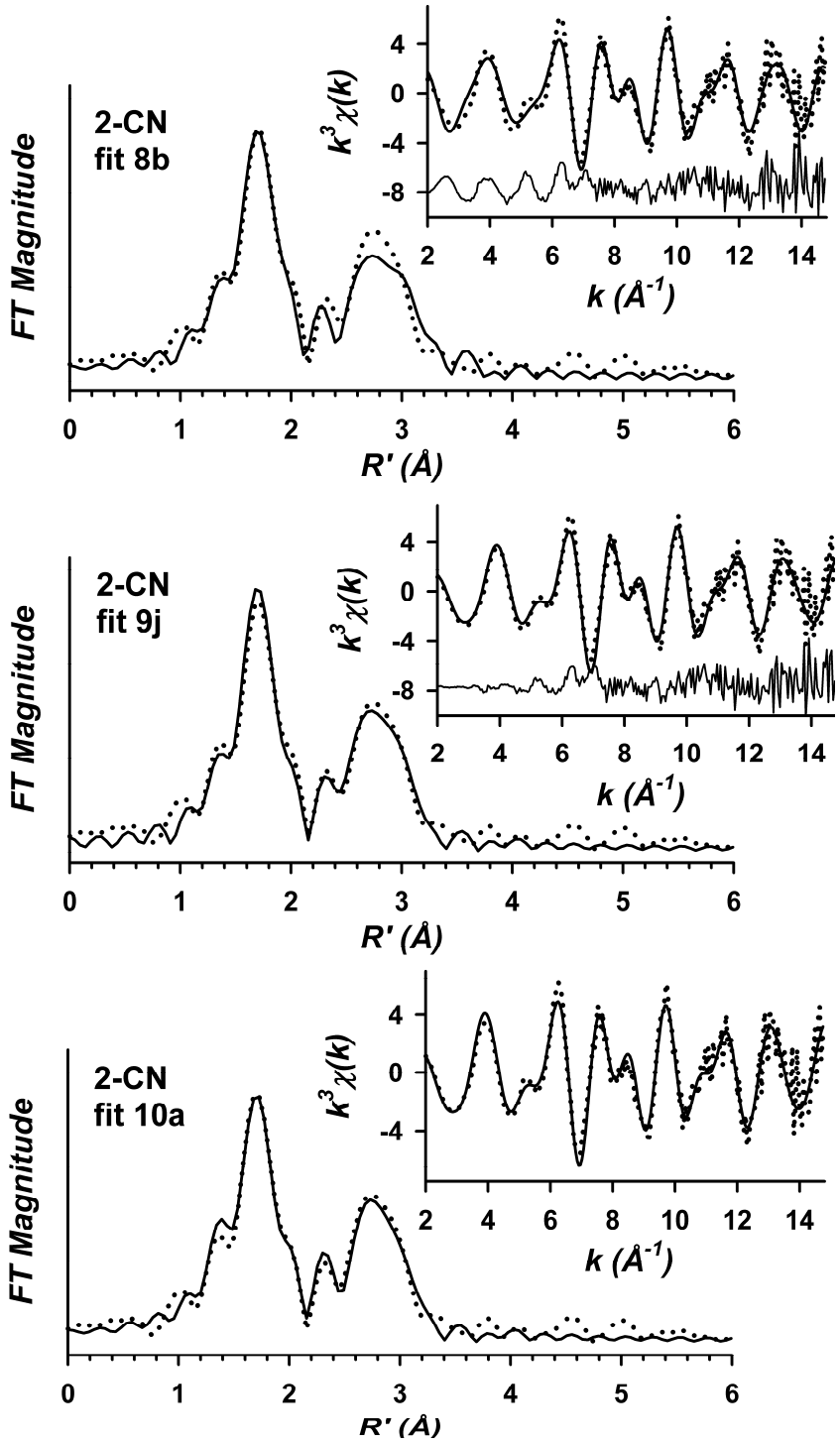

Figure 6.13. Fits to the Fourier transforms of the Fe K-edge EXAFS data ($k^3\chi(k)$) and unfiltered EXAFS spectra ($k^3\chi(k)$, insets) for **2-CN**. Experimental data is shown with dotted lines (•••), fits are shown with solid lines (——), and the offset fit residual (fits 8b and 9j only) is shown as a thin solid line. Fourier transformation range: $k = 2 - 14.8$ Å^{-1}. Fit parameters associated with the stated fit are shown in Table 6.6.

Table 6.7. Multiple-Scattering Analysis of Unfiltered EXAFS Data for **3-CN**.[a]

	Fe-N/C			Fe•••C			Fe•••C=N					
fit	**n**	**r**	**σ^2**	**n**	**r**	**σ^2**	**n**	**r**	**σ^2**	**F**	***F*-factor**	***F'***
2	3	2.02	2.1							943	0.703	5.02
3	4	2.01	3.7							943	0.703	5.02
6a	4	2.01	3.7	5	3.00	1.7				655	0.586	2.74
7d	4	1.99	3.8	8	3.35	3.0				677	0.596	2.92
8b	*4*	*2.01*	*3.9*	*6* *8*	*3.00* *3.39*	*1.9* *2.9*				*317*	*0.408*	*0.74*
9	4	2.01	3.4				2,1,1	3.21	1.7	576	0.550	2.11
9a	4	2.01	3.8	4	2.98	-0.9	2,1,1	3.24	-0.2	368	0.439	0.99
9b	4	2.01	3.8	5	2.98	0.3	2,1,1	3.24	0.3	396	0.455	1.15
9c	4	2.01	3.7	6	2.98	1.6	2,1,1	3.24	0.9	429	0.474	1.35
9d	4	2.01	3.7	7	2.98	2.6	2,1,1	3.24	1.6	466	0.494	1.59
9e	4	2.00	3.7	4	3.37	-1.4	2,1,1	3.16	-0.1	399	0.457	1.16
9f	4	1.99	3.7	6	3.37	0.3	2,1,1	3.16	0.2	397	0.456	1.15
9g	4	1.99	3.7	8	3.37	1.6	2,1,1	3.15	0.5	405	0.460	1.20
9h	4	1.99	3.8	10	3.36	2.7	2,1,1	3.15	0.7	419	0.469	1.28
9i	4	2.01	3.7	5 5	2.99 3.39	1.9 2.2	2,1,1	3.22	2.3	263	0.371	0.59
9j	***4***	***2.01***	***3.8***	***5*** ***7***	***2.99*** ***3.39***	***1.6*** ***4.8***	***2,1,1***	***3.23***	***2.4***	***254***	***0.365***	***0.55***
9k	4	2.01	3.7	5 6	2.99 3.39	1.8 3.4	2,1,1	3.22	2.6	257	0.367	0.56
9l	4	2.01	3.7	6 6	2.99 3.39	3.2 3.2	2,1,1	3.21	3.4	263	0.371	0.59
9m	4	2.01	3.8	6 7	2.99 3.39	3.3 3.8	2,1,1	3.21	3.8	259	0.368	0.57
9n	4	2.01	3.7	6 8	2.99 3.39	3.1 5.0	2,1,1	3.22	3.9	257	0.367	0.56
10	***3*** ***1***	***2.01*** ***2.06***	***3.2*** ***3.3***	***5*** ***7***	***2.99*** ***3.39***	***2.0*** ***4.1***	***2,1,1***	***3.22***	***3.3***	***253***	***0.363***	***0.54***
10a	3 1	2.01 2.07	2.2 27.1	5 7	2.99 3.40	1.9 4.7	2,1,1	3.23	2.4	240	0.354	0.54
10b	*3* *1*	*2.01* *2.07*	*2.8* *5**	*5* *7*	*2.99* *3.39*	*2.0* *4.2*	*2,1,1*	*3.22*	*2.9*	*250*	*0.362*	*0.53*
10c	*3* *1*	*2.00* *2.06*	*3.4* *2.5**	*5* *7*	*2.99* *3.39*	*2.0* *4.1*	*2,1,1*	*3.22*	*2.9*	*253*	*0.364*	*0.55*
10d	3 1	2.00 2.05	3.5 1.6				2,1,1	3.20	1.6	569	0.546	2.06
10a	3 1	2.00 2.05	3.2 2.5				2,1,1	3.20	1.6	570	0.546	2.21

[a] *r* is in units of Å; σ^2 is in units of 10^{-3} Å^2. All fits are to unfiltered data. Fourier transform range k = 2.0 – 14.5 Å^{-1} (resolution = 0.126 Å). In fits 10b and 10c, σ^2 was fixed to the given value.

[b] Goodness-of-fit parameter F defined as $\Sigma(\chi_{exptl}-\chi_{calc})^2$. *F-factor* = $[\Sigma k^6(\chi_{exptl}-\chi_{calc})^2 / \Sigma k^6\chi_{exptl}^2]^{1/2}$. A third parameter, *F'*, is defined as $F' = F^2 / \nu$, where $\nu = N_{IDP} - N_{VAR}$. N_{IDP} is the number of independent data points, while N_{VAR} is the number of floated variables in each optimization step. The values of *F'* shown have been divided by a factor of 10^4 for convenience. *F'* is a measure of whether an added shell significantly improves the fit.

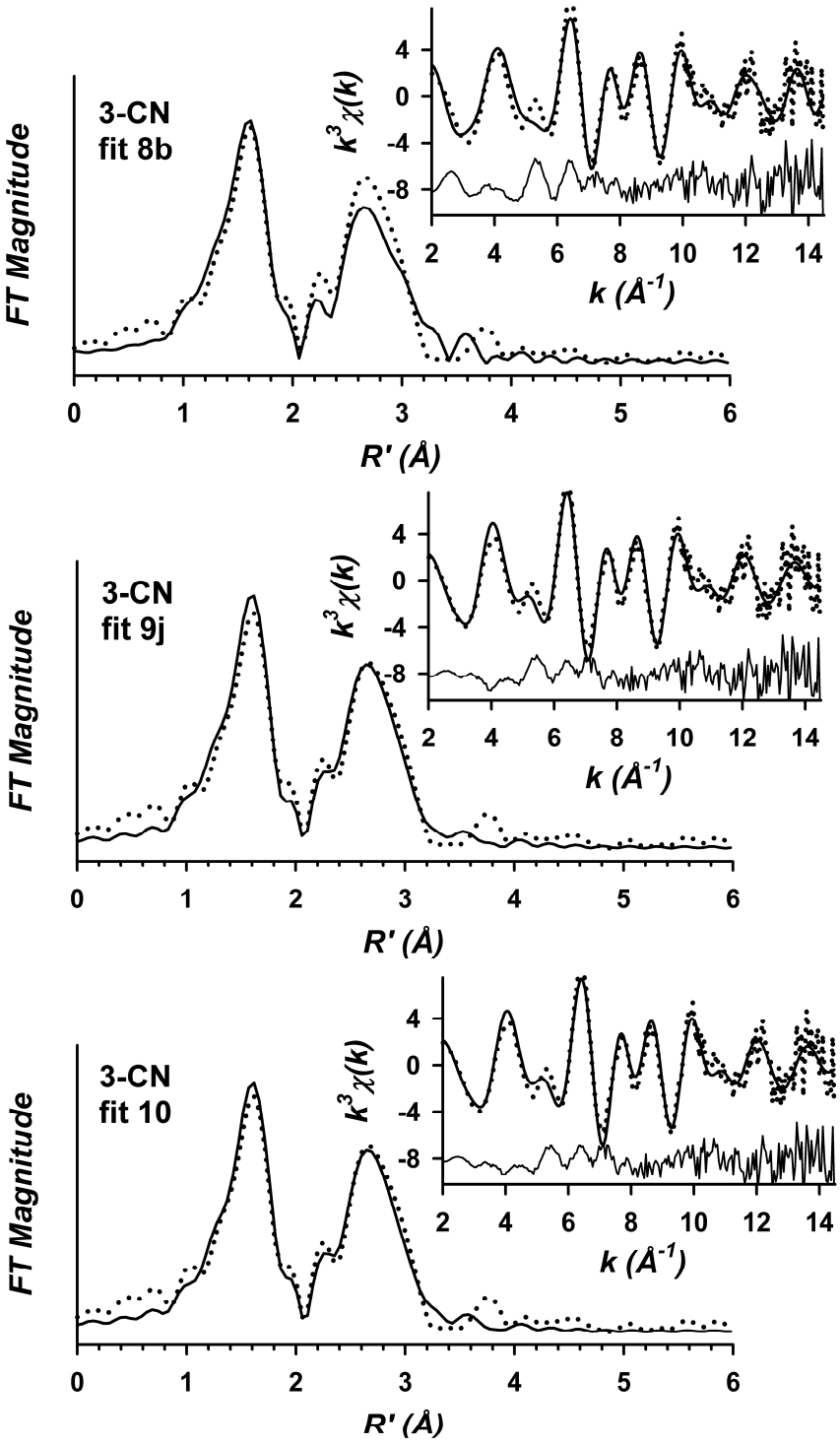

Figure 6.14. Fits to the Fourier transforms of the Fe K-edge EXAFS data ($k^3\chi(k)$) and unfiltered EXAFS spectra ($k^3\chi(k)$, insets) for **3-CN**. Experimental data is shown with dotted lines (•••), fits are shown with solid lines (——), and the offset fit residual with a thin solid line. Fourier transformation range: $k = 2 - 14.5$ Å^{-1}. Fit parameters associated with the stated fit are shown in Table 6.7.

Table 6.8. Multiple-Scattering Analysis of Unfiltered EXAFS Data for **4-CN**.[a]

	Fe-N/C			Fe-N			Fe•••C			Fe•••C=N					
fit	**n**	**r**	**σ^2**	**n**	**r**	**σ^2**	**n**	**r**	**σ^2**	**n**	**r**	**σ^2**	**F**	***F*-factor**	***F'***
5	3	1.82	2.1	1	2.03	1.3							815	0.664	3.65
6b	*3*	*1.83*	*2.2*	*1*	*2.04*	*0.4*	*6*	*2.87*	*2.5*				*434*	*0.485*	*1.16*
8b	*3*	*1.83*	*2.2*	*1*	*2.04*	*0.3*	*6* *4*	*2.86* *3.46*	*2.2* *3.7*				*388*	*0.459*	*0.93*
9	3	1.81	2.4	1	2.04	1.5				2,1,1	3.04	1.9	544	0.543	2.09
9a	3	1.82	2.1	1	2.03	1.5	3	2.83	-0.7	2,1,1	3.09	1.2	367	0.446	1.11
9b	3	1.82	2.1	1	2.03	1.3	4	2.84	0.8	2,1,1	3.09	2.4	372	0.449	1.13
9c	*3*	*1.82*	*2.2*	*1*	*2.03*	*1.2*	*5*	*2.85*	*2.3*	*2,1,1*	*3.08*	*3.9*	*380*	*0.453*	*1.18*
9d	3	1.82	2.2	1	2.04	1.0	6	2.86	3.4	2,1,1	3.07	5.5	388	0.459	1.24
9e	3	1.81	2.4	1	2.04	1.5	3	3.44	2.7	2,1,1	3.04	1.8	507	0.524	2.10
9f	3	1.81	2.4	1	2.04	1.4	4	3.43	5.5	2,1,1	3.04	1.9	504	0.522	2.08
9g	3	1.81	2.5	1	2.05	1.4	5	3.40	9.5	2,1,1	3.04	1.8	501	0.521	2.05
9h	3	1.81	2.5	1	2.05	1.3	6	3.39	12.3	2,1,1	3.04	1.8	498	0.519	2.03
9i	3	1.82	2.1	1	2.03	1.4	4 4	2.84 3.45	0.8 3.5	2,1,1	3.08	2.3	325	0.419	1.03
9j	3	1.82	2.1	1	2.03	1.5	4 5	2.84 3.45	0.7 4.8	2,1,1	3.08	2.1	326	0.420	1.04
9k	3	1.82	2.1	1	2.03	1.3	5 5	2.85 3.45	2.2 4.7	2,1,1	3.08	3.5	335	0.426	1.10
9l	***3***	***1.82***	***2.1***	***1***	***2.03***	***1.3***	***5*** ***4***	***2.85*** ***3.45***	***2.2*** ***3.4***	***2,1,1***	***3.08***	***3.5***	***333***	***0.425***	***1.09***
9m	3	1.82	2.2	1	2.03	1.1	6 4	2.86 3.46	3.3 3.4	2,1,1	3.06	5.1	341	0.430	1.14
9n	3	1.82	2.1	1	2.03	1.2	5 3	2.85 3.45	2.2 2.0	2,1,1	3.08	4.0	333	0.425	1.09

10	*3* *1*	*1.82* *1.88*	*3.4* *4.1*	*1*	*2.04*	*-0.6*	*5* *4*	*2.85* *3.45*	*2.5* *3.5*	*2,1,1*	*3.06*	*4.1*	*360*	*0.442*	*1.27*
10a	*2* *1*	*1.81* *1.89*	*0.8* *3.6*	*1*	*2.04*	*1.9*	*5* *4*	*2.85* *3.45*	*2.2* *3.3*	*2,1,1*	*3.07*	*3.6*	*330*	*0.423*	*1.07*
10b	3 1	1.82 1.88	3.4 4.1	1	2.04	-0.6	5 4	2.85 3.45	2.5 3.5	2,1,1	3.06	4.0	360	0.442	1.41
10c	3 1	1.80 1.87	4.4 1.6	1	2.04	-0.6				2,1,1	3.03	1.6	539	0.540	2.05
10d	3 1	1.79 1.86	5.0 -0.9	1	2.03	-0.4				2,1,1	3.02	1.5	537	0.540	2.19

[a] *r* is in units of Å; σ^2 is in units of 10^{-3} Å^2. All fits are to unfiltered data. Fourier transform range k = 2.0 – 14.8 Å^{-1} (resolution = 0.123 Å).

[b] Goodness-of-fit parameter F defined as $\Sigma(\chi_{exptl}-\chi_{calc})^2$. *F-factor* = $[\Sigma k^6(\chi_{exptl}-\chi_{calc})^2 / \Sigma k^6\chi_{exptl}^2]^{1/2}$. A third parameter, *F'*, is defined as $F' = F^2 / \nu$, where $\nu = N_{IDP} - N_{VAR}$. N_{IDP} is the number of independent data points, while N_{VAR} is the number of floated variables in each optimization step. The values of *F'* shown have been divided by a factor of 10^4 for convenience. *F'* is a measure of whether an added shell significantly improves the fit.

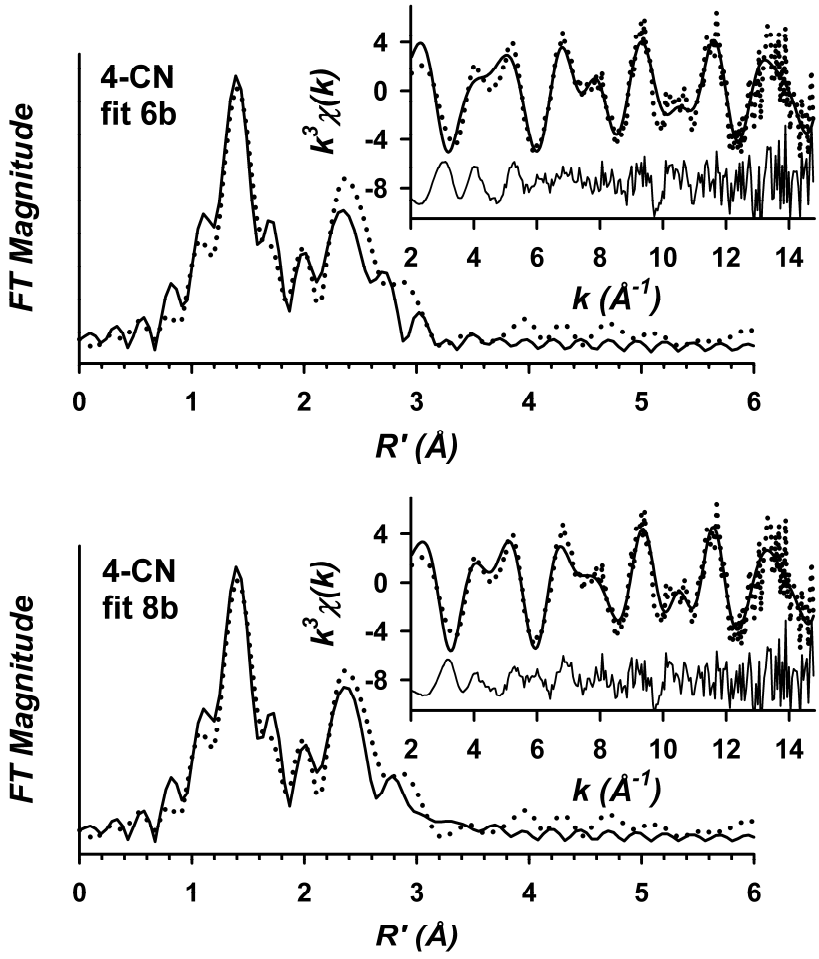

Figure 6.15. Single-scattering fits to the Fourier transforms of the Fe K-edge EXAFS data ($k^3\chi(k)$) and unfiltered EXAFS spectra ($k^3\chi(k)$, insets) for **4-CN**. Experimental data is shown with dotted lines (•••), fits are shown with solid lines (——), and the offset fit residual with a thin solid line. Fourier transformation range: k = 2 – 14.8 Å^{-1}. Fit parameters associated with the stated fit are shown in Table 6.8.

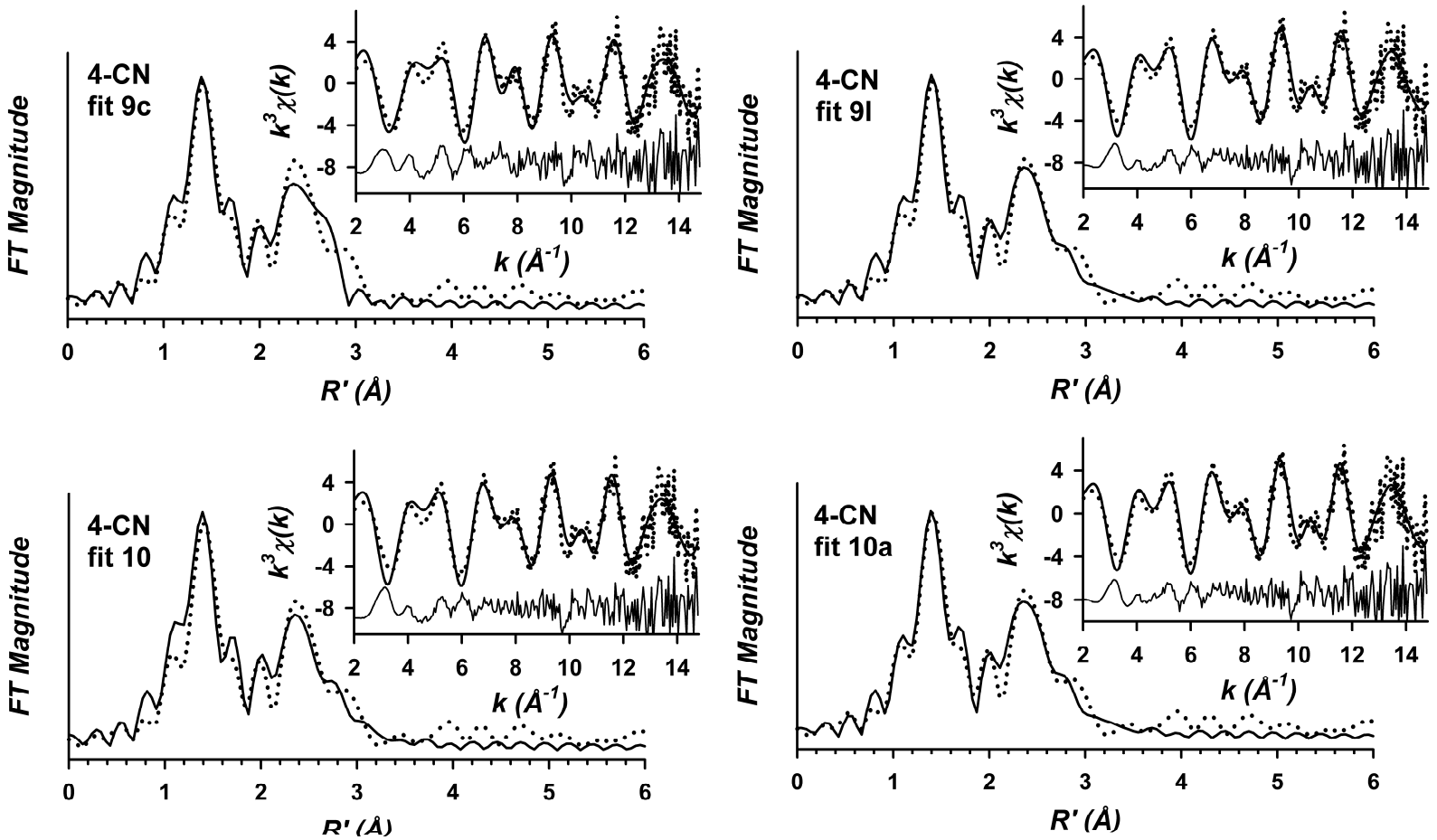

Figure 6.16. Multiple-scattering fits to the Fourier transforms of the Fe K-edge EXAFS data ($k^3\chi(k)$) and unfiltered EXAFS spectra ($k^3\chi(k)$, insets) for **4-CN**. Experimental data is shown with dotted lines (•••), fits are shown with solid lines (——), and the offset fit residual with a thin solid line. Fourier transformation range: $k = 2 - 14.8$ Å^{-1}. Fit parameters associated with the stated fit are shown in Table 6.8.

6.4 Discussion

We have described a comprehensive X-ray absorption spectroscopy study of a series of trigonal bipyramidal iron(II), iron(III), and iron(IV) complexes, including the first structural characterization of an $S = 2$ oxoiron(IV) model complex (**4-O**) and a diamagnetic $S = 0$ iron(IV)-cyanide complex (**4-CN**) generated using the same ligand framework. Table 6.9 summarizes the available structural data from X-ray crystallography for the **2-X**, **3-X**, and **4-X** complexes studied herein in comparison with the results of our EXAFS analyses of **2-CN**, **3-CN**, **3-OH**, **4-CN**, and **4-O**.

Table 6.9. Structural Parameters for **2-X**, **3-X**, and **4-X** Complexes. [a]

Complex	Method	Fe-$N_{eq(ave)}$ (Å)	Fe-N_{ax} (Å)	Fe-X (Å)	Fe···ΔN_{eq} (Å)	τ
2-N_3	**XRD**	2.099	2.260	2.050	0.390	0.991
2-F	**XRD**	2.132	2.345	1.921	0.481	0.944
2-NCMe	**XRD**	2.073	2.253	2.151	0.366	0.956
2-CN	**XRD**	2.110	2.302	2.129	0.430	1.055
	EXAFS	2.09	--	2.13	--	--
3-N_3	**XRD**	2.028	2.216	1.917	0.349	0.943
3-F	**XRD**	2.021	2.210	1.837	0.344	0.975
3-CN	**EXAFS**	2.01	2.01	2.06	--	--
3-OH	**EXAFS**	2.00	--	1.77	--	--
4-CN	**EXAFS**	1.82	2.03	1.88	--	--
4-O	**XRD**	2.005	2.112	1.661	--	--
	EXAFS	1.99	1.99	1.65	--	--

[a] XRD data for all complexes is from reference 185, except for **2-NCMe**, which is from reference 229 and **4-O**, which is from reference 93. EXAFS parameters are from this work. The Fe···ΔN_{eq} value reflects the deviation of the iron center from the plane formed by the three equatorial nitrogen atoms. τ values were calculated according to reference 156.

Our EXAFS analysis of **4-O** reveals an oxo scatterer at 1.65 Å and a set of Fe–N scatterers at 1.99 Å, in good agreement with the crystallographically refined distances of 1.661 Å and 2.005 Å ($Fe–N_{eq}$ only), respectively. The Fe=O distance of **4-**O is similar to those of a variety of low-spin $S = 1$ oxoiron(IV) complexes characterized by X-ray crystallography[173,184,188] and EXAFS[91,133,177,187,216,256] and also agrees well with the Fe=O distances of 1.62 – 1.66 Å measured by EXAFS for the high-spin $S = 2$ oxoiron(IV) intermediates of TauD,[13] CytC3,[19] and SyrB2.[21] The absence of a discernible difference in Fe=O bond length between the $S = 1$ and $S = 2$ cases based on both model complexes and enzyme intermediates illustrates the notion that the antibonding d_{z2} orbital will not be occupied in either configuration for pseudo-octahedral C_{4v} or trigonal bipyamidal C_{3v} geometries (Scheme 6.2). Rather, conversion to the $S = 2$ state will entail occupation of the d_{x2-y2} orbital, which will be involved in antibonding interactions with equatorial ligands. Despite this effect, **4-O** exhibits relatively short $Fe–N_{eq}$ bond lengths, which can be attributed principally to the lower coordination number of this complex and the tetramethylguanidinium donors. In support of this notion, the $Fe–N_{eq}$ bond lengths of the **2-X** series are some 0.1 Å shorter than those encountered for other high-spin iron(II) precursors to oxoiron(IV) complexes employing amine donors, sich as the TMC ligand,[91,133,210] and one would expect this effect to be extended to the high-valent complexes as well.

The principal structural change upon reduction of **4-O** to **3-OH** by treatment with 1,4-CHD is a lengthening in the Fe–O bond by 0.12 Å from 1.65 Å to 1.77 Å. The $Fe–N_{eq}$ distance is unaffected by reduction, and while one might expect an increase in bond length by virtue of the lower oxidation state of **3-OH**, the value of 2.00 Å obtained by

EXAFS is in fact in good agreement with the Fe–N_{eq} distances of 2.02 – 2.03 Å measured by X-ray crystallography for **2-F** and **2-N_3** (Table 6.9). We have assigned the 1.77 Å diastance to coordinated hydroxide based primarily on mass spectrometry evidence, and this value is in good agreement with the Fe(III)–OMe distances of 1.782(3) Å and 1.772(3) Å reported by Stack[257] and Que,[258,259] respectively, using pentadentate pyridine-containing ligands. Stack has also reported a Mn(III)–OH distance of 1.81 Å for a manganese lipoxygenase mimic using a pentadentate pyridine-containing ligand.[260] We believe that the short Fe–OH bond length in **3-OH** can be attributed principally to the neutral ligand employed and the lack of H-bonding interactions from the ligand. An apt illustration of both effects comes from structural studies reported by Borovik and coworkers with the TBP-enforcing trianionic H_3buea ligand. They have reported Fe–O(H) bond lengths of 1.813(3) Å and 1.926(2) Å for $[Fe^{III}(O)(H_3buea)]^{2-}$ and $[Fe^{III}(OH)(H_3buea)]^{-}$ complexes, respectively, a difference of *ca.* 0.113 Å,[228,261] and have also shown that removal of H-bonding interactions from the H_3buea framework leads to an decrease in the Fe–OH bond length of *ca.* 0.05 Å relative to $[Fe^{III}(OH)(H_3buea)]^{-}$ once all H-bond donors have been removed.[262]

We have also described EXAFS characterizations of **2-CN**, **3-CN**, and **4-CN**, with the parameters reported for **2-CN** being in good agreement with the X-ray crystal structure. Our EXAFS analysis of **3-CN** agrees nicely with the **3-F** and **3-N_3** crystal structures (Table 6.9), as well as with the EXAFS-derived structure of **3-OH**, illustrating the notion that the sterically congested TMG_3tren ligand imposes significant structural constraints upon the geometry of the iron center for a given oxidation state. The most interesting results were obtained for **4-CN**, which exhibits a remarkably short average

Fe–N_{eq} distance of 1.81 Å, some 0.2 Å shorter than the analogous distance in its high-spin $S = 2$ congener **4-O**. This compression in average bond lengths likely reflects the fact that the d_{xy} and d_{x2-y2} orbitals that are involved in antibonding interactions with the equatorial nitrogen ligands are no longer occupied, which would be expected to shorten the average metal-ligand bond lengths to some extent. In addition, the iron d orbitals will be expected to contract significantly as a result of spin-pairing, leading to further shortening in bond lengths. The stark structural differences between **4-O** and **4-CN** represent a unique example of the effect of spin-state on structure at a single iron site in nearly identical coordination environments.

XANES studies of **4-O** and **4-CN** provide a further illustration of the spin state differences, as the edge energy of **4-CN** is more than +3 eV higher than that of **4-O**, while the pre-edge feature is *ca.* 1 eV *lower* in energy. These observations indicate that the tricationic complex **4-CN** has a significantly greater effective nuclear charge than dicationic **4-O**, consistent with the significantly shorter bond lengths obtained for **4-CN** as a consequence of compression of the d orbitals induced by its low spin configuration. It should be emphasized that **4-O** exhibits a pre-edge feature with two peaks, consistent with theoretical predictions that spin polarization effects will be significantly greater in the $S = 2$ case.[235] The pre-edge feature of the oxoiron(IV) intermediate of SyrB2 also exhibits two features,[21] although we are unable to make a direct comparison with our results due to the fact that no peak-fitting analysis has been reported for that intermediate. The oxoiron(IV) intermediates of TauD and CytC3 exhibit only a single broad and asymmetric pre-edge feature,[13,19] but this is likely due to the lower resolution of the Si(111) double-crystal monochromator at the XAS beamline employed in those studies

relative to the Si(220) monochromator employed for the SyrB2 XAS experiments. XANES studies of additional $S = 2$ oxoiron(IV) model complexes should provide further insight into the properties of this unique pre-edge feature, and we suggest that it may ultimately be employed as a diagnostic spectroscopic handle for the presence of high-spin oxoiron(IV) centers in samples studied by XAS.

Finally, our discussion of the XANES properties of the **2-X** and **3-X** complexes studied herein is significantly hindered by the paucity of available experimental XAS data on TBP iron centers,[201,236,239] as well as the lack of theoretical predictions for this geometry, in contrast to the well-developed theoretical framework that exists for interpreting the XANES features of iron(II) and iron(III) complexes in octahedral, square pyramidal, and tetrahedral geometries.[214,263] Our studies reveal that the **2-X** and **3-X** complexes exhibit relatively similar edge shapes and pre-edge intensities for a given iron oxidation state, consistent with relatively modest structural differences across the series as demonstrated by results from both X-ray crystallography and EXAFS analysis. The integrated pre-edge intensities are on the high side compared to the majority of high spin five-coordinate square pyramidal iron(II) and iron(III) complexes reported thus far. We speculate that this reflects both the axial distortion in these complexes that is manifested as significantly different Fe–N_{ax} and Fe–**X** bond lengths, as well as the deviation of the iron center from the plane defined by the three equatorial nitrogen atoms, which ranges from *ca.* 0.35 Å in **3-F** and **3-N_3** to as much as 0.48 Å in **2-F** (*c.f.* Table 6.9). The combination of these effects should significantly enhance the intensity of the 1s-to-3d transition via 3d mixing with 4p orbitals from loss of centrosymmetry relative to an idealized D_{3h} trigonal bipyramidal geometry. Indeed, calculations reported by Solomon

and coworkers suggest that the extent of 4p mixing is relatively similar for C_{4v} square pyramidal and idealized symmetric D_{3h} trigonal bipyramidal geometries, but increases significantly as one lengthens an axial bond to approach a distorted C_{3v} geometry similar to those of **2-X** and **3-X**.[214] In support of this hypothesis, Fe K-edge XANES studies of Borovik's trigonal bipyramidal $[Fe^{III}(H_3buea)(X)]^{2-/-}$ ($X = O^{2-}$, S^{2-}, OH^-) complexes revealed that the fairly intense pre-edge features of these complexes could be accounted for by more extensive 3d/4p mixing brought about by the axial distortion imposed by the short Fe–X and long $Fe–N_{ax}$ bond lengths.[236] We anticipate that theoretical calculations of the electronic properties of this series of complexes will undoubtedly provide insights into the factors that contribute to both the shape and intensity of the pre-edge features of **2-X** and **3-X**.

In closing, we have characterized a number of new trigonal bipyramidal iron complexes by a combination of EXAFS and XANES analysis. The results obtained for **4-O** in particular confirmed a number of predictions that have been made from computational studies regarding the structural and spectroscopic properties of high-spin oxoiron(IV) centers.[219-222,235] In addition, the accumulated structural parameters and XANES data for the **2-X**, **3-X**, and **4-X** series should provide a firm basis for the development of an experimentally calibrated theoretical model for the Fe K-edge XANES properties of trigonal bipyramidal iron complexes, the results of which should be of direct utility for interpretation of XAS data obtained on high-valent oxoiron intermediates implicated in the catalytic cycles of many nonheme iron oxygenases.

Chapter 7.

XAS Studies of a New High-Valent Diiron(IV) Complex

Portions of this work have been previously published as:
Dong Wang, Erik R. Farquhar, Audria Stubna, Eckard Münck, and Lawrence Que, Jr. "A Diiron(IV) Complex that Cleaves Strong C–H and O–H Bonds." *Nat. Chem.* **2009**, *1*, 145-150.

7.1 Introduction

Oxygen activating iron enzymes employing a nonheme diiron active site cluster have attracted considerable attention from chemists and biochemists alike owing to their involvement in a number of oxidative processes of fundamental environmental and biological importance, such as the conversion of methane to methanol by methane monooxygenase,[5,6,264] the biosynthesis of ribonucleotides by ribonucleotide reductase[27,39] and fatty acids by diiron-containing desaturases,[42,265] and the hydroxylation of the novel amino acid deoxyhypusine in the cell growth regulating protein eIF5a by deoxyhypusine hydroxylase.[266] The catalytic cycles of these enzymes are thought to proceed through a common μ-1,2-diiron(III)-peroxo intermediate generated via binding of O_2 to the reduced diiron(II) form.[1,5] This species, while perhaps capable of acting as an oxidant itself,[26] then undergoes heterolytic O–O bond cleavage to afford a high-valent diiron-oxo oxidant. Two such intermediates have been observed and extensively characterized in enzymatic systems: the mixed valent diiron(III/IV) oxidant **X** of the R2 subunit of ribonucleotide reductase[31-34] and the diiron(IV) oxidant **Q** observed for methane monooxygenase.[24,267,268] MMO-**Q** has been shown to consist of two antiferromagnetically coupled high-spin $S = 2$ iron centers,[267,268] with EXAFS studies suggesting two bridging oxo ligands and an Fe•••Fe separation of *ca.* 2.5 Å,[24] a motif that has since come to be known as the "diamond core."

Interest in the origins of the exceptional reactivity and novel structural and electronic properties of MMO-**Q** have made it an attractive target for model studies by synthetic chemists. However, the first examples of genuine μ-oxo-bridged diiron(IV) complexes with a nonheme ligand set have only recently been reported, which is perhaps

a reflection of the reactivity of this oxidizing species. In 2005, Collins and coworkers described the structural characterization of a pair of μ-oxo bridged diiron(IV) complexes, with the tetraanionic ligand employed in their work likely accounting for the exceptional stability of these complexes.[269] More recently, Xue *et al.* described the electrochemical generation of a bis-μ-oxo diiron(IV) complex, $[Fe^{IV}_2(\mu\text{-}O)_2(N_4)_2]^{4+}$ (N_4 is an electron-rich ligand based on the tris(2-pyridyl)methylamine framework), with low-spin $S = 1$ iron(IV) centers that mimics the diamond core structure proposed for MMO-**Q**.[270] However, the reactivity of this complex towards hydrocarbon substrates falls short of that observed for the analogous mononuclear $S = 1$ oxoiron(IV) complex, let alone MMO-**Q**. Subsequent studies by the same group have revealed that the reactivity of this species can be enhanced by many orders of magnitude through opening of the diamond core to afford a terminal oxoiron(IV) moiety, along with conversion of the oxoiron(IV) center to the high-spin $S = 2$ state.[271,272]

An alternative approach to generate highly reactive diiron(IV) models is to identify complexes with a very high Fe(IV)/Fe(III) reduction potential, as these would be expected to be potent oxidizing agents. To this end, we recently initiated studies of $[Fe^{III}_2(\mu\text{-}O)(S\text{-}BPAE)_2]^{2+}$ (**1**, S-BPAE = *N*,*N*-bis-(3',5'-dimethyl-4'-methoxypyridyl-2'-methyl)-*N*′-acetyl-1,2-diaminoethane), a high-spin diiron(III) complex containing a single bridging oxo ligand and a mixed N_4O donor set from the S-BPAE ligand (Figure 7.1). Electrochemical studies of this complex revealed that **1** could be oxidized by one electron to $[Fe^{III}Fe^{IV}(\mu\text{-}O)(S\text{-}BPAE)_2]^{3+}$ (**2**) (E^o = +0.71 V versus Fc^+/Fc^0), or by two electrons to $[Fe^{IV}_2(\mu\text{-}O)(S\text{-}BPAE)_2]^{4+}$ (**3**) ((E^o = +1.50 V versus Fc^+/Fc^0 for this species). Generation of **3** from **2** was reversible on the cyclic voltammetry (CV) timescale, while the

generation of **2** from **1**, while irreversible by CV, was however found to be chemically reversible.[94] Both **2** and **3** proved sufficiently stable to be obtained in high yield by bulk electrolysis. Mössbauer studies of **2** demonstrated that it contained a valence delocalized S_T = ½ iron(III)/iron(IV) cluster, consistent with conversion of the high-spin iron(III) centers of **1** to a low-spin S = ½ Fe(III) and S = 1 iron(IV) combination in **2**, while **3** was found to contain a pair of antiferromagnetically coupled low-spin S = 1 iron(IV) centers.[94] The reduction potential of **3** is one of the highest measured to date for an iron complex, and it accordingly was found to be highly reactive towards both strong C–H and O–H bonds,[94] functioning principally as a dehydrogenase analogous to the chemistry observed for nonheme diiron desaturases.[42,265]

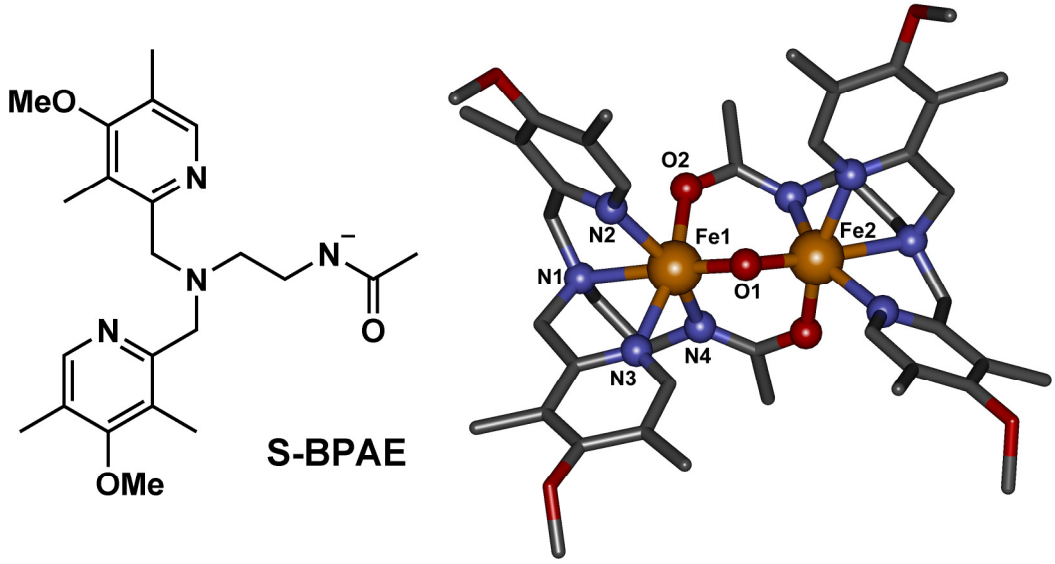

Figure 7.1. (left) Structure of the S-BPAE ligand. (right) Depiction of the crystal structure of the $[Fe^{III}_2(\mu\text{-}O)(S\text{-}BPAE)_2]^{2+}$ cation, generated in Accelerys Discovery Studio Visualizer 2.5 from the coordinates of the published crystal structure.[94] Iron is shown as large orange spheres, while coordinating nitrogens and oxygens are shown as smaller blue and red spheres, respectively. Important geometrical parameters include: Fe1–O1: 1.795 Å; Fe1–O2: 2.007 Å; Fe1–N1: 2.237 Å; Fe1–N2,N3: 2.157 Å; Fe1–N4: 2.088 Å; Fe1•••Fe2: 3.007 Å; Fe1–O1–Fe2: 113.68°.

However, neither **2** nor **3** has proven amenable to crystallization and subsequent structural analysis, and thus we lack a basis for understanding what, if any, structural changes occur upon oxidation of **1** to afford such an exceptionally potent oxidant. To this end, we describe herein the characterization of complexes **1**, **2**, and **3** via X-ray absorption spectroscopy and employ EXAFS analysis to obtain metrical parameters for the iron coordination environment in **2** and **3**. The results of this work demonstrate that one and two electron oxidations of **1** engender significant structural changes in iron coordination environment that are consistent with the lack of electrochemical reversibility and the spin state change observed by Mössbauer spectroscopy.

7.2 Experimental

7.2.1. XAS Sample Preparation

All high-valent samples were prepared using bulk electrolysis in conjunction with a UV/Vis spectrometer by Dong Wang.

$[Fe^{III}_2(O)(S\text{-}BPAE)_2]^{2+}$, 1. A sample of $[Fe^{III}_2(O)(S\text{-}BPAE)_2]^{2+}$ was prepared by mixing 4.4 mg of complex with 83 mg of boron nitride and grinding thoroughly in a motor and pestle. The resultant powder was packed into an SSRL powder sample holder and sealed with Kapton windows.

$[Fe^{III}Fe^{IV}(O)(S\text{-}BPAE)_2]^{3+}$, 2. A sample of $[Fe^{III}Fe^{IV}(O)(S\text{-}BPAE)_2]^{3+}$ was prepared by electrochemical oxidation of **1** in acetonitrile at -40 ºC, which was then quickly frozen in a tandem Mössbauer/EXAFS cup. The sample was 3.0 mM in [complex] and 6.0 mM in $[Fe]_T$ with 0.1 M KPF_6 as a supporting electrolyte. The sample was ~90% in the desired diiron(III/IV) form on the basis of UV/Vis measurements.

$[Fe^{IV}_2(O)(S\text{-}BPAE)_2]^{4+}$, 3A. A sample of $[Fe^{IV}_2(O)(S\text{-}BPAE)_2]^{4+}$ was prepared electrochemically from 1 in CD_3CN at -40 ºC by and frozen in a large tandem Mössbauer/EXAFS cell. The sample was 3.0 mM in [complex] and 6.0 mM in $[Fe]_T$ with 0.1 M KPF_6 as a supporting electrolyte. The sample was *ca.* 75% in $Fe(IV)_2$ based on UV/Vis measurements.

$[Fe^{IV}_2(O)(S\text{-}BPAE)_2]^{4+}$, 3B. A second sample of $[Fe^{IV}_2(O)(S\text{-}BPAE)_2]^{4+}$ was prepared electrochemically from **1** in CD_3CN at -40 ºC by and frozen in a large tandem Mössbauer/EXAFS cell. The sample was 3.0 mM in [complex] and 6.0 mM in $[Fe]_T$ with 0.1 M KPF_6 as a supporting electrolyte. The sample was *ca.* 75% in $Fe(IV)_2$ based on UV/Vis measurements.

7.2.2 X-ray Absorption Spectroscopy. Data Collection.

X-ray absorption spectra were measured on beamlines 7-3 (**3A** and **3B**) and 9-3 (**1** and **2**) at the Stanford Synchrotron Radiation Lightsource (SSRL) with the storage ring operating at 3 GeV and 80-100 mA. Fe K-edge XAS data were collected for frozen solutions maintained at ~ 10 – 15 K over an energy range of 6.9 – 8.0 keV using a Si(220) monochromator for energy selection and an Oxford Instruments CF1208 continuous flow liquid helium cryostat for temperature control. A rhodium-coated mirror upstream of the monochromator was used for harmonic rejection. Data were obtained as fluorescence excitation spectra with a 30 element solid-state germanium detector array (Canberra). An iron foil spectrum was recorded concomitantly for internal energy calibration and the first inflection point of the K-edge was assigned to 7112.0 eV. Several different spots were exposed for the samples of **2**, **3A**, and **3B** studied here to minimize the effects of possible photoreduction, and the position of the edge was

routinely monitored during data collection. The edge inflection was found to be invariant during collection, indicating that no significant photoreduction occurred in the X-ray beam for these samples.

7.2.3. Data Analysis

Data reduction, averaging, and normalization were performed using the program EXAFSPAK.[130] Following calibration and averaging of the data, background absorption was removed by fitting a Gaussian function to the pre-edge region and then subtracting this function from the entire spectrum. A three-segment spline with fourth order components was then fit to the EXAFS region of the spectrum in order to extract χ(k). Analysis of the pre-edge features was carried out with the program SSExafs[132] using an established methodology.[133] In all fits, the coordination number n of a given shell was a fixed parameter, and was varied iteratively while r and σ^2 were allowed to freely float. The scale factor S_0 was fixed at 0.9, while the edge shift parameter E_0 was allowed to float as a common value for all shells. Phase and amplitude parameters for a given absorber-scatterer pair at a defined distance were calculated using FEFF 8.40[135] at the single-scattering level of theory, and utilized by the opt program of the EXAFSPAK package during curve-fitting. For purposes of quantifying fit quality, the goodness-of-fit parameter F was defined as $[\Sigma k^6(\chi_{exptl}-\chi_{calc})^2 / \Sigma k^6\chi_{exptl}^2]^{1/2}$. Analysis of **3A** and **3B** revealed that both samples had identical $k^3\chi(k)$ EXAFS, Fourier transforms, and EXAFS analyses, and thus data for both samples was averaged together and analyzed as **3**.

7.3 Results

7.3.1. XANES Analysis

The XANES spectra and results of pre-edge fitting analysis of **1** and its oxidized congeners **2** and **3** are summarized in Figure 7.2 and Table 7.1. **1** exhibits an Fe K-edge inflection energy of 7124.1 eV and a single intense pre-edge transition centered at approximately 7115 eV with an integrated area of 17 units. Both features are consistent with those obtained for other μ-oxo bridged diiron(III) clusters,[214,273,274] in which the high intensity of the pre-edge peak for pseudo-octahedral iron(III) centers can be attributed to a geometric distortion imposed by the oxo bridge that significantly lowers centrosymmetry.[273] **2** exhibits a blueshift of approximately +1 eV in the edge inflection energy to ~7125.0 eV, consistent with one electron oxidation from the diiron(III) state of **1** to a mixed-valent diiron(III/IV) state in **2**. Unexpectedly, the pre-edge peak *red-shifts* by -0.9 eV to 7114.1 eV upon conversion of **1** to **2**, which likely reflects the spin-state conversion from high-spin S = 5/2 Fe(III) in **1** to low-spin S = 1 Fe(IV) in **2**. This somewhat counterintuitive trend was previously noted by Wieghardt and coworkers in their studies of a pair of $[Fe^{III}(\mu\text{-}O)(\mu\text{-}OAc)M^{III}(L)_2]^{2+}$ (M = Fe, Cr) complexes in which the high-spin S = 5/2 Fe(III) center was electrochemically converted to low-spin S = 1 Fe(IV).[244] We also reported a similar effect in Chapter 6 of this thesis, in which conversion of the high-spin $[Fe^{III}(CN)(TMG_3tren)]^{2+}$ complex to a diamagnetic S = 0 $[Fe^{IV}(CN)(TMG_3tren)]^{3+}$ species afforded a blue-shift in edge inflection energy coupled to a red-shift in the position of the pre-edge feature. Finally, further one electron oxidation of **2** to the diiron(IV) complex **3** elicits blue-shifts in both the edge and pre-edge energy, with the edge energy upshifting by +0.6 eV to 7125.6 eV, while the pre-

edge feature shifts by +0.3 eV to 7114.4 eV. The area of the principal pre-edge transition declines slightly along the progression from **1** to **3** (Table 7.1), suggesting that an increasing degree of centrosymmetric character as the diiron cluster becomes more oxidized. **3** exhibits a pre-edge area of 14, which is somewhat lower than the value of 19 units reported previously for a related bis-μ-oxo diiron(IV) complex $[Fe^{IV}_2(\mu\text{-}O)_2(N_4)_2]^{4+}$,[270] consistent with greater centrosymmetric distortion in the latter complex. **2** and **3** also exhibit a second feature that lies some 3 – 3.5 eV higher in energy than the primary pre-edge transition (this is also present in **1**, but is much weaker). The large splitting value suggests that this is not likely to be a 1s-to-3d transition,[214] and we therefore suggest that it is an edge transition related to the spin and oxidation states of the iron centers in **2** and **3**.

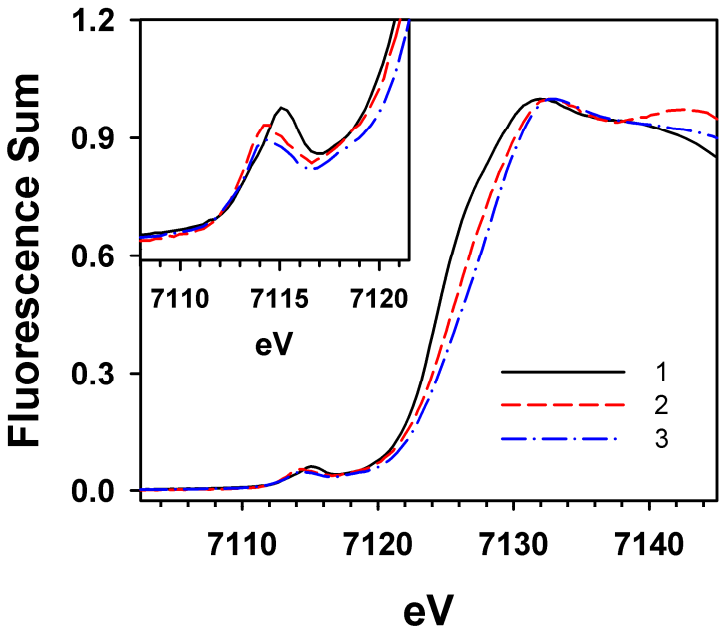

Figure 7.2. Comparison of the Fe K-edge X-ray absorption edge and pre-edge (inset) features of **1** (black, ——), **2** (red, – – –), and **3** (blue, –·–·–).

Table 7.1. Pre-edge Analysis Parameters for **1**, **2**, and **3**.[a]

Species	Purity	E_{edge} (eV)	E_{peak} (eV)	width	area
1	--	7124.10	7114.96	3.02	17.0
			7118.09	1.60	1.4
2	90%	7124.97	7114.09	2.95	15.7
			7117.35	3.10	5.6
3	75%	7125.61	7114.38	2.94	13.8
			7118.07	3.55	7.7

[a] The fits presented are those that give the best agreement to the experimental data. Purity was assessed by the UV/Vis features of the samples prepared for XAS.

7.3.2. EXAFS Analysis

We were able to obtain EXAFS data of excellent quality for all three species described in this study. **3A** and **3B** afforded identical $k^3\chi(k)$ EXAFS spectra, Fourier-transforms, and EXAFS analyses, and we therefore report the analysis of the combined data for both samples as **3**. The EXAFS spectra of **1**, **2**, and **3**, shown in Figure 7.3, reveal significant differences in the pattern of EXAFS modulations for **2** and **3**, compared to **1**, suggesting a significant alteration in structure occurs. In particular, the phase of the $k^3\chi(k)$ modulations broadens substantially in **2** and **3**, corresponding to a shortening in the average metal-ligand bond lengths.[133,216] In addition, both **2** and **3** exhibit extremely similar EXAFS spectra, implying that extraction of an electron from **2** to give the diiron(IV) complex **3** results in minimal changes to the iron site structure. Consistent with the above observations, the Fourier transforms of the $k^3\chi(k)$ EXAFS data obtained for **1**, **2**, and **3** indicate that **2** and **3** are very similar to one another while being dramatically different from **1** (Figure 7.4). The FT of **1** exhibits two intense features at r' = 1.7 Å and 2.6 Å, with the former being attributable to ligands in the first coordination sphere, while the latter can be assigned to outer-shell scattering from the second iron center and ligand carbon atoms. In **2** and **3**, the inner-shell feature downshifts to r' = 1.6 Å, consistent with a shortening in average bond length, while the intensity of the outer-shell feature over r' = 2.2 – 3.0 Å is reduced dramatically compared to **1**. Although it is tempting to suggest that this reflects the loss of backscattering from the second iron center, calculation of the Fourier transforms of **2** and **3** using $k^5\chi(k)$ weighted data reveals that the outer-shell feature at r' = 2.8 Å gains intensity relative to the normalized intensity of the inner-shell peak (Figure 7.5). Eidsness and Scott have shown that the calculation

of Fourier transforms using different k weightings is a simple and useful test to detect metal-metal scattering in dinuclear complexes,[275] since heavier atoms such as iron contribute to the EXAFS more strongly at high k and thus a higher k weighting will emphasize these features at the expense of those arising from light atoms such as nitrogen and oxygen.[88,275] As we expect the inner shell of **2** and **3** to consist solely of light atoms, we would expect no enhancement in the intensity of outer shell peaks in the Fourier transform with k^5 weighting only if those features also arise from light atoms of a similar Z. The observed intensity enhancement is strong evidence for the retention of a diiron core in **2** and **3**, consistent with the Mössbauer analyses of these two species.

Curve fitting of the EXAFS for **1** reveals a structure identical to that determined by X-ray crystallography (Table 7.2). The inner shell feature can be fit well to 4 Fe–N/O scatterers at 2.11 Å and a single Fe–O scatterer at 1.79 Å, in excellent agreement with the average Fe–N/O distance of 2.129 Å for the four nitrogens and one oxygen derived from the BPAE ligand, as well as the Fe–O distance of 1.795 Å for the bridging oxo.[94] Interestingly, fits to the outer shell employing either Fe•••Fe or Fe•••C shells at *ca.* 3.0 Å significantly improve the quality of fit, but require overestimation of the number of scatterers (fits 3 – 5, Table 7.2), in line with the observation from examination of the crystal structure of **1** that there are both iron and carbon atoms at this distance that would be expected to contribute to the EXAFS. Indeed, the best fit to the outer shell therefore requires a combination of 1 Fe•••Fe scatterer at 2.97 Å and 5-6 Fe•••C at 3.07 Å (fit 8, Table 7.2 and Figure 7.6). The Fe•••Fe separation is in good agreement with the crystallographic value of 3.007 Å, while the Fe•••C contribution can be attributed to

single-scattering paths involving the C_2 and C_6 carbons of coordinated pyridines, as well as the ligand backbone.[94,133,187,276]

As expected based on the appearance of the $k^3\chi(k)$ EXAFS data, EXAFS fits of both **2** and **3** (Tables 7.3 and 7.4) reveal nearly identical structures for both complexes, within the accuracy of the EXAFS technique,[87-89] both of which differ significantly from **1**. The distance of the primary shell of 4 Fe–N/O scatterers shortens appreciably by ~0.15 Å to 1.96 Å, consistent with the low-spin state of the iron centers in **2** and **3**, and in good agreement with the Fe–N distances measured for other high-valent mono- and diiron complexes containing pyridines.[133,187,188,270,271,276,277] The $Fe–O_{oxo}$ bond length also shortens by *ca.* 0.08 Å to 1.71 Å in both **2** and **3**. This bond length is not altered by the higher oxidation state of **3**, in contrast to earlier observations on bis-μ-oxo diiron(III/IV) and diiron(IV) complexes where the Fe–μ-O bond length shortened by 0.05 Å in the more highly oxidized form.[270] The Debye-Waller factor for this path in **3** is relatively large, even when the coordination number is adjusted to reflect sample purity (Table 7.4). This likely arises from static disorder contributed by as-yet unidentified decay products in the samples of **3** studied by XAS. Finally, the outer shell features of both **2** and **3** can be simulated with an Fe•••Fe interaction at 3.07 Å and 4-5 Fe•••C scatterers at *ca.* 2.9 Å (fit 11 for 2, fit 14 for 3, Tables 7.3 and 7.4, Figure 7.6). Examination of the progression of EXAFS fits for **2** and **3** reveals that addition of the Fe•••C shell to two-shell fits of the inner-shell affords a larger improvement in fit quality than when the Fe•••Fe shell is added (compare fits 7-8 with 9-11 in Table 7.4 for **3**). However, both the Fe•••C and Fe•••Fe components are required for good fits to **2** and **3**, as Fe•••C scattering alone does not adequately simulate the observed $k^3\chi(k)$ EXAFS modulations. Our assignment of the

shorter distance to Fe•••C scattering rests on the observation of similar Fe•••C distances in the crystal structure of a low-spin bis-μ-oxo diiron(III/IV) complex, $[Fe^{III}Fe^{IV}(\mu\text{-}O)_2(N_4)_2]^{3+}$,[276] and in EXAFS analyses of a number of other high-valent iron complexes containing pyridines.[133,187,270,271] Similarly, k^5 weighting of EXAFS data for **2** and **3** indicated that the intensity gains were centered at a *phase-uncorrected* distance of ~2.8 Å in the Fourier transform (Figure 7.5), which corresponds to the phase-corrected distance of *ca.* 3.1 Å obtained for the Fe•••Fe scatterer in our EXAFS analysis. An intensity gain at a *phase-uncorrected* distance of $r' \sim 2.4 - 2.5$ Å would be expected for an Fe•••Fe separation of 2.85 Å. The 0.2 Å decrease in the Fe•••C distance compared to **1** is also consistent with the low spin state of the iron centers in **2** and **3**, whereas an increase to *ca.* 3.1 Å would be more difficult to rationalize given the observed shortening of the $Fe–N_{py}$ bond lengths and the rigidity of the pyridine moieties. We note that the *ca.* 0.1 Å increase in the Fe•••Fe separation upon oxidation of **1** is in agreement with the 0.05 – 0.08 Å increases in this distance observed via EXAFS analysis for the one-electron oxidations of $[Fe^{III}(\mu\text{-}O)(\mu\text{-}OAc)M^{III}(L)_2]^{2+}$ by Slep *et al.*[244] and $[Fe^{III}Fe^{IV}(\mu\text{-}O)_2(N_4)_2]^{3+}$ by Xue *et al.*,[270] and likely reflects the effects of charge repulsion between the two highly-charged iron(IV) centers in these complexes.

Finally, our EXAFS analysis also sheds light on the dramatically different appearance of the outer-shell features in the Fourier transforms of **1** compared to **2** and **3**. Shown in Figures 7.7 and 7.8 are deconvolutions of the best fits to **1** (fit 8, Table 7.2) and **3** (fit 14, table 7.4). In **1**, both the Fe•••C and Fe•••Fe $k^3\chi(k)$ EXAFS contributions are in phase with one other, leading to constructive overlap between these two shells and a corresponding enhancement of their contributions to the EXAFS, and by extension, the

Fourier transform. This accounts nicely for the relatively short phase of the EXAFS modulations of **1**. In **3** (as well as **2**), on the other hand, both shells are very nearly out of phase with one another, leading to destructive overlap and effectively cancelling their contributions to the EXAFS. Consequently, the EXAFS of **2** and **3** is comprised primarily of scattering contributions from the Fe–N/O shell, with much weaker contributions from the Fe–O_{oxo}, Fe•••Fe, and Fe•••C shells than is the case for **1**. It is also interesting that the contribution of the Fe–O_{oxo} shell is far, far weaker in **3** than in **1**. In defense of including this shell in our fits of **2** and **3**, we note that there is a small but significant improvement in fit quality when the Fe–O_{oxo} shell is added to the fit. In addition, resonance Raman studies of **2** (Dong Wang, unpublished observations) reveal a vibration at 732 cm^{-1} that is sensitive to isotope labeling of the bridging oxo, the energy of which is consistent with assignment to the asymmetric stretching mode of the Fe–O–Fe moiety.[278,280] Although we lack analogous vibrational data for **3**, we see no reason to exclude this scatterer in our fits of **3** while including it for **2**, given the other structural similarities of the two complexes.

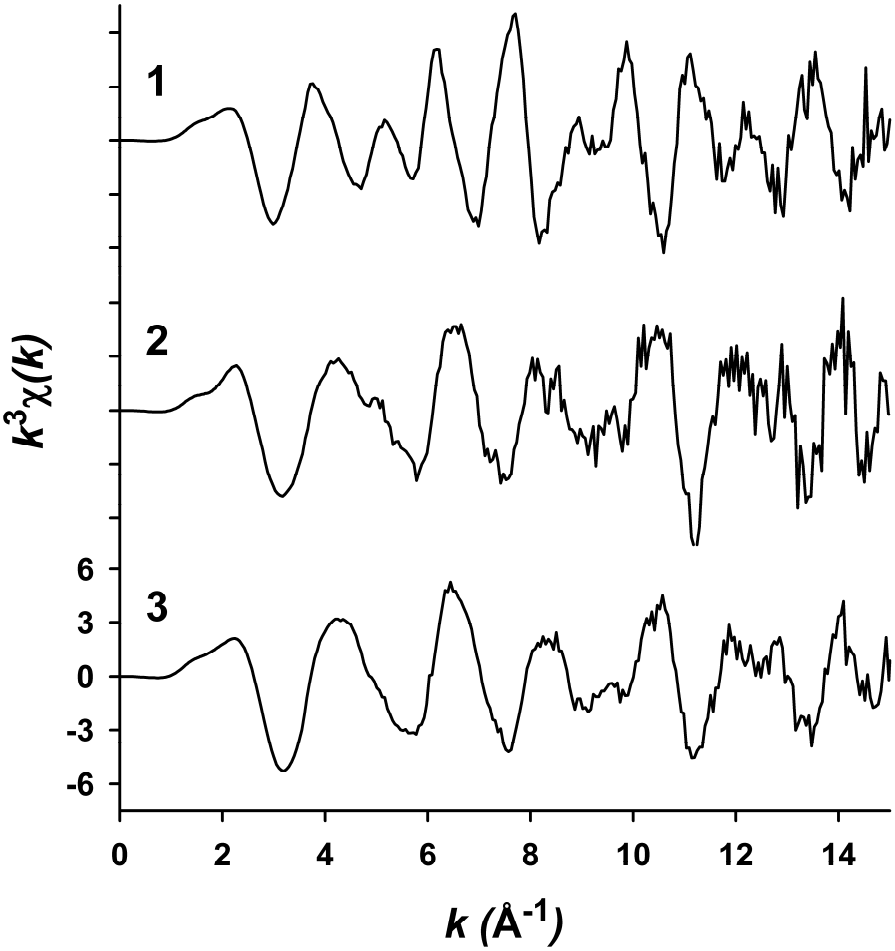

Figure 7.3. Comparison of the $k^3\chi(k)$ weighted EXAFS data for **1** (top), **2** (middle), and **3** (bottom) The y-axis scaling is identical for all plots.

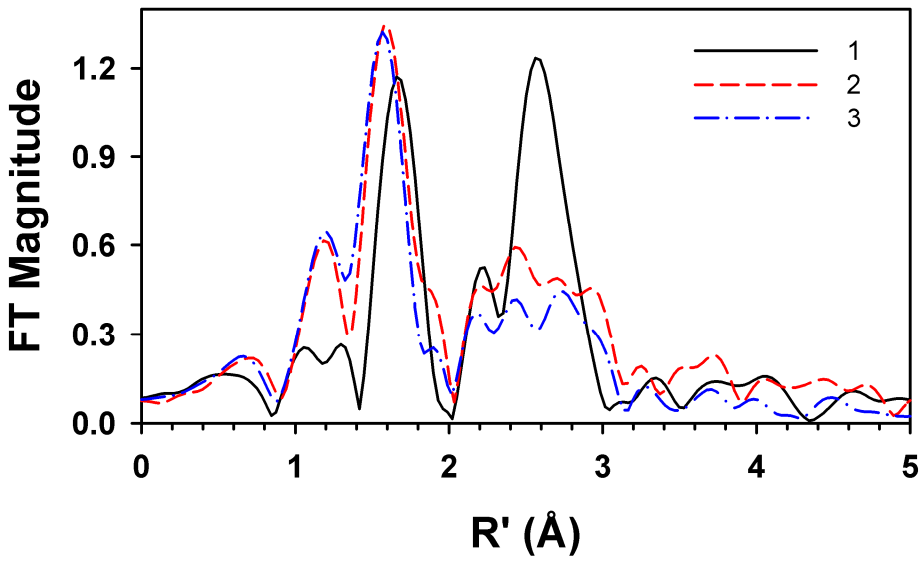

Figure 7.4. An overlay plot comparison of the Fourier transforms of **1** (black, ——), **2** (red, – – –), and **3** (blue, –·–·–). FT ranges were as follows: **1**, $k = 2 – 15$ Å^{-1}; **2**, $k = 2 – 14.9$ Å^{-1}; **3**, $k = 2 – 15$ Å^{-1}.

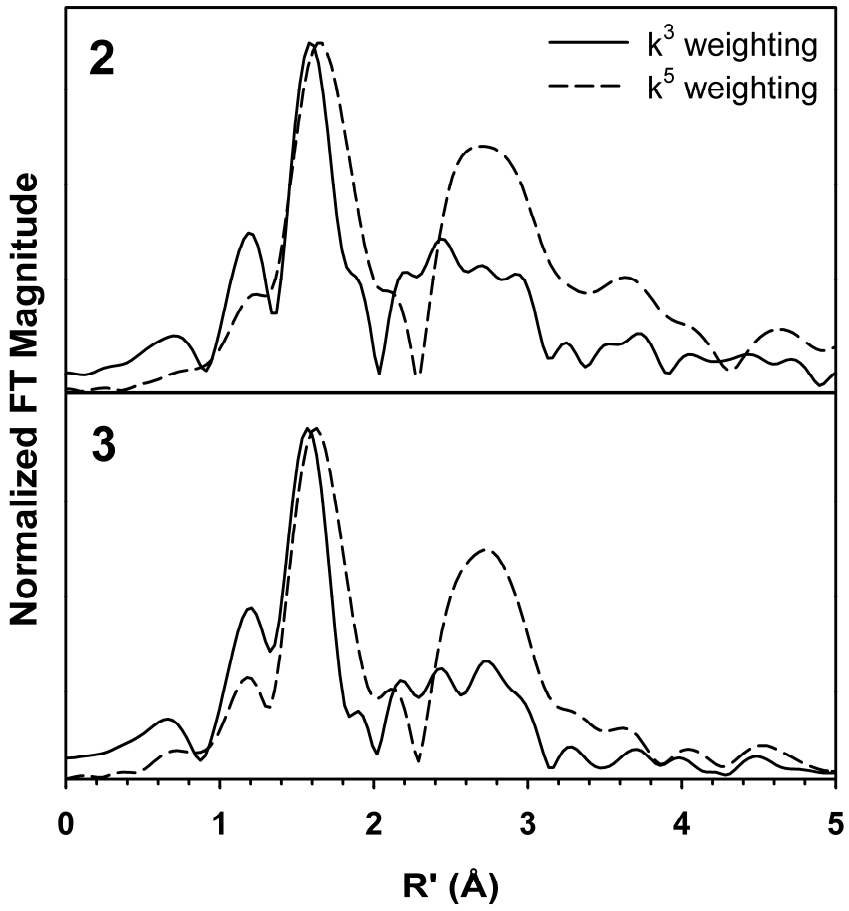

Figure 7.5. Effect of variable k weighting on the Fourier transforms of **2** and **3**. FTs obtained from $k^3\chi(k)$ EXAFS are shown with solid lines (——), while those obtained from $k^5\chi(k)$ EXAFS are shown with dashed lines (– – –). The FT intensities have been normalized to a value of 1.0 for the most intense peak. FT ranges were as follows: **2**, k = 2 – 14.9 Å^{-1}; **3**, k = 2 – 15 Å^{-1}.

Table 7.2. EXAFS Fitting Results for **1**.[a]

	Fe-N/O			Fe-O/N			Fe•••Fe			Fe•••C			
fit	**n**	**r**	**σ^2**	**n**	**r**	**σ^2**	**n**	**r**	**σ^2**	**n**	**r**	**σ^2**	***F*** [b]
1	4	2.13	6.3										0.859
2	4	2.11	5.5	1	1.79	1.3							0.792
3	4	2.10	5.6	1	1.78	1.0	1	2.98	0.5				0.427
4	4	2.10	5.4	1	1.78	1.2	2	2.98	3.1				0.374
5	4	2.10	5.6	1	1.78	1.1				8	3.00	1.1	0.404
6	4	2.11	5.5	1	1.78	1.2	1	2.97	-0.1	4	3.08	0.1	0.331
7	4	2.11	5.5	1	1.78	1.2	1	2.97	0.2	5	3.07	1.7	0.333
8	***4***	***2.11***	***5.5***	***1***	***1.78***	***1.2***	***1***	***2.97***	***0.6***	***6***	***3.07***	***3.9***	***0.340***

[a] Fourier transform range k = 2.0 – 15.0 Å^{-1} (resolution = 0.12 Å). σ^2 is in units of 10^{-3} Å^2. All fits are to unfiltered data. The first shell was fit using scatterers with nitrogen parameters, while the second shell was fit with oxygen parameters; however, EXAFS cannot distinguish between backscatterers differing by Z = 1.
[b] Goodness-of-fit parameter F defined as $[\Sigma k^6(\chi_{exptl}-\chi_{calc})^2 / \Sigma k^6\chi_{exptl}^2]^{1/2}$.

Table 7.3. EXAFS Fitting Results for **2**.[a]

	Fe-N/O			Fe-O/N			Fe•••Fe			Fe•••C			
fit	**n**	**r**	**σ^2**	**n**	**r**	**σ^2**	**n**	**r**	**σ^2**	**n**	**r**	**σ^2**	***F*** [b]
1	4	1.98	3.3										0.685
2	4	1.96	2.9	1	1.71	3.8							0.633
3	4	1.97	3.0	0.9	1.71	3.2							0.633
4	4	1.97	3.2	0.9	1.71	3.0	1	3.12	2.7				0.641
5	4	1.97	3.2	0.9	1.71	2.9	0.9	3.11	2.0				0.631
6	4	1.96	3.5	0.9	1.70	2.8				3	2.87	-0.6	0.484
7	4	1.96	3.4	0.9	1.70	2.8				4	2.87	0.4	0.491
8	4	1.96	3.3	0.9	1.70	2.8				5	2.87	1.3	0.506
9	4	1.97	3.6	0.9	1.70	2.8	0.9	3.06	6.5	3	2.88	-0.9	0.471
10	4	1.97	3.5	0.9	1.70	2.7	0.9	3.07	4.6	4	2.88	0.0	0.466
11	***4***	***1.96***	***3.5***	***0.9***	***1.70***	***2.7***	***0.9***	***3.07***	***3.6***	***5***	***2.89***	***0.9***	***0.468***
12	4	1.96	3.5	0.9	1.70	2.6	0.9	3.08	2.7	6	2.89	1.9	0.476

[a] Fourier transform range k = 2.0 – 14.9 Å^{-1} (resolution = 0.12 Å). σ^2 is in units of 10^{-3} Å^2. All fits are to unfiltered data. The first shell was fit using scatterers with nitrogen parameters, while the second shell was fit with oxygen parameters; however, EXAFS cannot distinguish between backscatterers differing by Z = 1. The value of n for the Fe-O/N and Fe•••Fe shells was fixed at 0.9 in view of the fact that the sample was determined to contain 90% **2** by UV/Vis spectroscopy.
[b] Goodness-of-fit parameter F defined as $[\Sigma k^6(\chi_{exptl}-\chi_{calc})^2 / \Sigma k^6 \chi_{exptl}^2]^{1/2}$.

Table 7.4. EXAFS Fitting Results for **3**.[a]

	Fe-N/O			Fe-O/N			Fe•••Fe			Fe•••C			
fit	**n**	**r**	**σ^2**	**n**	**r**	**σ^2**	**n**	**r**	**σ^2**	**n**	**r**	**σ^2**	***F*** [b]
1	4	1.97	4.0										0.515
2	5	1.97	5.8										0.557
3	4	1.97	3.3	1	1.73	7.8							0.497
4	4	1.97	3.4	0.8	1.72	5.8							0.495
5	5	1.96	4.8	1	1.70	4.9							0.509
6	5	1.96	5.0	0.8	1.70	3.3							0.506
7	4	1.96	3.4	0.8	1.72	5.7	1	3.12	3.9				0.492
8	4	1.96	3.4	0.8	1.72	5.6	0.8	3.12	2.4				0.471
9	4	1.96	3.6	0.8	1.71	5.4				2	2.87	-1.2	0.351
10	4	1.96	3.6	0.8	1.71	5.2				3	2.87	0.2	0.359
11	4	1.96	3.5	0.8	1.71	5.0				4	2.87	1.4	0.379
12	4	1.96	3.6	0.8	1.71	5.4	0.8	2.86	4.0	2	3.12	-0.8	0.322
13	4	1.96	3.6	0.8	1.71	5.3	0.8	3.08	4.9	3	2.88	0.2	0.316
14	***4***	***1.96***	***3.6***	***0.8***	***1.71***	***5.2***	***0.8***	***3.08***	***3.9***	***4***	***2.88***	***1.5***	***0.318***

[a] Fourier transform range k = 2.0 – 15.0 Å^{-1} (resolution = 0.12 Å). σ^2 is in units of 10^{-3} Å^2. All fits are to unfiltered data. The first shell was fit using scatterers with nitrogen parameters, while the second shell was fit with oxygen parameters; however, EXAFS cannot distinguish between backscatterers differing by Z = 1. The value of n for the Fe-O/N and Fe•••Fe shells was fixed at 0.8 in view of the fact that the sample was determined to contain 75% **2** by UV/Vis spectroscopy.
[b] Goodness-of-fit parameter F defined as $[\Sigma k^6(\chi_{exptl}-\chi_{calc})^2 / \Sigma k^6\chi_{exptl}^2]^{1/2}$.

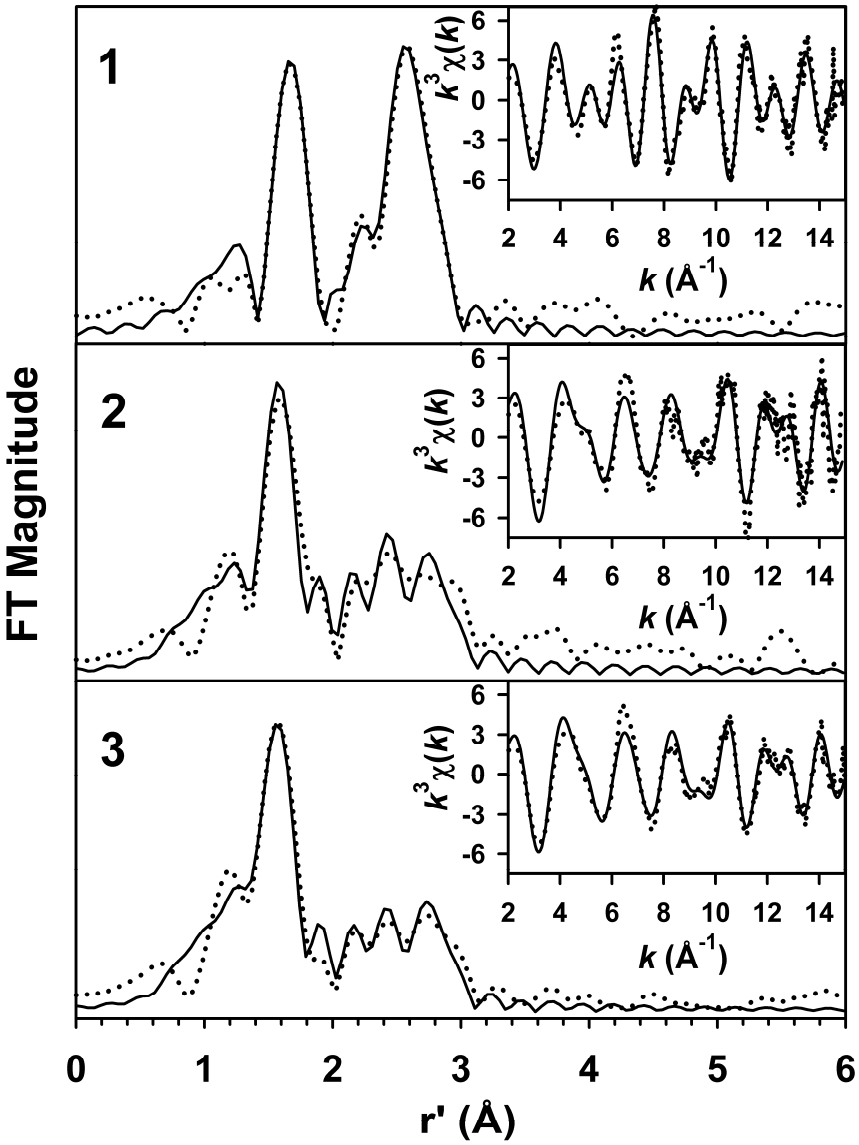

Figure 7.6. Fits to the Fourier transforms of the Fe K-edge EXAFS data ($k^3\chi(k)$) and unfiltered EXAFS spectra ($k^3\chi(k)$, insets) for **1**, **2**, and **3**. Experimental data is shown with dotted lines (•••), while fits are shown with solid lines (——). **1**, Fourier transform range of k = 2.0 – 15 Å^{-1}; **2**, k = 2.0 – 14.9 Å^{-1}; **3**, k = 2.0 – 15 Å^{-1}. Fits shown are those in bold italics in Tables 7.2 (**1**), 7.3 (**2**), and 7.4 (**3**).

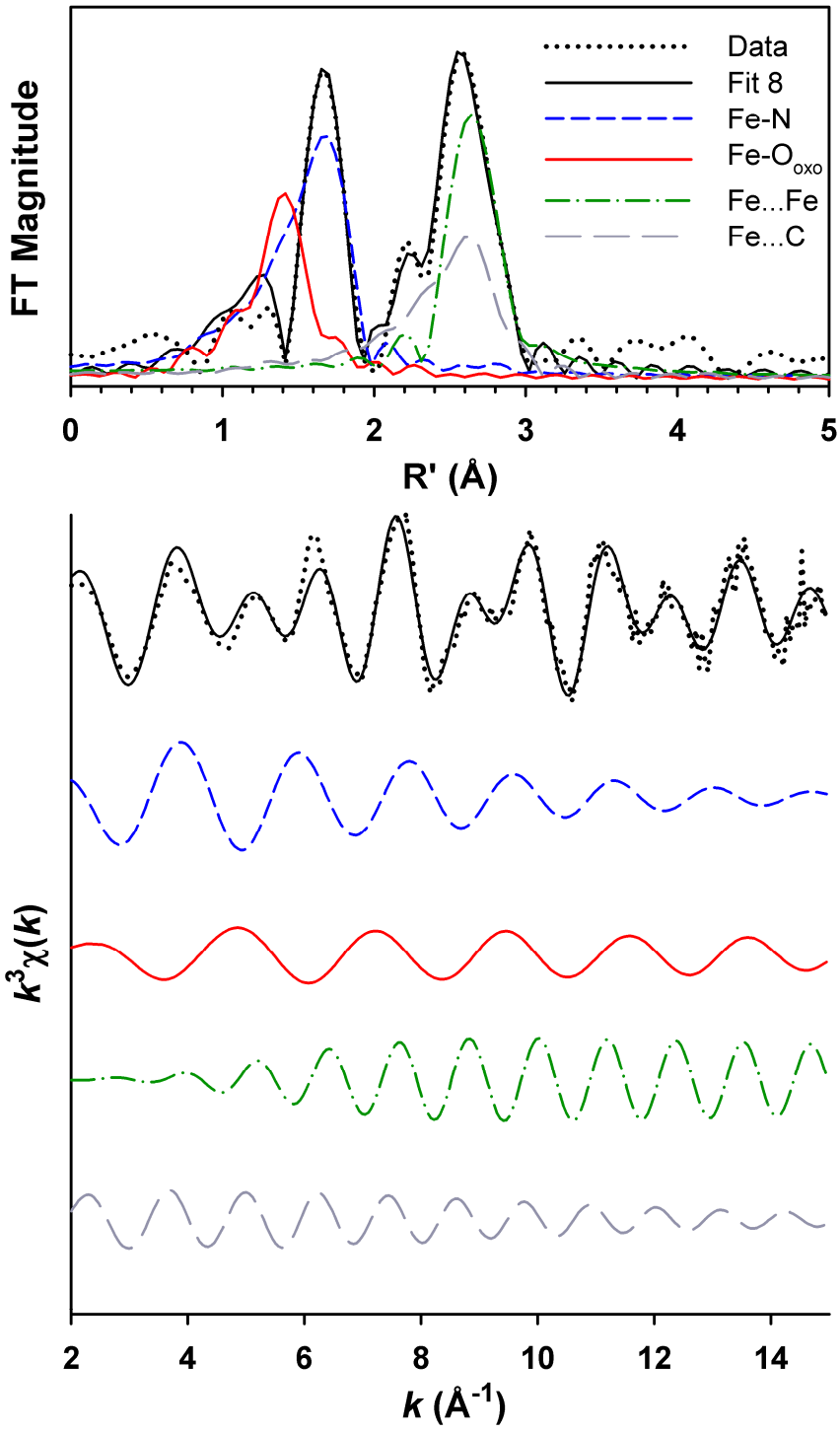

Figure 7.7. Deconvolution of the best EXAFS fit (fit 8, Table 7.2) for **1**.

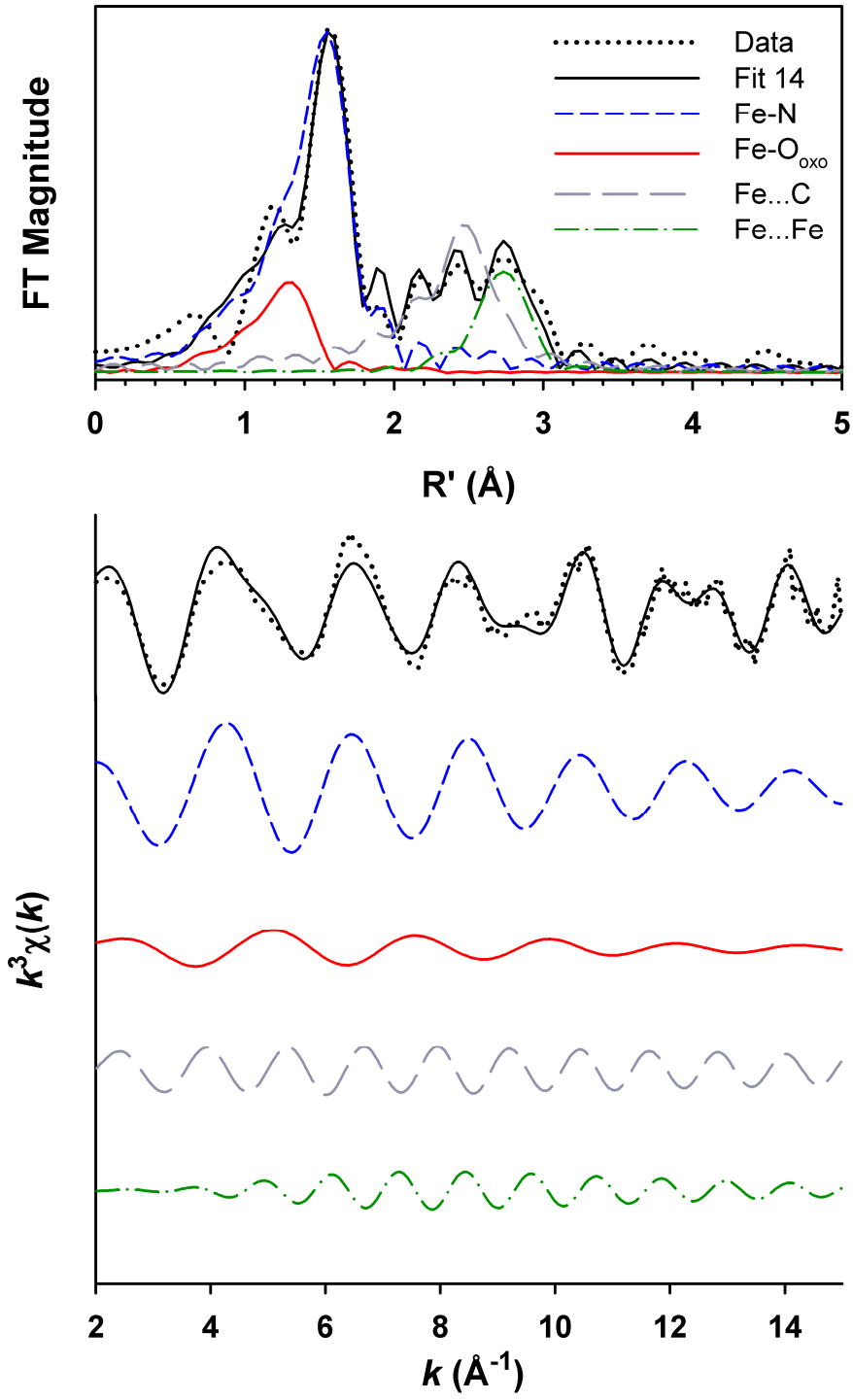

Figure 7.8. Deconvolution of the best EXAFS fit (fit 14, Table 7.4) for **3**.

7.4. Discussion

In this study, we have described the characterization via XAS of a set of three μ-oxo-bridged diiron complexes of progressively higher oxidation state. Our results indicate that a significant structural rearrangement takes place when **1** is oxidized to **2** as a consequence of a spin-state conversion of the iron centers from high-spin in **1** to low-spin in **2**, with a shortening of the Fe–(μ-O)–Fe bond lengths coupled to a lengthening of the Fe•••Fe separation. This nicely rationalizes the lack of electrochemical reversibility on the CV timescale between **1** and **2**,[94] as one would expect a significant energetic barrier to be associated with this rearrangement process. On the other hand, **2** and **3** exhibit effectively identical structures by EXAFS, consistent with the notion that, as both iron centers in **2** are already low-spin and remain low-spin in **3**, extraction of an additional electron from the diiron core will not exert a substantial effect either on electronic or geometric structure. This observation is in agreement with the reversibility of the redox couple associated with **2** and **3** observed by CV. Interestingly, we do not observe an increase in Fe•••Fe separation when **2** is oxidized to **3**, in contrast to to the 0.05 Å expansion in this distance observed by Xue *et al.* for the directly analogous conversion of the valence-delocalized $[Fe^{III}Fe^{IV}(\mu\text{-}O)_2(N_4)_2]^{3+}$ species to $[Fe^{IV}{}_2(\mu\text{-}O)_2(N_4)_2]^{3+}$. We speculate that this reflects weaker inter-iron charge repulsion in **3** as a consequence of the greater Fe•••Fe separation, in addition to a tethering effect imposed by the bridging amidate pendant arm of the S-BPAE ligand.

As noted earlier, Mössbauer studies suggested valence delocalized equivalent iron centers in **2**, consistent with an $[Fe^{+3.5}(\mu\text{-}O)(S\text{-}BPAE)]^{3+}$ formulation similar to that posited for $[Fe^{III}Fe^{IV}(\mu\text{-}O)_2(N_4)_2]^{3+}$.[279] The electronic equivalence of the iron centers in **2**

thus implies structural equivalence, and we therefore expect the bridging oxo to be symmetrically bound. A similar conclusion may be drawn for **3** in light of the electronic equivalence of the Fe(IV) centers. The metrical parameters obtained via EXAFS for r(Fe–O_{oxo}) and r(Fe•••Fe) allow us to suggest core structures for the Fe–O–Fe moiety in **2** and **3** as depicted in Scheme 7.1. These structures imply that the Fe–O–Fe bond angle in both **2** and **3** should be *ca.* 130°, in comparison to the 113.68° bond angle determined by **1** by X-ray crystallography and confirmed in our EXAFS analysis. This angle is in excellent agreement with the ν_{as}(Fe–O–Fe) values of 732 cm^{-1} obtained for **2**, based on the correlation of ν_{as}(Fe–O–Fe) with Fe–O–Fe that was noted first by Sanders-Loehr *et al.*[278] and augmented subsequently by Que and coworkers[280] for oxo-bridged diiron(III) complexes. We anticipate that measurement of either the symmetric or asymmetric Fe–O–Fe stretching modes of **3** by either resonance Raman methods or nuclear resonance vibrational spectroscopy,[217] along with calculation of geometry-optimized structures using DFT methods,[281] should provide further confirmation of our proposed core structure.

In summary, we have provided structural evidence for the retention of a μ-oxo bridged diiron core structure in two high-valent diiron complexes generated by electrochemical means, thus confirming the identity of the highly oxidizing diiron(IV) species obtained in this work. This work lays the groundwork for future studies of other singly-bridged μ-oxo diiron complexes that model the active sites and reactivity of nonheme diiron oxygenases.

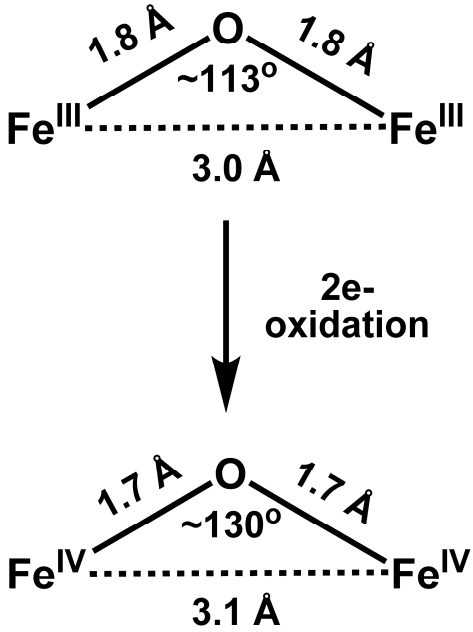

Scheme 7.1. Proposed Fe–O–Fe core structures for **1** (top) and **3** (bottom) based on EXAFS analysis. **2** is expected to exhibit a similar structure to **3**.

References

(1) Solomon, E. I.; Brunold, T. C.; Davis, M. I.; Kemsley, J. N.; Lee, S.-K.; Lehnert, N.; Neese, F.; Skulan, A. J.; Yang, Y.-S.; Zhou, J. *Chem. Rev.* **2000**, *100*, 235-349.

(2) Costas, M.; Mehn, M. P.; Jensen, M. P.; Que, L., Jr. *Chem. Rev.* **2004**, *104*, 939-986.

(3) Hausinger, R. P. *Crit. Rev. Biochem. Mol. Biol.* **2004**, *39*, 21-68.

(4) Kovaleva, E. G.; Lipscomb, J. D. *Nat. Chem. Biol.* **2008**, *4*, 186-193.

(5) Wallar, B. J.; Lipscomb, J. D. *Chem. Rev.* **1996**, *96*, 2625-2657.

(6) Merkx, M.; Kopp, D. A.; Sazinsky, M. H.; Blazyk, J. L.; Müller, J.; Lippard, S. J. *Angew. Chem. Int. Ed.* **2001**, *40*, 2782-2807.

(7) Kovaleva, E. G.; Neibergall, M. B.; Chakrabarty, S.; Lipscomb, J. D. *Acc. Chem. Res.* **2007**, *40*, 475-483.

(8) Sono, M.; Roach, M. P.; Coulter, E. D.; Dawson, J. H. *Chem. Rev.* **1996**, *96*, 2841-2887.

(9) Jin, S.; Bryson, T. A.; Dawson, J. H. *J. Biol. Inorg. Chem.* **2004**, *9*, 644-653.

(10) Denisov, I. G.; Makris, T. M.; Sligar, S. G.; Schlichting, I. *Chem. Rev.* **2005**, *105*, 2253-2278.

(11) Price, J. C.; Barr, E. W.; Tirupati, B.; Bollinger, J. M., Jr.; Krebs, C. *Biochemistry* **2003**, *42*, 7497-7508.

(12) Price, J. C.; Barr, E. W.; Glass, T. E.; Krebs, C.; Bollinger, J. M., Jr. *J. Am. Chem. Soc.* **2003**, *125*, 13008-13009.

(13) Riggs-Gelasco, P. J.; Price, J. C.; Guyer, R. B.; Brehm, J. H.; Barr, E. W.; Bollinger, J. M., Jr.; Krebs, C. *J. Am. Chem. Soc.* **2004**, *126*, 8108-8109.

(14) Price, J. C.; Barr, E. W.; Hoffart, L. M.; Krebs, C.; Bollinger, J. M., Jr. *Biochemistry* **2005**, *44*, 8138-8147.

(15) Proshlyakov, D. A.; Henshaw, T. F.; Monterosso, G. R.; Ryle, M. J.; Hausinger, R. P. *J. Am. Chem. Soc.* **2004**, *126*, 1022-1023.

(16) Grzyska, P. K.; Ryle, M. J.; Monterosso, G. R.; Liu, J.; Ballou, D. P.; Hausinger, R. P. *Biochemistry* **2005**, *44*, 3845-3855.

(17) Grzyska, P. K.; Appelman, E. H.; Hausinger, R. P.; Proshlyakov, D. A. *Proc. Natl. Acad. Sci. U.S.A.* **2010**, *107*, 3982-3987.

(18) Hoffart, L. M.; Barr, E. W.; Guyer, R. B.; Bollinger, J. M., Jr.; Krebs, C. *Proc. Natl. Acad. Sci. U.S.A.* **2006**, *103*, 14738-14743.

(19) Fujimori, D. G.; Barr, E. W.; Matthews, M. L.; Koch, G. M.; Yonce, J. R.; Walsh, C. T.; Bollinger, J. M., Jr.; Krebs, C.; Riggs-Gelasco, P. J. *J. Am. Chem. Soc.* **2007**, *129*, 13408-13409.

(20) Galonic, D. P.; Barr, E. W.; Walsh, C. T.; Bollinger, J. M., Jr.; Krebs, C. *Nat. Chem. Biol.* **2007**, *3*, 113-116.

(21) Matthews, M. L.; Krest, C. M.; Barr, E. W.; Vaillancourt, F. H.; Walsh, C. T.; Green, M. T.; Krebs, C.; Bollinger, J. M., Jr. *Biochemistry* **2009**, *48*, 4331-4343.

(22) Matthews, M. L.; Neumann, C. S.; Miles, L. A.; Grove, T. L.; Booker, S. J.; Krebs, C.; Walsh, C. T.; Bollinger, J. M., Jr. *Proc. Natl. Acad. Sci. U.S.A.* **2009**, *106*, 17723-17728.

(23) Eser, B. E.; Barr, E. W.; Frantom, P. A.; Saleh, L.; Bollinger, J. M., Jr.; Krebs, C.; Fitzpatrick, P. F. *J. Am. Chem. Soc.* **2007**, *129*, 11334-11335.

(24) Shu, L. J.; Nesheim, J. C.; Kauffmann, K.; Münck, E.; Lipscomb, J. D.; Que, L., Jr. *Science* **1997**, *275*, 515-518.

(25) Que, L., Jr. *J. Biol. Inorg. Chem.* **2004**, *9*, 684-690.

(26) Beauvais, L. G.; Lippard, S. J. *J. Am. Chem. Soc.* **2005**, *127*, 7370-7378.

(27) Stubbe, J.; Riggs-Gelasco, P. *Trends Biol. Sci.* **1998**, *23*, 438-443.

(28) Koehntop, K. D.; Emerson, J. P.; Que, L., Jr. *J. Biol. Inorg. Chem.* **2005**, *10*, 87-93.

(29) Goodwill, K. E.; Sabatier, C.; Stevens, R. C. *Biochemistry* **1998**, *37*, 13437-13445.

(30) Ellis, H. R.; Daubner, S. C.; McCulloch, R. I.; Fitzpatrick, P. F. *Biochemistry* **1999**, *38*, 10909-10914.

(31) Sturgeon, B. E.; Burdi, D.; Chen, S.; Huynh, B.-H.; Edmondson, D. E.; Stubbe, J.; Hoffman, B. M. *J. Am. Chem. Soc.* **1996**, *118*, 7551-7557.

(32) Willems, J.-P.; Lee, H.-I.; Burdi, D.; Doan, P. E.; Stubbe, J.; Hoffman, B. M. *J. Am. Chem. Soc.* **1997**, *119*, 9816-9824.

(33) Riggs-Gelasco, P. J.; Shu, L.; Chen, S.; Burdi, D.; Huynh, B. H.; Que, L., Jr.; Stubbe, J. *J. Am. Chem. Soc.* **1998**, *120*, 849-860.

(34) Shanmugam, M.; Doan, P. E.; Lees, N. S.; Stubbe, J.; Hoffman, B. M. *J. Am. Chem. Soc.* **2009**, *131*, 3370-3376.

(35) Sjöberg, B.-M.; Reichard, P.; Gräslund, A.; Ehrenberg, A. *J. Biol. Chem.* **1977**, *252*, 536-541.

(36) Larsson, A.; Sjöberg, B.-M. *EMBO J.* **1986**, *5*, 2037-2040.

(37) Stubbe, J.; Ackles, D. *J. Biol. Chem.* **1980**, *255*, 8027-8030.

(38) Sjöberg, B.-M.; Gräslund, A.; Eckstein, F. *J. Biol. Chem.* **1983**, *258*, 8060-8067.

(39) Nordlund, P.; Eklund, H. *J. Mol. Biol.* **1993**, *232*, 123-164.

(40) Uhlin, U.; Eklund, H. *Nature* **1994**, *370*, 533-539.

(41) Sjöberg, B.-M. *Structure* **1994**, *2*, 793-796.

(42) Shanklin, J.; Guy, J. E.; Mishra, G.; Lindqvist, Y. *J. Biol. Chem.* **2009**, *284*, 18559-18563.

(43) Logan, D. T.; deMaré, F.; Persson, B. O.; Slaby, A.; Sjöberg, B.-M.; Nordlund, P. *Biochemistry* **1998**, *37*, 10798-10807.

(44) Ormö, M.; Regnström, K.; Wang, Z.; Que, L., Jr.; Sahlin, M.; Sjöberg, B.-M. *J. Biol. Chem.* **1995**, *270*, 6570-6576.

(45) Ormö, M.; deMaré, F.; Regnström, K.; Åberg, A.; Sahlin, M.; Ling, J.; Loehr, T. M.; Sanders-Loehr, J.; Sjöberg, B.-M. *J. Biol. Chem.* **1992**, *267*, 8711-8714.

(46) Åberg, A.; Ormö, M.; Nordlund, P.; Sjöberg, B.-M. *Biochemistry* **1993**, *32*, 9845-9850.

(47) Ling, J.; Sahlin, M.; Sjöberg, B.-M.; Loehr, T. M.; Sanders-Loehr, J. *J. Biol. Chem.* **1994**, *269*, 5595-5601.

(48) Liu, A.; Sahlin, M.; Pötsch, S.; Sjöberg, B.-M.; Gräslund, A. *Biochem. Biophys. Res. Commun.* **1998**, *246*, 740-745.

(49) Parkin, S. E.; Chen, S.; Ley, B. A.; Mangravite, L.; Edmondson, D. E.; Huynh, B. H.; Bollinger, J. M., Jr. *Biochemistry* **1998**, *37*, 1124-1130.

(50) Tong, W. H.; Chen, S.; Lloyd, S. G.; Edmonson, D. E.; Huynh, B. H.; Stubbe, J. *J. Am. Chem. Soc.* **1996**, *118*, 2107-2108.

(51) Bollinger, J. M., Jr.; Tong, W. H.; Ravi, N.; Huynh, B. H.; Edmondson, D. E.; Stubbe, J. *J. Am. Chem. Soc.* **1994**, *116*, 8024-8032.

(52) Rova, U.; Goodtzova, K.; Ingemarson, R.; Behravan, G.; Gräslund, A.; Thelander, L. *Biochemistry* **1995**, *34*, 4267-4275.

(53) Ekberg, M.; Sahlin, M.; Eriksson, M.; Sjöberg, B.-M. *J. Biol. Chem.* **1996**, *271*, 20655-20659.

(54) Baldwin, J.; Voegtli, W. C.; Khidekel, N.; Moënne-Loccoz, P.; Krebs, C.; Pereira, A. S.; Ley, B. A.; Huynh, B. H.; Loehr, T. M.; Riggs-Gelasco, P. J.; Rosenzweig, A. C.; Bollinger, J. M., Jr. *J. Am. Chem. Soc.* **2001**, *123*, 7017-7030.

(55) Baldwin, J.; Krebs, C.; Saleh, L.; Stelling, M.; Huynh, B. H.; Bollinger, J. M., Jr.; Riggs-Gelasco, P. *Biochemistry* **2003**, *42*, 13269-13279.

(56) Bollinger, J. M., Jr.; Krebs, C.; Vicol, A.; Chen, S.; Ley, B. A.; Edmondson, D. E.; Huynh, B. H. *J. Am. Chem. Soc.* **1998**, *120*, 1094-1095.

(57) Moënne-Loccoz, P.; Baldwin, J.; Ley, B. A.; Loehr, T. M.; Bollinger, J. M., Jr. *Biochemistry* **1998**, *37*, 14659-14663.

(58) Kolberg, M.; Logan, D. T.; Bleifuss, G.; Pötsch, S.; Sjöberg, B.-M.; Gräslund, A.; Lubitz, W.; Lassmann, G.; Lendzian, F. *J. Biol. Chem.* **2005**, *280*, 11233-11246.

(59) Myllylä, R.; Majamaa, K.; Günzler, V.; Hanauske-Abel, H. N.; Kivirikko, K. I. *J. Biol. Chem.* **1984**, *259*, 5403-5405.

(60) Eichhorn, E.; van der Ploeg, J. R.; Kertesz, M. A.; Leisinger, T. *J. Biol. Chem.* **1997**, *272*, 23031-23036.

(61) Ho, R. Y. N.; Mehn, M. P.; Hegg, E. L.; Liu, A.; Ryle, M. J.; Hausinger, R. P.; Que, L., Jr. *J. Am. Chem. Soc.* **2001**, *123*, 5022-5029.

(62) Ryle, M. J.; Liu, A.; Muthukumaran, R. B.; Ho, R. Y. N.; Koehntop, K. D.; McCracken, J.; Que, L., Jr.; Hausinger, R. P. *Biochemistry* **2003**, *42*, 1854-1862.

(63) Ryle, M. J.; Koehntop, K. D.; Liu, A.; Que, L., Jr.; Hausinger, R. P. *Proc. Natl. Acad. Sci. U.S.A.* **2003**, *100*, 3790-3795.

(64) Koehntop, K. D.; Marimanikkuppam, S.; Ryle, M. J.; Hausinger, R. P.; Que, L., Jr. *J. Biol. Inorg. Chem.* **2006**, *11*, 63-72.

(65) Liu, A.; Ho, R. Y. N.; Que, L., Jr.; Ryle, M. J.; Phinney, B. S.; Hausinger, R. P. *J. Am. Chem. Soc.* **2001**, *123*, 5126-5127.

(66) Henshaw, T. F.; Feig, M.; Hausinger, R. P. *J. Inorg. Biochem.* **2004**, *98*, 856-861.

(67) Chowdhury, R.; Hardy, A.; Schofield, C. J. *Chem. Soc. Rev.* **2008**, *37*, 1308-1319.

(68) Chen, Y.-H.; Comeaux, L. M.; Herbst, R. W.; Saban, E.; Kennedy, D. C.; Maroney, M. J.; Knapp, M. J. *J. Inorg. Biochem.* **2008**, *102*, 2120-2129.

(69) Chen, Y.-H.; Comeaux, L. M.; Eyles, S. J.; Knapp, M. J. *Chem. Commun.* **2008**, 4768-4770.

(70) Lindstedt, S.; Rundgren, M. *J. Biol. Chem.* **1982**, *257*, 11922-11931.

(71) Bradley, F. C.; Lindstedt, S.; Lipscomb, J. D.; Que, L., Jr.; Roe, A. L.; Rundgren, M. *J. Biol. Chem.* **1986**, *261*, 11693-11696.

(72) Serre, L.; Sailland, A.; Sy, D.; Boudec, P.; Rolland, A.; Pebay-Peyroula, E.; Cohen-Addad, C. *Structure* **1999**, *7*, 977-988.

(73) Erlandsen, H.; Bjørgo, E.; Flatmark, T.; Stevens, R. C. *Biochemistry* **2000**, *39*, 2208-2217.

(74) Kinzie, S. D.; Thevis, M.; Ngo, K.; Whitelegge, J.; Loo, J. A.; Abu-Omar, M. M. *J. Am. Chem. Soc.* **2003**, *125*, 4710-4711.

(75) Smith, J. J.; Thomson, A. J.; Proudfoot, A. E.; Wells, T. N. *Eur. J. Biochem.* **1997**, *244*, 325-333.

(76) Cleasby, A.; Wonacott, A.; Skarzynski, T.; Hubbard, R. E.; Davies, G. J.; Proudfoot, A. E. I.; Bernard, A. R.; Payton, M. A.; Wells, T. N. C. *Nat. Struct. Biol.* **1996**, *3*, 470-479.

(77) Liu, P.; Mehn, M. P.; Yan, F.; Zhao, Z.; Que, L., Jr.; Liu, H.-w. *J. Am. Chem. Soc.* **2004**, *126*, 10306-10312.

(78) Higgins, L. J.; Yan, F.; Liu, P.; Liu, H.-w.; Drennan, C. L. *Nature* **2005**, *437*, 838-844.

(79) Shaik, S.; de Visser, S. P.; Kumar, D. *J. Biol. Inorg. Chem.* **2004**, *9*, 661-668.

(80) Mukherjee, A.; Cranswick, M. A.; Chakrabarti, M.; Paine, T. K.; Fujisawa, K.; Münck, E.; Que, L., Jr. *Inorg. Chem.* **2010**, *49*, 3618-3628.

(81) Krebs, C.; Fujimori, D. G.; Walsh, C. T.; Bollinger, J. M., Jr. *Acc. Chem. Res.* **2007**, *40*, 484-492.

(82) Hanauske-Abel, H. M.; Günzler, V. *J. Theor. Biol.* **1982**, *94*, 421-455.

(83) Karlsson, A.; Parales, J. V.; Parales, R. E.; Gibson, D. T.; Eklund, H.; Ramaswamy, S. *Science* **2003**, *299*, 1039-1042.

(84) Barlow, J. N.; Zhang, Z.; John, P.; Baldwin, J. E.; Schofield, C. J. *Biochemistry* **1997**, *36*, 3563-3569.

(85) Emerson, J. P.; Kovaleva, E. G.; Farquhar, E. R.; Lipscomb, J. D.; Que, L., Jr. *Proc. Natl. Acad. Sci. U.S.A.* **2008**, *105*, 7347-7352.

(86) Farquhar, E. R.; Emerson, J. P.; Koehntop, K. D.; Reynolds, M. F.; Trmčić, M.; Que, L., Jr. *J. Biol. Inorg. Chem.* **2010**, submitted for publication.

(87) Scott, R. A. *Methods Enzymol.* **1985**, *117*, 414-459.

(88) Riggs-Gelasco, P. J.; Stemmler, T. L.; Penner-Hahn, J. E. *Coord. Chem. Rev.* **1995**, *144*, 245-286.

(89) Penner-Hahn, J. E. *Coord. Chem. Rev.* **1999**, *190-192*, 1101-1123.

(90) Scott, R. A. In *Physical Methods in Bioinorganic Chemistry. Spectroscopy and Magnetism*; Que, L., Jr., Ed.; University Science Books: Sausalito, CA, 2000, p 465-527.

(91) McDonald, A. R.; Bukowski, M. R.; Farquhar, E. R.; Jackson, T. A.; Koehntop, K. D.; Seo, M. S.; DeHont, R. F.; Stubna, A.; Halfen, J. A.; Münck, E.; Nam, W.; Que, L., Jr. *J. Am. Chem. Soc.* **2010**, submitted for publication.

(92) England, J.; Martinho, M.; Farquhar, E. R.; Frisch, J. R.; Bominaar, E. L.; Münck, E.; Que, L., Jr. *Angew. Chem. Int. Ed.* **2009**, *48*, 3622-3626.

(93) England, J.; Guo, Y.; Farquhar, E. R.; Young Jr., V. G.; Münck, E.; Que, L., Jr. *J. Am. Chem. Soc.* **2010**, *132*, 8635-8644.

(94) Wang, D.; Farquhar, E. R.; Stubna, A.; Münck, E.; Que, L., Jr. *Nat. Chem.* **2009**, *1*, 145-150.

(95) Vaillancourt, F. H.; Bolin, J. T.; Eltis, L. D. *Crit. Rev. Biochem. Mol. Biol.* **2006**, *41*, 241-267.

(96) Lipscomb, J. D. *Curr. Op. Struct. Biol.* **2008**, *18*, 644-649.

(97) Kovaleva, E. G.; Lipscomb, J. D. *Science* **2007**, *316*, 453-457.

(98) Emerson, J. P.; Farquhar, E. R.; Que, L., Jr. *Angew. Chem. Int. Ed.* **2007**, *46*, 8553-8556.

(99) Farquhar, E. R.; Koehntop, K. D.; Emerson, J. P.; Que, L., Jr. *Biochem. Biophys. Res. Commun.* **2005**, *338*, 230-239.

(100) Olson, P. E.; Qi, B.; Que, L., Jr; Wackett, L. P. *Appl. Environ. Microbiol.* **1992**, *58*, 2820-2826.

(101) Boldt, Y. R.; Sadowsky, M. J.; Ellis, L. B.; Que, L., Jr.; Wackett, L. P. *J. Bacteriol.* **1995**, *177*, 1225-1232.

(102) Whiting, A. K.; Boldt, Y. R.; Hendrich, M. P.; Wackett, L. P.; Que, L., Jr. *Biochemistry* **1996**, *35*, 160-170.

(103) Miller, M. A.; Lipscomb, J. D. *J. Biol. Chem.* **1996**, *271*, 5524-5535.

(104) Wang, Y. Z.; Lipscomb, J. D. *Prot. Expr. Purif.* **1997**, *10*, 1-9.

(105) Vetting, M. W.; Wackett, L. P.; Que, L., Jr.; Lipscomb, J. D.; Ohlendorf, D. H. *J. Bacteriol.* **2004**, *186*, 1945-1958.

(106) Gunderson, W. A.; Zatsman, A. I.; Emerson, J. P.; Farquhar, E. R.; Que, L., Jr.; Lipscomb, J. D.; Hendrich, M. P. *J. Am. Chem. Soc.* **2008**, *130*, 14465-14467.

(107) Lord, R. C.; Yu, N.-t. *J. Mol. Biol.* **1970**, *50*, 509-524.

(108) Riviere, L. R.; Tempst, P. *Curr. Protoc. Protein Sci.* **1995**, 11.1.1-19.

(109) Haavik, J.; Martinez, A.; Olafsdottir, S.; Mallet, J.; Flatmark, T. *Eur. J. Biochem.* **1992**, *210*, 23-31.

(110) Martinez, A.; Andersson, K. K.; Haavik, J.; Flatmark, T. *Eur. J. Biochem.* **1991**, *198*, 675-682.

(111) Andersson, K. K.; Cox, D. D.; Que, L., Jr.; Flatmark, T.; Haavik, J. *J. Biol. Chem.* **1988**, *263*, 18621-18626.

(112) Michaud-Soret, I.; Andersson, K. K.; Que, L., Jr.; Haavik, J. *Biochemistry* **1995**, *34*, 5504-5510.

(113) Gaber, B. P.; Sheridan, J. P.; Bazer, F. W.; Roberts, R. M. *J. Biol. Chem.* **1979**, *254*, 8340-8342.

(114) Antanaitis, B. C.; Strekas, T.; Aisen, P. *J. Biol. Chem.* **1982**, *257*, 3766-3770.

(115) Cox, D. D.; Benkovic, S. J.; Bloom, L. M.; Bradley, F. C.; Nelson, M. J.; Que, L., Jr.; Wallick, D. E. *J. Am. Chem. Soc.* **1988**, *110*, 2026-2032.

(116) Bratsch, S. G. *J. Phys. Chem. Ref. Data* **1989**, *18*, 1-21.

(117) Lloyd, M. D.; Lee, H.-J.; Harlos, K.; Zhang, Z.-H.; Baldwin, J. E.; Schofield, C. J.; Charnock, J. M.; Garner, C. D.; Hara, T.; Terwisscha van Scheltinga, A. C.; Valegård, K.; Viklund, J. A. C.; Hajdu, J.; Andersson, I.; Danielsson, Å.; Bhikhabhai, R. *J. Mol. Biol.* **1999**, *287*, 943-960.

(118) Yang, C.-G.; Yi, C.; Duguid, E. M.; Sullivan, C. T.; Jian, X.; Rice, P. A.; He, C. *Nature* **2008**, *452*, 961-965.

(119) Roach, P. L.; Clifton, I. J.; Fulop, V.; Harlos, K.; Barton, G. J.; Hajdu, J.; Andersson, I.; Schofield, C. J.; Baldwin, J. E. *Nature* **1995**, *375*, 700-704.

(120) Yu, B.; Edstrom, W. C.; Benach, J.; Hamuro, Y.; Weber, P. C.; Gibney, B. R.; Hunt, J. F. *Nature* **2006**, *439*, 879-884.

(121) Hayaishi, O.; Katagiri, M.; Rothberg, S. *J. Am. Chem. Soc.* **1955**, *77*, 5450-5451.

(122) Hayaishi, O. *Biochem. Biophys. Res. Commun.* **2005**, *338*, 2-6.

(123) Hayaishi, O. *J. Biol. Chem.* **2008**, *283*, 19165-19175.

(124) Clifton, I. J.; McDonough, M. A.; Ehrismann, D.; Kershaw, N. J.; Granatino, N.; Schofield, C. J. *J. Inorg. Biochem.* **2006**, *100*, 644-669.

(125) Ferraro, D. J.; Gakhar, L.; Ramaswamy, S. *Biochem. Biophys. Res. Commun.* **2005**, *338*, 175-190.

(126) Arciero, D. M.; Orville, A. M.; Lipscomb, J. D. *J. Biol. Chem.* **1985**, *260*, 14035-14044.

(127) Fielding, A. J.; Farquhar, E. R.; Emerson, J. P.; Kovaleva, E. G.; Lipscomb, J. D.; Que, L., Jr.; unpublished observations.

(128) Schaab, M. R.; Barney, B. M.; Francisco, W. A. *Biochemistry* **2006**, *45*, 1009-1016.

(129) Merkens, H.; Kappl, R.; Jakob, R. P.; Schmid, F. X.; Fetzner, S. *Biochemistry* **2008**, *47*, 12185-12196.

(130) George, G. N.; EXAFSPAK; Stanford Synchrotron Radiation Lightsource, SLAC National Accelerator Laboratory: Stanford, CA, 2000.

(131) Tenderholt, A.; Hedman, B.; Hodgson, K. O. *AIP Conf. Proc.* **2007**, *882*, 105-107.

(132) Scarrow, R. C.; Brennan, B. A.; Cummings, J. G.; Jin, H.; Duong, D. J.; Kindt, J. T.; Nelson, M. J. *Biochemistry* **1996**, *35*, 10078-10088.

(133) Rohde, J.-U.; Torelli, S.; Shan, X.; Lim, M. H.; Klinker, E. J.; Kaizer, J.; Chen, K.; Nam, W.; Que, L., Jr. *J. Am. Chem. Soc.* **2004**, *126*, 16750-16761.

(134) Randall, C. R.; Shu, L.; Chiou, Y.-M.; Hagen, K. S.; Ito, M.; Kitajima, N.; Lachicotte, R. J.; Zang, Y.; Que, L., Jr. *Inorg. Chem.* **1995**, *34*, 1036-1039.

(135) Ankudinov, A. L.; Ravel, B.; Rehr, J. J.; Conradson, S. D. *Phys. Rev. B* **1998**, *58*, 7565.

(136) Padden, K. M.; Krebs, J. F.; Trafford, K. T.; Yap, G. P. A.; Rheingold, A. H.; Borovik, A. S.; Scarrow, R. C. *Chem. Mater.* **2001**, *13*, 4305-4313.

(137) Padden, K. M.; Krebs, J. F.; MacBeth, C. E.; Scarrow, R. C.; Borovik, A. S. *J. Am. Chem. Soc.* **2001**, *123*, 1072-1079.

(138) Bonnitcha, P. D.; Hall, M. D.; Underwood, C. K.; Foran, G. J.; Zhang, M.; Beale, P. J.; Hambley, T. W. *J. Inorg. Biochem.* **2006**, *100*, 963-971.

(139) Hall, M. D.; Underwood, C. K.; Failes, T. W.; Foran, G. J.; Hambley, T. W. *Aust. J. Chem.* **2007**, *60*, 180-183.

(140) Yachandra, V.; Powers, L.; Spiro, T. G. *J. Am. Chem. Soc.* **1983**, *105*, 6596-6604.

(141) Zhang, J. H.; Kurtz, D. M.; Maroney, M. J.; Whitehead, J. P. *Inorg. Chem.* **1992**, *31*, 1359-1366.

(142) della Longa, S.; Bianconi, A.; Palladino, L.; Simonelli, B.; Congiu Castellano, A.; Borghi, E.; Barteri, M.; Beltramini, M.; Rocco, G. P.; Salvato, B.; Bubacco, L.; Magliozzo, R. S.; Peisach, J. *Biophys. J.* **1993**, *65*, 2680-2691.

(143) Ma, H.; Jensen, M. P., personal communication.

(144) Leitch, S.; Bradley, M. J.; Rowe, J. L.; Chivers, P. T.; Maroney, M. J. *J. Am. Chem. Soc.* **2007**, *129*, 5085-5095.

(145) Iwig, J. S.; Leitch, S.; Herbst, R. W.; Maroney, M. J.; Chivers, P. T. *J. Am. Chem. Soc.* **2008**, *130*, 7592-7606.

(146) Strange, R. W.; Blackburn, N. J.; Knowles, P. F.; Hasnain, S. S. *J. Am. Chem. Soc.* **1987**, *109*, 7157-7162.

(147) Wang, S.; Lee, M. H.; Hausinger, R. P.; Clark, P. A.; Wilcox, D. E.; Scott, R. A. *Inorg. Chem.* **1994**, *33*, 1589-1593.

(148) Stemmler, T. L.; Sossong, T. M.; Goldstein, J. I.; Ash, D. E.; Elgren, T. E.; Kurtz, D. M.; Penner-Hahn, J. E. *Biochemistry* **1997**, *36*, 9847-9858.

(149) Cosper, N. J.; Stålhandske, C. M. V.; Saari, R. E.; Hausinger, R. P.; Scott, R. A. *J. Biol. Inorg. Chem.* **1999**, *4*, 122-129.

(150) Blackburn, N. J.; Strange, R. W.; McFadden, L. M.; Hasnain, S. S. *J. Am. Chem. Soc.* **1987**, *109*, 7162-7170.

(151) Zhang, H. H.; Filipponi, A.; Di Cicco, A.; Scott, M. J.; Holm, R. H.; Hedman, B.; Hodgson, K. O. *J. Am. Chem. Soc.* **1997**, *119*, 2470-2478.

(152) Periyannan, G. R.; Costello, A. L.; Tierney, D. L.; Yang, K.-W.; Bennett, B.; Crowder, M. W. *Biochemistry* **2005**, *45*, 1313-1320.

(153) Hawk, M. J.; Breece, R. M.; Hajdin, C. E.; Bender, K. M.; Hu, Z.; Costello, A. L.; Bennett, B.; Tierney, D. L.; Crowder, M. W. *J. Am. Chem. Soc.* **2009**, *131*, 10753-10762.

(154) Rheingold, A. L.; Liable-Sands, L. M.; Golen, J. A.; Yap, G. P. A.; Trofimenko, S. *Dalton Trans.* **2004**, 598-604.

(155) Kremer-Aach, A.; Klaui, W.; Bell, R.; Strerath, A.; Wunderlich, H.; Mootz, D. *Inorg. Chem.* **1997**, *36*, 1552-1563.

(156) Addison, A. W.; Rao, T. N.; Reedijk, J.; Rijn, J. v.; Verschoor, G. C. *J. Chem. Soc., Dalton Trans.* **1984**, 1349-1356.

(157) Davis, M. I.; Wasinger, E. C.; Decker, A.; Pau, M. Y. M.; Vaillancourt, F. H.; Bolin, J. T.; Eltis, L. D.; Hedman, B.; Hodgson, K. O.; Solomon, E. I. *J. Am. Chem. Soc.* **2003**, *125*, 11214-11227.

(158) Wasinger, E. C.; Mitic, N.; Hedman, B.; Caradonna, J.; Solomon, E. I.; Hodgson, K. O. *Biochemistry* **2002**, *41*, 6211-6217.

(159) Kemsley, J. N.; Wasinger, E. C.; Datta, S.; Mitic, N.; Acharya, T.; Hedman, B.; Caradonna, J. P.; Hodgson, K. O.; Solomon, E. I. *J. Am. Chem. Soc.* **2003**, *125*, 5677-5686.

(160) Chow, M. S.; Eser, B. E.; Wilson, S. A.; Hodgson, K. O.; Hedman, B.; Fitzpatrick, P. F.; Solomon, E. I. *J. Am. Chem. Soc.* **2009**, *131*, 7685-7698.

(161) Thorp, H. H. *Inorg. Chem.* **1992**, *31*, 1585-1588.

(162) Liu, W.; Thorp, H. H. *Inorg. Chem.* **1993**, *32*, 4102-4105.

(163) Thorp, H. H. *Inorg. Chem.* **1998**, *37*, 5690-5692.

(164) Shu, L.; Chiou, Y.-M.; Orville, A. M.; Miller, M. A.; Lipscomb, J. D.; Que, L., Jr. *Biochemistry* **1995**, *34*, 6649-6659.

(165) Vaillancourt, F. H.; Barbosa, C. J.; Spiro, T. G.; Bolin, J. T.; Blades, M. W.; Turner, R. F. B.; Eltis, L. D. *J. Am. Chem. Soc.* **2002**, *124*, 2485-2496.

(166) Horsman, G. P.; Jirasek, A.; Vaillancourt, F. H.; Barbosa, C. J.; Jarzecki, A. A.; Xu, C.; Mekmouche, Y.; Spiro, T. G.; Lipscomb, J. D.; Blades, M. W.; Turner, R. F. B.; Eltis, L. D. *J. Am. Chem. Soc.* **2005**, *127*, 16882-16891.

(167) Furutachi, H.; Okawa, H. *Inorg. Chem.* **1997**, *36*, 3911-3918.

(168) Kita, S.; Furutachi, H.; Okawa, H. *Inorg. Chem.* **1999**, *38*, 4038-4045.

(169) Cini, R. *Acta Cryst.* **2001**, *C57*, 1171-1173.

(170) Du, M.; An, D.-L.; Guo, Y.-M.; Bu, X.-H. *J. Mol. Struct.* **2002**, *641*, 193-198.

(171) Rodriguez, L.; Labisbal, E.; Sousa-Pedrares, A.; García-Vazquez, J. A.; Romero, J.; Duran, M. L.; Real, J. A.; Sousa, A. *Inorg. Chem.* **2006**, *45*, 7903-7914.

(172) Que, L., Jr. *Acc. Chem. Res.* **2007**, *40*, 493-500.

(173) Rohde, J. U.; In, J. H.; Lim, M. H.; Brennessel, W. W.; Bukowski, M. R.; Stubna, A.; Münck, E.; Nam, W.; Que, L., Jr. *Science* **2003**, *299*, 1037-1039.

(174) Rohde, J.-U.; Que, L., Jr. *Angew. Chem. Int. Ed.* **2005**, *44*, 2255-2258.

(175) Sastri, C. V.; Park, M. J.; Ohta, T.; Jackson, T. A.; Stubna, A.; Seo, M. S.; Lee, J.; Kim, J.; Kitagawa, T.; Münck, E.; Que, L.; Nam, W. *J. Am. Chem. Soc.* **2005**, *127*, 12494-12495.

(176) Sastri, C. V.; Lee, J.; Oh, K.; Lee, Y. J.; Lee, J.; Jackson, T. A.; Ray, K.; Hirao, H.; Shin, W.; Halfen, J. A.; Kim, J.; Que, L., Jr.; Shaik, S.; Nam, W. *Proc. Natl. Acad. Sci. U.S.A.* **2007**, *104*, 19181-19186.

(177) Jackson, T. A.; Rohde, J.-U.; Seo, M. S.; Sastri, C. V.; DeHont, R.; Stubna, A.; Ohta, T.; Kitagawa, T.; Münck, E.; Nam, W.; Que, L., Jr. *J. Am. Chem. Soc.* **2008**, *130*, 12394-12407.

(178) Bukowski, M. R.; Koehntop, K. D.; Stubna, A.; Bominaar, E. L.; Halfen, J. A.; Münck, E.; Nam, W.; Que, L., Jr. *Science* **2005**, *310*, 1000-1002.

(179) Grapperhaus, C. A.; Mienert, B.; Bill, E.; Weyhermüller, T.; Wieghardt, K. *Inorg. Chem.* **2000**, *39*, 5306-5317.

(180) Berry, J. F.; Bill, E.; Bothe, E.; Weyhermüller, T.; Wieghardt, K. *J. Am. Chem. Soc.* **2005**, *127*, 11550-11551.

(181) Aliaga-Alcalde, N.; George, S. D.; Mienert, B.; Bill, E.; Wieghardt, K.; Neese, F. *Angew. Chem. Int. Ed.* **2005**, *44*, 2908-2912.

(182) Berry, J. F.; Bill, E.; Bothe, E.; Neese, F.; Wieghardt, K. *J. Am. Chem. Soc.* **2006**, *128*, 13515-13528.

(183) Berry, J. F.; Bill, E.; Bothe, E.; George, S. D.; Mienert, B.; Neese, F.; Wieghardt, K. *Science* **2006**, *312*, 1937-1941.

(184) Thibon, A.; England, J.; Martinho, M.; Young, V. G.; Frisch, J. R.; Guillot, R.; Girerd, J. J.; Münck, E.; Que, L., Jr.; Banse, F. *Angew. Chem. Int. Ed.* **2008**, *47*, 7064-7067.

(185) England, J.; Young Jr, V. G.; Que, L., Jr.; unpublished observations.

(186) England, J.; Martinho, M.; Bominaar, E. L.; Münck, E.; Que L., Jr.; unpublished observations.

(187) Rohde, J.-U.; Stubna, A.; Bominaar, E. L.; Münck, E.; Nam, W.; Que, L., Jr. *Inorg. Chem.* **2006**, *45*, 6435-6445.

(188) Klinker, E. J.; Kaizer, J.; Brennessel, W. W.; Woodrum, N. L.; Cramer, C. J.; Que, L., Jr. *Angew. Chem. Int. Ed.* **2005**, *44*, 3690-3694.

(189) Frisch, J. R. Ph.D. dissertation, University of Minnesota, 2010.

(190) Jung, C. *Biochim. Biophys. Acta* **2010**, in press, doi: 10.1016/j.bbapap.2010.06.007.

(191) Stone, K. L.; Behan, R. K.; Green, M. T. *Proc. Natl. Acad. Sci. U.S.A.* **2005**, *102*, 16563-16565.

(192) Green, M. T.; Dawson, J. H.; Gray, H. B. *Science* **2004**, *304*, 1653-1656.

(193) Behan, R. K.; Green, M. T. *J. Inorg. Biochem.* **2006**, *100*, 448-459.

(194) Behan, R. K.; Hoffart, L. M.; Stone, K. L.; Krebs, C.; Green, M. T. *J. Am. Chem. Soc.* **2006**, *128*, 11471-11474.

(195) Green, M. T. *Curr. Op. Chem. Biol.* **2009**, *13*, 84-88.

(196) Kurtz, D.; Coulter, E. *J. Biol. Inorg. Chem.* **2002**, *7*, 653-658.

(197) Kovacs, J. A. *Chem. Rev.* **2004**, *104*, 825-848.

(198) Kurtz, D. M. *J. Inorg. Biochem.* **2006**, *100*, 679-693.

(199) Kovacs, J. A.; Brines, L. M. *Acc. Chem. Res.* **2007**, *40*, 501-509.

(200) Roach, P. L.; Clifton, I. J.; Hensgens, C. M. H.; Shibata, N.; Schofield, C. J.; Hajdu, J.; Baldwin, J. E. *Nature* **1997**, *387*, 827-830.

(201) Randall, C. R.; Zang, Y.; True, A. E.; Que, L., Jr.; Charnock, J. M.; Garner, C. D.; Fujishima, Y.; Schofield, C. J.; Baldwin, J. E. *Biochemistry* **1993**, *32*, 6664-6673.

(202) Simmons, C. R.; Liu, Q.; Huang, Q.; Hao, Q.; Begley, T. P.; Karplus, P. A.; Stipanuk, M. H. *J. Biol. Chem.* **2006**, *281*, 18723-18733.

(203) Gardner, J. D.; Pierce, B. S.; Fox, B. G.; Brunold, T. C. *Biochemistry* **2010**, in press, doi: 10.1021/bi100189h.

(204) Joseph, C. A.; Maroney, M. J. *Chem. Commun.* **2007**, 3338-3349.

(205) Grapperhaus, C. A.; Darensbourg, M. Y. *Acc. Chem. Res.* **1998**, *31*, 451-459.

(206) Harrop, T. C.; Mascharak, P. K. *Acc. Chem. Res.* **2004**, *37*, 253-260.

(207) Decker, A.; Rohde, J.-U.; Que, L., Jr.; Solomon, E. I. *J. Am. Chem. Soc.* **2004**, *126*, 5378-5379.

(208) Decker, A.; Rohde, J.-U.; Klinker, E. J.; Wong, S. D.; Que, L., Jr.; Solomon, E. I. *J. Am. Chem. Soc.* **2007**, *129*, 15983-15996.

(209) Bukowski, M. R.; Zhu, S. R.; Koehntop, K. D.; Brennessel, W. W.; Que, L., Jr. *J. Biol. Inorg. Chem.* **2004**, *9*, 39-48.

(210) Fiedler, A. T.; Halfen, H. L.; Halfen, J. A.; Brunold, T. C. *J. Am. Chem. Soc.* **2005**, *127*, 1675-1689.

(211) Cocolios, P.; Lagrange, G.; Guilard, R.; Oumous, H.; Lecomte, C. *J. Chem. Soc., Dalton Trans.* **1984**, 567-574.

(212) Heinrich, L.; Li, Y.; Vaissermann, J.; Chottard, G.; Chottard, J.-C. *Angew. Chem. Int. Ed.* **1999**, *38*, 3526-3528.

(213) Noveron, J. C.; Olmstead, M. M.; Mascharak, P. K. *J. Am. Chem. Soc.* **2001**, *123*, 3247-3259.

(214) Westre, T. E.; Kennepohl, P.; DeWitt, J. G.; Hedman, B.; Hodgson, K. O.; Solomon, E. I. *J. Am. Chem. Soc.* **1997**, *119*, 6297-6314.

(215) DeWitt, J. G.; Rosenzweig, A. C.; Salifoglou, A.; Hedman, B.; Lippard, S. J.; Hodgson, K. O. *Inorg. Chem.* **1995**, *34*, 2505-2515.

(216) Yoon, J.; Wilson, S. A.; Jang, Y. K.; Seo, Mi S.; Nehru, K.; Hedman, B.; Hodgson, K. O.; Bill, E.; Solomon, E. I.; Nam, W. *Angew. Chem. Int. Ed.* **2009**, *48*, 1257-1260.

(217) Bell, C. B.; Wong, S. D.; Xiao, Y. M.; Klinker, E. J.; Tenderholt, A. L.; Smith, M. C.; Rohde, J.-U.; Que, L., Jr.; Cramer, S. P.; Solomon, E. I. *Angew. Chem. Int. Ed.* **2008**, *47*, 9071-9074.

(218) Dey, A.; Chow, M.; Taniguchi, K.; Lugo-Mas, P.; Davin, S.; Maeda, M.; Kovacs, J. A.; Odaka, M.; Hodgson, K. O.; Hedman, B.; Solomon, E. I. *J. Am. Chem. Soc.* **2005**, *128*, 533-541.

(219) Krebs, C.; Price, J. C.; Baldwin, J.; Saleh, L.; Green, M. T.; Bollinger, J. M. *Inorg. Chem.* **2005**, *44*, 742-757.

(220) Sinnecker, S.; Svensen, N.; Barr, E. W.; Ye, S.; Bollinger, J. M., Jr.; Neese, F.; Krebs, C. *J. Am. Chem. Soc.* **2007**, *129*, 6168-6179.

(221) Solomon, E. I.; Wong, S. D.; Liu, L. V.; Decker, A.; Chow, M. S. *Curr. Op. Chem. Biol.* **2009**, *13*, 99-113.

(222) Ye, S.; Neese, F. *Curr. Op. Chem. Biol.* **2009**, *13*, 89-98.

(223) Janardanan, D.; Wang, Y.; Schyman, P.; Que, L., Jr.; Shaik, S. *Angew. Chem. Int. Ed.* **2010**, *49*, 3342-3345.

(224) Pestovsky, O.; Bakac, A. *J. Am. Chem. Soc.* **2004**, *126*, 13757-13764.

(225) Pestovsky, O.; Stoian, S.; Bominaar, E. L.; Shan, X.; Münck, E.; Que, L., Jr.; Bakac, A. *Angew. Chem. Int. Ed.* **2005**, *44*, 6871-6874.

(226) Krebs, C.; Price, J. C.; Baldwin, J.; Saleh, L.; Green, M. T.; Bollinger, J. M., Jr. *Inorg. Chem.* **2005**, *44*, 742-757.

(227) Cummins, C. C.; Schrock, R. R. *Inorg. Chem.* **1994**, *33*, 395-396.

(228) MacBeth, C. E.; Golombek, A. P.; Young, V. G., Jr.; Yang, C.; Kuczera, K.; Hendrich, M. P.; Borovik, A. S. *Science* **2000**, *289*, 938-941.

(229) Wittmann, H.; Raab, V.; Schorm, A.; Plackmeyer, J.; Sundermeyer, J. *Eur. J. Inorg. Chem.* **2001**, *2001*, 1937-1948.

(230) Schatz, M.; Raab, V.; Foxon, S. P.; Brehm, G.; Schneider, S.; Reiher, M.; Holthausen, M. C.; Sundermeyer, J.; Schindler, S. *Angew. Chem. Int. Ed.* **2004**, *43*, 4360-4363.

(231) Würtele, C.; Gaoutchenova, E.; Harms, K.; Holthausen, M. C.; Sundermeyer, J.; Schindler, S. *Angew. Chem. Int. Ed.* **2006**, *45*, 3867-3869.

(232) Maiti, D.; Lee, D.-H.; Gaoutchenova, K.; Würtele, C.; Holthausen, Max C.; Narducci Sarjeant, Amy A.; Sundermeyer, J.; Schindler, S.; Karlin, Kenneth D. *Angew. Chem. Int. Ed.* **2008**, *47*, 82-85.

(233) Macikenas, D.; Skrzypczak-Jankun, E.; Protasiewicz, J. D. *J. Am. Chem. Soc.* **1999**, *121*, 7164-7165.

(234) Kaizer, J.; Klinker, E. J.; Oh, N. Y.; Rohde, J.-U.; Song, W. J.; Stubna, A.; Kim, J.; Munck, E.; Nam, W.; Que, L., Jr. *J. Am. Chem. Soc.* **2003**, *126*, 472-473.

(235) Berry, J. F.; George, S. D.; Neese, F. *Phys. Chem. Chem. Phys.* **2008**, *10*, 4361-4374.

(236) Dey, A.; Hocking, R. K.; Larsen, P.; Borovik, A. S.; Hodgson, K. O.; Hedman, B.; Solomon, E. I. *J. Am. Chem. Soc.* **2006**, *128*, 9825-9833.

(237) Zang, Y.; Que, L., Jr. *Inorg. Chem.* **1995**, *34*, 1030-1035.

(238) Siefert, F.; Olesch, M. *Am. Miner.* **1977**, *62*, 547-553.

(239) Wilke, M.; Farges, F.; Petit, P.-E.; Brown, G. E., Jr.; Martin, F. *Am. Miner.* **2001**, *86*, 714-730.

(240) Farges, F. *Phys. Chem. Minerals* **2001**, *28*, 619-629.

(241) Saigo, S.; Hashimoto, H.; Shibayama, N.; Nomura, M.; Nagamura, T. *Biochim. Biophys. Acta* **1993**, *1202*, 99-106.

(242) Cartier, C.; Momenteau, M.; Dartyge, E.; Fontaine, A.; Tourillon, G.; Bianconi, A.; Verdaguer, M. *Biochim. Biophys. Acta* **1992**, *1119*, 169-174.

(243) Cowley, R. E.; DeYonker, N. J.; Eckert, N. A.; Cundari, T. R.; DeBeer, S.; Bill, E.; Ottenwaelder, X.; Flaschenriem, C.; Holland, P. L. *Inorg. Chem.* **2010**, *49*, 6172-6187.

(244) Slep, L. D.; Mijovilovich, A.; Meyer-Klaucke, W.; Weyhermüller, T.; Bill, E.; Bothe, E.; Neese, F.; Wieghardt, K. *J. Am. Chem. Soc.* **2003**, *125*, 15554-15570.

(245) Muñoz-Paez, A.; Díaz-Moreno, S.; Sánchez Marcos, E.; Rehr, J. J. *Inorg. Chem.* **2000**, *39*, 3784-3790.

(246) Jalilehvand, F.; Maliarik, M.; Sandstrom, M.; Mink, J.; Persson, I.; Persson, P.; Toth, I.; Glaser, J. *Inorg. Chem.* **2001**, *40*, 3889-3899.

(247) Westre, T. E.; Di Cicco, A.; Filipponi, A.; Natoli, C. R.; Hedman, B.; Solomon, E. I.; Hodgson, K. O. *J. Am. Chem. Soc.* **1995**, *117*, 1566-1583.

(248) Westre, T. E.; Di Cicco, A.; Filipponi, A.; Natoli, C. R.; Hedman, B.; Solomon, E. I.; Hodgson, K. O. *J. Am. Chem. Soc.* **1994**, *116*, 6757-6768.

(249) Scarrow, R. C.; Strickler, B. S.; Ellison, J. J.; Shoner, S. C.; Kovacs, J. A.; Cummings, J. G.; Nelson, M. J. *J. Am. Chem. Soc.* **1998**, *120*, 9237-9245.

(250) Rich, A. M.; Armstrong, R. S.; Ellis, P. J.; Lay, P. A. *J. Am. Chem. Soc.* **1998**, *120*, 10827-10836.

(251) Rich, A. M.; Ellis, P. J.; Tennant, L.; Wright, P. E.; Armstrong, R. S.; Lay, P. A. *Biochemistry* **1999**, *38*, 16491-16499.

(252) Clay, M. D.; Jenney, F. E.; Hagedoorn, P. L.; George, G. N.; Adams, M. W. W.; Johnson, M. K. *J. Am. Chem. Soc.* **2001**, *124*, 788-805.

(253) Aitken, J. B.; Thomas, S. E.; Stocker, R.; Thomas, S. R.; Takikawa, O.; Armstrong, R. S.; Lay, P. A. *Biochemistry* **2004**, *43*, 4892-4898.

(254) Immoos, C. E.; Sulc, F.; Farmer, P. J.; Czarnecki, K.; Bocian, D. F.; Levina, A.; Aitken, J. B.; Armstrong, R. S.; Lay, P. A. *J. Am. Chem. Soc.* **2004**, *127*, 814-815.

(255) Levina, A.; Armstrong, R. S.; Lay, P. A. *Coord. Chem. Rev.* **2005**, *249*, 141-160.

(256) Ray, K.; England, J.; Fiedler, A. T.; Martinho, M.; Münck, E.; Que, L., Jr. *Angew. Chem. Int. Ed.* **2008**, *47*, 8068-8071.

(257) Jonas, R. T.; Stack, T. D. P. *J. Am. Chem. Soc.* **1997**, *119*, 8566-8567.

(258) Roelfes, G.; Lubben, M.; Chen, K.; Ho, R. Y. N.; Meetsma, A.; Genseberger, S.; Hermant, R. M.; Hage, R.; Mandal, S. K.; Young, V. G.; Zang, Y.; Kooijman, H.; Spek, A. L.; Que, L., Jr.; Feringa, B. L. *Inorg. Chem.* **1999**, *38*, 1929-1936.

(259) Roelfes, G.; Vrajmasu, V.; Chen, K.; Ho, R. Y. N.; Rohde, J.-U.; Zondervan, C.; la Crois, R. M.; Schudde, E. P.; Lutz, M.; Spek, A. L.; Hage, R.; Feringa, B. L.; Münck, E.; Que, L., Jr. *Inorg. Chem.* **2003**, *42*, 2639-2653.

(260) Goldsmith, C. R.; Cole, A. P.; Stack, T. D. P. *J. Am. Chem. Soc.* **2005**, *127*, 9904-9912.

(261) MacBeth, C. E.; Gupta, R.; Mitchell-Koch, K. R.; Young, V. G.; Lushington, G. H.; Thompson, W. H.; Hendrich, M. P.; Borovik, A. S. *J. Am. Chem. Soc.* **2004**, *126*, 2556-2567.

(262) Mukherjee, J.; Lucas, R. L.; Zart, M. K.; Powell, D. R.; Day, V. W.; Borovik, A. S. *Inorg. Chem.* **2008**, *47*, 5780-5786.

(263) DeBeer George, S.; Petrenko, T.; Neese, F. *J. Phys. Chem. A* **2008**, *112*, 12936-12943.

(264) Balasubramanian, R.; Rosenzweig, A. C. *Acc. Chem. Res.* **2007**, *40*, 573-580.

(265) Fox, B. G.; Lyle, K. S.; Rogge, C. E. *Acc. Chem. Res.* **2004**, *37*, 421-429.

(266) Vu, V. V.; Emerson, J. P.; Martinho, M.; Kim, Y. S.; Münck, E.; Park, M. H.; Que, L., Jr. *Proc. Natl. Acad. Sci. U.S.A.* **2009**, *106*, 14814-14819.

(267) Lee, S.-K.; Fox, B. G.; Froland, W. A.; Lipscomb, J. D.; Münck, E. *J. Am. Chem. Soc* **1993**, *115*, 6450-6451.

(268) Liu, K. E.; Valentine, A. M.; Wang, D.; Huynh, B. H.; Edmondson, D. E.; Salifoglou, A.; Lippard, S. J. *J. Am. Chem. Soc* **1995**, *117*, 10174-10185.

(269) Ghosh, A.; Oliveira, F. T. d.; Yano, T.; Nishioka, T.; Beach, E. S.; Kinoshita, I.; Münck, E.; Ryabov, A. D.; Horwitz, C. P.; Collins, T. J. *J. Am. Chem. Soc* **2005**, *127*, 2505-2513.

(270) Xue, G. Q.; Wang, D.; De Hont, R.; Fiedler, A. T.; Shan, X. P.; Münck, E.; Que, L., Jr. *Proc. Natl. Acad. Sci. U.S.A.* **2007**, *104*, 20713-20718.

(271) Xue, G. Q.; Fiedler, A. T.; Martinho, M.; Münck, E.; Que, L., Jr. *Proc. Natl. Acad. Sci. U.S.A.* **2008**, *105*, 20615-20620.

(272) Xue, G.; De Hont, R.; Münck, E.; Que, L., Jr. *Nat. Chem.* **2010**, *2*, 400-405.

(273) Roe, A. L.; Schneider, D. J.; Mayer, R. J.; Pyrz, J. W.; Widom, J.; Que, L., Jr. *J. Am. Chem. Soc.* **1984**, *106*, 1676-1681.

(274) Fiedler, A. T.; Shan, X.; Mehn, M. P.; Kaizer, J.; Torelli, S.; Frisch, J. R.; Kodera, M.; Que, L., Jr. *J. Phys. Chem. A* **2008**, *112*, 13037-13044.

(275) Scott, R. A.; Eidsness, M. K. *Comments Inorg. Chem.* **1988**, *7*, 235 - 267.

(276) Hsu, H. F.; Dong, Y. H.; Shu, L. J.; Young, V. G.; Que, L., Jr. *J. Am. Chem. Soc.* **1999**, *121*, 5230-5237.

(277) Klinker, E. J.; Jackson, T. A.; Jensen, M. P.; Stubna, A.; Juhász, G.; Bominaar, E. L.; Münck, E.; Que, L., Jr. *Angew. Chem. Int. Ed.* **2006**, *45*, 7394-7397.

(278) Sanders-Loehr, J.; Wheeler, W. D.; Shiemke, A. K.; Averill, B. A.; Loehr, T. M. *J. Am. Chem. Soc.* **1989**, *111*, 8084-8093.

(279) Dong, Y.; Fujii, H.; Hendrich, M. P.; Leising, R. A.; Pan, G.; Randall, C. R.; Wilkinson, E. C.; Zang, Y.; Que, L., Jr. *J. Am. Chem. Soc.* **1995**, *117*, 2778-2792.

(280) Zheng, H.; Zang, Y.; Dong, Y.; Young, V. G.; Que, L., Jr. *J. Am. Chem. Soc.* **1999**, *121*, 2226-2235.

(281) Neese, F. *Coord. Chem. Rev.* **2009**, *253*, 526-563.

Appendix

The graphical and tabular material shown in this Appendix is provided to supplement the data and results presented in preceding chapters in this thesis, specifically Chapters 2, 3, 4, 5, and 6. The numbering scheme corresponds to the chapter for which a given plot or table is associated with. For example, Figure A2.1 shows data related to the project described in Chapter 2.

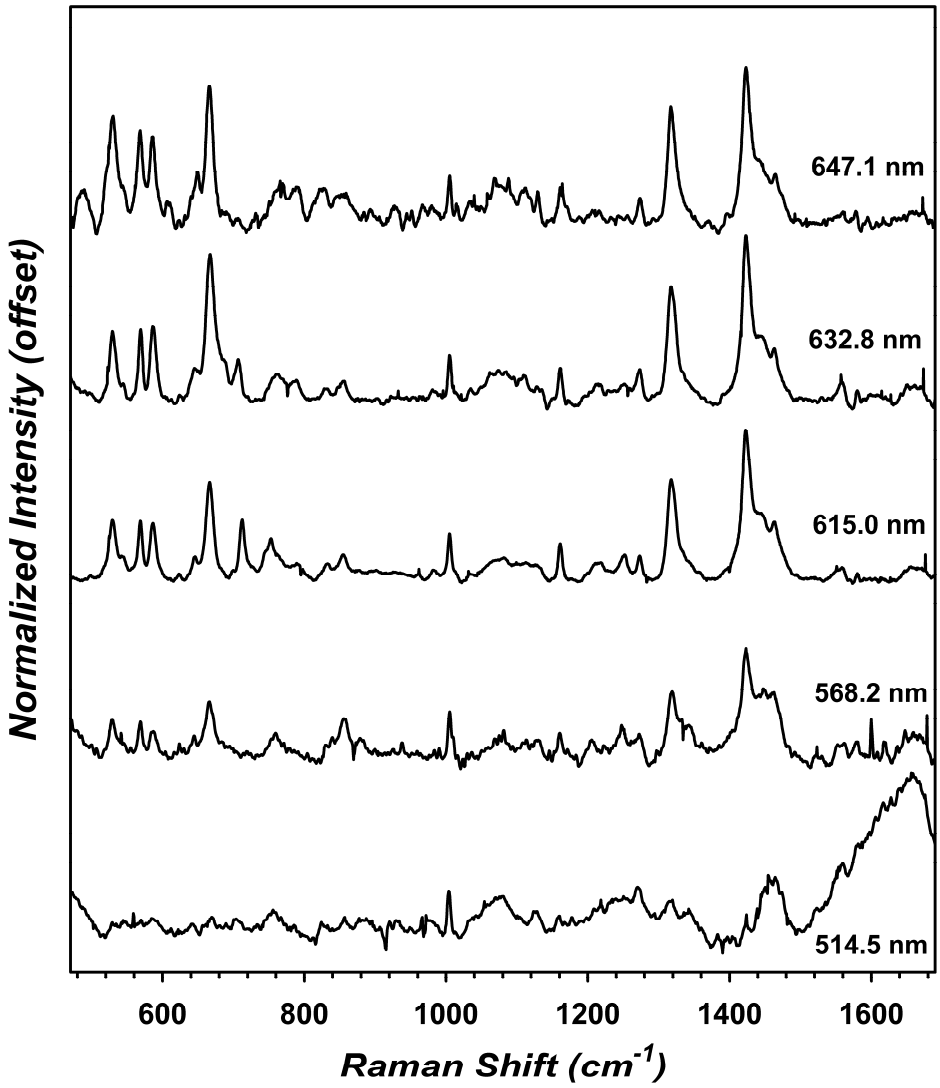

Figure A2.1. Resonance Raman spectra for BG-FeMndD obtained at five different excitation wavelengths, which were used to generate the excitation profile shown in Figure 2.3. The spectral intensities are relative to the normalized intensity of the non-resonance enhanced 1005 cm^{-1} band corresponding to a phenylalanine ring mode,[107] and have been offset for clarity.

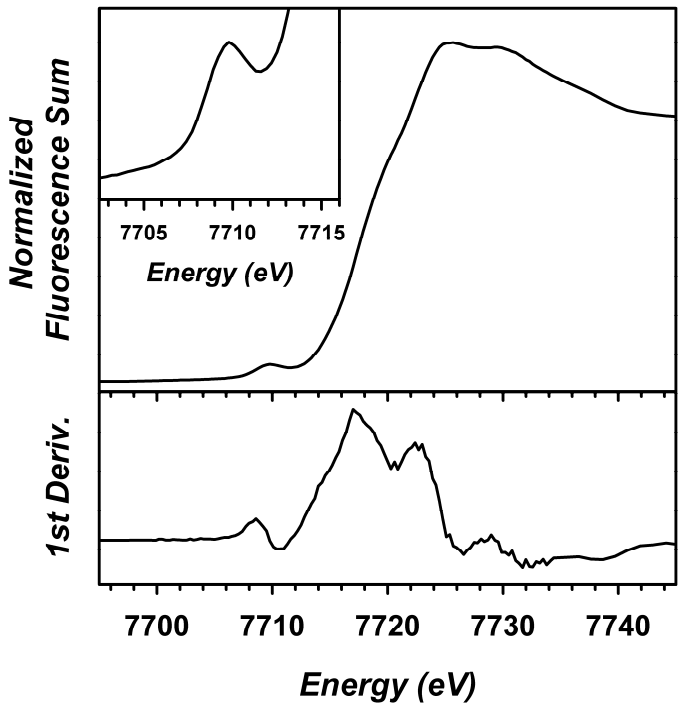

Figure A3.1. Edge spectra and 1st derivatives thereof for **1-S_2COEt**.

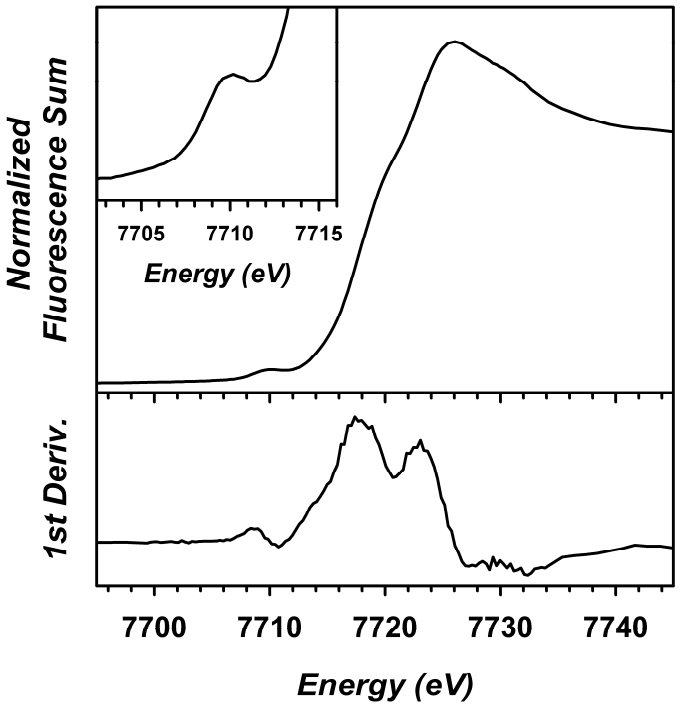

Figure A3.2. Edge spectra and 1st derivatives thereof for **1-S_2CNPh$_2$**.

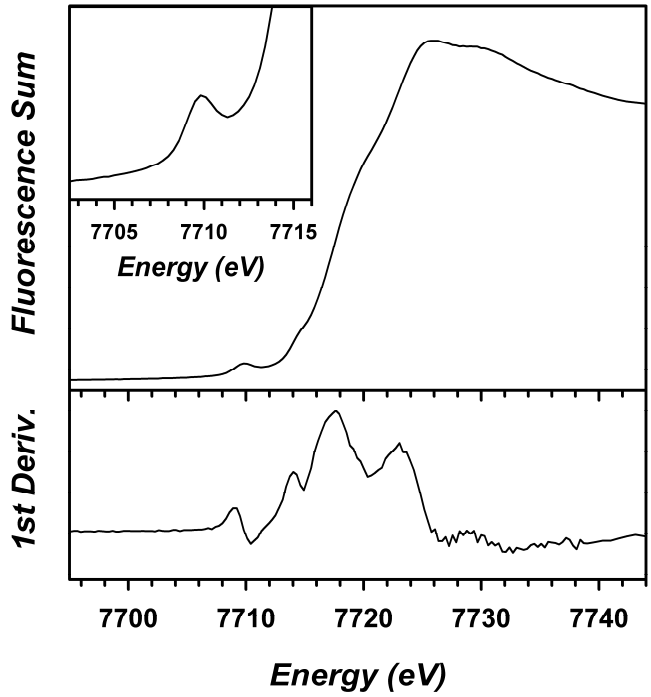

Figure A3.3. Edge spectra and 1st derivatives thereof for **1-S_2CNEt_2**.

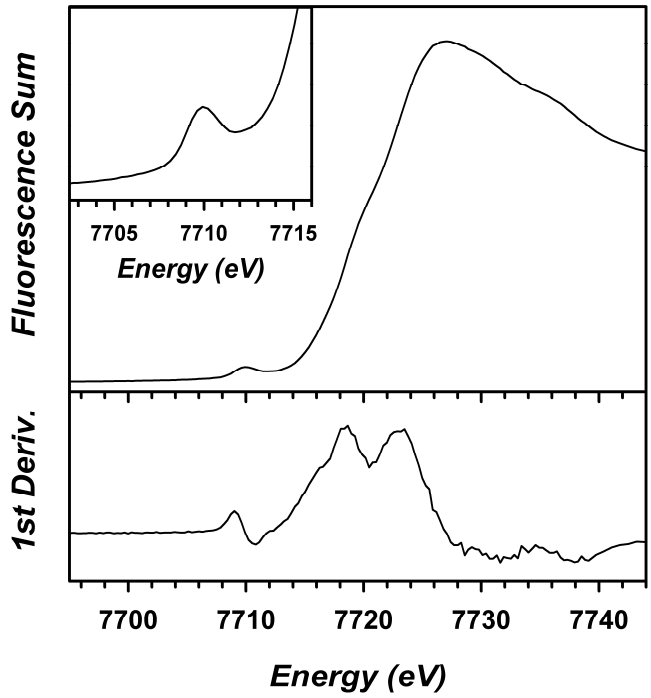

Figure A3.4. Edge spectra and 1st derivatives thereof for **1-acac**.

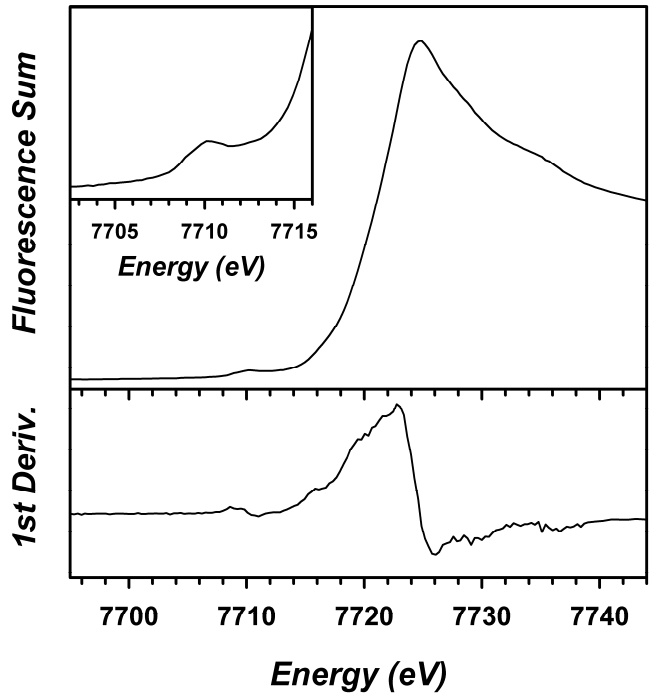

Figure A3.5. Edge spectra and 1st derivatives thereof for **CoHPCD**.

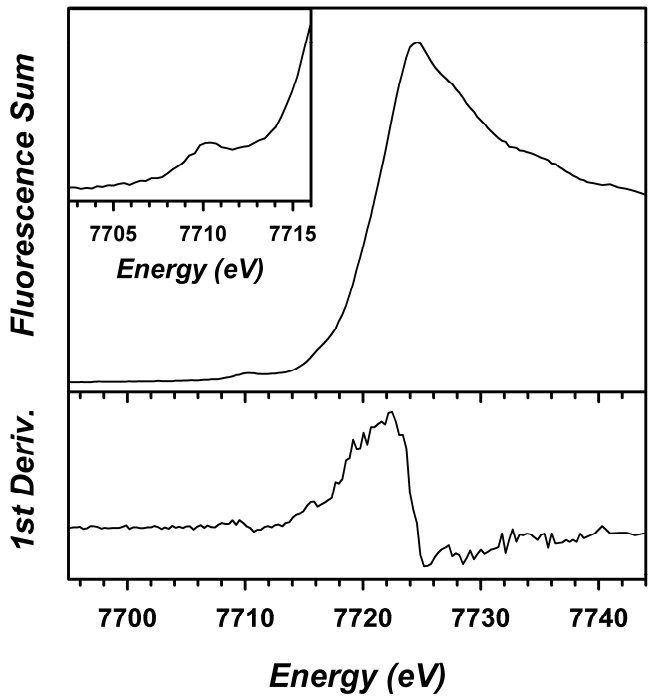

Figure A3.6. Edge spectra and 1st derivatives thereof for **CoHPCD-HPCA**.

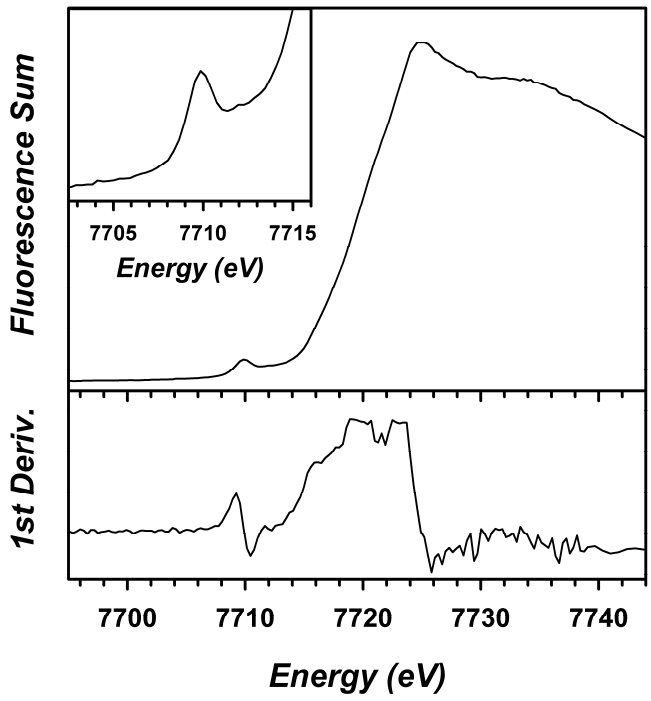

Figure A3.7. Edge spectra and 1st derivatives thereof for **CoHPCD-3HPA**.

Table A4.1. Fourier-Filtered EXAFS Analysis of **1-Bl.S.**.[a]

	Fe-N/O			Fe-O/N			Fe•••C			Fe•••C				
fit	**n**	**r**	**σ^2**	**n**	**r**	**σ^2**	**n**	**r**	**σ^2**	**n**	**r**	**σ^2**	**F**	***F'***
27	3	2.04	2.5										421.5	1.110
28	4	2.04	3.9										406.5	1.033
29	5	2.04	5.3										445.9	1.243
30	6	2.04	6.8										524.4	1.719
31	3	2.04	2.3	1	1.66	2.4							302.6	0.654
31a	3	2.04	2.2	0.9	1.66	1.7							285.1	0.581
32	4	2.04	3.9	1	1.66	2.8							233.1	0.388
32a	4	2.04	3.9	0.9	1.66	2.2							224.7	0.361
33	5	2.03	5.4	1	1.67	3.0							213.6	0.326
33a	5	2.04	5.4	0.9	1.67	2.4							213.2	0.325
34	4 1	2.04 2.22	3.9 27.2	0.9	1.67	2.2							210.1	0.368
35	3 1	2.00 2.09	2.1 -0.3	0.9	1.66	2.8							221.3	0.408
36	3 2	2.03 2.02	3.1 14.0	0.9	1.66	2.1							229.4	0.439
37	4 1	2.07 1.98	5.7 0.6										440.8	1.388
38	4 1	2.04 2.22	3.9 27.9	0.9	1.66	2.2							210.1	0.368
39	3 1	2.08 1.96	0.9 -1.8										387.4	1.072
40	3 1	2.05 1.98	3.5 4.5	0.9	1.66	2.3							232.5	0.450
41	5	2.03	5.4	0.9	1.67	2.4	3	2.95	9.1				178.6	0.266
42	*5*	*2.03*	*5.4*	*0.9*	*1.67*	*2.5*	*4*	*2.94*	*11.5*				*179.9*	*0.270*
43	5	2.03	5.4	0.9	1.67	2.4	5	2.93	13.5				184.7	0.284

44	5	2.03	5.4	0.9	1.67	2.6	4 2	2.85 3.02	9.5 1.8				180.1	0.324
45	5	2.03	5.4	0.9	1.67	2.6	4 3	2.83 3.01	8.4 3.3				185.7	0.345
46	*5*	*2.03*	*5.4*	*0.9*	*1.67*	*2.5*	*3* *3*	*2.82* *3.00*	*6.0* *3.3*				*179.7*	*0.323*
47	5	2.03	5.4	0.9	1.67	2.5	3 2	2.85 3.02	7.0 1.6				172.5	0.298
48	5	2.03	5.4	0.9	1.67	2.4	4	2.94	11.7	2	3.42	1.8	140.5	0.197
49	5	2.03	5.4	0.9	1.67	2.4	4	2.95	11.7	3	3.42	3.5	133.0	0.177
50	5	2.03	5.4	0.9	1.67	2.4	4	2.95	11.5	4	3.43	5.0	128.8	0.166
51	*5*	*2.03*	*5.4*	*0.9*	*1.67*	*2.4*	*4*	*2.95*	*11.5*	*5*	*3.43*	*6.6*	*127.1*	*0.162*
52	5	2.03	5.4	0.9	1.67	2.4	4	2.96	11.4	6	3.44	8.3	127.2	0.162
53	5	2.03	5.4	0.9	1.67	2.5	4	2.96	11.2	7	3.44	10.2	128.7	0.166
54	5	2.03	5.4	0.9	1.67	2.6	4 2	2.87 3.03	10.1 2.0	5	3.42	6.0	116.7	0.170
55	5	2.03	5.4	0.9	1.67	2.5	3 2	2.86 3.02	7.2 1.5	5	3.43	5.9	115.0	0.165
56	***5***	***2.03***	***5.4***	***0.9***	***1.67***	***2.5***	***3*** ***3***	***2.84*** ***3.01***	***6.1*** ***3.2***	***5***	***3.42***	***6.1***	***116.0***	***0.168***

[a] Fourier transform range k = 2.0 - 14.0 Å^{-1} (resolution = 0.13 Å). r is in units of Å; σ^2 is in units of 10^{-3} Å^2. All fits shown here were to Fourier-filtered data employing back transformation ranges of 0.7 – 3.2 Å.

[b] Goodness-of-fit parameter F defined as $\Sigma(\chi_{exptl}-\chi_{calc})^2$. A second parameter, F', is defined as $F' = F^2 / \nu$, where $\nu = N_{IDP} - N_{VAR}$. N_{IDP} is the number of independent data points, while N_{VAR} is the number of floated variables in each optimization step. The values of F' shown have been divided by a factor of 10^4 for convenience. F' is a measure of whether an added shell significantly improves the fit.

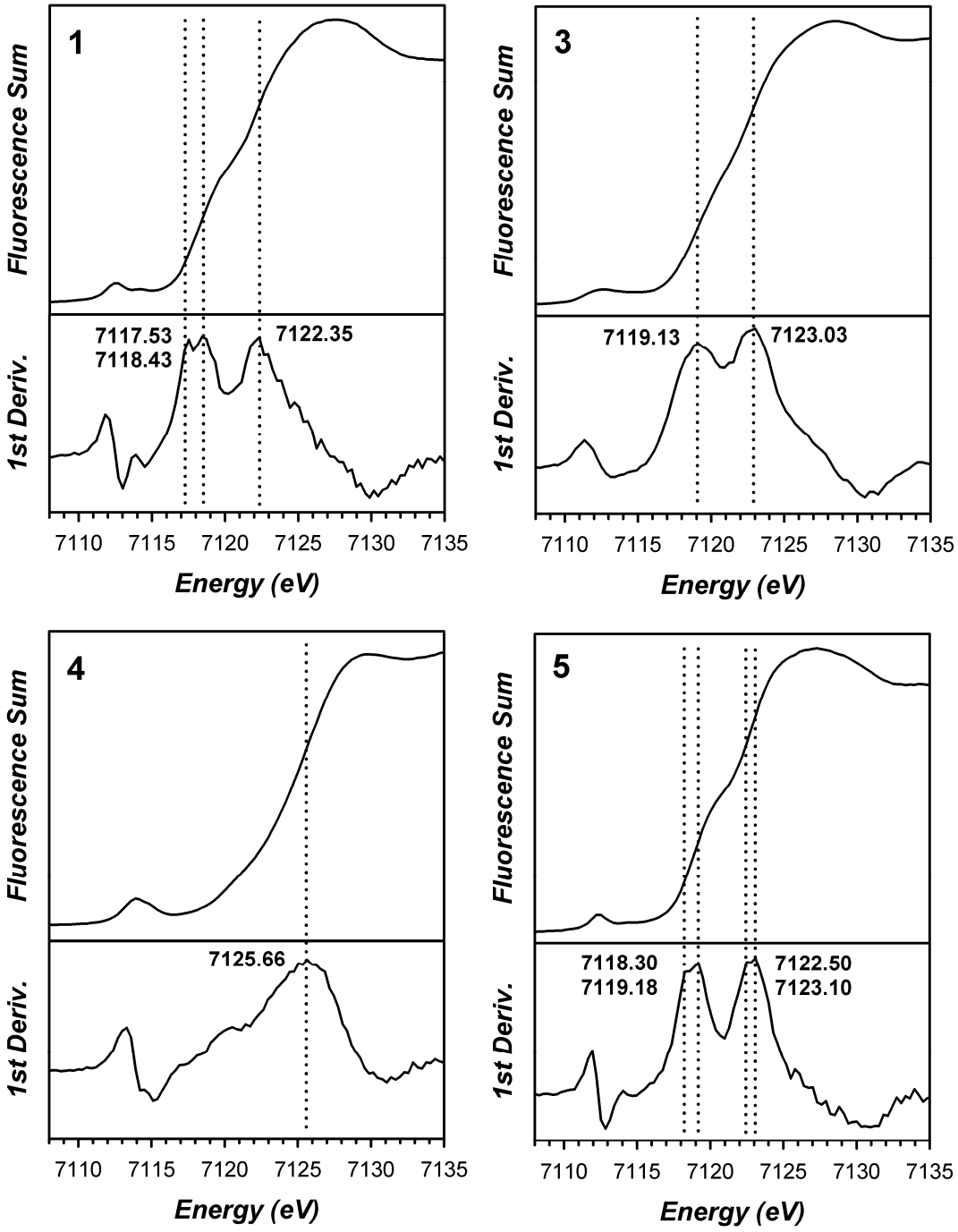

Figure A5.1. Fe K-edge XANES spectra and first derivatives thereof for **1** (upper left), **3** (upper right), **4** (lower left), and **5** (lower right). The dotted lines indicate the position of maxima in the first derivative associated with inflection points in the XANES spectra, with energies shown in bold-face.

Table A6.1. Single-Scattering Analysis of Unfiltered EXAFS Data for **2-CN**.[a]

	Fe-N/C			Fe•••C			Fe•••C					
fit	**n**	**r**	**σ^2**	**n**	**r**	**σ^2**	**n**	**r**	**σ^2**	**F** [b]	***F*-factor** [b]	***F'*** [b]
1	2	2.09	-0.7							684	0.636	2.37
2	3	2.09	0.8							640	0.615	2.07
3	4	2.09	2.2							676	0.632	2.31
4	5	2.09	3.5							765	0.672	2.96
5	3 1	2.09 2.30	0.8 29.7							634	0.612	2.26
6	3	2.09	0.8	3	3.06	1.0				490	0.538	1.35
6a	3	2.09	0.8	4	3.06	1.9				486	0.535	1.32
6b	3	2.09	0.7	5	3.06	2.8				493	0.540	1.37
6c	3	2.09	0.7	6	3.06	3.6				510	0.549	1.46
7	3	2.09	0.9				4	3.41	0.7	490	0.538	1.35
7a	3	2.09	0.9				5	3.41	1.4	488	0.536	1.34
7b	3	2.09	0.9				6	3.41	2.1	491	0.538	1.35
7c	3	2.09	0.9				7	3.42	3.0	499	0.543	1.40
8	3	2.09	1.0	4	3.06	0.9	5	3.41	0.6	261	0.392	0.43
8a	3	2.09	0.9	5	3.06	2.0	6	3.42	1.7	252	0.386	0.40
8b	***3***	***2.09***	***0.9***	***6***	***3.06***	***3.0***	***7***	***3.42***	***2.6***	***250***	***0.384***	***0.39***
8c	3	2.09	0.9	6	3.06	2.9	6	3.42	1.8	255	0.388	0.41
8d	3	2.09	0.9	7	3.06	3.9	7	3.42	2.7	256	0.389	0.42

[a] *r* is in units of Å; σ^2 is in units of 10^{-3} Å^2. All fits are to unfiltered data. Fourier transform range k = 2.0 – 14.8 Å^{-1} (resolution = 0.123 Å).

[b] Goodness-of-fit parameter F defined as $\Sigma(\chi_{exptl}-\chi_{calc})^2$. *F-factor* = $[\Sigma k^6(\chi_{exptl}-\chi_{calc})^2 / \Sigma k^6\chi_{exptl}^2]^{1/2}$. A third parameter, *F'*, is defined as $F' = F^2 / \nu$, where $\nu = N_{IDP} - N_{VAR}$. N_{IDP} is the number of independent data points, while N_{VAR} is the number of floated variables in each optimization step. The values of *F'* shown have been divided by a factor of 10^4 for convenience. *F'* is a measure of whether an added shell significantly improves the fit.

Table A6.2. Single-Scattering Analysis of Unfiltered EXAFS Data for **3-CN**.[a]

	Fe-N/C			Fe•••C			Fe•••C					
fit	**n**	**r**	**σ^2**	**n**	**r**	**σ^2**	**n**	**r**	**σ^2**	**F** [b]	***F*-factor** [b]	***F'*** [b]
1	2	2.02	0.4							1020	0.731	5.88
2	3	2.02	2.1							943	0.703	5.02
3	4	2.01	3.7							943	0.703	5.02
4	5	2.01	5.3							993	0.721	5.57
5	3 1	2.02 2.07	2.2 25.5							931	0.698	5.52
5a	4 1	2.02 2.28	3.5 15.0							933	0.699	5.54
6	4	2.01	3.8	4	3.00	1.0				663	0.589	2.80
6a	4	2.01	3.7	5	3.00	1.7				655	0.586	2.74
6b	4	2.01	3.6	6	3.00	2.5				660	0.588	2.78
6c	4	2.01	3.5	7	3.00	2.9				674	0.594	2.89
7	4	2.01	3.8				4	3.37	1.0	745	0.625	3.53
7a	4	2.01	3.7				5	3.37	1.8	723	0.616	3.33
7b	4	2.00	3.7				6	3.37	2.4	705	0.608	3.17
7c	4	2.00	3.7				7	3.36	2.6	690	0.601	3.03
7d	4	1.99	3.8				8	3.35	3.0	677	0.596	2.92
7e	4	1.99	3.9				10	3.33	3.5	655	0.586	2.73
8	4	2.01	3.9	5	3.00	0.7	5	3.38	0.5	362	0.436	0.96
8a	4	2.01	3.9	7	3.00	2.5	7	3.38	2.3	331	0.416	0.80
8b	***4***	***2.01***	***3.9***	***6***	***3.00***	***1.9***	***8***	***3.39***	***2.9***	***317***	***0.408***	***0.74***
8c	4	2.01	3.9	6	3.00	2.0	10	3.39	4.1	312	0.404	0.71
8d	4	2.01	3.8	8	3.00	3.6	12	3.39	5.6	300	0.396	0.66

[a] *r* is in units of Å; σ^2 is in units of 10^{-3} Å^2. All fits are to unfiltered data. Fourier transform range k = 2.0 – 14.5 Å^{-1} (resolution = 0.126 Å).

[b] Goodness-of-fit parameter F defined as $\Sigma(\chi_{exptl}-\chi_{calc})^2$. *F-factor* = $[\Sigma k^6(\chi_{exptl}-\chi_{calc})^2 / \Sigma k^6\chi_{exptl}^2]^{1/2}$. A third parameter, *F'*, is defined as $F' = F^2 / \nu$, where $\nu = N_{IDP} - N_{VAR}$. N_{IDP} is the number of independent data points, while N_{VAR} is the number of floated variables in each optimization step. The values of *F'* shown have been divided by a factor of 10^4 for convenience. *F'* is a measure of whether an added shell significantly improves the fit.

Table A6.3. Single-Scattering Analysis of Unfiltered EXAFS Data for **4-CN**.[a]

	Fe-N/C			Fe-N			Fe•••C			Fe•••C					
fit	**n**	**r**	**σ^2**	**n**	**r**	**σ^2**	**n**	**r**	**σ^2**	**n**	**r**	**σ^2**	**F** [b]	***F*-factor**$_b$	***F'*** [b]
1	2	1.81	0.4										841	0.675	3.89
2	3	1.81	2.1										866	0.685	4.12
3	4	1.81	3.8										966	0.723	5.12
4	5	1.80	5.7										1101	0.772	6.66
5	3	1.82	2.1	1	2.03	1.3							815	0.664	4.10
5a	4	1.82	4.2	1	2.04	-0.4							850	0.678	4.45
6	3	1.83	2.2	1	2.04	0.4	4	2.87	1.0				457	0.498	1.47
6a	3	1.83	2.3	1	2.04	0.3	5	2.87	1.8				439	0.488	1.36
6b	***3***	***1.83***	***2.2***	***1***	***2.04***	***0.4***	***6***	***2.87***	***2.5***				***434***	***0.485***	***1.33***
6c	3	1.83	2.2	1	2.04	0.5	7	2.87	3.1				441	0.489	1.37
7	3	1.82	2.1	1	2.03	2.0				4	3.33	15.1	768	0.645	4.15
7a	3	1.82	2.1	1	2.03	2.0				5	3.33	16.6	761	0.642	4.08
8	3	1.83	2.2	1	2.04	0.3	4	2.86	0.9	4	3.46	3.4	414	0.474	1.41
8a	3	1.83	2.2	1	2.04	0.2	5	2.86	1.6	4	3.46	3.6	394	0.462	1.27
8b	***3***	***1.83***	***2.2***	***1***	***2.04***	***0.3***	***6***	***2.86***	***2.2***	***4***	***3.46***	***3.7***	***388***	***0.459***	***1.24***
8c	3	1.83	2.2	1	2.04	0.4	5	2.86	1.6	5	3.46	5.7	397	0.464	1.29
8d	3	1.83	2.2	1	2.04	0.5	6	2.86	2.3	5	3.46	6.4	391	0.460	1.25
8e	3	1.83	2.2	1	2.04	0.6	6	2.87	2.4	6	3.35	23.9	381	0.454	1.19

[a] *r* is in units of Å; σ^2 is in units of 10^{-3} Å^2. All fits are to unfiltered data. Fourier transform range $k = 2.0 - 14.8$ Å^{-1} (resolution = 0.123 Å).

[b] Goodness-of-fit parameter F defined as $\Sigma(\chi_{exptl}-\chi_{calc})^2$. *F-factor* = $[\Sigma k^6(\chi_{exptl}-\chi_{calc})^2 / \Sigma k^6\chi_{exptl}^2]^{1/2}$. A third parameter, *F'*, is defined as $F' = F^2 / \nu$, where $\nu = N_{IDP} - N_{VAR}$. N_{IDP} is the number of independent data points, while N_{VAR} is the number of floated variables in each optimization step. The values of *F'* shown have been divided by a factor of 10^4 for convenience. *F'* is a measure of whether an added shell significantly improves the fit.

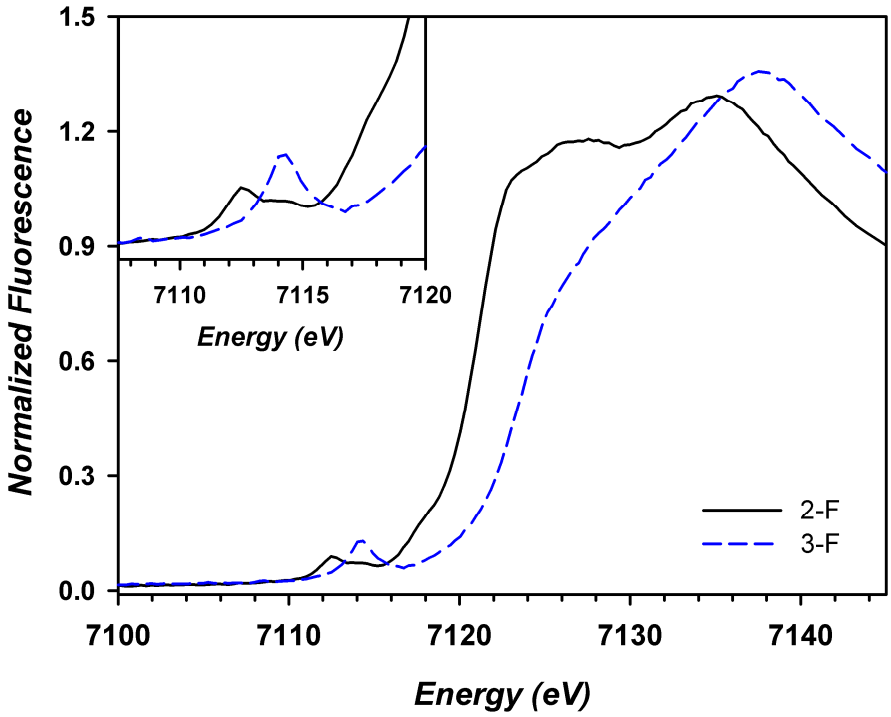

Figure A6.1. Comparison of the Fe K-edge X-ray absorption edge and pre-edge (inset) features of **2-F** (black, ——) and **3-F** (blue, – – –).

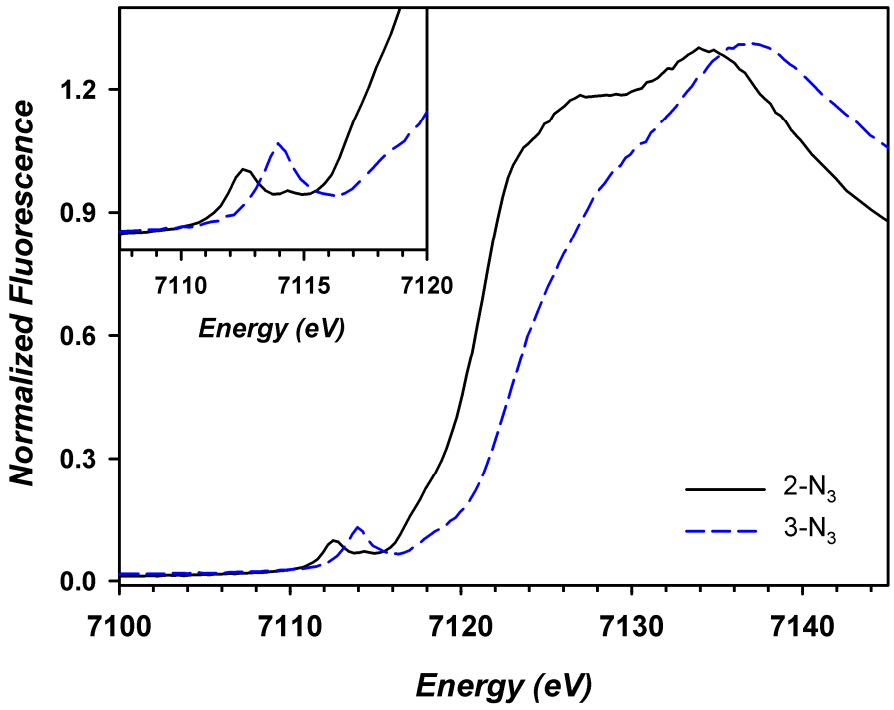

Figure A6.2. Comparison of the Fe K-edge X-ray absorption edge and pre-edge (inset) features of **2-N_3** (black, ——) and **3-N_3** (blue, – – –).

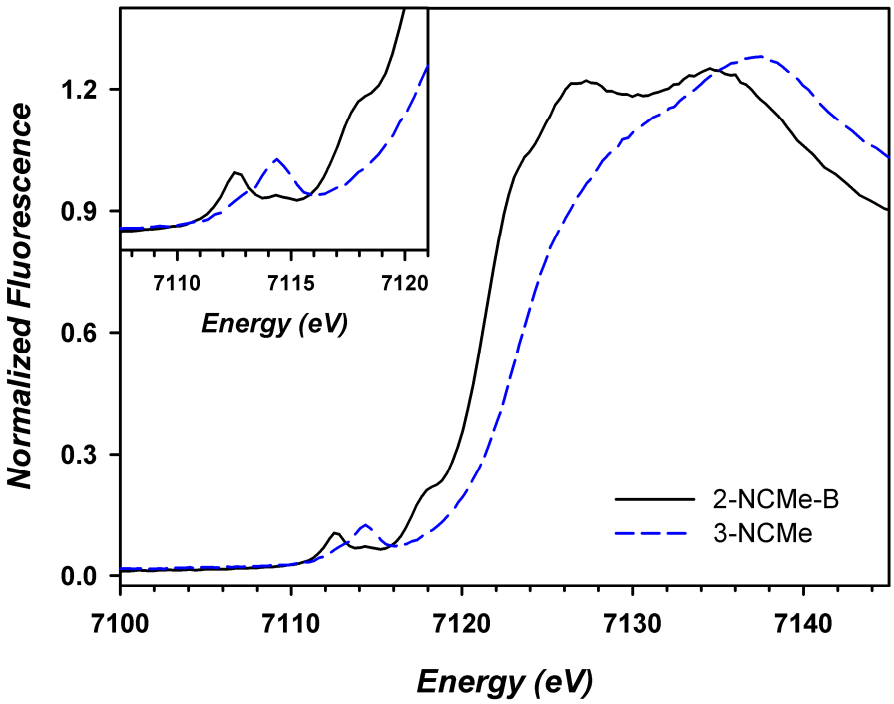

Figure A6.3. Comparison of the Fe K-edge X-ray absorption edge and pre-edge (inset) features of **2-NCMe-B** (black, ——) and **3-NCMe** (blue, – – –).

Shown below are XANES spectra and their first and second derivatives for all **2-**, **3-**, and **4-X** complexes examined in this work (**X** = $\mathbf{F^-}$, $\mathbf{N_3^-}$, **NCMe**, and $\mathbf{CN^-}$). Dashed drop lines indicate the positions of pre-edge peaks and peaks along the rising edge that were considered in the XANES analysis, as well as the position of the Fe K-edge inflection point.

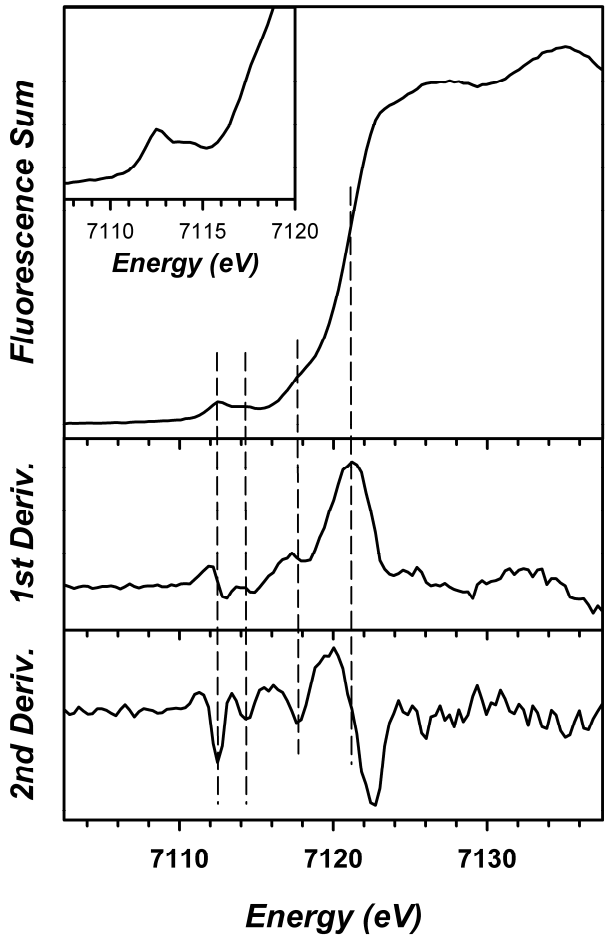

Figure A6.4. XANES spectra and first and second derivatives thereof for **2-F**.

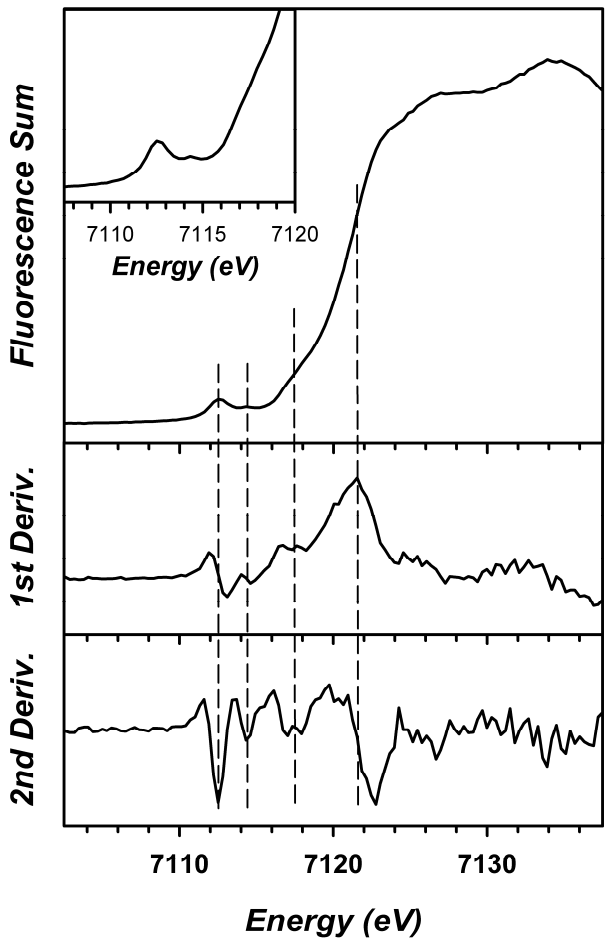

Figure A6.5. XANES spectra and first and second derivatives thereof for **2-N_3**.

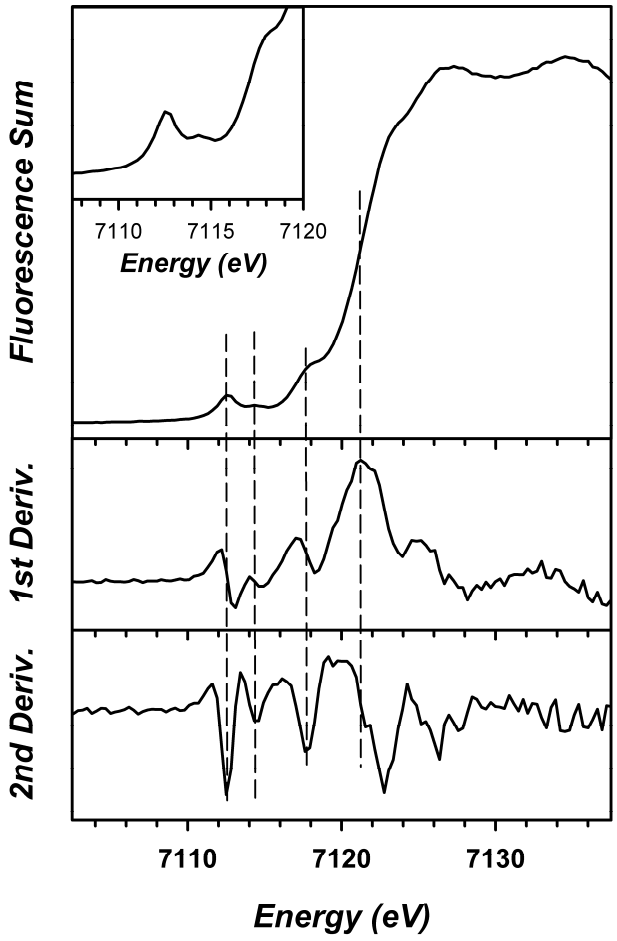

Figure A6.6. XANES spectra and first and second derivatives thereof for **2-NCMe-B**.

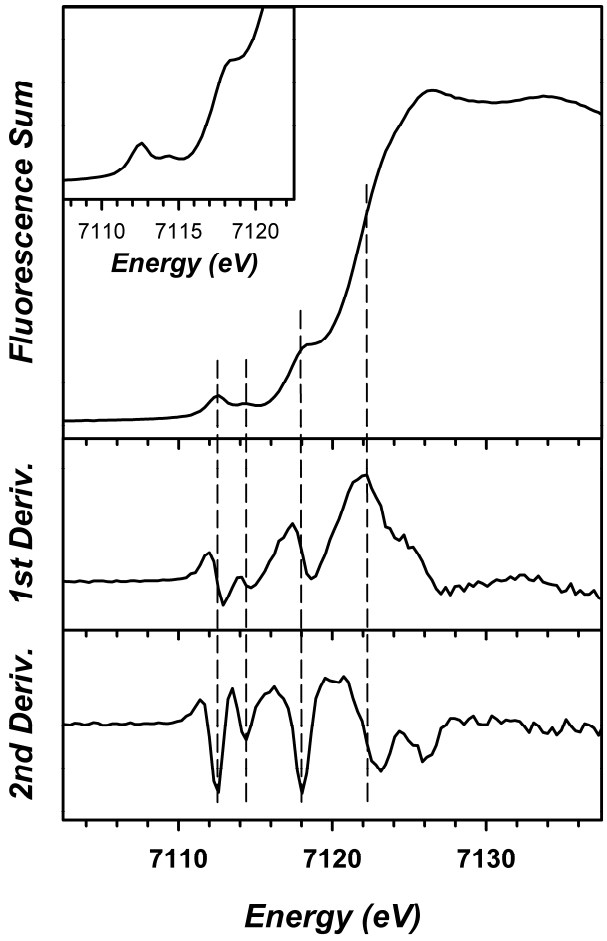

Figure A6.7. XANES spectra and first and second derivatives thereof for **2-CN**.

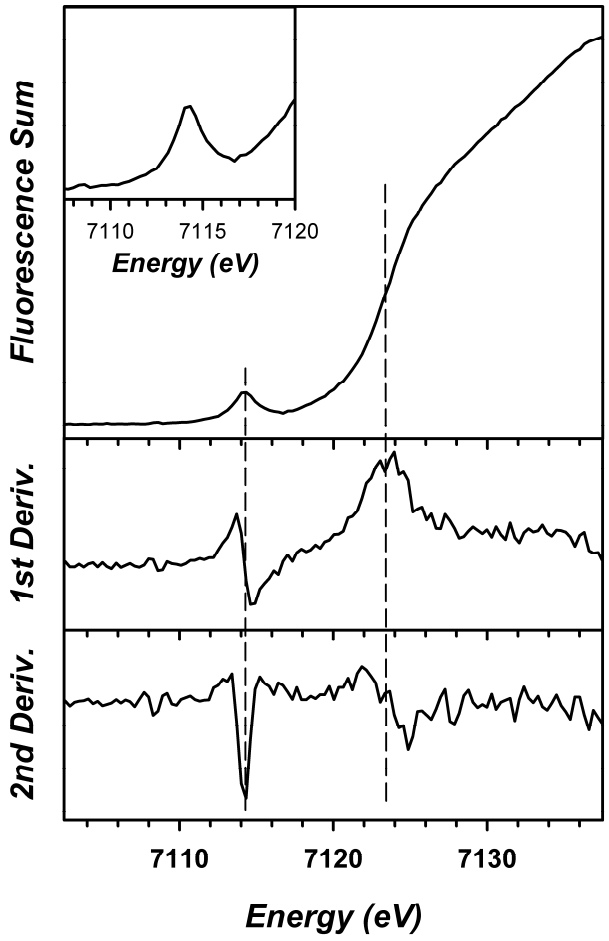

Figure A6.8. XANES spectra and first and second derivatives thereof for **3-F**.

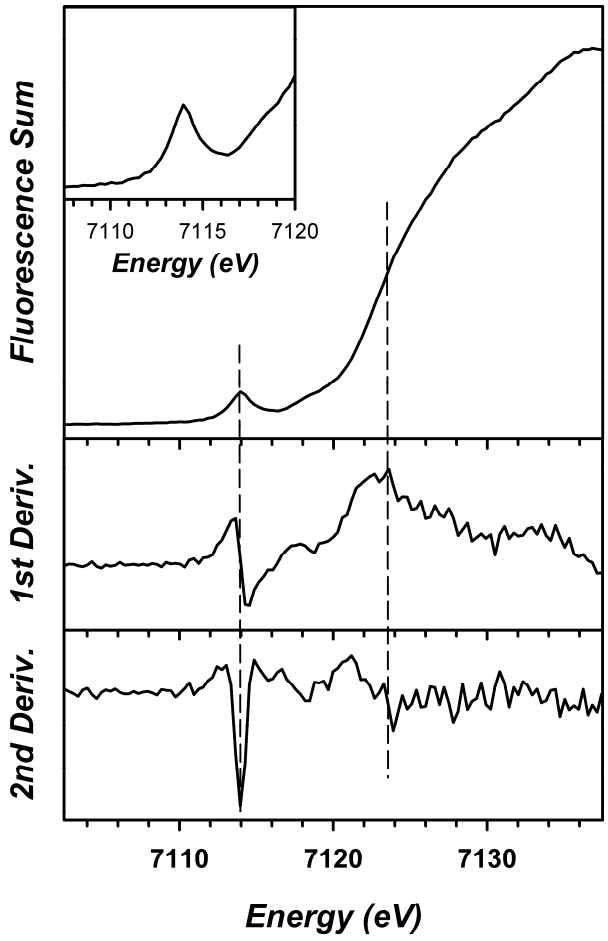

Figure A6.9. XANES spectra and first and second derivatives thereof for **3-N_3**.

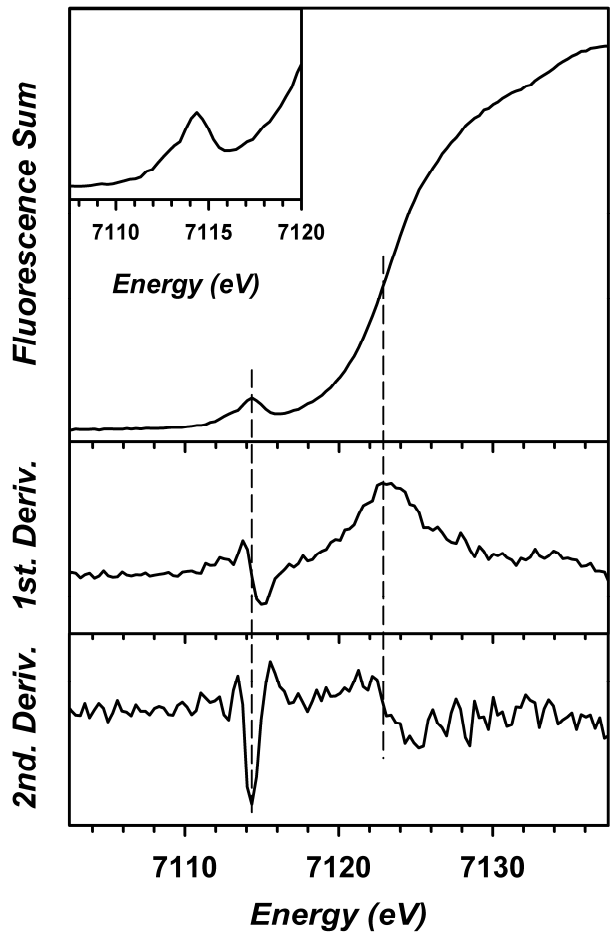

Figure A6.10. XANES spectra and first and second derivatives thereof for **3-NCMe**.

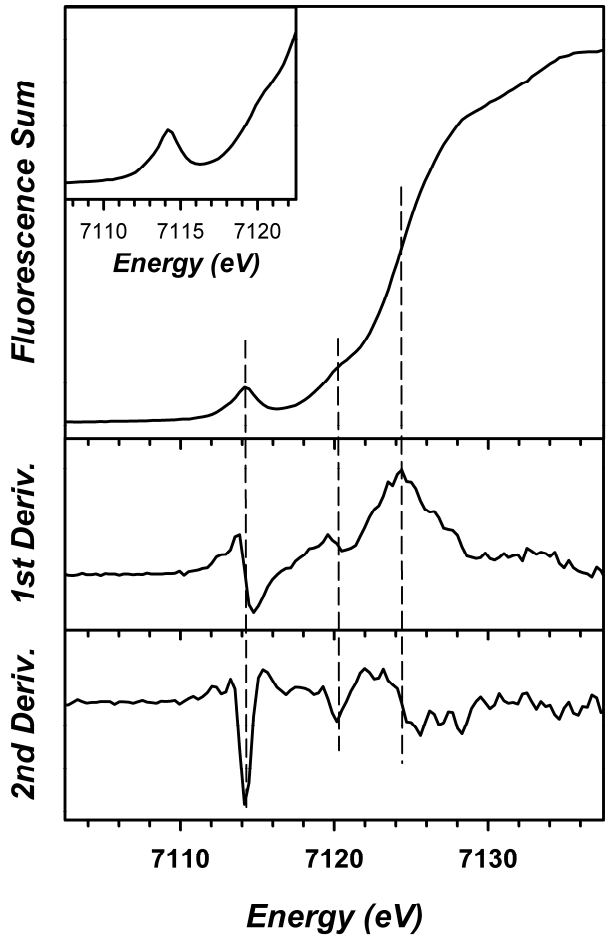

Figure A6.11. XANES spectra and first and second derivatives thereof for **3-CN**.

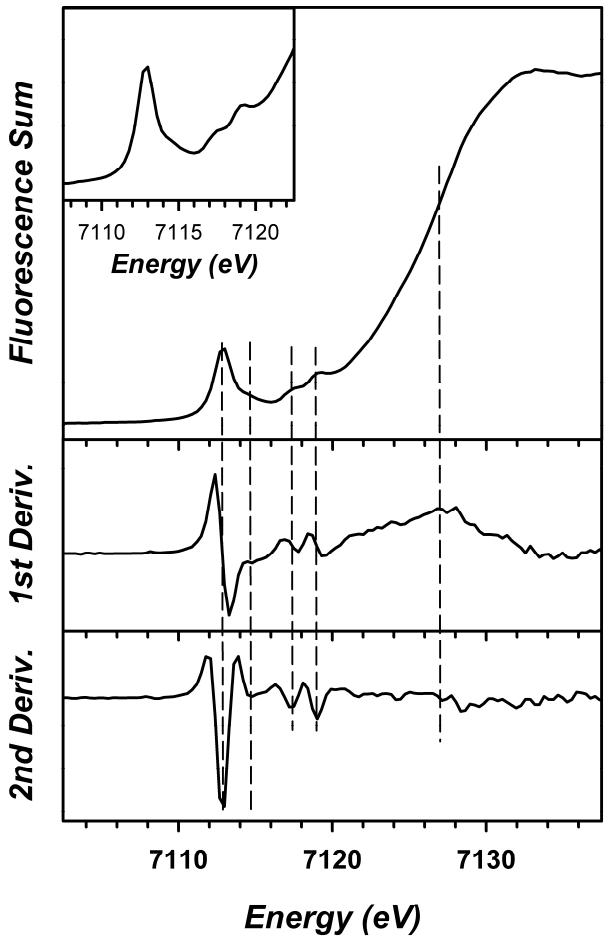

Figure A6.12. XANES spectra and first and second derivatives thereof for **4-CN**.

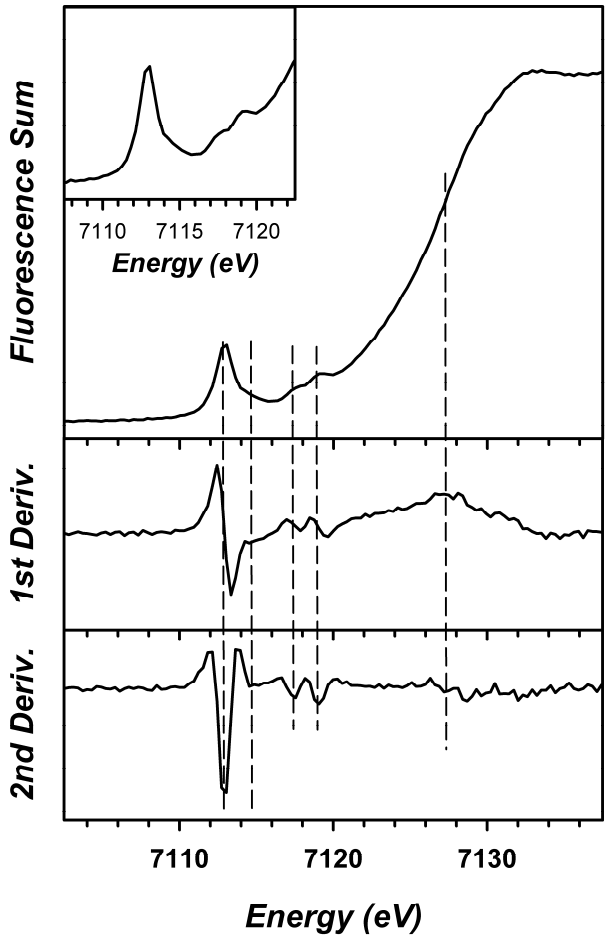

Figure A6.13. XANES spectra and first and second derivatives thereof for **4-CN-B**.